UNIVERSITY OF CALIFORNIA
SANTA CRUZ

Applications of Metal Functionalized Mesoporous Silicate Nanomaterials

And

Synthetic Routes Toward Metal Organic Framework Thin Films on Conductive Substrates

A dissertation submitted in partial satisfaction
of the requirements for the degree of

DOCTOR OF PHILOSOPHY

in

CHEMISTRY

by

Jesse Lee Hauser

June 2019

The Dissertation of Jesse L. Hauser is approved by:

_____
Professor Scott Oliver: Chair

_____
Professor Jin Zhang

_____
Professor Yat Li

_____
Lori Kletzer

Vice Provost and Dean of Graduate Studies

Table of Contents

SECTION TWO

Synthesis Routes Toward Metal Organic Framework Thin Films on Conductive Substrates

List of figures

List of Tables

Acknowledgements

My sincerest thanks to the many people who have assisted with the work contained within this thesis: Karren Bustillo, Dat Tran, Jessica Palomino, Yashar Abdollahian, Ian Colinas, Monique Tso, Edward Conley, John Saunders Gaby Amberchan, Jin Zhang, Yat Li, Tianyi Kou, Susan Citrak, Ana Kareh, Eaindar Soe, Beatriz Ehlke, Pradip Mascharak, and Scott Oliver.

SECTION ONE

Applications of Metal Functionalized Mesoporous Silicate Nanomaterials

Abstract

Presented here are two projects highlighting the metallization of mesoporous silica nanoparticles (MSN) for specific applications in adsorption and heterogeneous catalysis.

The intra-framework incorporation of aluminum during synthesis gives rise to mesoporous aluminosilicate nanoparticles (MASN), which are the primary scaffold presented throughout this work. Because aluminum is trivalent, its tetrahedral coordination by oxygen upon substitution into the SiO_2 framework gives rise to negatively charged sites. This negative surface charge can be taken advantage of in the anchoring of positively charged species such as metal cations and metal-organic complexes.

In the first project, presented in chapter 2, the further metallization of MASN was explored for application in the adsorptive desulfurization of military logistics fuels (i.e. JP8 and JP5), as a portable alternative to the conventional process of industrial hydrodesulfurization (HDS). It was found that the addition of 20w% Ag^+ to MASN by wet impregnation resulted in an adsorbent with good desulfurization capacity (12.7 $mgS \cdot g^{-1}$) for the removal of the refractory pollutant dibenzothiophene (DBT) from model fuel (n-decane). Reuse of the material upon removal of DBT from Ag-MASN with appropriate solvents, however, was not possible, and ICP elemental analysis revealed Ag^+ leached from the MASN in the process. To stabilize the reusability of this Ag-MASN in

model fuel tests, the reduction of extra-framework Ag^{+} to Ag^{0} was performed via glow discharge plasma in a low-pressure argon atmosphere. An average initial desulfurization capacity of 15 $mgS \cdot g^{-1}$, and retention of 79% desulfurization capacity after six reuse cycles, was achieved using this plasma treated Ag-MASN (PT-Ag-MASN), although some silver was still observed to leach from the adsorbent upon cycling.

In another study (chapter 3), MASN was used as a solid support for the heterogeneous catalyst referred commonly referred to as amorphous nickel boride. Sodium borohydride ($NaBH_4$) reduction of $NiCl_2$ impregnated MASN resulted in a thin coating of a highly dispersed nickel-boron composite (NBC). Compared to unsupported bulk NBC, the supported NBC-MASN catalyst was more active for the selective reduction of the nitro group on a variety of substituted nitroarenes reduced with hydrazine hydrate ($N_2H_4 \bullet H_2O$). Up to nine reuse cycles of NBC-MASN for the reduction of *p*-nitrotoluene to *p*-toluidine could be achieved when equimolar $NaBH_4$ (catalyst regenerating agent) was present in-situ with $N_2H_4 \bullet H_2O$. Fundamental questions arose concerning the difference in physical character between supported and unsupported NBC. These questions are discussed in light of considerable uncertainty in the literature as to the actual composition of such amorphous material. Preliminary evidence suggests the presence of residual borohydrides within bulk unsupported NBC is responsible for the materials partial conversion to crystalline nickel boride upon heating in inert atmosphere, and the long history of referring to these materials as amorphous borides.

Finally, chapter 4 reports on the attempted substitution of transition metals such as Cu and Ni into the SiO_2 framework, in the context of creating robust and reusable adsorbents for desulfurization. These adsorbent materials did not perform well as desulfurizing adsorbents, compared to MSN or MASN. Even upon impregnation with

$AgNO_3$ or subsequent plasma treatment, these materials did not perform better than Ag-MASN or PT-Ag-MASN ($AgNO_3$ wet impregnated MASN and the subsequent plasma treated material, respectively). Additionally, the location of Ni and Cu in these materials was not confirmed beyond the general association of the transition elements with the MSN framework, as shown by energy-dispersive x-ray spectroscopy (EDS). Because of the lack of performance as desulfurization adsorbents, and ambiguity of the incorporation/substitution of the transition elements into the SiO_2 framework, investigation into these materials was discontinued. An attempt was also made to create an Ag/Cu binary metallic extra-framework metallized sorbent by galvanic a galvanic exchange method. The product GE-Ag/Cu-MASN shows some promise for enhanced cyclability in the desulfurization of model fuel. The data for this mixed metal species work is briefly discussed in chapter 4.

Chapter 1

Mesoporous Silica Nanomaterials

1.1 Introduction: MS and MSN

Fabrication of high surface area inorganic porous materials is currently an extensive area of research, with applications spanning fields as divergent as intracellular drug delivery and heterogeneous catalysis. The most representative examples of such materials include natural and synthetic zeolites, and mesoporous silica (MS). This chapter is focused on MS, owing to the ease of fabrication and tuning of material characteristics, such as particle size, shape, pore volume and surface area. In general, *mesoporous* is defined by the International Union of Pure and Applied Chemistry (IUPAC) as a description of materials with pore widths between 2 and 50 nm.[1] Specifically, the works presented in this thesis deal primarily with MCM-41 type materials (pore width ranging 3—10 nm), synthesized using amphiphilic surfactants as structure directing agents (SDAs), and alkoxide silica sources ($Si(OR)_4$).

Mesoporous silica materials were first synthesized by Mobil Oil Corporation in the early 1990s, and have been the subject of much research owing to their tunable channel diameter, narrow channel size distribution, high surface area, high thermal and mechanical stability, and biocompatibility. With the advent of nanoparticle synthesis routes, mesoporous silica nanoparticles (MSN) have been explored for their potential in applications where small particle size and increased surface area are desirable.

Mesoporous silica materials are typically synthesized by the hydrolysis and condensation of a silica precursor (usually alkoxides such as tetramethyl- or tetraethyl-orthosilicate, TMOS or TEOS), which hydrolyze and then polymerize by condensation

around an organic SDA mesophase template (Figure 1.1). Hydrolysis of the silica precursor can be initiated by acidic or basic conditions, and the SDAs are typically organic ionic surfactants, or neutral di- or tri-block organic copolymers. The most common SDAs are amphiphilic surfactants such as alkyltrimethylammonium salts of varying carbon chain length (usually 8 to 20 carbons), which form concentration dependent micellular self-assemblies in water and water/alcohol solvent systems—so called liquid crystal systems.[2,3] The spontaneous formation of lyotropic liquid crystal mesophases, which vary according to the choice of surfactant(s), surfactant concentration, and temperature, determine the porous mesostructure, or mesophase, of the resulting MS. Some common mesophase examples are the lamellar mesophase of MCM-50, the 3-D wormhole-like mesophase of MCM-48, and the well-known 2-D hexagonal mesophase of MCM-41 (Figure 1.2). After silicate polymerization, the templating surfactants are subsequently removed, typically by thermal (calcination) or solvent (refluxing) methods. The morphology, pore size, surface area, and surface functionality of the resulting mesoporous material can be tailored by the surfactant choice and the addition of organic and inorganic modifiers during synthesis (swelling agents to increase pore size, such as trimethylbenzene, or metal salts or oxides to create surface charge, such as $NaAlO_2$), as well has how the SDA template is removed—with calcining generally producing more physically robust materials due to greater degree of condensation among surface silanol groups (Si-OH).[4,5]

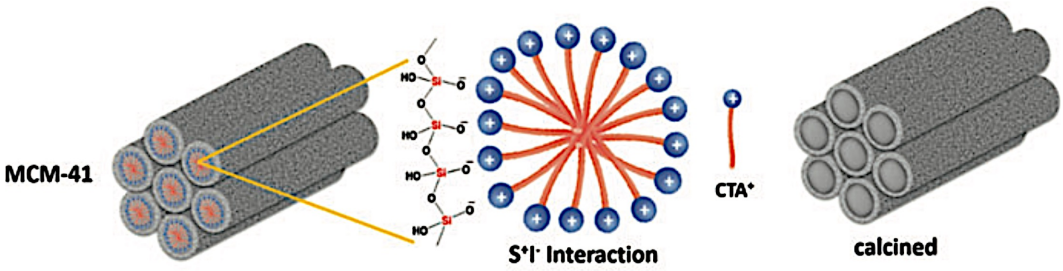

Figure 1.1 Formation of MCM-41 by condensation of silica precursor around cetyltrimethylammonium (CTA^+) micellular template.

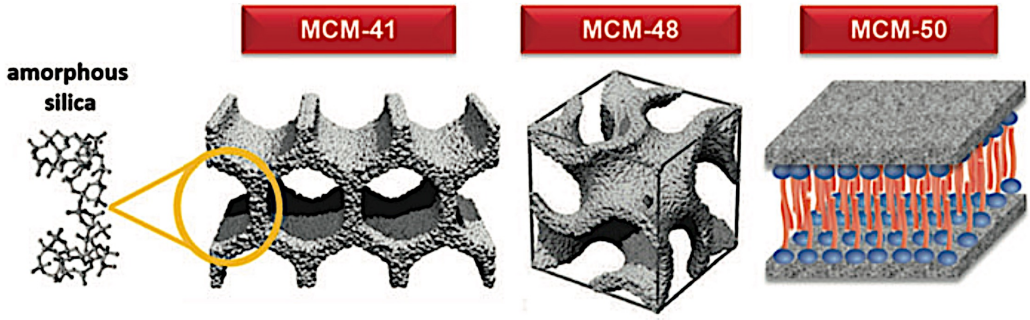

Figure 1.2 Template concentration dependent formation of various MS mesophases. Left to right: 2D hexagonal MCM-41 (space group *p6mm*), 3D cubic MCM-48 (space group *ia3d*), and lamellar MCM-50 (space group *p2*).

In addition to bulk synthesis of MS, numerous MS particle morphologies have been reported, including spheres, fibers and tubules. These discrete particles of MS can be grown in sizes ranging from nanometers to centimeters, depending on the reaction conditions (pH, temperature, silica source, concentrations, the presence of co-templates, co-solvents present, stirring rate, etc.).[6–8] Simultaneous control of both particle size and particle aggregation has been demonstrated by the addition of copolymers (e.g. Pluronic F127, poly(ethylene)glycol, etc.) to the surfactant templating solutions.[9] These copolymers can act as capping agents and restrict the condensation of silonal groups on neighboring particles.[10] Additionally, obtaining MS nanoparticles (MSN) that are non-

aggregated and narrowly size dispersed, without the use of co-polymers, has been demonstrated simply by employing dilute surfactant synthesis conditions.[11,12]

1.2 Metal Functionalization of MSNs

The addition of metal species either substituted within the SiO_2 framework, adhered onto the SiO_2 surface, or both, allow for the functionalization of MS supports targeting a wide variety of applications.[10] Metal functionalization of MS or MSN can be achieved at the time of synthesis, post-synthetically, or both. Metal functionalization can be viewed in terms of atomic substitution for Si^{4+} in the amorphous SiO_2 framework (intra-framework, see Figure 1.3) or in terms of grafting metallic species (ions, oxides or metal nanoparticles) onto the exterior surface (extra-framework) either by electrostatic interactions or by condensation reactions with silanol groups (Figure 1.4).

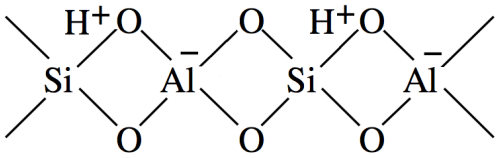

Figure 1.3 Intra-framework aluminum incorporated in SiO2, giving negative surface charge.

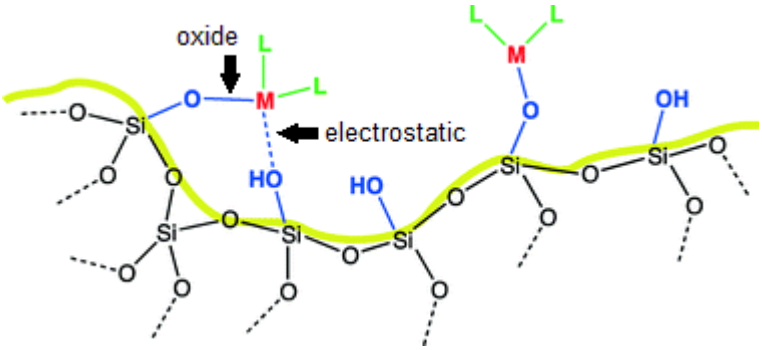

Figure 1.4 Extra-framework metal interaction with SiO2 framework, via condensation to form oxide bridge or electrostatic interaction with silanol groups. The ligand species in green (L), may be other coordinating species such as counter ions (X^-, NO_3^-, etc.) or organic ligands (pyridine or amine moieties, etc.).

Intra-framework metallization of MS typically involves one-pot synthesis routes where metallic precursors (salts, oxides or alkoxides) are added along with the silicon precursor to the surfactant solution. For example, the addition of an aluminum precursor (e.g. $AlNaO_2$ or Al-isopropoxide) at the time of MSN synthesis allows for the substitution of Al into the SiO_2 framework, giving rise to mesoporous aluminosilicate nanoparticles (MASN).[13–15] This intra-framework aluminum substitution in SiO_2 creates negative surface charge in MASN, owing to the tetrahedral coordination of Al^{3+}, which are then charge balanced by various cationic species.[16] This negative surface charge can aid in the retention and distribution of positively charged species (such as metal cations) exchanged along the surface area of MASN.[17–19] It should be noted that intra-framework metallization and in-situ, or one-pot, extra-framework metallization schemes typically can only achieve low M:Si ratios, before the mesophase and particle morphology are significantly altered. This is because the long-range order of the liquid crystal mesophase and silica polymerization are heavily dependent on Coulombic interactions at the interface of the SDA and silicate species.[12] The addition of metal cations or other charged species are then likely to interfere with both the polymerization of negatively charged silicate species and their interaction with the cationic micellular surface.

Extra-framework metallization of MS is typically achieved post-synthetically. The simplest example of this is the electrostatic interaction of metal cations directly with silonal groups (Si-OH) on the silica surface, by soaking or wet impregnation of MS with a metal salt solution. Intra-framework incorporation of aluminum can increase retention and dispersion of these cations, as previously discussed. Taken a step further, metallic nanoparticles can be grown within the mesochannels or on the surface of metal salt

impregnated MS post-synthetically by the chemical,[20] thermal, or plasma reduction of the metal salt precursors.[17] Another commonly reported extra-framework metallization route is to first incorporate organic functional groups (e.g. akylthiols or alkylamines) onto the MS surface, in order to capture metallic cations by coordination. These functional groups are typically introduced as alkoxysilanes [R—$Si(OR')_3$ where R' is an alkoxide, and R is typically a thiol or amino group], either at the time of synthesis (co-condensation) or post synthetically (grafting).[21] Further modification of the incorporated functional groups have been reported (e.g. converting R-SH to R–SO_3H by exposure to H_2O_2)[22] which can enhance specific metal interactions. However, both the co-condensation and grafting methods can be tedious. Removal of the surfactant template must be done by long periods of refluxing in the co-condensation method (quick template removal by calcination not being an option); while post synthetic grafting poses difficulty in controlling the dispersion of functional groups on the MS surface, as well as the likelihood of channel-blocking polymerization of the alkoxysilane itself.[23] Alkoxysilanes are also quite toxic and moisture sensitive, requiring careful handling procedures. Also, their incorporation during co-condensation has the tendency to disrupt the mesophase of the resulting structure, and hinder complete removal of the templating surfactant.[24] For these reasons, the following work has omitted research on metallization of MS materials by prior organosilane functionalization, and focuses instead on direct intra-framework metal substitution and/or extra-framework metallization schemes.

1.3 Applications of Metal Functionalized MSNs

Applications of metal functionalized MSNs in research and industry include adsorption,[17,25] catalysis,[26] and intracellular drug delivery,[18,27] to name a few. Among

these, catalysis is the most frequently reported application. In this work, the lesser-examined use of metalized MSN for adsorption is explored.

Removal of pollutant species by adsorption is important in a variety of settings—water purification, gas purification, and hydrocarbon fuel purification, to name a few. Mesoporous silica has found use most notably in the removal of toxic ions from aqueous systems, often as a result of surface modifications resulting from the incorporation of organosilanes, as discussed above, where amino groups are typically used to coordinate transition metal cations.[28,29] Alternatively, incorporated metal species themselves can be used to bind with electron donor species, such as organosulfurs.[17,19]

The removal of organosulfur species from hydrocarbon fuels using metal functionalized MSN is studied and reported in chapters 2 and 4. Though desulfurization of fuels is of environmental importance in limiting the emission of toxic sulfur oxides (SO_xs),[30,31] it is also important for the effective conversion of hydrocarbon fuels to hydrogen gas for hydrogen fuel cells. Sulfur species within military logistics fuels (JP-5 and JP-8, which are high sulfur content) can poison the catalytic fuel reformers responsible for producing hydrogen gas from the liquid hydrocarbon feedstock fuels.[32] MSN functionalized with thiophilic metal species has shown good results for adsorptive desulfurization of such fuels, compared with zeolites and other porous inert scaffolds.[33–35]

In a subsequent chapter, the use of metal functionalized MSN as a catalyst support platform will be examined. The ability to disperse catalytically active metallic species on MSNs give the advantage of increasing catalytic surface area, while overcoming the diffusion limitations of bulk MS materials, owing to the much shorter channel lengths of the nanoparticle morphology. MASN, in particular, has the advantage of negative surface charge, which aids in the dispersion and retention of catalytic metal species when

introduced in the form of ionic salt precursors. Reduction of salt precursors to form metallic nanoparticles that remain dispersed and tethered to the MSN framework allows for increased stability against agglomeration that may increase the longevity of the catalyst system upon cycling.[20,36]

1.4 References

(1) Everett, D. H. Manual of Symbols and Terminology for Physicochemical Quantities and Units, Appendix II: Definitions, Terminology and Symbols in Colloid and Surface Chemistry. *Pure Appl. Chem.* **1972**, *31* (4), 577–638. https://doi.org/10.1351/pac197231040577.

(2) Attard, G. S.; Glyde, J. C.; Göltner, C. G. Liquid-Crystalline Phases as Templates for the Synthesis of Mesoporous Silica. *Nature* **1995**, *378* (6555), 366–368. https://doi.org/10.1038/378366a0.

(3) Monnier, A.; Schuth, F.; Huo, Q.; Kumar, D.; Margolese, D.; Maxwell, R. S.; Stucky, G. D.; Krishnamurty, M.; Petroff, P.; Firouzi, A.; et al. Cooperative Formation of Inorganic-Organic Interfaces in the Synthesis of Silicate Mesostructures. *Science* **1993**, *261* (5126), 1299–1303. https://doi.org/10.1126/science.261.5126.1299.

(4) Kresge, C. T.; Leonowicz, M. E.; Roth, W. J.; Vartuli, J. C.; Beck, J. S. Ordered Mesoporous Molecular Sieves Synthesized by a Liquid-Crystal Template Mechanism. *Nature* **1992**, *359* (6397), 710–712. https://doi.org/10.1038/359710a0.

(5) Yanagisawa, T.; Shimizu, T.; Kuroda, K.; Kato, C. The Preparation of Alkyltriinethylaininonium–Kaneinite Complexes and Their Conversion to Microporous Materials. *Bull. Chem. Soc. Jpn.* **1990**, *63* (4), 988–992. https://doi.org/10.1246/bcsj.63.988.

(6) Ying, J. Y.; Mehnert, C. P.; Wong, M. S. Synthesis and Applications of Supramolecular-Templated Mesoporous Materials. *Angew. Chem. Int. Ed.* **1999**, *38* (1–2), 56–77. https://doi.org/10.1002/(SICI)1521-3773(19990115)38:1/2<56::AID-ANIE56>3.0.CO;2-E.

(7) Mann, S.; Burkett, S. L.; Davis, S. A.; Fowler, C. E.; Mendelson, N. H.; Sims, S. D.; Walsh, D.; Whilton, N. T. Sol–Gel Synthesis of Organized Matter. *Chem. Mater.* **1997**, *9* (11), 2300–2310. https://doi.org/10.1021/cm970274u.

(8) Hoffmann, F.; Cornelius, M.; Morell, J.; Fröba, M. Silica-Based Mesoporous Organic–Inorganic Hybrid Materials. *Angew. Chem. Int. Ed.* **2006**, *45* (20), 3216–3251. https://doi.org/10.1002/anie.200503075.

(9) Suzuki, K.; Ikari, K.; Imai, H. Synthesis of Silica Nanoparticles Having a Well-Ordered Mesostructure Using a Double Surfactant System. *J. Am. Chem. Soc.* **2004**, *126* (2), 462–463. https://doi.org/10.1021/ja038250d.

(10) Wu, S.-H.; Mou, C.-Y.; Lin, H.-P. Synthesis of Mesoporous Silica Nanoparticles. *Chem. Soc. Rev.* **2013**, *42* (9), 3862. https://doi.org/10.1039/c3cs35405a.

(11) Fowler, C. E.; Khushalani, D.; Lebeau, B.; Mann, S. Nanoscale Materials with Mesostructured Interiors. *Adv. Mater.* **2001**, *13* (9), 649–652. https://doi.org/10.1002/1521-4095(200105)13:9<649::AID-ADMA649>3.0.CO;2-G.

(12) Monnier, A.; Schuth, F.; Huo, Q.; Kumar, D.; Margolese, D.; Maxwell, R. S.; Stucky, G. D.; Krishnamurty, M.; Petroff, P.; Firouzi, A.; et al. Cooperative Formation of Inorganic-Organic Interfaces in the Synthesis of Silicate Mesostructures. *Science* **1993**, *261* (5126), 1299–1303. https://doi.org/10.1126/science.261.5126.1299.

(13) Park, K.-C.; Yim, D.-J.; Ihm, S.-K. Characteristics of Al-MCM-41 Supported Pt Catalysts: Effect of Al Distribution in Al-MCM-41 on Its Catalytic Activity in Naphthalene Hydrogenation. *Catal. Today* **2002**, *74* (3–4), 281–290. https://doi.org/10.1016/S0920-5861(02)00024-X.

(14) Betiha, M. A.; Hassan, H. M. A.; Al-Sabagh, A. M.; Khder, A. E. R. S.; Ahmed, E. A. Direct Synthesis and the Morphological Control of Highly Ordered Mesoporous AlSBA-15 Using Urea-Tetrachloroaluminate as a Novel Aluminum Source. *J. Mater. Chem.* **2012**, *22* (34), 17551. https://doi.org/10.1039/c2jm32941g.

(15) Busio, M.; Jänchen, J.; van Hooff, J. H. C. Aluminum Incorporation in MCM-41 Mesoporous Molecular Sieves. *Microporous Mater.* **1995**, *5* (4), 211–218. https://doi.org/10.1016/0927-6513(95)00063-1.

(16) Kosslick, H.; Lischke, G.; Parlitz, B.; Storek, W.; Fricke, R. Acidity and Active Sites of Al-MCM-41. *Appl. Catal. Gen.* **1999**, *184* (1), 49–60. https://doi.org/10.1016/S0926-860X(99)00078-2.

(17) Hauser, J. L.; Tran, D. T.; Conley, E. T.; Saunders, J. M.; Bustillo, K. C.; Oliver, S. R. J. Plasma Treatment of Silver Impregnated Mesoporous Aluminosilicate Nanoparticles for Adsorptive Desulfurization. *Chem. Mater.* **2016**, *28* (2), 474–479. https://doi.org/10.1021/acs.chemmater.5b03018.

(18) Chakraborty, I.; Carrington, S. J.; Hauser, J.; Oliver, S. R. J.; Mascharak, P. K. Rapid Eradication of Human Breast Cancer Cells through Trackable Light-Triggered CO Delivery by Mesoporous Silica Nanoparticles Packed with a Designed PhotoCORM. *Chem. Mater.* **2015**, *27* (24), 8387–8397. https://doi.org/10.1021/acs.chemmater.5b03859.

(19) Palomino, J. M.; Tran, D. T.; Hauser, J. L.; Dong, H.; Oliver, S. R. J. Mesoporous Silica Nanoparticles for High Capacity Adsorptive Desulfurization. *J Mater Chem A* **2014**, *2* (36), 14890–14895. https://doi.org/10.1039/C4TA02570A.

(20) Hauser, J. L.; Amberchan, G.; Tso, M.; Manley, R.; Bustillo, K.; Cooper, J.; Golden, J. H.; Singaram, B.; Oliver, S. R. J. A Mesoporous Aluminosilicate Nanoparticle-

Supported Nickel–Boron Composite for the Catalytic Reduction of Nitroarenes. *ACS Appl. Nano Mater.* **2019**. https://doi.org/10.1021/acsanm.8b02351.

(21) Brühwiler, D. Postsynthetic Functionalization of Mesoporous Silica. *Nanoscale* **2010**, *2* (6), 887. https://doi.org/10.1039/c0nr00039f.

(22) Das, D.; Lee, J.-F.; Cheng, S. Sulfonic Acid Functionalized Mesoporous MCM-41 Silica as a Convenient Catalyst for Bisphenol-A Synthesis. *Chem. Commun.* **2001**, No. 21, 2178–2179. https://doi.org/10.1039/b107155f.

(23) Gartmann, N.; Schütze, C.; Ritter, H.; Brühwiler, D. The Effect of Water on the Functionalization of Mesoporous Silica with 3-Aminopropyltriethoxysilane. *J. Phys. Chem. Lett.* **2010**, *1* (1), 379–382. https://doi.org/10.1021/jz9002795.

(24) Huh, S.; Wiench, J. W.; Trewyn, B. G.; Song, S.; Pruski, M.; Lin, V. S.-Y. Tuning of Particle Morphology and Pore Properties in Mesoporous Silicas with Multiple Organic Functional Groups. *Chem. Commun.* **2003**, No. 18, 2364. https://doi.org/10.1039/b306255d.

(25) Yoshitake, H. Highly-Controlled Synthesis of Organic Layers on Mesoporous Silica: Their Structure and Application to Toxic Ion Adsorptions. *New J. Chem.* **2005**, *29* (9), 1107. https://doi.org/10.1039/b504957a.

(26) Taguchi, A.; Schüth, F. Ordered Mesoporous Materials in Catalysis. *Microporous Mesoporous Mater.* **2005**, *77* (1), 1–45. https://doi.org/10.1016/j.micromeso.2004.06.030.

(27) Vallet-Regí, M.; Balas, F.; Arcos, D. Mesoporous Materials for Drug Delivery. *Angew. Chem. Int. Ed.* **2007**, *46* (40), 7548–7558. https://doi.org/10.1002/anie.200604488.

(28) Evans, J.; Zaki, A. B.; El-Sheikh, M. Y.; El-Safty, S. A. Incorporation of Transition-Metal Complexes in Functionalized Mesoporous Silica and Their Activity toward the Oxidation of Aromatic Amines. *J. Phys. Chem. B* **2000**, *104* (44), 10271–10281. https://doi.org/10.1021/jp000564p.

(29) Corriu, R. J. P.; Mehdi, A.; Reyé, C.; Thieuleux, C. Direct Synthesis of Functionalized Mesoporous Silica by Non-Ionic Assembly Routes. Quantitative Chemical Transformations within the Materials Leading to Strongly Chelated Transition Metal Ions. *Chem. Mater.* **2004**, *16* (1), 159–166. https://doi.org/10.1021/cm034903d.

(30) Smith, S. J.; van Aardenne, J.; Klimont, Z.; Andres, R. J.; Volke, A.; Delgado Arias, S. Anthropogenic Sulfur Dioxide Emissions: 1850–2005. *Atmospheric Chem. Phys.* **2011**, *11* (3), 1101–1116. https://doi.org/10.5194/acp-11-1101-2011.

(31) Delucchi, M. A.; Murphy, J. J.; McCubbin, D. R. The Health and Visibility Cost of Air Pollution: A Comparison of Estimation Methods. *J. Environ. Manage.* **2002**, *64* (2), 139–152. https://doi.org/10.1006/jema.2001.0515.

(32) Hu, J.; Wang, Y.; VanderWiel, D.; Chin, C.; Palo, D.; Rozmiarek, R.; Dagle, R.; Cao, J.; Holladay, J.; Baker, E. Fuel Processing for Portable Power Applications. *Chem. Eng. J.* **2003**, *93* (1), 55–60. https://doi.org/10.1016/S1385-8947(02)00108-0.

(33) Natelson, R. H.; Kurman, M. S.; Cernansky, N. P.; Miller, D. L. Experimental Investigation of Surrogates for Jet and Diesel Fuels. *Fuel* **2008**, *87* (10–11), 2339–2342. https://doi.org/10.1016/j.fuel.2007.11.009.

(34) Hernández-Maldonado, A. J.; Yang, R. T. Desulfurization of Liquid Fuels by Adsorption via π Complexation with Cu(I)−Y and Ag−Y Zeolites. *Ind. Eng. Chem. Res.* **2003**, *42* (1), 123–129. https://doi.org/10.1021/ie020728j.

(35) Hernández-Maldonado, A. J.; Yang, R. T.; Cannella, W. Desulfurization of Commercial Jet Fuels by Adsorption via π-Complexation with Vapor Phase Ion Exchanged Cu(I)−Y Zeolites. *Ind. Eng. Chem. Res.* **2004**, *43* (19), 6142–6149. https://doi.org/10.1021/ie049533x.

(36) Patel, N.; Fernandes, R.; Edla, R.; Lihitkar, P. B.; Kothari, D. C.; Miotello, A. Superior Hydrogen Production Rate by Catalytic Hydrolysis of Ammonia Borane Using Co-B Nanoparticles Supported over Mesoporous Silica Particles. *Catal. Commun.* **2012**, *23*, 39–42. https://doi.org/10.1016/j.catcom.2012.02.030.

Chapter 2

Plasma treatment of silver impregnated mesoporous aluminosilicate nanoparticles for adsorptive desulfurization

Abstract

A regenerable adsorbent for the removal of refractory organosulfur compounds from fossil fuels was synthesized. The material is comprised of well-dispersed silver nanoparticles confined within the mesochannels of aluminum doped MCM-41 nanoparticles. With an average initial desulfurization capacity of 15 $mgS \cdot g^{-1}$, 79% desulfurization capacity is retained after six cycles for the removal of dibenzothiophene from n-decane. The addition of intra-framework aluminum to form a mesoporous aluminosilicate nanoparticle (MASN) aids in the retention and dispersion of silver ions within the mesochannels (Ag-MASN). The nanoparticles are subsequently reduced by glow discharge plasma treatment in argon (PT-Ag-MASN). The size dispersion, surface area and structural integrity were characterized by scanning electron microscopy (SEM), annular dark field scanning transmission electron microscopy (ADF-STEM), nitrogen adsorption analysis (BET) and powder X-ray diffraction (PXRD). Silver nanoparticle formation within the mesochannels of MASN was confirmed by ADF-STEM and diffuse reflectance UV-vis spectroscopy (DR-UV-vis). Model fuel testing revealed that PT-Ag-MASN had the highest regeneration capacity after six cycles compared to non-plasma treated (Ag-MASN) and aluminum free materials (Ag-MSN and PT-Ag-MSN). Initial testing of the military jet fuel JP-8 also shows a high desulfurization capacity of 41 $mgS \cdot g^{-1}$.

2.1 Introduction

Liquid hydrocarbon fuels can be used as a hydrogen source for charging solid oxide fuel cells (SOFCs). SOFCs are of considerable military interest for their high energy density, portability and silent operation. Use of SOFCs in the field would greatly facilitate missions requiring extended use of auxiliary power. Their stealth operation compared to conventional generators would greatly benefit silent watch missions.[1] The jet fuel formulation JP-8 serves as the US military's logistic fuel. It powers all manner of vehicles as well as electrical generators and is an ideal hydrogen-dense feedstock for charging SOFCs.[2] However, the high organosulfur content (up to 3000 ppm_wS) of JP-8 poses serious limitations for use in SOFCs. Sulfur compounds poison thiophilic components of both the anode materials of the SOFC and the catalytic fuel reformers used to harvest hydrogen from the liquid fuel. Low ppm_wS concentrations are desired to increase the longevity of both fuel reformers and SOFCs.[1,3]

The conventional method of sulfur removal from hydrocarbon fuels is hydrodesulfurization (HDS). HDS is employed within refinery infrastructure and requires hydrogen gas at high temperature and pressure. HDS is suitable for the removal of smaller organosulfur species (thiols and thiophenes) from lighter fuels (e.g. gasoline) but the refractory organosulfur compounds in jet fuel (dibenzothiophene and its methylated analogs) cannot be removed by this method.[3,4] Adsorptive desulfurization has been proposed as a portable and efficient method for cleaning JP-8 of refractory organosulfur compounds under ambient conditions. A variety of zeolite and mesoporous metal oxide frameworks supporting thiophilic ionic, metallic and metal oxide species have been investigated for treatment of both model and real jet fuels.[5-9] In the majority of

this work, ionic silver is reported to have the highest desulfurization capacity when compared to other transition metals such as copper, nickel, cerium, manganese or zinc. For example, a recent publication by Tatarchuck *et al*. reported a maximum desulfurization capacity for JP-8 of 8.01 $mgS \cdot g^{-1}$ using a silver loaded TiO_x–Al_2O_3 adsorbent.[10]

Similar work previously reported a high desulfurization capacity material consisting of $AgNO_3$ impregnated MCM-41 mesoporous silica nanoparticles (Ag-MSN).[11] This material demonstrated high capacity desulfurization for both model fuel (12.7 $mgS \cdot g^{-1}$) and JP-8 (32.6 $mgS \cdot g^{-1}$). However, upon solvent regeneration with diethyl ether, a 30% loss of silver was typically observed, resulting in a corresponding reduction in desulfurization capacity in the subsequent cycle.

In recognizing the need for a material that exhibits both high sulfur absorptivity and regenerability, we have investigated a method for reducing the ionic metal species onto the mesoporous framework by exposure to glow discharge plasma. Glow discharge plasma offers several advantages over chemical or thermal reduction methods, being rapid, non-toxic, and energy efficient. This method has been recently explored by researchers seeking to improve the performance and lifetime of supported metallic nanoparticle catalysts.[12-14] Recent work by Chen *et al*. has demonstrated the formation of metallic (Au or Pd) and bi-metallic (Au/Pd) nanoparticles, well dispersed within the channels of the mesoporous silica support SBA-15. The nanoparticles were grown by Ar glow discharge plasma treatment after aqueous impregnation with the respective metal salt(s).[15]

In the present work, aluminum was incorporated into the framework during synthesis of Al-MCM-41 type mesoporous aluminosilicate nanoparticles (MASN).

Alumination was found to greatly improve the regenerability of both the non-plasma treated material (Ag-MASN) and the plasma treated material (PT-Ag-MASN), considerably extending the lifetime desulfurization capacity of the material.

2.2 Experimental

All chemicals were used as received without further purification. Tetraethylorthosilicate (TEOS), diethyl ether and dibenzothiophene (DBT) were obtained from Acros Organics. 200 proof ethanol was obtained from Decon Laboratories. Silver nitrate, sodium aluminum oxide, cetyltrimethylammonium bromide (CTAB) and n-decane were obtained from Sigma Aldrich.

2.2.1 Synthesis of MSN and MASN

Mesoporous silica nanoparticles (MSN) were synthesized using a method previously published.[11] Briefly, a solution containing 1.0 g CTAB, 0.28 g NaOH, and 483.5 g doubly distilled deionized water was stirred at a rate of 625 rpm at 80 °C for 15 min. To this homogenous solution 4.58 g of TEOS was added dropwise over a two-minute period. The solution was allowed to stir for 2 h, after which the solution was removed from heat and stirring, then allowed to age statically for 30 min until near room temperature. The solid precipitate was rinsed with 500 mL doubly distilled deionized water during filtration, then allowed to dry overnight in a vacuum oven at 100 °C. The thoroughly dried material was ground to a fine powder and calcined at 560 °C for 4 h, with a heating ramp rate of 1 °C per minute. Mesoporous aluminosilicate nanoparticles (MASN) were synthesized in the same manner as MSN, with the addition of 0.098 g $NaAlO_2$ before adding TEOS.

2.2.2 Synthesis of PT-Ag-MSN and PT-Ag-MASN

In a typical plasma treatment, 100 mg of calcined MSN or MASN was placed in a vacuum oven for 1 h at 100 °C, in an open glass scintillation vial. Upon removal, the vial was immediately sealed to limit exposure to atmospheric moisture. Once cooled to room temperature, the vial was opened and the material immediately loaded with $AgNO_3$ dissolved in a 50/50 wt/wt water-ethanol solution *via* wet impregnation. Optimal silver loading was 20 wt.% as determined previously.[11] After $AgNO_3$ loading, the material was again dried in vacuo at 100 °C for 1 h to remove the solvent. The material was then ground to a fine powder and distributed evenly over two small borosilicate dishes, which were placed into a barrel reactor plasma oven (Plasma Prep II, operating at 13.56 MHz). Argon was allowed to profuse the plasma chamber during evacuation to approximately 250 mTorr. Plasma exposure times were 15 min, followed by manual mixing to expose all material. During the mixing process, it was discovered that only the top layer of exposed material changed color after treatment (initially from white to dark gray, and then progressively darkening to black), while the material underneath appeared unchanged. Plasma treatments and mixing were repeated 6 times, ensuring that the material was homogenous in color.

2.2.3 Characterization of adsorbent materials

Thermogravimetric analysis (TGA) was performed on a TA Instruments 2050 TGA with nitrogen purge, heating from 30 to 800 °C at a heating rate of 10 $°C \cdot min^{-1.}$ Powder X-ray diffraction (PXRD) was performed on a Rigaku SmartLab X-ray diffractometer with Cu Kα (1.54 Å) radiation. All samples were analyzed from 2° to 80°

(2θ) with a step size of 0.01° and scan rate of $1°\cdot min^{-1}$. BET surface area was measured by physical adsorption of N_2 at 77 K using a Micrometrics physisorption analyzer (TriStar II 3020 v1.03). Adsorption/desorption isotherm measurements were collected within a relative pressure range (P/P_0) from 0.01 to 1.00. UV-vis spectroscopy was performed on a Hewlett-Packard Model 8452A spectrophotometer. Diffuse reflectance UV-vis (DR-UV-vis) spectra were obtained using a Varian Cary 5000 UV-vis-NIR spectrophotometer (Harrick Praying Mantis diffuse reflectance cell attachment, Teflon standard). Scanning electron microscopy (SEM) and scanning transmission electron microscopy (STEM) data were collected with a FEI Quanta 3D dual beam microscope operated at 10 kV. Scanning transmission electron microscopy (ADF-STEM) was performed on a FEI Titan TEM operated at 200 kV and 300kV. The STEM probe had a convergence semi-angle, α, of 10 mrad and a beam current of 60 pA (200kV) and 35 pA (300kV). ADF-STEM images were acquired using a Fischione annular dark-field (ADF) detector with an inner semi-angle, β, of 63 mrad (200kV) and 45 mrad (300kV). Samples were robust under the focused beam with no damage evident. Inductively coupled plasma optical emission spectra (ICP-OES) were collected on a Perkin-Elmer Optima 7000 DV.

2.2.4 Model fuel and JP-8 testing

The procedures for model fuel and JP-8 testing were similar to those previously published.[11] Initial batch testing was conducted using a model fuel comprised of 500 ppm_wS dibenzothiophene (DBT) in n-decane. Prior to model fuel testing, approximately 50 mg of the PT-Ag-MASN adsorbent material was loaded into a clean 20 mL glass scintillation vial and placed in a vacuum oven at 100°C overnight to remove adsorbed

moisture. The model fuel to adsorbent mass ratio was 50 to 1 for all model fuel tests. Adsorbent samples were combined with model fuel and mildly agitated for 1 hour prior to UV-vis spectroscopic analysis to determine the remaining DBT concentration in the fuel. JP-8 batch tests were performed over 24 h with approximately 40 mg of adsorbent in 5 g of JP-8 (average concentration 750 ppm_wS). The remaining sulfur concentration was then analyzed using a UV total sulfur analyzer (multi EA 3100, Analytikjena) with a detection limit of 45 ppb. Regeneration of adsorbent materials was achieved by rinsing the used material with 50 mL of diethyl ether.

2.3 Results and Discussion

Initial model fuel desulfurization capacities for PT-Ag-MSN, PT-Ag-MASN and untreated Ag-MASN were consistent with our previously synthesized Ag-MSN. Table 2.1 depicts a single experiment comparing eight different adsorbents over the course of six regenerations. Small variation in the desulfurization capacity for each material likely reflects incomplete sulfur removal during a particular regeneration, but the overall trend is clear. In general, the aluminosilicate versions displayed better regeneration capacities compared to the non-aluminated material, with plasma treatment yielding further improvement over six cycles. JP-8 fuel tests were limited to individual 24 h saturation tests and showed high desulfurization capacity for PT-Ag-MASN (41.1 $mgS \cdot g^{-1}$) compared to that previously reported for Ag-MSN (32.6 $mgS \cdot g^{-1}$).[11] The initial reduction in sulfur concentration was from ~765 ppmS to ~400 ppmS and is expected to continue to decrease with exposure to additional material. Further JP-8 column tests of regenerated material have given poor results thus far for the plasma treated materials. BET analysis shows a marked decrease in surface area (758.1 m^2/g) after ether regeneration of JP-8

saturated PT-Ag-MASN, indicating that incomplete removal of fuel components may be the issue.

Alumination of MSN was the first step in this work towards stabilizing the regeneration capacity of the adsorbent in model fuel. Tetrahedrally coordinated aluminum ions in the framework of aluminosilicate Al-MCM-41 materials are known to generate localized sites of negative surface charge.[16] It is possible that these periodic sites of negative charge in MASN help to electrostatically retain silver ions within the mesochannels, compared to the more neutral surface charge of MSN. This difference would explain the slight improvement in regeneration capacity for Ag-MASN compared to Ag-MSN. The regenerative capacity of the material is further stabilized by plasma treatment in argon, which reduces the silver ions to metallic silver nanoparticles within the mesochannels.

A rough estimate of the silver-sulfur adsorption sites present in fresh PT-Ag-MASN can be made by comparing the silver present to sulfur removed, assuming each silver atom can coordinate with one sulfur bearing molecule. At 20 wt.% Ag, there is about 1.85 mmol of silver per gram of fresh adsorbent. Accordingly, in freshly synthesized PT-Ag-MASN, 69% of these theoretical silver sites appear used when desulfurizing JP-8, but only 25% appear available when desulfurizing model fuel consisting of DBT in n-decane. This discrepancy can be explained by considering the variety of smaller organosulfur species in JP-8 compared to DBT in our model fuel. In addition to DBT, JP-8 contains primarily alkyl benzothiophenes along with many smaller species such as thiophene and alkanethiols.[4] DBT is larger than most of these organosulfur species and will interact with the silver species through both direct metal-sulfur binding and pi-interactions. These interactions will be weaker for thiophene or

benzothiophenes, which have fewer aromatic rings.[17] The majority of organosulfur species in JP-8 are much less sterically hindered than DBT for silver interaction, and 69% binding site availability is more probable. Moreover, the apparently high percentage of binding sites is impressive when considering that many silver atoms will be bound up in the centers of metallic nanoparticles.

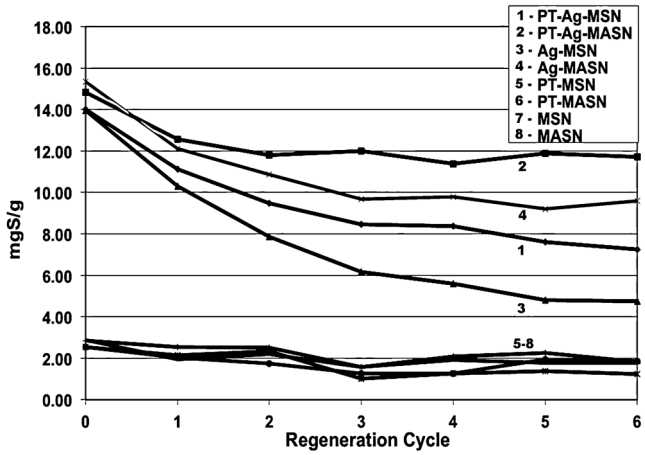

Figure 2.1 The mass of sulfur removed during successive fuel testing and regeneration cycles for eight different adsorbents.

Table 2.1 Percentage of initial desulfurization capacity retained after successive regeneration cycles. The far right column is the corresponding percentage of silver recovered from the ether rinse during regeneration of PT-Ag-MASN (determined by ICP-OES)

Cycle	Ag-MSN	Ag-MASN	PT-Ag-MSN	PT-Ag-MASN	PT-Ag-MASN Ag loss
1	73.8%	81.7%	79.4%	84.6%	15.1%
2	56.2%	73.2%	67.6%	79.5%	4.8%
3	44.1%	65.2%	60.3%	80.8%	2.4%
4	40.1%	65.9%	59.8%	76.7%	1.6%
5	34.5%	62.0%	54.3%	80.2%	1.1%
6	34.0%	64.7%	51.7%	78.9%	1.1%

Silver loss was determined by ICP-OES analysis of the ether rinse solution after each successive model fuel regeneration cycle (Table 2.1). Negligible silver (> 20 ppb) was found in the fuel itself after testing, which is important for potential silver recovery from the ether rinse, as well as avoiding the introduction of additional metal ions to the SOFC and fuel reformer. The initial silver loss from PT-Ag-MASN is roughly 15%, but quickly plateaus towards a steady loss of approximately 1% of the initial silver content by the fourth cycle. This reduced loss represents a significant improvement over our previously reported Ag-MSN material, which showed 26% and 44% silver losses after the first and second cycles, respectively.

The decrease in desulfurization capacity for all materials tested correlates to the loss of silver upon regeneration. For the plasma treated materials, this loss is likely from a combination of residual ionic silver and free metallic nanoparticles not bound to the framework. It is also interesting to consider whether DBT that is coordinated to silver ions—either initially bound to the framework or weakly associated with the metallic surface—can be more easily removed during the ether rinse. If so, this might help explain the slow, gradual loss of silver after the fourth regeneration cycle. This aspect was not investigated further and we are not aware of any report addressing such a mechanism. It could not be determined from electron microscopy whether there was any significant loss (or shrinking) of the embedded silver nanoparticles in either PT-Ag-MASN or PT-Ag-MSN materials.

Other groups investigating metallic silver nanoparticles supported on pure silica[18] or alumina[19] have noted the potential for bonding between metallic silver and silanol oxygen in silica or framework oxygen in alumina. Because of the increased negative charge on oxygen coordinating Al in MASN, it is assumed that the silver-oxygen

interaction will be stronger than in MSN, at least for ionic silver. Whether the energy involved during plasma treatment is enough to form covalent silver-oxygen bonding or whether the metal-framework interaction is dominated by electrostatics warrants further investigation.

During plasma treatment in argon, nitrogen or ambient atmosphere, the material gradually changed in color from white to dark gray and finally to black, implying decomposition of $AgNO_3$ to metallic silver. No color change was observed during plasma treatment in oxygen, nor did electron microscopy reveal any metallic nanoparticles within the mesochannels. The regeneration results for PT-Ag-MASN plasma treated in oxygen were similar to those of Ag-MASN. Argon was chosen as the process gas for all subsequent experiments because its distinct fuchsia glow could be monitored to ensure all atmosphere had been purged from the reactor.

The redox mechanism of glow discharge plasma is not completely understood. Wang *et al*. have proposed two possible routes for the formation of gold and palladium nanoparticles on a mesoporous silica support *via* glow discharge plasma treatment. One is a direct process of recombination between the high-energy electrons generated in the plasma and the metal ions of the deposited metal salt. The second is an indirect process mediated by the generation of hydrated electrons and hydrogen radicals from a plasma-induced dissociation of the water molecules that naturally adsorb onto the silica framework under ambient conditions.[14] The result is the decomposition of silver nitrate to form metallic silver nanoparticles within the mesochannels of the framework (Figures 2 and 3).

The penetration depth of the plasma into the mesoporous particles and the completeness of reduction of ionic silver are important for optimizing the synthesis. In

preparation for plasma treatment, the silver loaded material was spread as thin and evenly as possible over a glass plate. After plasma treatment, only the top layer of material showed a color change from white to black, with the underlayers remaining white or gray. It was reasoned that a thorough mixing of the material between treatments should aid in complete reduction of the impregnated silver ions. It was generally observed that no significant changes in either desulfurization or regeneration capacity occurred for materials receiving more than 45 minutes (up to 90 minutes was tested) of total plasma exposure, regardless of the number of mixings (5 or 15 minute exposures). For plasma exposures totaling less than 15 minutes, the regeneration capacity over six cycles of fuel testing began to mirror that of the non-plasma treated material. Additionally, the visual color change from white to black appears complete and homogenous after three 15-minute plasma treatments.

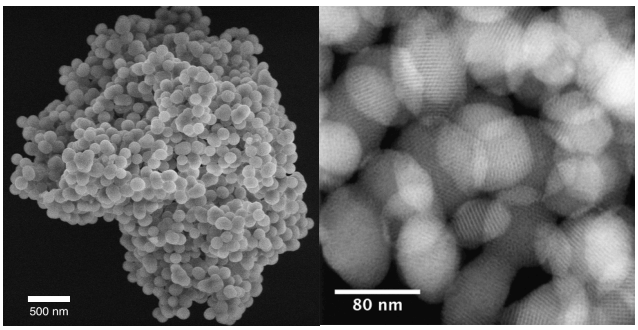

Figure 2.2 SEM image of a cluster of MASN (left) where each MASN nanoparticle has a spherical morphology. HRSTEM image of MASN (right) showing ordered mesochannels.

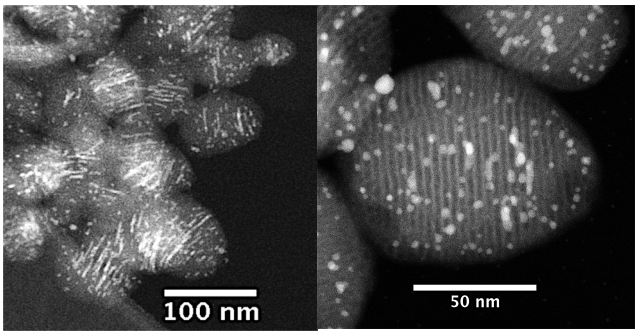

Figure 2.3 ADF-STEM images of 20 wt.% PT-Ag-MASN showing silver nanoparticles (bright contrast) within the mesochannels of MASN.

The silver loading of 20 wt.% was chosen based on previous optimization of Ag-MSN.[11] Increase in silver loading beyond this amount lead to a decrease in desulfurization capacity, likely due to silver aggregates blocking the mesochannels. It can be seen in the ADF-STEM images of the plasma treated materials that solid plugs of silver are able to form in the mesochannels (Figure 3). It was also observed that a 10% loss in surface area occurred between 20 wt.% and 25 wt.% silver loading (Table 2.2), most likely due to an increase in channel blocking by solid silver plug formation.

Powder X-ray diffraction data revealed that neither the silver loading nor plasma treatment of the material degraded the MASN framework (Figure 4). This is evidenced by the intense low angle (100) peak observed at approximately 2.5° 2-theta for all spectra. This peak corresponds to the ordered mesochannels, along with the less intense (110) and (200) peaks at approximately 4.5° and 5° 2-theta, respectively.[20,21] The (100) peak drops in intensity after silver nitrate loading and then increases again after plasma treatment. This observation may be due to the coalescence of the dispersed silver ions into discrete silver nanoparticles, liberating periodic free spaces within the mesochannels. The absence or low intensity of metallic silver peaks for PT-Ag-MASN is not necessarily

indicative of an absence of silver nanoparticles, since metallic particles with a diameter of less than 5 nm are not observable by X-ray diffraction.[22,23] For PT-Ag-MASN, PXRD peaks arise at 44.5° 2-theta, corresponding to metallic silver for the 10 min and 20 min cumulative plasma exposure times. These peaks then disappear again after 30 min of plasma exposure for the same sample. This result may be explained by the fragmentation of silver nanoparticles (larger than 5 nm), which initially formed exterior to the MASNs, upon continued plasma exposure.

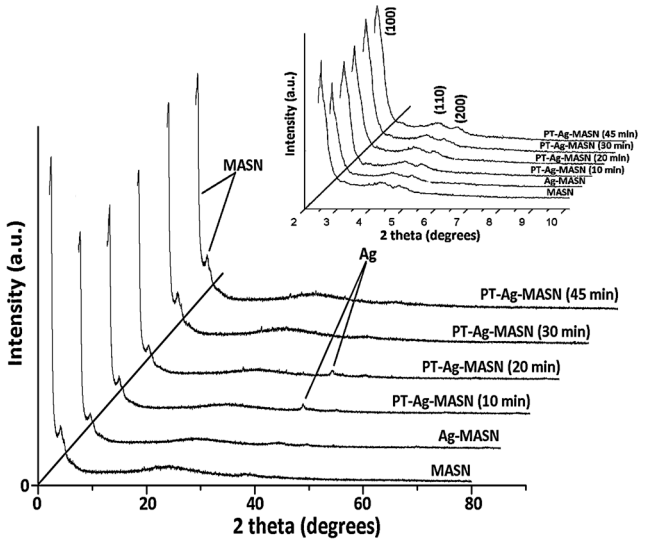

Figure 2.4 PXRD data for MASN before and after silver loading and successive plasma treatment time (inset: expansion of the low angle region and labeled Miller indices).

Diffuse Reflectance UV-visible (DR-UV-vis) spectroscopy was performed to monitor the surface plasmon resonance (SPR) of silver nanoparticles during successive plasma treatments of Ag-MASN. This data shed light on the average silver nanoparticle size within and potentially surrounding the MASN framework. Figure 5 shows the size-dependent blue-shifting of the SPR peak for metallic silver nanoparticles.[24,25] The maximum shifts from *ca*. 404 nm to 374 nm over the course of nine successive 5 minute

plasma treatments (Figure 6), indicating a decrease in the average Ag particle size with exposure time. A moderate narrowing of this peak versus time implies that the size dispersion is also reduced over successive plasma treatments.[26] This data supports the idea that larger metallic particles initially formed on the outer surface of the MASN may have been subsequently reduced in size by the etching effect of the plasma.

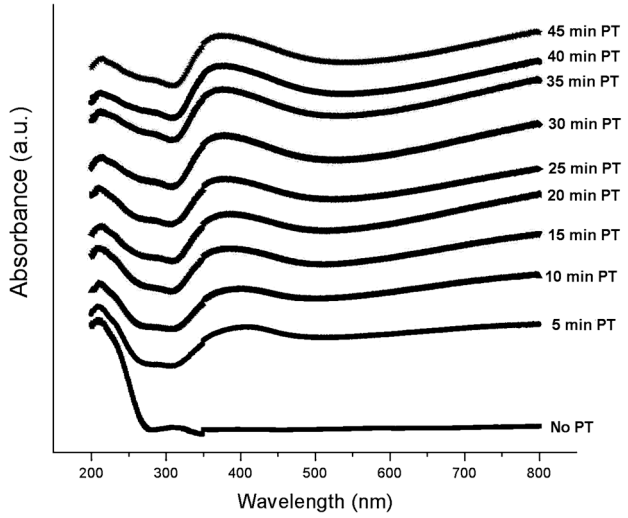

Figure 2.5 DR-UV-Vis of PT-Ag-MASN versus successive plasma treatment time.

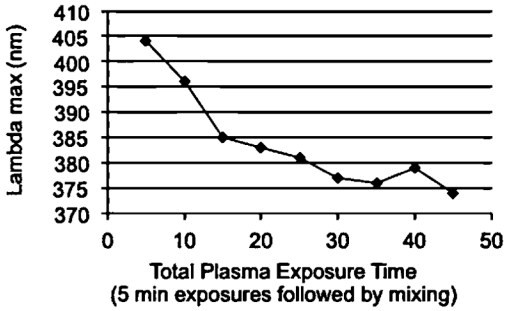

Figure 2.6 Silver nanoparticle SPR maximum versus successive plasma treatment time.

Table 2.2 BET surface area versus silver loading of PT-Ag-MASN

PT-Ag-MASN	10 wt.% Ag	15 wt.% Ag	20 wt.% Ag	25 wt.% Ag
BET surface area (m^2/g)	1054.4	1047.1	1020.6	918.3

Thermogravimetric analysis (TGA) was performed to ensure that all CTAB was removed from MASN or MSN upon calcination and to estimate the amount of physisorbed water in the material. The TGA data revealed an average 18% mass loss for either material near 100 °C, indicative of physisorbed water. Roughly the same percentage of mass loss could be observed after drying the material in vacuo for 1 h at 100 °C. Upon re-exposing the dried material to atmosphere for 12 h, the same initial mass was again observed, indicating readsorption of atmospheric moisture. Throughout the course of this work, it was noticed that the average model fuel desulfurization capacity of vacuum oven dried PT-Ag-MSN was consistently ~ 20% higher than that of the atmosphere exposed material. This observation suggests that physisorbed water needs to be removed in order for the hydrophobic fuel to make contact with the interior surface of the material.

2.4 Conclusion

The desulfurization and regeneration capacities of silver loaded mesoporous silica nanoparticles have been greatly improved by the addition of intraframework aluminum and the reduction of silver ions to silver nanoparticles within the mesochannels *via* glow discharge plasma treatment. Model fuel testing shows 78.9% desulfurization capacity for PT-Ag-MASN after 6 cycles using diethyl ether for regeneration. A high capacity desulfurization of JP-8 fuel of 41.1 mgS/g was also obtained. Further work remains to optimize this material for the desulfurization of JP-8 fuel, as well as to understand the mechanism of plasma reduction of ionic silver and the nature of the metallic silver interaction with the MASN framework.

2.5 References

(1) Samokhvalov, A.; Tatarchuk, B. J. Review of Experimental Characterization of Active Sites and Determination of Molecular Mechanisms of Adsorption, Desorption and Regeneration of the Deep and Ultradeep Desulfurization Sorbents for Liquid Fuels. Catal. Rev.: Sci. Eng. **2010**, *52*, 381−410.

(2) Hernandez-Maldonado, A. J.; Yang, R. T. Desulfurization of Transportation Fuels by Adsorption. Catal. Rev.: Sci. Eng. **2004**, *46*, 111−150.

(3) Yang, R. T.; Hernandez-Maldonado, A. J.; Yang, F. H. Desulfurization of transportation fuels with zeolites under ambient conditions. Science **2003**, *301*, 79−81.

(4) Song, C. An overview of new approaches to deep desulfurization for ultra-clean gasoline, diesel fuel and jet fuel. Catal. Today **2003**, *86*, 211−263.

(5) Ma, X.; Sun, L.; Song, C. A new approach to deep desulfurization of gasoline, diesel fuel and jet fuel by selective adsorption for ultra- clean fuels and for fuel cell applications. Catal. Today **2002**, *77*, 107− 116.

(6) Nair, S.; Tatarchuk, B. J. Supported silver adsorbents for selective removal of sulfur species from hydrocarbon fuels. Fuel **2010**, *89*, 3218−3225.

(7) McKinley, S. G.; Angelici, R. J. Deep desulfurization by selective adsorption of dibenzothiophenes on Ag^{+}/SBA-15 and Ag^{+}/SiO_2. Chem. Commun. **2003**, *39*, 2620−2621.

(8) Chen, H.; Wang, Y.; Yang, F. H.; Yang, R. T. Desulfurization of high-sulfur jet fuel by mesoporous π-complexation adsorbents. Chem. Eng. Sci**. 200**9, *64*, 5240−5246.

(9) Hernández-Maldonado,A.J.;Yang,R.T.Desulfurizationof Liquid Fuels by Adsorption via π Complexation with Cu(I)−Y and Ag−Y Zeolites. Ind. Eng. Chem. Res. **2003**, *42*, 123−129.

(10) Shahadat Hussain, A. H. M.; Yang, H.; Tatarchuk, B. J. Investigation of Organosulfur Adsorption Pathways from Liquid Fuels onto $Ag/TiO_x-Al_2O_3$ Adsorbents at Ambient Conditions. Energy Fuels **2013**, *27*, 4353−4362.

(11) Palomino, J. M.; Tran, D. T.; Hauser, J. L.; Dong, H.; Oliver, S. R. J. Mesoporous silica nanoparticles for high capacity adsorptive desulfurization. J. Mater. Chem. A **2014**, *2*, 14890−14895.

(12) Zhu, X.; Huo, P.-p.; Zhang, Y.-p.; Liu, C.-j. Characterization of Argon Glow Discharge Plasma Reduced Pt/Al_2O_3 Catalyst. Ind. Eng. Chem. Res. **2006**, *45*, 8604−8609.

(13) Liu, C.-j.; Zou, J.; Yu, K.; Cheng, D.; Han, Y.; Zhan, J.; Ratanatawanate, C.; Jang, B. W.-L. Plasma application for more environmentally friendly catalyst preparation. Pure Appl. Chem. **2006**, *78* (6), 1227−1238.

(14) Wang, Z.-j.; Xie, Y.; Liu, C.-j. Synthesis and Characterization of Noble Metal (Pd, Pt, Au, Ag) Nanostructured Materials Confined in the Channels of Mesoporous SBA-15. J. Phys. Chem. C **2008**, *112*, 19818−19824.

(15) Chen, Y.; Wang, H.; Liu, C. J.; Zeng, Z.; Zhang, H.; Zhou, C.; Jia, X.; Yang, Y. Formation of monometallic Au and Pd and bimetallic Au−Pd nanoparticles confined in mesopores via Ar glow-discharge plasma reduction and their catalytic applications in aerobic oxidation of benzyl alcohol. J. Catal. **2012**, *289*, 105−117.

(16) Kosslick, H.; Lischke, G.; Parlitz, B.; Storek, W.; Fricke, R. Acidity and active sites of Al-MCM-41. Appl. Catal., A **1999**, *184*, 49− 60.

(17) Hussain, A. H. M. S.; McKee, M. L.; Heinzel, J. M.; Sun, X.; Tatarchuk, B. J. Density Functional Theory Study of Organosulfur Selective Adsorption on Ag-TiO_2 Adsorbents. J. Phys. Chem. C **2014**, *118*, 14938−14947.

(18) Pol, V. G.; Srivastava, D. N.; Palchik, O.; Palchik, V.; Slifkin, M. A.; Weiss, A. M.; Gedanken, A. Sonochemical deposition of silver nanoparticles on silica spheres. Langmuir **2002**, *18*, 3352−3357.

(19) Johnson, K. H.; Pepper, S. V. Molecular-orbital model for metal- sapphire interfacial strength. J. Appl. Phys. **1982**, *53*, 6634−6637.

(20) Mercier, L.; Pinnavaia, T. Heavy Metal Ion Adsorbents Formed by the Grafting of a Thiol Functionality to Mesoporous Silica Molecular Sieves: Factors Affecting Hg(II) Uptake. Environ. Sci. Technol. **1998**, *32*, 2749−2754.

(21) Marler, B.; Oberhagemann, U.; Vortmann, S.; Gies, H. Influence of the sorbate type on the XRD peak intensities of loaded MCM-41. Microporous Mater. **1996**, *6*, 375−383.

(22) Yan, W.; Chen, B.; Mahurin, S. M.; Schwartz, V.; Mullins, D. R.; Lupini, A. R.; Pennycook, S. J.; Dai, S.; Overbury, S. H. Preparation and Comparison of Supported Gold Nanocatalysts on Anatase, Brookite, Rutile, and P25 Polymorphs of TiO_2 for Catalytic Oxidation of CO. J. Phys. Chem. B **2005**, *109*, 10676−19685.

(23) Kondrat, S. A.; Shaw, G.; Freakley, S. J.; He, Q.; Hampton, J.; Edwards, J. K.; Miedziak, P. J.; Davies, T. E.; Carley, A. F.; Taylor, S. H.; Kiely, C. J.; Hutchings, G. J. Physical mixing of metal acetates: a simple, scalable method to produce active chloride free bimetallic catalysts. Chem. Sci. **2012**, *3*, 2965−2971.

(24) Agnihotri, S.; Mukherji, S.; Mukherji, S. Size-controlled silver nanoparticles synthesized over the range 5−100 nm using the same protocol and their antibacterial efficacy. RSC Adv. **2014**, *4*, 3974− 3983.

(25) Jing, A. N.; De-song, W.; Xiao-yan, Y. Synthesis of Stable Silver Nanoparticles with Antimicrobial Activities in Room-temperature Ionic Liquids. Chem. Res. Chin. Univ. **2009**, *25* (4), 421−425.

(26) Ahmad, M. M.; Abdel-Wahab, E. A.; El-Maaref, A. A.; Rawway, M.; Shaaban, E. R. Irradiation of silver and agar/silver nanoparticles with argon, oxygen glow discharge plasma, and mercury lamp. SpringerPlus **2014**, *3* (443), 1−9.

Chapter 3

A Supported Nickel Boron Composite for the Catalytic Reduction of Nitroarenes

Abstract

An amorphous nickel and boron composite (NBC) was synthesized from nickel chloride hexahydrate ($NiCl_2 \bullet 6H_2O$) and sodium borohydride ($NaBH_4$) in absolute ethanol, both in bulk and supported on mesoporous aluminosilicate nanoparticles (MASN). Comparatively, NBC-MASN demonstrated better catalytic activity for the selective reduction of the nitro group on a variety of polysubstituted nitroarenes, using hydrazine hydrate ($N_2H_4 \bullet H_2O$) as the reducing agent at 25 °C. Reuse and regeneration of NBC-MASN for the reduction of *p*-nitrotoluene to *p*-toluidine were studied with $NaBH_4$ acting as regeneration agent. Good catalytic activity was sustained through nine reuse cycles when equimolar $NaBH_4$ was present in-situ with $N_2H_4 \bullet H_2O$ (99%-67% isolated aniline yield). The structure and composition of NBC and NBC-MASN were examined by electron microscopy, energy dispersive X-ray spectroscopy (EDS), powder X-ray diffraction (PXRD), X-ray photoelectron spectroscopy (XPS), thermogravimetric analysis (TGA), and inductively coupled plasma optical emission spectroscopy (ICP-OES). The results for NBC-MASN show that a thin (< 10 nm) amorphous coating forms over the MASN surface, consisting of a mixture of metallic and oxidized nickel (9_w% Ni), and various species of boron (atomic ratio of Ni:B = 2). For unsupported NBC, metallic nickel nanocrystals (1-3 nm) were discovered imbedded within an amorphous matrix of a similar composition. Upon calcination at 550 °C in N_2 atmosphere, partial

conversion of unsupported NBC to crystalline Ni_3B was observed, whereas only crystalline metallic Ni was observed for NBC-MASN. To explain these differences, further evidence is given to suggest the presence of residual boron hydrides encapsulated in the bulk unsupported NBC, suggesting Ni_3B was an artifact of processing rather than an initial product.

3.1 Introduction

The reduction of nitroarenes to aromatic amines is of general interest for industrial as well as biological applications. Aromatic amines are used as intermediates in the production of dyes, pharmaceuticals, fertilizers, pesticides, and numerous polymers; and are found as the byproducts in the neutralization of nitro-containing explosives.[1] Traditionally, the synthesis of aromatic amines from their corresponding nitro compounds is carried out at high temperatures and pressures, in the presence of hydrogen gas and a metallic catalyst such as Pt, Pd, Fe, Sn, or the well-known Raney Nickel (equation 1).[2–4]

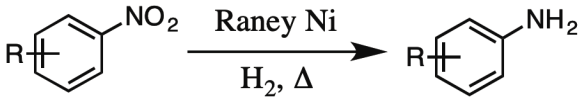

Equation 3.1 Reduction of arylnitro catalyzed by Raney Ni to the arylamine products.[5]

Drawbacks associated with these heterogeneous catalysis systems include high monetary cost, large energy consumption and safety hazards associated with the use of compressed hydrogen gas at elevated temperatures and pressures. Alternatively, amorphous heterogeneous catalysts composed of mixtures of transition metal and various boron species, formed from reacting metal salts (typically those of Ni or Co) with sodium borohydride ($NaBH_4$) in protic solvents, have a long history of success in a wide variety of reduction reaction schemes.[6–9] In aqueous media, sodium borohydride will generally

reduce metal salts (such as $NiCl_2$ and $CoBr_2$) to their corresponding metallic (M^0) phase, while undergoing hydrolysis to form borate species and liberate hydrogen gas (equation 2).[10]

$$BH_4^- + 2M^{2+} + 2H_2O \rightarrow 2M + BO_2^- + 4H^+ + 2H_2$$

Equation 3.2 General scheme for the reduction of transition metal divalent cations by borohydride in water.

The metals obtained from such reductions precipitate from the aqueous solution as black solids that could be best described as nickel or cobalt based borate composites. It has been shown that both nickel and cobalt based composites perform excellently in the catalytic hydrogenation of a variety of organic substrates containing reducible functional groups. Furthermore, the hydrolytic degradation of BH_4^-,[11–13]and nickel based composites are particularly successful at selectively reducing nitroarene compounds to their corresponding aniline derivatives.[14,15]However, the reusability of such catalysts is typically limited due to particle sintering, agglomeration, and surface oxidation. More recently it has been shown that supporting these composites on inert scaffolds (such as titania, silica gel or mesoporous silica nanoparticles) can enhance activity and reusability, compared to the bulk powders, by increasing catalyst surface area and stabilizing against particle agglomeration.[16,17] These catalysis schemes have also benefited from the use of safer and more stable chemical sources of hydrogen, such as hydrazine hydrate ($N_2H_4 \bullet H_2O$).[14,16,18,19]

The motivation for our study was to investigate the safe and economically efficient reduction of nitroarenes, using $N_2H_4 \bullet H_2O$ and a reusable amorphous nickel boron composite (NBC) catalyst, derived from the reaction of Ni^{2+} salts with $NaBH_4$, and supported on mesoporous aluminosilicate nanoparticles (MASN). In the course of this

work, fundamental questions arose concerning the difference in physical character between supported and unsupported versions of NBC. These questions are discussed in light of considerable uncertainty in the literature as to the actual composition of such amorphous composites.[20–25]

In protic solvents at ambient pressure and temperature, most salts of the first row transition metals to the left of copper generate precipitates containing various boron species when reacted with excess $NaBH_4$, whereas copper and noble metal salts with more favorable reduction potentials tend to give pure metallic phases.[26] In the case of nickel (and similarly for cobalt), these precipitates have historically been referred to as amorphous nickel borides (Ni_3B, Ni_2B, etc.), a designation initially based on a combination of elemental analysis and powder X-ray diffraction studies of the crystalline structures evolved upon heating in inert atmosphere.[27–29] These amorphous precipitates are now known to be more structurally complex, possessing a variety of possible compositions and morphologies, depending on the choice of synthetic parameters (solvent system, pH, temperature, mixing rate and the presence of oxygen in solution), the ratio of borohydride to nickel reacted, and the choice of nickel salt precursor.[26,30]

To explain the characteristically high activity of amorphous catalysts such as nickel boron and cobalt boron composites (NBC and CBC, respectively) earlier works in this field suggested the presence of a direct metal-boron interaction based on X-ray photoelectron spectroscopy (XPS) data. One scenario put forward is that electron donation occurs from boron to symmetry related transition metal d-orbitals, and therefore increases catalytic activity through electron enrichment of the metal surface, while also sacrificially protecting the metal from oxidation.[30–37] However, a review of the previously published XPS data reveals a certain amount of ambiguity in assigning both the B 1s and

Ni or Co 2p binding energy shifts to that of the corresponding borides, as well as debate about the direction of electron donation between the metal and boron, in both the amorphous and crystalline compounds.[38]

With careful use of electron microscopy and elemental analysis, some authors have shown that bulk NBC and CBC powders are nanocomposites comprising single-nanometer sized crystalline metal particles imbedded in an amorphous matrix containing boron oxides (transition or alkali metal borates, (poly)borates, etc.).[20–24,39] Although many of these authors invoke the presence of borides, they presume that the main function of the amorphous matrix is to physically prevent sintering and rapid oxidation of the catalytically active metal particles during synthesis, thereby preserving the large catalytic surface area claimed to be responsible for high activity.

While the exact nature of the metal-boron interaction in these amorphous materials remains uncertain, it is known that crystalline borides of transition metals are routinely formed under much more energetically demanding conditions than those of protic solvent synthesis at near-ambient conditions. Traditional nickel borides are synthesized in solid state reactions such as laser ablation or melt quenching of elemental Ni and B,[40] or in non-protic solvent systems at elevated temperatures (~90 °C).[26] Given that borohydrides are known to decompose readily in protic solvents[38] to produce $H_{2(g)}$ and various borates ($B(OH)_4^-$, BO_2^-, B_2O_3, polyborates, etc.), and given that this process is autocatalyzed in-situ by the very same precipitates formed during the reaction of borohydrides with certain transition metal salts, particularly Ni^{2+} and Co^{2+},[12] it seems self-evident that protic solvent synthesis routes cannot produce true transition metal borides. It is much more plausible that such reactions primarily produce oxides of boron, which may then interact strongly with metallic precipitates to form amorphous transition

metal and borate composites.[41] We are therefore careful not to label the bulk NBC and supported NBC-MASN catalysts studied in this work as a *nickel boride*, in recognition that the exact identities of the boron species present in such composites are still not entirely known.

Reported here is the synthesis of an NBC-MASN catalyst for the efficient and selective reduction of arylnitro compounds to the corresponding arylamines using hydrazine hydrate as the hydrogen source. Additionally, NBC catalyst was examined to delineate the differences between supported and unsupported catalysts and to offer a preliminary explanation as to why the Ni_3B phase is only observed upon calcination of unsupported NBC in inert atmosphere.

3.2 Experimental

All reagents were used as received without further purification. Milli-Q water (18.2 MΩ) was used throughout all steps of synthesis. High purity, dry argon (Ar) was used during catalyst synthesis, storage and use. 200 proof ethanol (EtOH) and hydrazine hydrate ($N_2H_4 \bullet H_2O$) were purchased from Acros. Nickel chloride hexahydrate ($NiCl_2 \bullet 6H_2O$), sodium hydroxide (NaOH), aluminum isopropoxide ($Al(O\text{-}i\text{-}Pr)_3$) and sodium borohydride ($NaBH_4$) were purchased from Spectrum Laboratories. Cetyltrimethylammonium bromide (CTAB), tetraethoxysilane (TEOS), nitroarene substrates, and methanol (MeOH) were all purchased from Sigma Aldrich.

3.2.1 Synthesis of MASN

Mesoporous aluminosilicate nanoparticles (MASN) were synthesized by adding a mixture of TEOS (4.58 g, 21.98 mmol) and $Al(O\text{-}i\text{-}Pr)_3$ (0.244 g, 1.19 mmol) (briefly

sonicated) to a previously prepared solution consisting of water (485 g), CTAB (1.0 g, 2.74 mmol) and solid NaOH (2.80 g, 70.01 mmol). The CTAB and NaOH solution was first stirred for 15 minutes at 80 °C to homogenize, before adding the alkoxide mixture drop wise over 5 minutes. The combined solution was stirred at 80 °C for 2 h, then allowed to cool to room temperature while stirring for an additional hour. The cooled precipitate was filtered and washed with 1.0 L of Milli-Q water and then dried in vacuo overnight at 100 °C. The dried material was then ground to a fine powder and calcined in air at 550 °C for 5 h (at a heating rate of 1 °C per minute) to remove the organic template.

3.2.2 Synthesis of NBC-MASN Catalyst

In a typical synthesis of NBC-MASN catalyst, MASN support (0.65 g) was dried in a vacuum oven overnight at 100 °C, cooled to room temperature, and then soaked in a solution of $NiCl_2 \bullet 6H_2O$ (0.26 g, 1.09 mmol) dissolved in 50/50 v/v EtOH and water. A minimal amount (~3 mL) of solvent was used to create a thick slurry with the MASN. This slurry was sonicated in a tightly sealed 20 mL scintillation vial for 90 minutes and then allowed to soak for 5 d before drying overnight in a thoroughly $Ar_{(g)}$ purged vacuum oven at 100°C. Dried $NiCl_2$-MASN was mechanically ground with $NaBH_4$ (0.084 g, 2.20 mmol) until thoroughly mixed together as a fine powder. The powder mixture was then gently purged with $Ar_{(g)}$ while cooling in a 0 °C water bath for 20 min, before rapidly introducing 19 mL of 0 °C absolute EtOH (200 proof) with vigorous magnetic stirring. The synthesis was carried out in a semi-sealed scintillation vial with two small ports in the cap, one to allow for the introduction of a glass cannula into the reaction solution to deliver $Ar_{(g)}$, and the other for gas ventilation. The synthesis proceeded with continuous argon purging of the solution and rapid stirring for approximately 2 h, or until no more

effervescent bubbling from $H_{2(g)}$ production could be observed. The solution was then diluted with 30 mL of room temperature water to help remove excess salts, centrifuged to isolate the solid, and the solid was dried overnight in a $Ar_{(g)}$ purged vacuum oven at 100 °C. The dry NBC-MASN catalyst was then stored under $Ar_{(g)}$ until use in catalysis or characterization.

3.2.3 Synthesis of NBC Catalyst

Unsupported, bulk NBC catalyst powder was synthesized by adding a solution of $NiCl_2 \bullet 6H_2O$ (0.26 g, 1.09 mmol) dissolved in 8.5 mL of absolute EtOH to a solution of $NaBH_4$ (0.084 g, 2.20 mmol) suspended in 8.5 mL of absolute EtOH, with rapid stirring at 0 °C under continuous $Ar_{(g)}$ purging as described above. Synthesis proceeded for approximately 20 min or until no more $H_{2(g)}$ production could be observed, at which point the material was rinsed, retrieved and dried as described above.

3.2.4 Calcination of as-synthesized catalysts

A custom-made calcination furnace with a quartz tube was used to heat the catalyst materials in either flowing nitrogen or air at 550 °C for 2 h, at a heating rate of 10 °C·min^{-1}.

3.2.5 General Procedure for the Reduction of Nitroarenes

To an argon-purged 50-mL round bottom flask the NBC-MASN catalyst (0.235 g, 0.4 mmol of Ni), nitroarene (4 mmol), MeOH (8 mL), and either $N_2H_4 \bullet H_2O$ (20 mmol) or a combination of $N_2H_4 \bullet H_2O$ (20 mmol) and $NaBH_4$ (20 mmol) were added and allowed to stir at room temperature for 24 h. The reaction mixture was then centrifuged,

and the supernatant decanted into a pre-weighed 100 mL round bottom flask. The solid catalyst was rinsed with 15 mL of MeOH under brief sonication, followed by centrifugation and the supernatant was decanted into the same 100 mL flask. This rinse step was repeated, and the combined supernatants were then concentrated by rotary evaporation and analyzed via ^{1}H and ^{13}C NMR.

3.2.6 General Procedure for Cleaning NBC-MASN

The used NBC-MASN catalyst and methanol (2 × 15 mL) were combined in an argon-purged Falcon tube, the mixture was sonicated for 10 min, then centrifuged and the supernatant decanted. Ethanol (2 × 15 mL) was added to the catalyst and sonicated for 10 min, centrifuged, and the supernatant decanted. Methanol (10 mL) was added to the catalyst before sonication for 10 min, centrifuged, and the supernatant decanted. The catalyst was then immediately reused.

3.2.7 General Procedure for the Regeneration of NBC-MASN

Cleaned (as above) and dried NBC-MASN and $NaBH_4$ (2 mol equivalent to Ni, assuming Ni was 10_w% of NBC-MASN) were added to an argon-purged Falcon tube capped with a rubber septum. The tube was cooled to 0 °C before adding 5 mL of 0 °C ethanol. The cold mixture was rapidly stirred for approximately 1 h or until no more $H_{2(g)}$ production was observed. The mixture was then centrifuged, the supernatant decanted, and the recovered solid was rinsed as described above and dried in an argon-purged vacuum oven until further use.

3.2.8 General Procedure for Hydrogen Evolution by Gas Burette

To the gas burette reservoir, outfitted with a rubber septum, 1 M HCl (15mL), methanol (15mL), and tetrahydrofuran (15mL) were added and allowed to stir. A few trials of sacrificial hydride sources were used for the purpose of equilibrating the system. In a separate Ar-purged round bottom flask, anhydrous $NiCl_2$ (0.065 g, 0.5 mmol) and solid $NaBH_4$ (0.038 g, 1 mmol) were added and the flask cooled to 0 °C. A cannula connected the round bottom flask to the gas burette reservoir. The system was allowed to equilibrate before the addition of 4 mL of 0 °C ethanol via syringe. By the controlled relief of pressure in the closed system into a graduated cylinder, the volume of gas generated, plus total volume injected, was measured by water displacement. The temperature of the displaced water and barometric pressure was also measured, and the temperature dependent vapor pressure of water. The quantity of hydrogen produced was determined by following a previously published method.[42]

3.2.9 Characterization

Powder X-ray diffraction (PXRD) was performed on a Rigaku SmartLab X-ray diffractometer with Cu-Kα (1.54 Å) radiation (40 kV, 44 mA). All samples were prepared fresh and handled with minimal exposure to atmosphere prior to scanning. All samples were ground under $Ar_{(g)}$ and evenly dispersed on an amorphous SiO_2 sample holder and scanned with a step size of 0.01° and scan rate of $1°\cdot min^{-1}$. High angle annular dark field scanning transmission electron microscopy (HAADF-STEM) imaging was performed on an FEI Titan TEM operated at 300 kV. The STEM probe had a convergence semiangle, α, of 10 mrad and a beam current of 25 pA (300 kV). HAADF-

STEM images were acquired using a Fischione annular dark-field (ADF) detector with an inner semiangle, β, of 45 mrad. EDS data was simultaneously collected along with HAADF-STEM data on four silicon drift detectors with a solid angle of 0.7 steradians (SuperX) and analyzed using Bruker's Espirit software. HRTEM images were acquired using an FEI ThemIS microscope operated at 300kV with a FEI Ceta 2 Camera. All electron microscopy and EDS data collection were carried out on fresh samples suspended by brief sonication in absolute ethanol and deposited on 400 mesh copper TEM grids with lacey carbon support. Inductively coupled plasma optical emission spectroscopy (ICP-OES) data were collected on a PerkinElmer Optima 7000 DV. Samples for ICP-OES were prepared by digestion in an aqueous solution comprised of 50_v% concentrated HNO_3 and 5_v% H_2O_2 (30% stock solution) at 85 °C, rapidly stirring in a sealed polypropylene container for 2 h prior to dilution with Milli-Q water. Thermogravimetric analysis (TGA) was performed on a TA Q500 Thermoanalyzer, using a platinum weighing boat and flowing air during heating fresh samples at a rate of 10 °C·min^{-1}. X-ray photoelectron spectroscopy was performed on a Kratos Axis Ultra spectrometer using an Al-K_α source ($h\nu = 1486.69$ eV) operated at 150 W and a hemispherical electron energy analyzer. Spectral positions were calibrated using adventitious alkyl carbon signals by shifting the C 1*s* peak to 284.8 eV. For samples which exhibited charging, a flood gun was used to neutralize the sample.

The products of catalysis reactions were analyzed by nuclear magnetic resonance (NMR) spectroscopy measured in ppm and recorded on a Bruker 500 MHz spectrometer at 297 K using $CDCl_3$ (δ = 7.26) as an internal standard for ^{1}H NMR and 125.7 MHz using $CDCl_3$ (δ = 77.0) as an internal standard for ^{13}C NMR. Using a different probe, ^{11}B NMR analysis occurred on a 160 MHZ spectrometer using BF_3•Et_2O (δ = 0) as an

external standard. Coupling constants (*J*) are given in Hertz (Hz) and signal multiplicities are abbreviated as s = singlet, d = doublet, t = triplet, m = multiplet, and br = broad. NMR data can be found in appendix A1.

3.3 Results and Discussion

This work was begun by screening a number of catalysts made from different transition metal salts reacted with $NaBH_4$ in ethanol, for the reduction of *p*-nitrotoluene to *p*-toluidine using hydrazine hydrate ($N_2H_4 \bullet H_2O$) (Table S3.1). It was found that $NiCl_2 \bullet 6H_2O$ was the most suitable precursor in forming a catalyst to this effect. The percent yield of *p*-toluidine was determined by isolation and the purity was verified by ^1H NMR spectroscopy. It was also found that supporting this catalyst, which was termed nickel boron composite (NBC), on an inert scaffold made of mesoporous aluminosilicate nanoparticles (MASN) improved catalytic activity over the unsupported catalyst. MASN was chosen as a support owing to the material's robust aluminosilicate structure, high surface area (~100 nm average diameter, ~1000 $m^2 \cdot g^{-1}$) and mildly negative surface charge.[43] It was hypothesized that these features would allow for good incorporation of Ni^{2+} into the support during impregnation with $NiCl_2 \bullet 6H_2O$, and also slow diffusion of Ni^{2+} out of MASN during reaction of dried $NiCl_2$-MASN with $NaBH_4$ in absolute ethanol. Attempts to support NBC on non-aluminated mesoporous silicate nanoparticles (MSN) resulted in a greater quantity of large, detached NBC particles formed separate from the MSN support, as observed by electron microscopy (Figure S1). The better retention and slowed diffusion of Ni^{2+} from MASN appears to allow for even distribution of the resulting composite material formed close to the MASN surface, and possibly anchored within its mesochannels. Low temperature (0 °C) synthesis was likewise

chosen to allow for slower and more complete reaction of Ni^{2+} with BH_4^-. Indeed, the synthesis of NBC-MASN was found to take approximately 2 h to complete, compared to approximately 20 min for the synthesis of unsupported NBC.

The initial catalysis reaction using fresh NBC-MASN in the reduction of *p*-nitrotoluene to *p*-toluidine reached completion after 2 h. Subsequent reuse cycles of the catalyst, however, showed progressively longer incubation periods to achieve full conversion of *p*-toluidine (Figure 1).

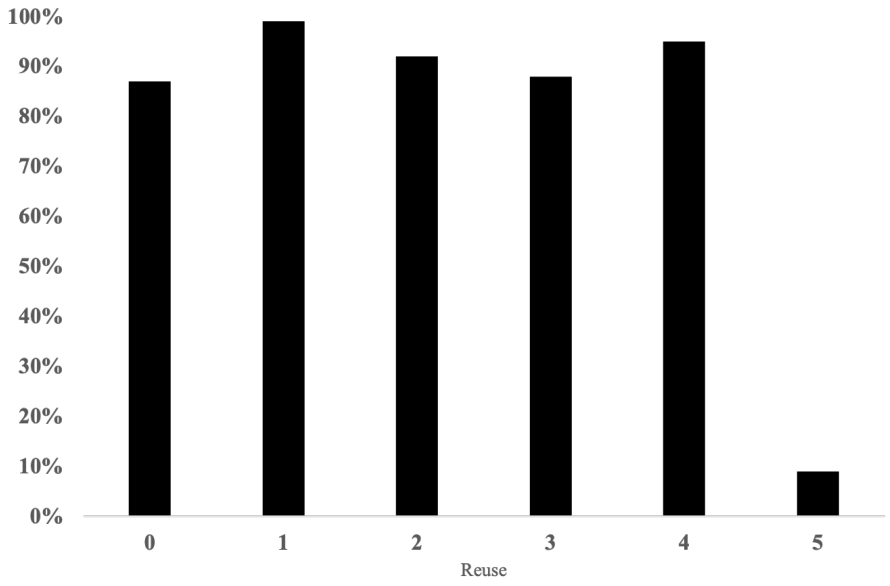

Figure 3.1 Percent yield of *p*-toluidine after successive reuse cycles of NBC-MASN. Yields based on ^1H NMR ratios.

It was speculated the cause of this increasing incubation period might be due to a loss of catalytic surface area, from the agglomeration of active Ni, and/or passivation of the catalytic surface by NiO formation during successive catalyses. This prompted us to characterize the catalytic surface of NBC-MASN using various techniques. For structural comparison the characterization of unsupported NBC as included well.

High angle annular dark field scanning transmission electron microscopy (HAADF-STEM) imaging of NBC-MASN revealed a very thin (< 10 nm) amorphous coating of material covering the honeycombed MASN particles (Figure 2a) after synthesis (Figure 2b). Synthesis of unsupported NBC typically gave particles in the hundreds of nanometers size regime (Figure 3a). Energy-dispersive X-ray spectroscopy (EDS) confirmed the presence of nickel in both NBC-MASN and unsupported NBC (Figure 3b), but detection of boron could not be confirmed due to its low signal intensity and overlap from the adjacent carbon signal (Figures S2 and S3). Given the more positive reduction potential of nickel, the majority of oxygen present in NBC (Figure 3c) is likely from borate species, rather than NiO, since freshly synthesized and carefully handled NBC should contain mostly reduced nickel. No information from EDS mapping of oxygen in NBC-MASN can be gained since the signal from SiO_2 overwhelms any contribution from borates.

Both HAADF-STEM and high-resolution transmission electron microscopy (HRTEM) imaging of fresh NBC-MASN indicated the NBC coating was amorphous. If NBC-MASN particles were subjected to several minutes of continuous electron flux, however, it was observed that small spots of high contrast material developed on or within NBC-MASN (Figure 3.2c). EDS mapping revealed that these spots appear to correspond with higher concentrations of Ni compared to the bulk of the composite (Figure 3.2d). HRTEM shows these tiny regions have crystallinity (Figure 3.2e,f), indicating the amorphous nickel in the composite segregated into larger particles and partially crystallized under the electron beam. The segregation/crystallization was particularly difficult to avoid during EDS mapping, wherein the samples were necessarily subjected to long exposures and higher beam current (Figure 3.2c, d). Figure S4 shows

the progression of this segregation starting at 30 s and after 5 min. By comparison, HRTEM imaging of fresh unsupported NBC immediately revealed the presence of approximately 1 to 3 nm nanocrystalline domains of metallic Ni deposited within a surrounding amorphous matrix (Figure 3.3d-f, and S3.5), an observation consistent with previous reports of a similarly formed composite.[39] The unsupported NBC appeared much more stable under the electron beam than the amorphous surface of NBC-MASN, and additional segregation/crystallization of Ni was more difficult to observe during longer beam exposures in the case of unsupported NBC. This suggests that much of the metallic nickel resides as these pre-formed nanocrystals in unsupported NBC, whereas nickel in NBC-MASN is more homogenously amorphous and evenly distributed within the NBC structure that coats the MASN.

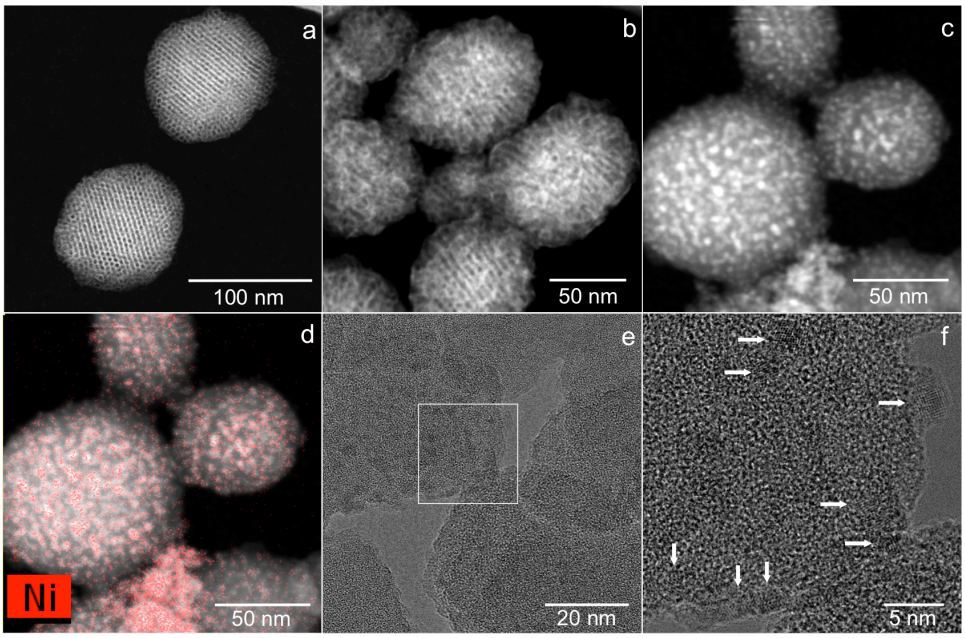

Figure 3.2 HAADF-STEM images of (a) as-synthesized MASN, (b) NBC-MASN imaged within 30 s of beam exposure, (c) NBC-MASN after EDS mapping for 5 min, with (d) the corresponding Ni EDS map. (e) HRTEM images of NBC-MASN after 5 min

exposure to electron beam showing segregated regions of Ni, and (f) a magnified section (box in e) showing lattice fringes associated with these regions (arrows).

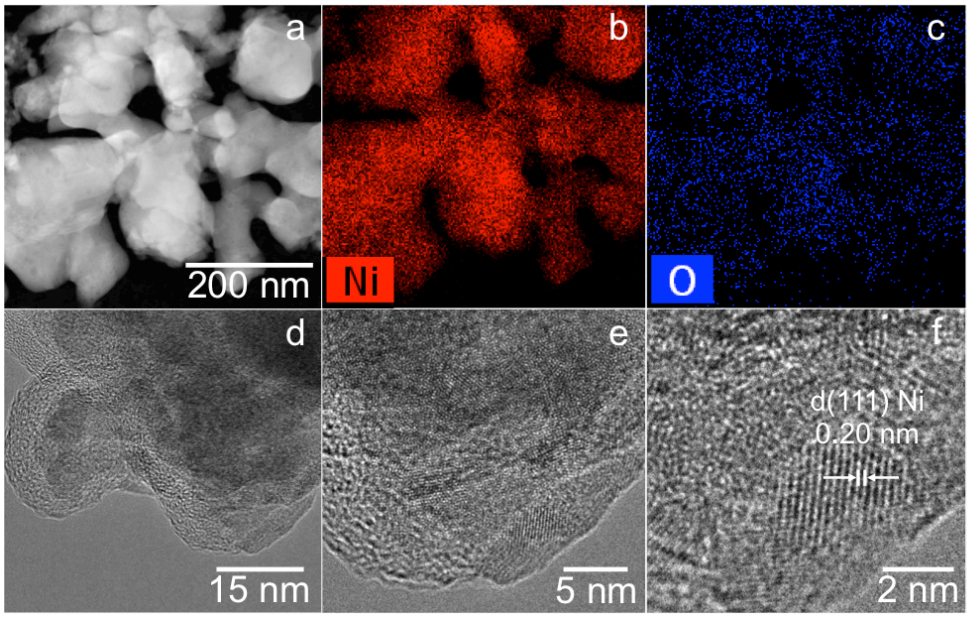

Figure 3.3 HAADF-STEM image of (a) unsupported NBC, and corresponding EDS elemental maps of (b) Ni and (c) O present in the composite. HRTEM of unsupported NBC, imaged within 2 min of beam exposure, progressively magnified (d-f) to show lattice fringes for Ni nanocrystals embedded within an amorphous matrix.

As reported in the literature, heating these amorphous composites in inert atmospheres typically yields a mixture of crystalline nickel and nickel boride in bulk materials such as NBC.[27–29] Figures 3.4 and 3.5 show the powder X-ray diffraction (PXRD) profiles for NBC-MASN and NBC, respectively, in their as-synthesized (or fresh) form, and after calcination in air or flowing nitrogen at 550 °C for 2 h. The high angle diffraction data for as-synthesized NBC-MASN displays an amorphous profile, while that of unsupported NBC gives only a broad peak occurring near the (111) reflection for fcc Ni (44.5° 2θ). This lack of appreciable diffraction from the

nanocrystalline nickel present in fresh unsupported NBC can be explained by their small size, below the ~5 nm domain cut-off necessary to produce X-ray diffraction in metallic nanoparticles.[44,45] Calcining NBC and NBC-MASN in either air or $N_{2(g)}$ gave crystalline diffraction profiles in both cases, likely due in part to the same segregation/crystallization phenomena observed by electron microscopy. Interestingly, the air-calcined NBC-MASN diffraction profile shows only peaks indexed to NiO, whereas the unsupported NBC calcined in air gave a profile showing predominantly metallic Ni, with relatively low intensity peaks for NiO. The $N_{2(g)}$-calcined NBC-MASN gave a profile for metallic Ni, whereas similar calcination of unsupported NBC yielded a mixture of crystalline Ni and Ni_3B (ICDD 00-048-1223).

In an attempt to explain this commonly reported formation of Ni_3B upon calcination of NBC in an inert atmosphere, we offer preliminary evidence to suggest there may be residual boron hydrides within the amorphous matrix of NBC. It has been previously shown that various alkali earth and transition metal borohydrides and boranes [$Mg(BH_4)$, $Ti(BH_4)_3$, $Zr(BH_4)_4$, $Hf(BH_4)_4$, and $Cr(B_3H_8)_2$] can undergo thermal decomposition to form the corresponding metal borides at moderately high temperatures (> 400 °C).[46–51] In particular, it has been shown that Ni_3B can be formed at 530 °C from the precursors $NiCl_2$ and various boranes (B_5H_9 or $B_{10}H_{14}$).[52] Thermal decomposition of residual boron hydrides during calcination of NBC would explain why crystalline nickel boride phases were observed in NBC catalyst (equation 3).

$$NiCl_2 + 2NaBH_4 \rightarrow Ni(BH_4)_2 + NaCl \xrightarrow{\Delta} "Ni_2B" \xrightarrow{Ni^{\circ}} Ni_3B \qquad (3)$$

It should be pointed out that if unsupported NBC is first refluxed in MeOH for several hours prior to $N_{2(g)}$-calcination, then only crystalline Ni is observed (Figure S3.6).

Refluxing in methanol has been previously shown to remove residual boron hydrides from similar materials,[8] which may become trapped in the composite during the rapid reaction of Ni^{2+} and BH_4^-. ^{11}B NMR analysis of the supernatant solution of the refluxed material provided a singlet at 18 ppm, suggesting that a borate is formed from hydrolysis of borohydride (Figure S3.7). Trapped boron hydride [possibly $Ni(BH_4)_2$][26] or hydrogen adducts[53] in the matrix of unsupported NBC may then decompose during heating, explaining the formation of Ni_3B upon $N_{2(g)}$-calcination (equation 3), as well as the predominance of Ni over NiO upon air-calcination of unsupported NBC. The slow formation of the thin NBC layer in NBC-MASN may prevent this entrapment of boron hydrides, and would explain the formation of both Ni upon $N_{2(g)}$-calcination and NiO upon air-calcination of NBC-MASN.

The predominance of Ni compared to NiO in the PXRD profile of air-calcined NBC may also be attributed to the sintering and surface passivation of the Ni nanocrystals during heating. These agglomerated Ni nanocrystals may retain interior particle domains of Ni sufficiently large to diffract X-rays, while being protected from further oxidation by an exterior layer composed of NiO and borate, as previously shown for similarly formed cobalt boron composites.[33] In the case of air-calcined NBC-MASN, where only NiO is present in the PXRD profile, it may be that the very thin layer of homogenously amorphous NBC coating the MASN is more extensively oxidized than in bulk unsupported NBC. Finally, in the case of $N_{2(g)}$-calcination of NBC-MASN, amorphous Ni present in the NBC-MASN simply segregates and crystalizes in domains large enough to diffract X-rays.

Calcining NBC or NBC-MASN in either air or $N_{2(g)}$ atmosphere diminished the catalytic activity toward the reduction of aromatic nitro groups, likely due to nickel

segregation/crystallization and a subsequent loss of catalytic surface area, as well as catalytically inactive surface NiO in the case of air-calcination.

The location of NBC on the external surface of MASN is apparent in Figure 3.2, but whether this material extends into the mesochannels of the support is less apparent due to the low contrast between NBC and SiO_2. Some information can be determined, however, from low angle PXRD of the material. The inset in Figure 3.4 shows the change in the (100) peak position and intensity for the MASN support, before and after NBC formation and subsequent calcination in air or nitrogen. This peak corresponds to the distance between the walls of the ~3 nm diameter channels that run through the MASN spheres. The reduction of intensity and slight shift to lower 2-theta angles may be attributed, respectively, to inclusion of NBC material within the channels, and a subtle expansion of the pores as a result of their partial degradation during calcination.[40] This degradation is not typically seen upon template extraction during MASN synthesis, which occurs at the same temperature of 550 °C, so it may result here in part from the growth of a crystalline nickel phase within the mesochannels upon calcination of NBC-MASN. Inclusion of the NBC coating within the channels of MASN may indicate that the composite is partially anchored in the pores of the MASN, allowing it to remain highly dispersed and catalytically active over multiple reuse cycles (vide infra).

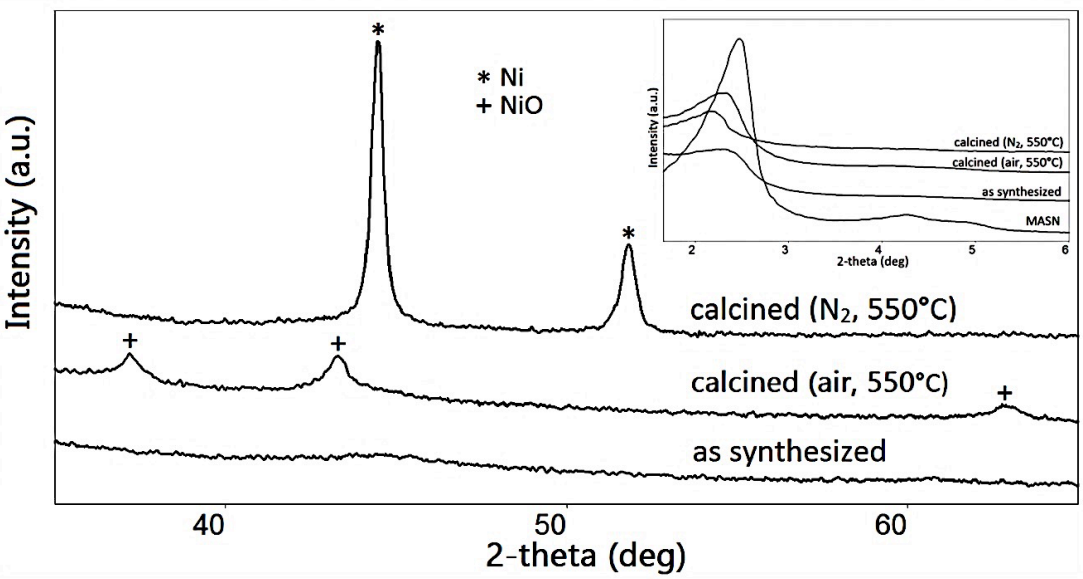

Figure 3.4. A comparison of PXRD profiles for as-synthesized (fresh) NBC-MASN and after calcination in air or flowing nitrogen. The inset shows the low angle diffraction pattern for the bare MASN compared to as-synthesized NBC-MASN before and after calcination.

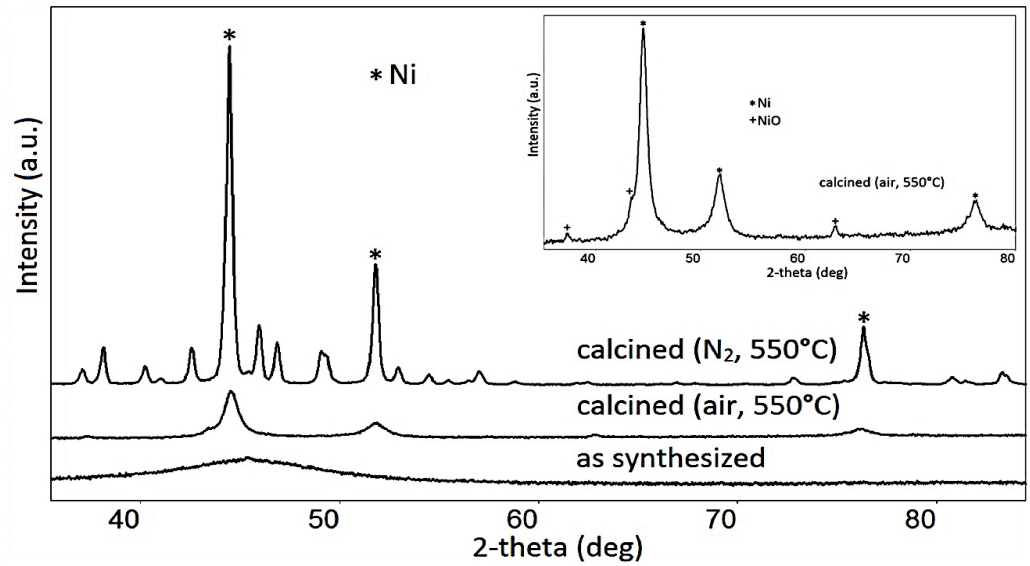

Figure 3.5. A comparison of PXRD profiles for as-synthesized (fresh) unsupported NBC and after calcination in air or flowing nitrogen. All peaks in the N_2 calcined sample not assigned to Ni (asterisks) can be assigned to Ni_3B (ICDD 00-048-1223). The inset shows an enlargement of the profile for the air-calcined material, indicating the presence of NiO.

Thermogravimetric analysis (TGA) of both unsupported NBC and NBC-MASN was performed to investigate the possible decomposition of trapped borohydride in NBC in general, as well as the oxidation of metallic nickel in both materials (Figure 3.6). Upon heating to 800 °C in air, NBC-MASN shows only the expected mass loss associated with removal of physically adsorbed water, with no appreciable mass gain that would indicate oxidation of boron or nickel. Considering that PXRD clearly shows the formation of NiO at 550 °C in air-calcined NBC-MASN, this TGA result is not easily explained. However, a similar TGA of unsupported NBC demonstrated two increases in mass initiating at approximately 350 °C and 650 °C. The first mass gain initiates very close to that observed for $NaBH_4$ similarly heated in air, which initiates at a temperature

of ~360 °C, and may indicate the presence of residual borohydride in unsupported NBC, while the second mass increase starting at ~650 °C is consistent with the oxidation of Ni nanoparticles in the nanometer size regime.[54]

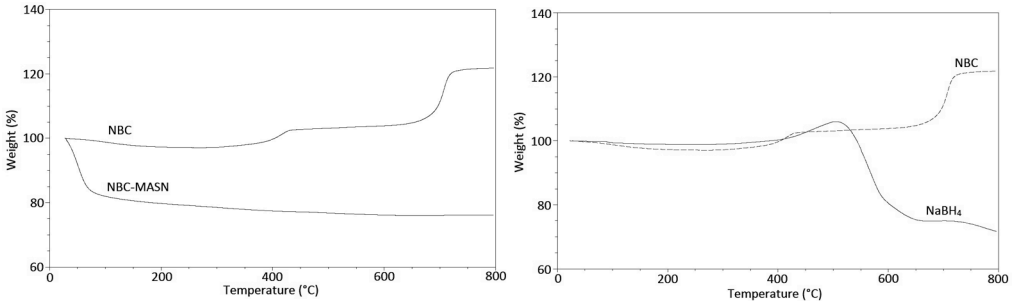

Figure 3.6. TGA data in air for NBC vs. NBC-MASN (left) and NBC vs $NaBH_4$ (right).

Because the surface of a catalytic material is of particular interest, X-ray photoelectron spectroscopy (XPS) was used in an attempt to identify the surface species present in both NBC-MASN and unsupported NBC. Figures 3.7 and 3.8 show the wide-scans and core-level scans for freshly prepared samples of both NBC-MASN and NBC, respectively. Table 3.1 gives the relevant electron binding energies for Ni, B and O in each material. It is evident from the Ni 2p core-level scans that the catalyst surface in both cases contains a mixture of metallic and oxidized nickel. The B 1s core-level scans show the presence of oxidized boron as well as a peak occurring at 187.7 eV for both materials, which is within the region typically assigned to nickel boride in the literature.[30–32] The interpretation of this B 1s peak and its assignment to nickel boride is notably difficult to make when considering the very slight shifts in binding energy observed between elemental boron, borohydride, and the relevant borides.[38] As for the B 1s shifts in these materials, the assigned shifts for Ni 2p binding energies are also typically less than 1 eV from that of metallic Ni.[30,32,55] There is also considerable and

longstanding disagreement as to whether electron donation occurs from boron to metal or vice versa in amorphous nickel borides.[38] Finally, evidence has been given of residual hydrides or hydrogen adducts in both nickel and cobalt composites, particularly when synthesized in ethanol, though the specific identity of these purported hydrides (M-H or B-H) has not been resolved.[53] Considering the interpretation of PXRD and TGA data in this work, we reason that the B 1s binding energy previously reported by others as evidence of amorphous nickel boride, may actually be indicative of residual borohydride sequestered in the composite upon formation. Indeed, the presence of residual borohydride in similar nickel based composites has been previously reported.[8] In comparing the spectra for NBC-MASN and unsupported NBC, the greatly diminished intensity of this B 1s peak at 187.7 eV relative to the adjacent borate peak implies a much lower surface concentration of this boron species in NBC-MASN. Considering the NBC layer on MASN appears by HAADF-STEM to be quite thin (perhaps only a few nanometers on average), the XPS analysis, with a reliable surface penetration depth of 5 to 10 nm, may largely account for the entire composition of the NBC layer in NBC-MASN. Assuming the B 1s peak at 187.7 eV arises from sequestered borohydride, then its lower concentration in NBC-MASN could account for the lack of any Ni_3B phase observed by PXRD after calcining in $N_{2(g)}$. Of course some portion of the initial $NaBH_4$ will fully react and become borate in the composite matrix (or rinse away as boric acid), which explains why a mixture of metallic nickel and nickel boride are typically seen after calcination.

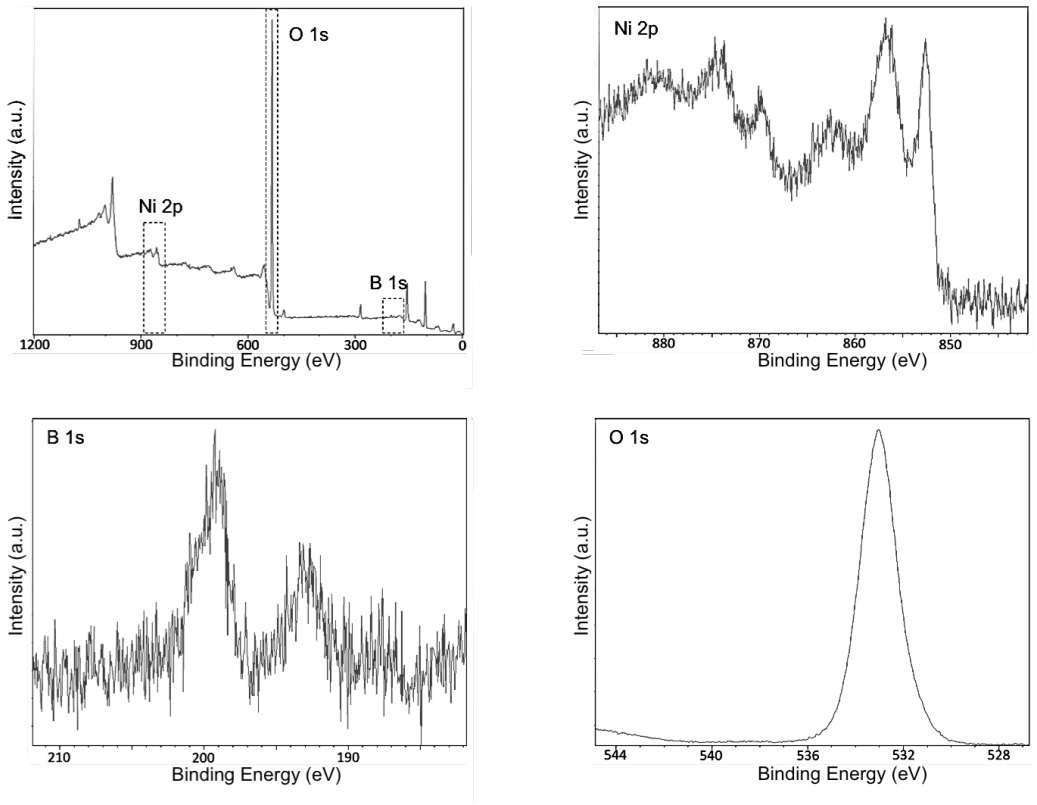

Figure 3.7 XPS data for NBC-MASN.

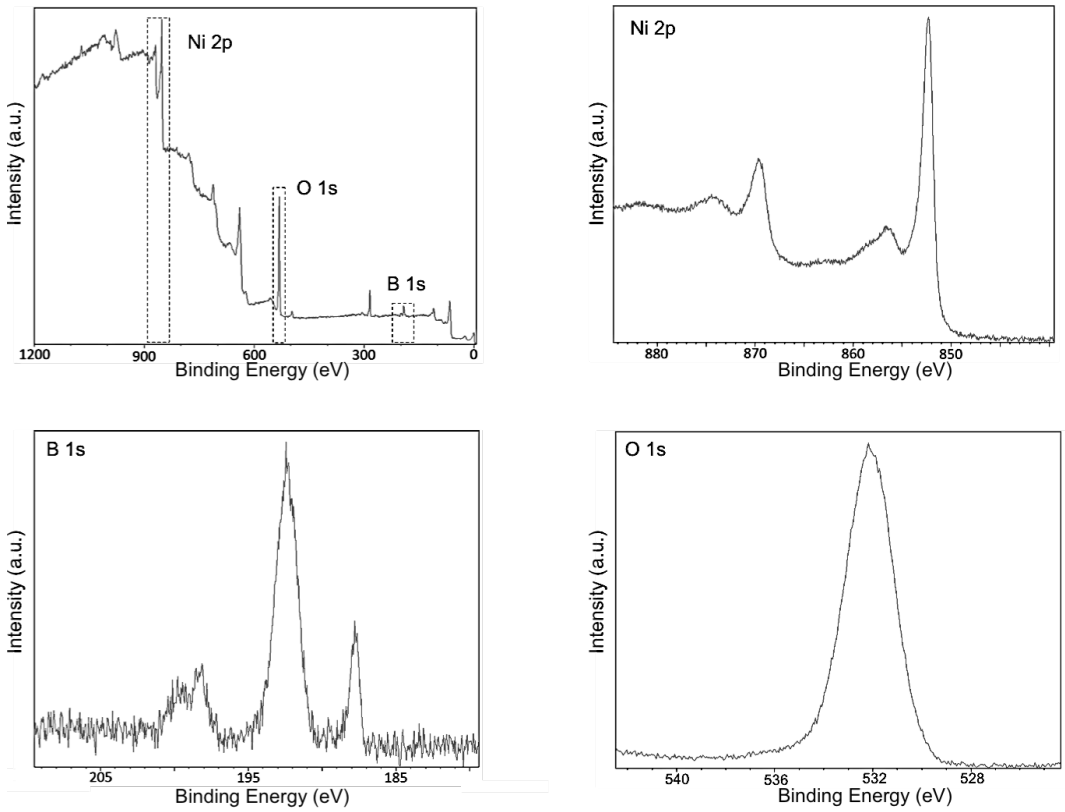

Figure 3.8 XPS data for unsupported NBC.

Table 3.1 Binding Energies of NBC-MASN and NBC

Element	NBC-MASN (eV)	NBC (eV)	Possible Compounds
Ni 2p	852.6	852.3	Ni
	856.8	856.6	NiO, $Ni(OH)_2$, $Ni(BO_2)_2$
B 1s	187.7	187.7	B_xH_y
	193.0	192.4	BO_2^-, B_2O_3
O 1s	532.8	532.3	NiO, BO_2^-, B_2O_3

Further evidence for the presence of borohydride trapped within the matrix of NBC was given by examining the quantity of hydrogen evolved during synthesis of both unsupported and supported NBC (Table S3.2). For unsupported NBC, only 51% of the theoretical amount of hydrogen was released when $NiCl_2$:$NaBH_4$ (1:2) were allowed to react at 0 °C in ethanol. Even when varying the ratio of $NiCl_2$:$NaBH_4$ from 1:1 to 1:0.5, the amount of hydrogen evolved were 43% and 54%, respectively. Similar results were obtained for $NiCl_2$-MASN:$NaBH_4$ (1:2), which liberated 56% of the theoretical amount of hydrogen, indicating that some B-H compound remains unreacted, possibly sequestered within the interstitial spaces of the material.

The bulk nickel and boron content in both NBC-MASN and unsupported NBC were determined by inductively coupled plasma optical emission spectroscopy (ICP-OES). Throughout this work, the content of Ni initially present in fresh NBC-MASN averaged 9.0_w%, while the calculated loading of Ni^{2+} into MASN via impregnation with $NiCl_2 \bullet 6H_2O$ was $10._w$%. However, no significant amount of Ni was observed by ICP-OES in the ethanol/water supernatant collected after the syntheses of either NBC or NBC-MASN. Therefore, additional moisture adsorbed in the hydrated nickel salt and instrumental error inherent during ICP-OES may account for the discrepancy. The initial

ratio of Ni:B was approximately 2 in both NBC and NBC-MASN and remained unchanged for both catalysts after calcination in either nitrogen or air.

ICP-OES was further used to track changes in the nickel and boron content after successive reuses of NBC-MASN in the reduction of *p*-nitrotoluene to *p*-toluidine. Figures 3.9 and 3.10 show, respectively, the Ni:B ratio NBC-MASN and the percent yield of *p*-toluidine determined after 24 h by ^{1}H NMR for two different reuse studies. In both studies, 5 mmol of $N_2H_4 \bullet H_2O$ was used as the reducing agent for 1 mmol of *p*-nitrotoluene, in the presence of NBC-MASN containing approximately 0.1 mmol of nickel. Sodium borohydride was used either ex-situ or in-situ with $N_2H_4 \bullet H_2O$, in an attempt to prolong the catalyst's reusable lifetime. In the ex-situ-$NaBH_4$ study, when the percent yield of *p*-toluidine was observed to decrease significantly (below 80%) upon cycling, the used NBC-MASN catalyst was cleaned, dried, (see Experimental section) and regeneration attempted by reacting it with a quantity of $NaBH_4$ equivalent to twice the molar amount of Ni assumed to be present in the catalyst. In the in-situ-$NaBH_4$ reuse study, a combination of $N_2H_4 \bullet H_2O$ and equimolar $NaBH_4$ were used, with the intention of affecting continuous in-situ regeneration of the catalyst by reaction with $NaBH_4$. As can be seen in Figure 3.9, a progressive loss of boron from NBC-MASN is observed upon each cycle in both studies, but is more dramatic in the study where only $N_2H_4 \bullet H_2O$ is present, compared to in-situ regeneration by $NaBH_4$. As can be seen in Figure 3.10, the use of $NaBH_4$ along with $N_2H_4 \bullet H_2O$ extends the lifetime of the catalyst up to nine reuse cycles, compared to only four cycles when regeneration is performed ex-situ. No significant loss of nickel from NBC-MASN was observed during either reuse study, indicating that all of the Ni^{2+} initially loaded onto MASN was reacted during the synthesis of the catalyst.

It must be pointed out that $N_2H_4 \bullet H_2O$ will not reduce NiO to Ni^0 at 25°C, and oxidation from continuous reaction with the substrate nitro group during catalysis makes oxidation of the catalyst inevitable.[56] The sustained catalytic activity of NBC-MASN observed when both $NaBH_4$ and $N_2H_4 \bullet H_2O$ were present during each catalysis cycle (Figure 3.10) is attributed to the ability of borohydride to reduce passivating surface NiO. It is also possible, given the higher average boron content compared to the ex-situ study, that in-situ $NaBH_4$ may replenish some protective borate species that physically prevent agglomeration of the active nickel or its more rapid oxidation. In contrast, it was found that exposing the catalyst to additional borohydride ex-situ, as soon as catalytic activity was observed to decrease, did not improve catalytic performance upon subsequent reuse. As can be seen in Figure 3.9, the boron content in NBC-MASN did increase after these ex-situ borohydride treatments prior to reuse 7 and 9, but sharply decreased again upon further cycling. It is reasonable to interpret this as evidence that $NaBH_4$ is reducing oxides formed on the catalytically active nickel surface, so long as the oxidation is not too extensive—as may be the case in the ex-situ regeneration study. Severe oxidation of the amorphous nickel, along with loss of the surrounding borate matrix, may leave the nickel constituent vulnerable to agglomeration, and loss of surface area, during subsequent reduction by borohydride. Further XPS and electron microscopy studies examining the surface oxidation and agglomeration/crystallization of nickel at each reuse cycle, would likely elucidate the point at which surface oxidation and/or segregation/crystallization deactivates the catalyst, and either in-situ or ex-situ borohydride regeneration is no longer possible for NBC-MASN.

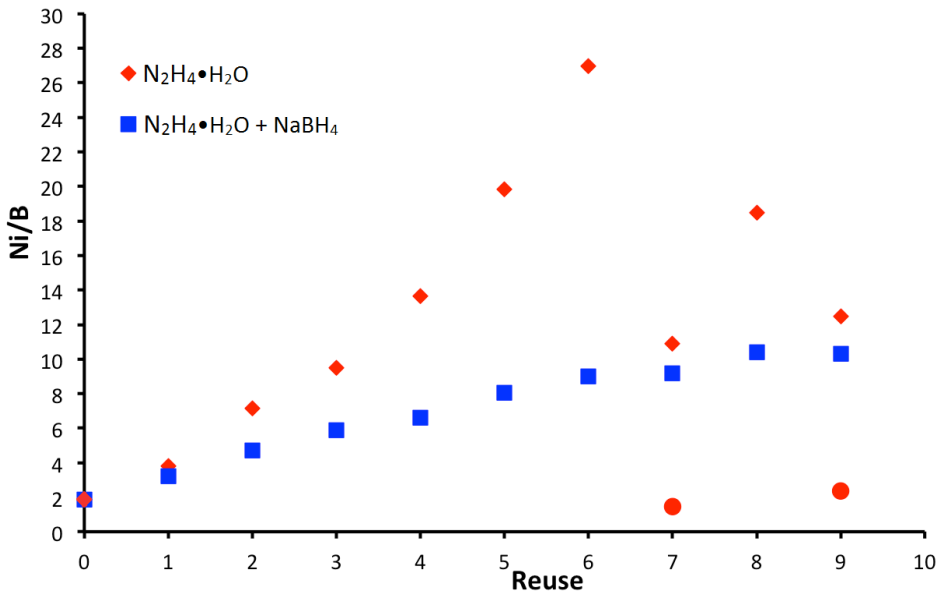

Figure 3.9 ICP-OES data for the Ni:B molar ratio in NBC-MASN after successive reuses in the catalytic hydrogenation of *p*-nitrotoluene. Two reaction conditions are compared: $N_2H_4•H_2O$ as reducing agent (red diamonds), and $N_2H_4•H_2O$ with an equimolar addition of $NaBH_4$ (blue squares). The two red circular markers for reuse numbers 7 and 9 indicate the Ni:B ratio after ex-situ regeneration of NBC-MASN with $NaBH_4$ but before catalysis using $N_2H_4•H_2O$.

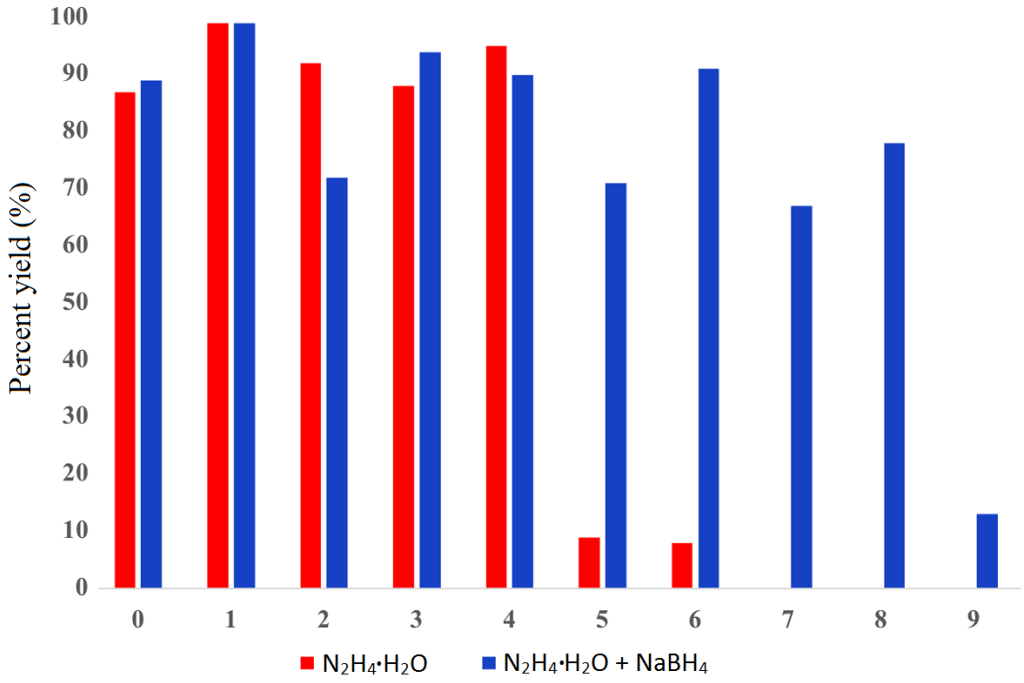

Figure 3.10 The percent yield for the conversion of *p*-nitrotoluene to *p*-toluidine is plotted against reuse cycle number, using either $N_2H_4 \bullet H_2O$ as the reducing agent or a combination of $N_2H_4 \bullet H_2O$ and $NaBH_4$ as reducing and regenerating agents. The product yields were determined after 24 h reaction. Yield was determined by isolation and the purity was verified by ^{1}H NMR spectroscopy.

A tandem ^{1}H NMR spectroscopy study was performed during the reuse study where NBC-MASN was regenerated with $NaBH_4$ ex-situ (Figure 3.11). The first catalysis reaction using fresh NBC-MASN to reduce *p*-nitrotoluene to *p*-toluidine reached completion after 2 h. However, subsequent reuses of the catalyst showed progressively longer incubation periods to achieve full conversion of *p*-toluidine. This may be evidence of the formation of an oxide layer on the catalytic nickel surface, which inhibits the interaction of hydrazine.[4] Although full conversion to *p*-toluidine was not achieved in the 5th cycle, all of the starting material was consumed and several intermediates were

identified (Figure S3.8) that did not fully react with the catalyst to finish conversion into *p*-toluidine.

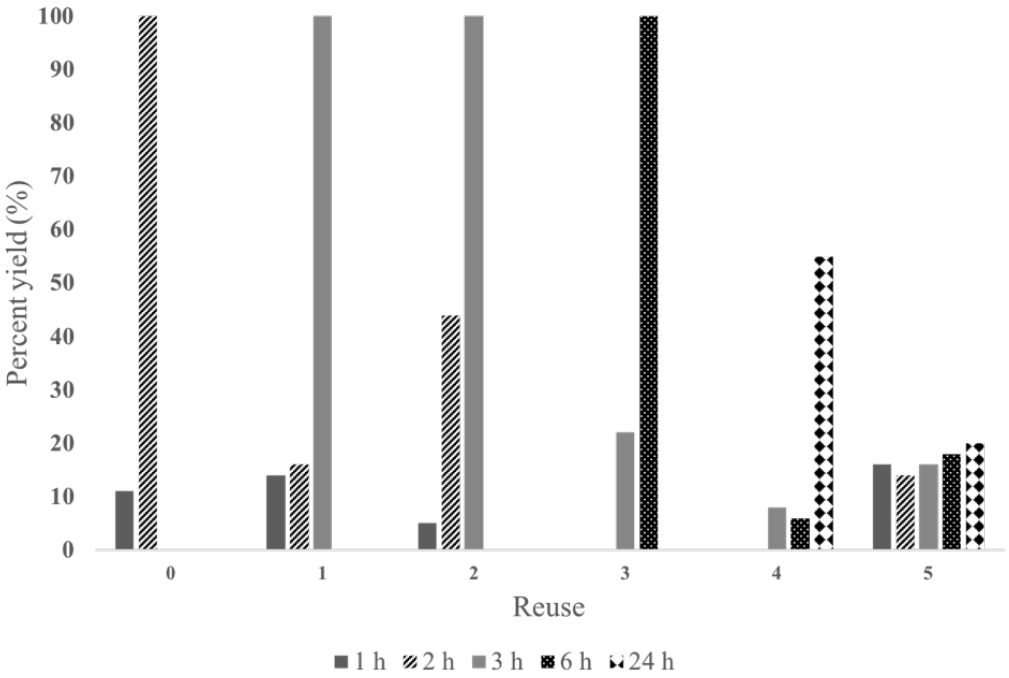

Figure 3.11 Percent yield of *p*-toluidine after 24 h. Yields are based on ^{1}H NMR ratios.

A possible reaction pathway (Figure 3.12) can be elucidated based on the types of intermediates present in the ^{1}H NMR. The presence of 4,4-dimethylazoxybenzene and 4,4-dimethylhydrazobenzene suggests that the reduction of *p*-nitrotoluene begins with the reduction of the nitro group to a nitroso intermediate (Figure 3.12, A). The nitroso intermediate then condenses with a molecule of the hydroxylamine (B) to generate the 4,4-dimethylazoxybenzene intermediate (C), which leads to the 4,4-dimethylhydrazobenzene (E) intermediate and lastly the desired *p*-toluidine.[14,57–61]

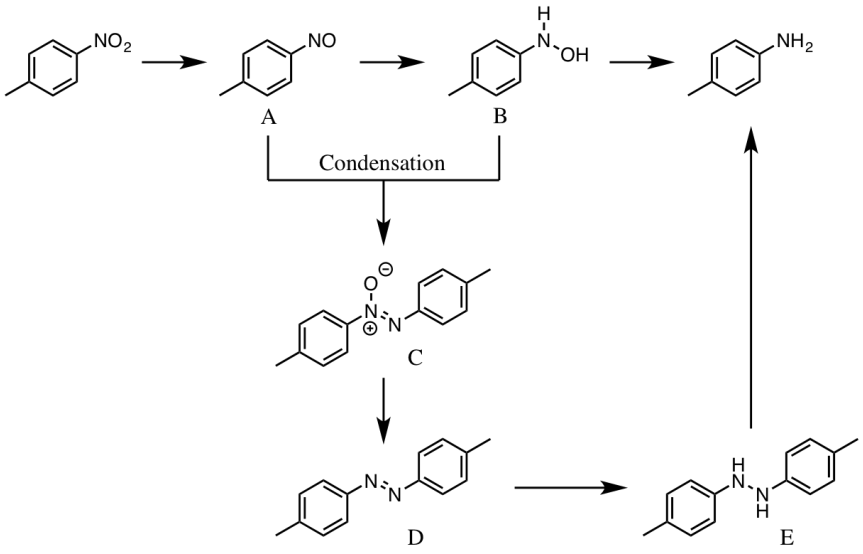

Figure 3.12 Possible mechanism for the reduction of *p*-nitrotoluene to *p*-toluidine.

In order to verify the catalytic ability of NBC-MASN for the reduction of other nitroarenes, a preliminary substrate scope was investigated (Table 3.2). Simple nitroarenes, such as *p*-nitrotoluene and nitrobenzene easily produced the aniline products (entries 1 and 2). Halogenated nitroarenes were reduced in excellent yields to the corresponding aniline derivatives and no dehalogenated product was observed (entry 3). Both trisubstituted and pyrene nitroarene derivatives were tolerated as well (entries 4 and 5).

Interestingly, 4-nitro-benzonitrile was selectively reduced to 4-cyano-benzylamine (entry 6) while the nitrile in 4-cyanotoluene remained unreacted during the catalysis (entry 7). This selectivity differs from previously published catalyst systems, which reduced both nitro and nitrile groups simultaneously.[5,62,63] In those methodologies, the reducing agent was H_2 generated from $NaBH_4$, while our catalysis system uses $N_2H_4 \bullet H_2O$. This result confirms that the reducing agent can dictate functional group

selectivity.[58] Thus, the formation of a diimide, from the oxidation of hydrazine[64–67], reacts preferentially with the nitro substituent before decomposing into nontoxic $N_{2(g)}$.

Table 3.2 NBC-MASN vs NBC for selective nitro group reduction

Entry	Substrate	Product	Catalyst[a]	
			NBC-MASN[b]	NBC[c]
1	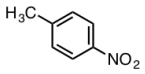	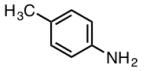	94%	85%
2			99%	58%
3	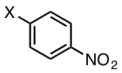 X = Br, Cl, I	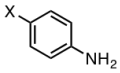 X = Br, Cl, I	99% X= Br, Cl, I	X = Br 83% X = Cl 96% X = I 87%
4	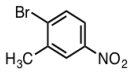	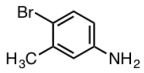	99%	99%
5	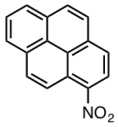	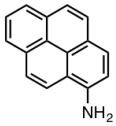	99%	89%
6	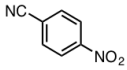	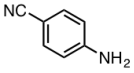	48%	19%
7	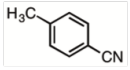	--	0%	--

[a]Isolated yield; [b] Reaction conditions for supported catalyst: nitroarene (4 mmol), NBC-MASN (10 mol%), MeOH (8 mL), hydrazine hydrate (20 mmol), 25 °C, 24 h, under argon atmosphere; [c] Reaction conditions for unsupported catalyst: nitroarene (4 mmol), NBC (10 mol%), MeOH (8 mL), hydrazine hydrate (20 mmol), 25 °C, 24 h, under argon atmosphere.

Overall, the initial arylamine product yield was higher for a variety of substrates when using supported NBC-MASN catalyst, compared with the unsupported NBC catalyst. This is likely due to the more amorphous character of NBC grown on MASN, potentially possessing a larger proportion of minimally coordinated nickel sites for

catalysis, compared to the more crystalline character of NBC.[68,69] Similar arguments have been made for the enhanced activity of Co-B when dispersed on mesoporous silica nanoparticles (MSN) versus solid silica beads or bulk Co-B, where larger domains of metallic Co tend to aggregate.[70]

3.4 Conclusions

In this work, we have shown that a nickel boron composite (NBC) supported on mesoporous aluminosilicate nanoparticles (NBC-MASN) increases catalytic activity compared to unsupported NBC, for the selective reduction of several different nitroarenes to their corresponding aniline derivatives. The catalytically active amorphous nickel in NBC-MASN may be deactivated by oxidation and/or agglomeration/crystallization of nickel during catalysis, leading to an average reusable lifetime of four cycles. The reusable lifetime of the catalyst could be prolonged up to nine cycles (for the reduction of *p*-nitrotoluene) when equimolar $NaBH_4$ was used with $N_2H_4 \bullet H_2O$ during catalysis, but not when $NaBH_4$ was used ex-situ to attempt regeneration of the exhausted catalyst. Introducing $NaBH_4$ in-situ during catalysis likely reduces surface NiO back to Ni and may help to fortify the borate content believed responsible for preventing agglomeration and rapid oxidation of the amorphous nickel present in NBC.

The structural character and negative surface charge of the MASN support appears to aid in forming a thin, highly dispersed amorphous coating of NBC on MASN during synthesis. Comparatively, unsupported NBC consists of much larger particles containing 1-3 nm metallic nickel nanocrystals embedded in an amorphous matrix. The boron content in NBC-MASN, observed by ICP-OES and XPS, is attributed largely to the presence of unknown borate species rather than amorphous nickel boride, since the

degradation of borohydrides in protic solvents prohibits the formation of elemental boron or true borides. The XPS, TGA, and PXRD analyses, along with the results of methanol refluxing, indicate the possible entrapment of borohydrides within the rapidly formed precipitate of unsupported NBC. This residual borohydride may explain the formation of Ni_3B upon $N_{2(g)}$-calcining of unsupported NBC. The slower formation of the thin NBC layer grown on MASN may allow for a more complete reaction of $NaBH_4$ and would explain why only crystalline Ni is observed by PXRD upon $N_{2(g)}$-calcining of NBC-MASN, as well as the greatly reduced intensity of the B 1s peak at 187.7 eV in the case of NBC-MASN compared to that of unsupported NBC. The same 2:1 Ni:B ratio observed by ICP-OES for both NBC-MASN and unsupported NBC may be explained if the majority of boron present in the supported catalyst is oxidized, while some portion of the boron in NBC is residual boron hydride trapped within the amorphous matrix. Preliminary evidence has been given indicating the presence of residual boron hydrides in unsupported NBC. A follow up study is underway to further elucidate the nature of these B-H compounds and the manner in which they may become sequestered during synthesis of NBC.

3.5 References

(1) Vogt, P. F.; Gerulis, J. J. Amines, Aromatic. In *Ullmann's Encyclopedia of Industrial Chemistry*; Wiley-VCH Verlag GmbH & Co. KGaA, Ed.; Wiley-VCH Verlag GmbH & Co. KGaA: Weinheim, Germany, 2000. https://doi.org/10.1002/14356007.a02_037.

(2) Booth, G. Nitro Compounds, Aromatic. In *Ullmann's Encyclopedia of Industrial Chemistry*; Wiley-VCH Verlag GmbH & Co. KGaA, Ed.; Wiley-VCH Verlag GmbH & Co. KGaA: Weinheim, Germany, 2000. https://doi.org/10.1002/14356007.a17_411.

(3) Wehner, V.; Jäger, V. Synthesis OfD- AndL-2-Amino-2-Deoxyarabinose and 1,4-Dideoxy-1,4-Iminolyxitol by(C2+ C3)-Nitroaldol Addition with 2-O-Benzylglyceraldehyde. *Angew. Chem. Int. Ed. Engl.* **1990**, *29* (10), 1169–1171. https://doi.org/10.1002/anie.199011691.

(4) Petkar, D. R.; Kadu, B. S.; Chikate, R. C. Highly Efficient and Chemoselective Transfer Hydrogenation of Nitroarenes at Room Temperature over Magnetically Separable Fe–Ni Bimetallic Nanoparticles. *RSC Adv.* **2014**, *4* (16), 8004. https://doi.org/10.1039/c3ra45787g.

(5) Schreifels, J. A.; Maybury, P. C.; Swartz, W. E. Comparison of the Activity and Lifetime of Raney Nickel and Nickel Boride in the Hydrogenation of Various Functional Groups. *J. Org. Chem.* **1981**, *46* (7), 1263–1269. https://doi.org/10.1021/jo00320a008.

(6) Ahuja, V. Catalytic Hydrogenation, VI. The Reaction of Sodium Borohydride with Nickel Salts in Ethanol Solution. P-2Nickel, A Highly Convenient, New, Selective Hydrogenation Catalyst with Great Sensitivity to Substrate Structure. 5.

(7) Paul, R.; Buisson, P.; Joseph, N. Catalytic Activity of Nickel Borides. *Ind. Eng. Chem.* **1952**, *44* (5), 1006–1010. https://doi.org/10.1021/ie50509a029.

(8) Belisle, C. M.; Young, Y. M.; Singaram, B. Catalytic Reaction. 1. Catalytic 1,4-Hydrogenation of α,β-Unsaturated Aldehydes and Ketones Using SC-1 Nickel Boride. *Tetrahedron Lett.* **1994**, *35* (31), 5595–5598. https://doi.org/10.1016/S0040-4039(00)77255-8.

(9) Leggans, E. K.; Barker, T. J.; Duncan, K. K.; Boger, D. L. Iron(III)/$NaBH_4$ -Mediated Additions to Unactivated Alkenes: Synthesis of Novel 20′-Vinblastine Analogues. *Org. Lett.* **2012**, *14* (6), 1428–1431. https://doi.org/10.1021/ol300173v.

(10) Schaefer, Z. L.; Ke, X.; Schiffer, P.; Schaak, R. E. Direct Solution Synthesis, Reaction Pathway Studies, and Structural Characterization of Crystalline Ni_3B Nanoparticles. *J. Phys. Chem. C* **2008**, *112* (50), 19846–19851. https://doi.org/10.1021/jp8082503.

(11) Wade, R. C.; Holah, D. G.; Hughes, A. N.; Hui, B. C. Catalytically Active Borohydride-Reduced Nickel and Cobalt Systems. *Catal. Rev.* **1976**, *14* (1), 211–246. https://doi.org/10.1080/03602457608073412.

(12) Schlesinger, H. I.; Brown, H. C.; Finholt, A. E.; Gilbreath, J. R.; Hoekstra, H. R.; Hyde, E. K. Sodium Borohydride, Its Hydrolysis and Its Use as a Reducing Agent and in the Generation of Hydrogen[1]. *J. Am. Chem. Soc.* **1953**, *75* (1), 215–219. https://doi.org/10.1021/ja01097a057.

(13) Khurana, J. M.; Gogia, A. SYNTHETICALLY USEFUL REACTIONS WITH NICKEL BORIDE. A REVIEW. *Org. Prep. Proced. Int.* **1997**, *29* (1), 1–32. https://doi.org/10.1080/00304949709355171.

(14) Zhang, J.; Lu, G.; Cai, C. Chemoselective Transfer Hydrogenation of Nitroarenes by Highly Dispersed Ni-Co BMNPs. *Catal. Commun.* **2016**, *84*, 25–29. https://doi.org/10.1016/j.catcom.2016.05.023.

(15) Nose, A.; Kudo, T. Reduction with Sodium Borohydride-Transition Metal Salt Systems. I. Reduction of Aromatic Nitro Compounds with the Sodium Borohydride-Nickelous Chloride System. *Chem. Pharm. Bull. (Tokyo)* **1981**, *29* (4), 1159–1161. https://doi.org/10.1248/cpb.29.1159.

(16) Rahman, A.; Jonnalagadda, S. B. Swift and Selective Reduction of Nitroaromatics to Aromatic Amines with Ni–Boride–Silica Catalysts System at Low Temperature. *Catal. Lett.* **2008**, *123* (3–4), 264–268. https://doi.org/10.1007/s10562-008-9417-5.

(17) Wong, S.-T.; Lee, J.-F.; Chen, J.-M.; Mou, C.-Y. Preparation and Characterization of MCM-41 and Silica Supported Nickel Boride Catalysts. *J. Mol. Catal. Chem.* **2001**, *165* (1–2), 159–167. https://doi.org/10.1016/S1381-1169(00)00409-X.

(18) Rai, R. K.; Mahata, A.; Mukhopadhyay, S.; Gupta, S.; Li, P.-Z.; Nguyen, K. T.; Zhao, Y.; Pathak, B.; Singh, S. K. Room-Temperature Chemoselective Reduction of Nitro Groups Using Non-Noble Metal Nanocatalysts in Water. *Inorg. Chem.* **2014**, *53* (6), 2904–2909. https://doi.org/10.1021/ic402674z.

(19) Prathap, K. J.; Wu, Q.; Olsson, R. T.; Dinér, P. Catalytic Reductions and Tandem Reactions of Nitro Compounds Using in Situ Prepared Nickel Boride Catalyst in Nanocellulose Solution. *Org. Lett.* **2017**, *19* (18), 4746–4749. https://doi.org/10.1021/acs.orglett.7b02090.

(20) Arzac, G. M.; Rojas, T. C.; Fernández, A. Boron Compounds as Stabilizers of a Complex Microstructure in a Co-B-Based Catalyst for $NaBH_4$ Hydrolysis. *ChemCatChem* **2011**, *3* (8), 1305–1313. https://doi.org/10.1002/cctc.201100101.

(21) Cavaliere, S.; Hannauer, J.; Demirci, U. B.; Akdim, O.; Miele, P. Ex Situ Characterization of N2H4-, NaBH4- and NH3BH3-Reduced Cobalt Catalysts Used

in NaBH4 Hydrolysis. *Catal. Today* **2011**, *170* (1), 3–12. https://doi.org/10.1016/j.cattod.2011.02.016.

(22) Kalidindi, S. B.; Vernekar, A. A.; Jagirdar, B. R. Co–Co $_2$ B, Ni–Ni $_3$ B and Co–Ni–B Nanocomposites Catalyzed Ammonia–Borane Methanolysis for Hydrogen Generation. *Phys Chem Chem Phys* **2009**, *11* (5), 770–775. https://doi.org/10.1039/B814216E.

(23) Demirci, U. B.; Miele, P. Cobalt-Based Catalysts for the Hydrolysis of NaBH4 and NH3BH3. *Phys. Chem. Chem. Phys.* **2014**, *16* (15), 6872. https://doi.org/10.1039/c4cp00250d.

(24) Ozerova, A. M.; Bulavchenko, O. A.; Komova, O. V.; Netskina, O. V.; Zaikovskii, V. I.; Odegova, G. V.; Simagina, V. I. Cobalt Boride Catalysts for Hydrogen Storage Systems Based on NH3BH3 and NaBH4. *Kinet. Catal.* **2012**, *53* (4), 511–520. https://doi.org/10.1134/S0023158412040088.

(25) Geng, J.; Jefferson, D. A.; Johnson, B. F. G. Exploring the Structural Complexities of Metal-Metalloid Nanoparticles: The Case of Ni・B as Catalyst. *Chem. - Eur. J.* **2009**, *15* (5), 1134–1143. https://doi.org/10.1002/chem.200801146.

(26) Glavee, G. N.; Klabunde, K. J.; Sorensen, C. M.; Hadjipanayis, G. C. Borohydride Reduction of Nickel and Copper Ions in Aqueous and Nonaqueous Media. Controllable Chemistry Leading to Nanoscale Metal and Metal Boride Particles. *Langmuir* **1994**, *10* (12), 4726–4730. https://doi.org/10.1021/la00024a055.

(27) Hofer, L. J. E.; Shultz, J. F.; Panson, R. D.; Anderson, R. B. The Nature of the Nickel Boride Formed by the Action of Sodium Borohydride on Nickel Salts. *Inorg. Chem.* **1964**, *3* (12), 1783–1785. https://doi.org/10.1021/ic50022a031.

(28) He, Y.; Qiao, M.; Hu, H.; Pei, Y.; Li, H.; Deng, J.; Fan, K. Preparation of Amorphous Ni–B Alloy: The Effect of Feeding Order, Precursor Salt, PH and Adding Rate. *Mater. Lett.* **2002**, *56* (6), 952–957. https://doi.org/10.1016/S0167-577X(02)00644-4.

(29) Corrias, A.; Ennas, G.; Licheri, G.; Marongiu, G.; Paschina, G. Amorphous Metallic Powders Prepared by Chemical Reduction of Metal Ions with Potassium Borohydride in Aqueous Solution. *Chem. Mater.* **1990**, *2* (4), 363–366. https://doi.org/10.1021/cm00010a010.

(30) Teranishi, S. Surface Characterisation of Nickel b r i d e and Nickel Phosphide Catalysts by X-Ray Photoelectron Spectroscopy. 13.

(31) Legrand, J.; Gota, S.; Guittet, M.-J.; Petit, C. Synthesis and XPS Characterization of Nickel Boride Nanoparticles. *Langmuir* **2002**, *18* (10), 4131–4137. https://doi.org/10.1021/la0117247.

(32) Schreifels, J. X-Ray Photoelectron Spectroscopy of Nickel Boride Catalysts: Correlation of Surface States with Reaction Products in the Hydrogenation of Acrylonitrile. *J. Catal.* **1980**, *65* (1), 195–206. https://doi.org/10.1016/0021-9517(80)90294-8.

(33) Yoshida, S.; Yamashita, H.; Funabiki, T.; Yonezawa, T. Catalysis by Amorphous Metal Alloys. Part 1.—Hydrogenation of Olefins over Amorphous Ni–P and Ni–B Alloys. *J. Chem. Soc. Faraday Trans. 1 Phys. Chem. Condens. Phases* **1984**, *80* (6), 1435. https://doi.org/10.1039/f19848001435.

(34) Deng, J. The Study of Ultrafine Ni-B and Ni-P Amorphous Alloy Powders as Catalysts. *J. Catal.* **1994**, *150* (2), 434–438. https://doi.org/10.1006/jcat.1994.1362.

(35) Li, H. Liquid Phase Hydrogenation of Acetonitrile to Ethylamine over the Co_B Amorphous Alloy Catalyst. *J. Catal.* **2003**, *214* (1), 15–25. https://doi.org/10.1016/S0021-9517(02)00038-6.

(36) Fernandes, R.; Patel, N.; Miotello, A.; Filippi, M. Studies on Catalytic Behavior of Co–Ni–B in Hydrogen Production by Hydrolysis of NaBH4. *J. Mol. Catal. Chem.* **2009**, *298* (1–2), 1–6. https://doi.org/10.1016/j.molcata.2008.09.014.

(37) Liu, Y.-C.; Huang, C.-Y.; Chen, Y.-W. Hydrogenation of P-Chloronitrobenzene on Ni–B Nanometal Catalysts. *J. Nanoparticle Res.* **2006**, *8* (2), 223–234. https://doi.org/10.1007/s11051-005-5944-9.

(38) Carenco, S.; Portehault, D.; Boissière, C.; Mézailles, N.; Sanchez, C. Nanoscaled Metal Borides and Phosphides: Recent Developments and Perspectives. *Chem. Rev.* **2013**, *113* (10), 7981–8065. https://doi.org/10.1021/cr400020d.

(39) Geng, J.; Jefferson, D. A.; Johnson, B. F. G. The Unusual Nanostructure of Nickel–Boron Catalyst. *Chem Commun* **2007**, No. 9, 969–971. https://doi.org/10.1039/B615529D.

(40) Akopov, G.; Yeung, M. T.; Kaner, R. B. Rediscovering the Crystal Chemistry of Borides. *Adv. Mater.* **2017**, *29* (21), 1604506. https://doi.org/10.1002/adma.201604506.

(41) C. P., P.; Joseph, E.; A, A.; D. S., N.; Ibnusaud, I.; Raskatov, J.; Singaram, B. Stabilization of $NaBH_4$ in Methanol Using a Catalytic Amount of NaOMe. Reduction of Esters and Lactones at Room Temperature without Solvent-Induced Loss of Hydride. *J. Org. Chem.* **2018**, *83* (3), 1431–1440. https://doi.org/10.1021/acs.joc.7b02993.

(42) Clary, J. W.; Rettenmaier, T. J.; Snelling, R.; Bryks, W.; Banwell, J.; Wipke, W. T.; Singaram, B. Hydride as a Leaving Group in the Reaction of Pinacolborane with Halides under Ambient Grignard and Barbier Conditions. One-Pot Synthesis of

Alkyl, Aryl, Heteroaryl, Vinyl, and Allyl Pinacolboronic Esters. *J. Org. Chem.* **2011**, *76* (23), 9602–9610. https://doi.org/10.1021/jo201093u.

(43) Hauser, J. L.; Tran, D. T.; Conley, E. T.; Saunders, J. M.; Bustillo, K. C.; Oliver, S. R. J. Plasma Treatment of Silver Impregnated Mesoporous Aluminosilicate Nanoparticles for Adsorptive Desulfurization. *Chem. Mater.* **2016**, *28* (2), 474–479. https://doi.org/10.1021/acs.chemmater.5b03018.

(44) Kondrat, S. A.; Shaw, G.; Freakley, S. J.; He, Q.; Hampton, J.; Edwards, J. K.; Miedziak, P. J.; Davies, T. E.; Carley, A. F.; Taylor, S. H.; et al. Physical Mixing of Metal Acetates: A Simple, Scalable Method to Produce Active Chloride Free Bimetallic Catalysts. *Chem. Sci.* **2012**, *3* (10), 2965. https://doi.org/10.1039/c2sc20450a.

(45) Yan, W.; Chen, B.; Mahurin, S. M.; Schwartz, V.; Mullins, D. R.; Lupini, A. R.; Pennycook, S. J.; Dai, S.; Overbury, S. H. Preparation and Comparison of Supported Gold Nanocatalysts on Anatase, Brookite, Rutile, and P25 Polymorphs of TiO_2 for Catalytic Oxidation of CO. *J. Phys. Chem. B* **2005**, *109* (21), 10676–10685. https://doi.org/10.1021/jp044091o.

(46) Saldan, I. Decomposition and Formation of Magnesium Borohydride. *Int. J. Hydrog. Energy* **2016**, *41* (26), 11201–11224. https://doi.org/10.1016/j.ijhydene.2016.05.062.

(47) Crociani, L.; Rossetto, G.; Kaciulis, S.; Mezzi, A.; El-Habra, N.; Palmieri, V. Study of Magnesium Boride Films Obtained From Mg(BH4)2 by CVD. *Chem. Vap. Depos.* **2007**, *13* (8), 414–419. https://doi.org/10.1002/cvde.200606525.

(48) Jensen, J. A.; Gozum, J. E.; Pollina, D. M.; Girolami, G. S. Titanium, Zirconium, and Hafnium Tetrahydroborates as "Tailored" CVD Precursors for Metal Diboride Thin Films. *J. Am. Chem. Soc.* **1988**, *110* (5), 1643–1644. https://doi.org/10.1021/ja00213a058.

(49) Jayaraman, S.; Yang, Y.; Kim, D. Y.; Girolami, G. S.; Abelson, J. R. Hafnium Diboride Thin Films by Chemical Vapor Deposition from a Single Source Precursor. *J. Vac. Sci. Technol. Vac. Surf. Films* **2005**, *23* (6), 1619–1625. https://doi.org/10.1116/1.2049307.

(50) Rice, G. W.; Woodin, R. L. Zirconium Borohydride as a Zirconium Boride Precursor. *J. Am. Ceram. Soc.* **1988**, *71* (4), C-181-C–183. https://doi.org/10.1111/j.1151-2916.1988.tb05867.x.

(51) Goedde, D. M.; Girolami, G. S. A New Class of CVD Precursors to Metal Borides: $Cr(B_3H_8)_2$ and Related Octahydrotriborate Complexes. *J. Am. Chem. Soc.* **2004**, *126* (39), 12230–12231. https://doi.org/10.1021/ja046906c.

(52) Kher, S. S.; Spencer, J. T. Chemical Vapor Deposition Precursor Chemistry. 3. Formation and Characterization of Crystalline Nickel Boride Thin Films from the Cluster-Assisted Deposition of Polyhedral Borane Compounds. *Chem. Mater.* **1992**, *4* (3), 538–544. https://doi.org/10.1021/cm00021a011.

(53) Maybury, P. C.; Mitchell, R. W.; Hawthorne, M. F. Hydrogen Adducts of Cobalt and Nickel Boride. *J. Chem. Soc. Chem. Commun.* **1974**, No. 14, 534. https://doi.org/10.1039/c39740000534.

(54) Beygi, H.; Sajjadi, S. A. Magnetic Properties of Crystalline Nickel and Low Phosphorus Amorphous Ni 1-X P x Nanoparticles. *Mater. Chem. Phys.* **2018**, *204*, 403–409. https://doi.org/10.1016/j.matchemphys.2017.10.079.

(55) Hendrickson, D. N.; Hollander, J. M.; Jolly, W. L. Core-Electron Binding Energies for Compounds of Boron, Carbon, and Chromium. *Inorg. Chem.* **1970**, *9* (3), 612–615. https://doi.org/10.1021/ic50085a035.

(56) Chekin, F.; Sadeghi, S. Room Temperature Decomposition of Hydrazine Catalyzed by Nickel Oxide Nanoparticles. 6.

(57) Pogorelić, I.; Filipan-Litvić, M.; Merkaš, S.; Ljubić, G.; Cepanec, I.; Litvić, M. Rapid, Efficient and Selective Reduction of Aromatic Nitro Compounds with Sodium Borohydride and Raney Nickel. *J. Mol. Catal. Chem.* **2007**, *274* (1–2), 202–207. https://doi.org/10.1016/j.molcata.2007.05.020.

(58) Vernekar, A. A.; Patil, S.; Bhat, C.; Tilve, S. G. Magnetically Recoverable Catalytic Co–Co2B Nanocomposites for the Chemoselective Reduction of Aromatic Nitro Compounds. *RSC Adv.* **2013**, *3* (32), 13243. https://doi.org/10.1039/c3ra41090k.

(59) Gabriel, C. M.; Parmentier, M.; Riegert, C.; Lanz, M.; Handa, S.; Lipshutz, B. H.; Gallou, F. Sustainable and Scalable Fe/Ppm Pd Nanoparticle Nitro Group Reductions in Water at Room Temperature. *Org. Process Res. Dev.* **2017**, *21* (2), 247–252. https://doi.org/10.1021/acs.oprd.6b00410.

(60) Moore', R. E.; Furst, A. Reductions with Hydrazine Hydrate Catalyzed by Raney Nickel. 111. Effect of the Catalyst on the Reduction of 2,2'-Dinitrobiphenyl. *23*, 3.

(61) Corma, A.; Concepción, P.; Serna, P. A Different Reaction Pathway for the Reduction of Aromatic Nitro Compounds on Gold Catalysts. *Angew. Chem. Int. Ed.* **2007**, *46* (38), 7266–7269. https://doi.org/10.1002/anie.200700823.

(62) Caddick, S.; Judd, D. B.; Lewis, A. K. d. K.; Reich, M. T.; Williams, M. R. . A Generic Approach for the Catalytic Reduction of Nitriles. *Tetrahedron* **2003**, *59* (29), 5417–5423. https://doi.org/10.1016/S0040-4020(03)00858-5.

(63) Osby, J. O.; Heinzman, S. W.; Ganem, B. Studies on the Mechanism of Transition-Metal-Assisted Sodium Borohydride and Lithium Aluminum Hydride Reductions. *J. Am. Chem. Soc.* **1986**, *108* (1), 67–72. https://doi.org/10.1021/ja00261a011.

(64) Cantillo, D.; Moghaddam, M. M.; Kappe, C. O. Hydrazine-Mediated Reduction of Nitro and Azide Functionalities Catalyzed by Highly Active and Reusable Magnetic Iron Oxide Nanocrystals. *J. Org. Chem.* **2013**, *78* (9), 4530–4542. https://doi.org/10.1021/jo400556g.

(65) Larsen, J. W.; Freund, M.; Kim, K. Y.; Sidovar, M.; Stuart, J. L. Mechanism of the Carbon Catalyzed Reduction of Nitrobenzene by Hydrazine. *Carbon* **2000**, *38* (5), 655–661. https://doi.org/10.1016/S0008-6223(99)00155-4.

(66) Kumarraja, M. Simple and Efficient Reduction of Nitroarenes by Hydrazine in Faujasite Zeolites. *Appl. Catal. Gen.* **2004**, *265* (2), 135–139. https://doi.org/10.1016/j.apcata.2004.01.009.

(67) Zhao, Z.; Yang, H.; Li, Y.; Guo, X. Cobalt-Modified Molybdenum Carbide as an Efficient Catalyst for Chemoselective Reduction of Aromatic Nitro Compounds. *Green Chem* **2014**, *16* (3), 1274–1281. https://doi.org/10.1039/C3GC42049C.

(68) Prathap, K. J.; Wu, Q.; Olsson, R. T.; Dinér, P. Catalytic Reductions and Tandem Reactions of Nitro Compounds Using in Situ Prepared Nickel Boride Catalyst in Nanocellulose Solution. *Org. Lett.* **2017**, *19* (18), 4746–4749. https://doi.org/10.1021/acs.orglett.7b02090.

(69) Zhang, J.; Cai, Y.; Lu, G.; Cai, C. Facile and Selective Hydrogenolysis of β-O-4 Linkages in Lignin Catalyzed by Pd–Ni Bimetallic Nanoparticles Supported on ZrO_2. *Green Chem.* **2016**, *18* (23), 6229–6235. https://doi.org/10.1039/C6GC02265K.

(70) Patel, N.; Fernandes, R.; Edla, R.; Lihitkar, P. B.; Kothari, D. C.; Miotello, A. Superior Hydrogen Production Rate by Catalytic Hydrolysis of Ammonia Borane Using Co-B Nanoparticles Supported over Mesoporous Silica Particles. *Catal. Commun.* **2012**, *23*, 39–42. https://doi.org/10.1016/j.catcom.2012.02.030.

Chapter 4

Mixed Metallic Species in Mesoporous Silica Nanoparticles

4.1 Introduction

Mesoporous silica (MS) materials are uniquely suitable inorganic frameworks for applications such as catalysis, sorption, separation, and drug delivery, owing to their high surface area, tunable pore diameter, narrow size distribution, and potential for surface functionalization.[1] Among the wide range of surface functionalization schemes that have been reported, the incorporation of metallic species is of considerable interest. A large and growing body of research has explored the potential for creating highly dispersed metallic coatings, involving both the interior and exterior surface area of MS particles, and the direct substitution of metal ions into the SiO_2 framework.

Accessibility of chemical species by diffusion through the mesoporous volume is of considerable importance in any application, making MS nanoparticles (MSN) advantageous compared to bulk MS where pore volume and internal surface area may be less accessible. Whenever possible, the functionalization of the interior surface area of MSN should not significantly obstruct or restrict species access to interior surface area. This less desirable scenario is easy to imagine in the case where MS or MSN materials are post-synthetically modified by, for example, the direct coating or impregnation with metallic species,[2] or the preliminary grafting of organosilanes,[3] where the mesochannels can easily become completely blocked. To retain maximal access to interior surface area, the functional sites should ideally be either incorporated into the silica surface of the mesopores by substitution of Si,[1] or consist of thin and closely adhered surface layers

coating the mesochannels.[4] Alternatively, the pore diameter can be increased to accommodate the additional volume occupied by bulkier functional groups (e.g. for post-synthetic aminopropyl grafting, SBA-15 is a better choice than MCM-41), however this still results in an overall loss of MSN internal surface area and volume for nanoparticles of the same size.

If mitigating significant pore blockage is inefficiently tedious or entirely unavoidable in the process of surface functionalization, there may still be an advantage to using small MSN particle supports, in that the external MSN particle surface area represents a considerable improvement over other inorganic supports such as solid silica nanoparticles or bulk MS. In this scenario the focus shifts to using the interior volume and/or surface area of MSN to adsorb and store reactive precursors (such as metal salts) as a preliminary step in the functionalization of the exterior MSN surface. The mesoporous structure provides a unique exterior surface texture to MSNs, that may serve as a means of directing the growth morphology of an external surface coating. For example, Patel et al., discovered that growing a coating of Co-B on the exterior of ~100 nm MCM-41 nanoparticles, by first impregnating the MSN with $CoCl_2$ and then reacting the composite with $NaBH_4$, gave very fine and evenly dispersed Co-B particles compared to that achieved using similar diameter support nanoparticles made of solid silica.[5] This was probably due to the many nucleation sites afforded at the regularly dispersed channel openings, or pores, that give the MSN exterior surface a naturally roughened texture. Each channel running through the spherical MSN acts as a straw that has been previously loaded with a chemical precursor ($CoCl_2$ in this case). Upon exposing the Co^{2+} loaded MSN to the reducing agent (BH^-) nucleation occurs most readily at MSN surface pores. The result is a highly dispersed array of Co-B nanoparticles on the MSN surface, and a

highly textured surface coating. Additionally some of this reaction product may grow into the channel as the reaction continues, and may provide for a physical anchoring of the material in the mesochannel (like the root of a tooth in its socket).

This chapter will consider the single and multiple species metallization of MSN, primarily aimed at the removal of organosulfur species from liquid hydrocarbon fuels (as discussed in chapter 2). In general, MS metallization schemes include in situ (or one-pot) syntheses,[6,7] wet impregnation,[8] template ion-exchange,[9] and post synthesis grafting.[10] Depending on the scheme and the final metal(s) location, MSN metallization can be termed intra-framework metallization (incorporating metallic species directly into the SiO_2 framework) or extra-framework metallization (metal species anchored onto the internal and/or external surface area of MSN). The relevance of the previous discussion on utilizing the interior versus exterior surface area of MSN should become apparent, in distinguishing the advantages of intra- versus extra-framework metallization. The former should preserve access to the interior surface area, whereas the later may, depending on the extent of pore and/or channel blockage, shift the research focus to utilizing the exterior surface area of MSN.

A larger number of publications describe synthetic routes either for the post synthetic metallization of MS or MSN, or for the in situ (or one-pot) metallization of bulk MS materials, compared to those which deal with similar in-situ incorporation of metal species within nanoparticles (MSN). This is in part because of the difficulty in simultaneously controlling MSN particle morphology, mesostructure, and precipitation of metal ions in alkaline media during in situ metal incorporation (intra-framework metallization).[11] It is often noted that the subtlest change in experimental conditions (pH, temperature, stirring rate, reaction time, template concentration, etc.) tend to have

dramatic results on nanoparticle morphology and mesostructure.[6,12] And while acidic synthesis routes for bulk MS are known, and would be more amenable to the incorporation of metal cations during synthesis, the majority of synthetic routes toward small (colloidal size regime, d < 1000 nm) MSNs require alkaline conditions, which favor the formation of metal oxides.[13] Rational design of intra-framework metallized MSN materials is therefore a tedious endeavor, and much trial and error is often necessary before discovering a suitable synthetic route. Several pertinent examples of successful metallization synthesis routes and good characterization of metallic oxidation state and location in MS or MSN are described next.

Derrien, et al. have demonstrated copper incorporation into MCM-41 type MSN, occurring as a fine surface dispersion of CuO that does not disrupt the mesostructure or spherical morphology of the MSN, and preserves the internal surface area and volume typical of MCM-41.[4] This success was accomplished by a combination of low metal loading ($_{wt}$2% Cu), and the use of organic phase Cu salt (copper(II) acetylacetonate), along with ethylene glycol as a co-solvent. The co-solvent allows for better sulubilization of the organic phase copper salt (dissolved in chloroform) in the organic template (dodecyltrimethylammonium bromide (DTAB)). Transmission electron microscopy (TEM) and powder x-ray diffraction (PXRD) characterization were sufficient to conclude that no discernable metallic nanoparticles formed. Temperature programed reduction (TPR) and diffuse reflectance UV-Vis (DRUV-Vis) characterization indicated the oxidation state and location of Cu. Even though this is an example of extra-framework metallization, it is well executed in terms of allowing for retaining MCM-41's mesostructure, typically high surface area and pore volume (1260 $m^2 g^{-1}$, and 0.66 mL g^{-1} respectively), and a narrow size dispersion of small nanospheres (~200 nm).

In another study, Qin, et al., produced an intra-framework Ni substituted MCM-41 type bulk MS. In their synthesis scheme the authors used both an ammonia based $Ni(HH_3)_6^{2+}$ solution, and concentrated ammonia (ammonium hydroxide solution) rather than alkali hydroxide, to achieve the high solution pH necessary for hydrolysis and polymerization of the silica precursor (tetraethylorthosilicate, or TEOS). Ammonia is known to form ammine complexes with almost any metal, and these complexes are generally more stable in aqueous environments than their corresponding aquo complexes.[14] Thus the Ni ions are protected from immediate reaction with water and subsequent precipitation as a separate nickel oxide phase prior to incorporation into the condensing SiO_2 framework. Characterization with X-ray photon spectroscopy (XPS), TPR, and Fourier-transform infrared (FT-IR) spectroscopy determined that the Ni was tetrahedrally coordinated and substituted within the SiO_2 framework of MS. However, PXRD showed that increasing the theoretical Ni content beyond 8.8 $_w$% greatly degraded the mesoporous structure, and corresponded to a decrease in both mesoporous volume and surface area.

In another study, Qian, et al., demonstrated the intra-framework incorporation of either Fe or V into MCM-48 type MSN, as well as bi-metallic V-Fe-MSN.[1] Characterization by XPS, XRD, and DRUV-Vis confirmed the tetrahedral coordination of both Fe^{3+} and V^{4+} in either the mono- or bi-metallic metalized MSN, suggesting these metals were substituted into the SiO_2 framework. The particle morphology (spherical) and mesostructure were not dramatically affected, as shown by preservation of the typically high surface area and pore volume of MCM-48 type MSN, and the particle size distribution was within the range of 150—250 nm. In their synthesis, the researchers also used concentrate ammonia to create the basic template solution. As in the work of Qin et

al., this use of ammonia may explain the successful substitution of Fe and V into MSN silica framework, rather than the formation of separate metal oxide phase, though the authors do not discuss this aspect of synthesis.

Depending on the application, the metallization of MSN may involve a single metallic species or several metallic species. Examples of the synergistic effect of bi-metallic systems on material stability and catalytic performance are well documented,[15–17] and in the case of aluminum substitution in the silica framework (aluminosilicate) the resulting negative surface charge has been well documented to aid in the interaction of a wide range of chemical species.[18,19] The research presented here encompasses both intra- and extra- framework metallization of MSN, using single and multiple metal species. The intended application for this research is in the adsorptive desulfurization of liquid hydrocarbon fuels, but many of the materials discussed below may find suitable application in other fields, such as catalysis.

4.2 Experimental

4.2.1 Intra-framework M-MSN (M = Cu, Ni, Co, Nd, or Ce) and Cu/Ni-MSN

A solution containing 50.0 mL H_2O, 25.0 mL ethanol, 1.2g cetyltrimethylammonium bromide (CTAB) or the molar equivalent of dodecyltrimethylammonium bromide (DTAB), and 6 mL of NH_4OH was heated to 50 °C to dissolve CTAB, then cooled to room temperature, all the while stirring at 620 rpm. A separate solution containing 0.35 mmol of hydrated metal nitrate salt dissolved in 10 mL of H_2O and added immediately prior to adding 1.7g tetraethylorthosilicate (TEOS) over the course of a few minutes. The molar ratio of Si to M was maintained throughout all syntheses at 28:1. In the case of Cu/Ni-MSN the mol ratio of Cu to Ni was 1:1. Addition

of metal salt and TEOS coincided with heating of the combined solutions to 40 °C. The synthesis solution was stirred at 620 rpm for 4 to 6 hours and then allowed to cool to room temperature. The precipitate was filtered with 1.0 L H_2O, dried in a vacuum oven at 100 °C over night, and then calcined in air at 350 °C for 6 hours to remove the organic template.

4.2.2 $AgNO_3$ loaded Cu-MSN and either plasma or $NaBH_4$ treatment

Cu-MSN was loaded with 10_w% $AgNO_3$ in a $50/50_{v/v}$ solution of H_2O/EtOH by wet impregnation. The impregnated material was then dried overnight in a vacuum oven at 100 °C. Further treatment of 25 mg of $AgNO_3$-Cu-MSN to reduce Ag^+ to Ag^0 was carried out, either by plasma treatment (90 min in Ar) or exposure to a solution of 0.4 M $NaBH_4$ (molar equivalent to Ag in sample) for 1 hr at 25 °C.

4.2.3 Intra-framework Cu/Ni-MSN (dilute solutions synthesis)

A solution containing 483.5g H_2O, 1.0 g CTAB, and 29.0 mL of concentrated NH_4OH was heated to 50 °C to dissolve CTAB and then allowed to cool to 35 °C, all the while stirring at 620 rpm. A separate solution consisting of $Cu(NO_3)_2$ (0.092g) and $Ni(NO_3)_2$ (0.1142g) dissolved in 2.0 g EtOH (the mol ratio of Si to metal(s) was 28:1, with the metal to metal mol ratio being 1:1) was then added to 4.61g of TEOS. This TEOS and metal salt solution was added dropwise to the CTAB solution over the course of several minutes. The synthesis solution was heated to 80 °C at a rate of 10deg/min, and stirred for 24 hr. The solution was allowed to cool to room temperature while stirring. The precipitate was filtered with 1.0 L of water and 50 mL of EtOH, then dried over night at 80 °C in a vacuum oven. The dried and filtered product was light blue/green in color. The dried product was then subjected to template removal either by

refluxing (0.5g Cu-Ni-MSN) in 100 mL EtOH with 2.0 mL of concentrated HCl, at stirred at 900 rpm and 80 °C for 24 hr. The reflux solution was decanted and replaced and the procedure repeated for an additional 24 hr. Refluxed material turned white in color. Alternatively, template removal was achieved by calcination at 550 °C for 5 hr (ramp rate 1C/min).

4.2.4 Reduction of Cu and Ni oxidation state in intra-Cu/Ni-MSN

Attempts to reduce the oxidation state of Cu and/or Ni associated with the MSN framework were carried out either by plasma treatment or $NaBH_4$ reduction.

Plasma treatment of the calcined material was carried out on a borosilicate watch glass place in a barrel plasma reactor (Plasma Prep II, operating at 13.56 MHz), in a reduced pressure Ar atmosphere (~250 mTorr) for five 10 minute treatments with manual mixing of the powder between treatments. The material was slightly brownish in color after plasma treatment. The plasma treated material was thin impregnated with a minimal volume of a solution of $AgNO_3$ dissolved in ($50/50_{v/v}$ H_2O/EtOH). The Ag loading of Cu/Ni-MSN was 10_w%. The Ag loaded material turned gray after a few seconds, but then light blue again after drying overnight in a vacuum oven at 100°C. Fuel tests: Calcined Cu/Ni-MSN was investigated for desulfurization capaicity, as was the plasma treated material after solvent impregnation with AgNO3.

4.2.5 Synthesis of Intra-(Al)-/Extra-(Ag/Cu)-Framework GE-Ag/Cu-MASN

4.2.5.1 Synthesis of Intra-framework MASN

Mesoporous aluminosilicate nanoparticles (MASN) were synthesized as follows. A solution consisting of of 1 g cetyltrimethylammonium bromide (CTAB) and 0.28 g NaOH dissolved in 483.5 g of water was stirred at 80°C at a rate of 625 rpm for 20 minutes. A second solution consisting of of 0.2442 g aluminum isopropoxide ($Al(OiPr)_3$) suspended in in 5 mL isopropanol was made by sonication. To this suspension was added 4.58 g tetraethylorthosilicate (TEOS), and the resulting alkoxide mixture was added dropwise to the aqueous solution over a period of several minutes. Under continuous stirring, the solution was heated for 2 hours before being cooled to room temperature. The solid product was filtered and rinsed with 1.0 L of water, and then dried overnight at 100°C in a vacuum oven. The dried material was ground to a fine powder and calcined in air at 550°C for 5 h, with a heating ramp rate of 1°C/min to remove the organic template.

4.2.5.2 Synthesis of Extra-Cu-MASN

Prior to metal loading, approximately 50 mg of calcined MASN was dried overnight in a vacuum oven at 100°C. Dried MASN was impregnated with 5.54 wt% Cu, from Copper(II) nitrate hemi(pentahydrate) ($Cu(NO_3)_2 \bullet 2.5H_2O$) dissolved in a minimal amount of a 50/50 vol/vol water/ethanol solution (~3 g). The wet material formed a sludge which was was sonicated for 90 minutes in a tightly sealed vial, and then allowed to soak for at least 4 days to ensure all the copper was completely adsorbed by the framework. Then the material was dried overnight in a vacuum oven at 100°C.

Sodium borohydride was used in attempting to reduce the copper ions adsorbed to the framework to metallic Cu^0. Dried $Cu(NO_3)_2$-MASN was ground to a powder with a glass rod and magnetically stirred with solid $NaBH_4$ (2 mol BH_4^-:mol Cu^{2+}). Upon addition of 20 mL cold ethanol (< 0°C), the reaction mixture immediately turned black. The borohydride reduction was allowed to occur in an ice bath while stirring under continuous argon purging, until H_2 gas formation was no longer observable (~2.5 h). The reaction mixture was diluted to 50 mL with room temperature nanopure water and centrifuged at a rate of 4200 rpm for 10 min. After decanting, the solid product was washed by being briefly resuspended in water, and then centrifuged again. The precipitate was then dried overnight in argon at 100°C in a thoroughly purged vacuum oven.

4.2.5.3 Galvanic Exchange of Ag^+ for Cu using Cu-MASN

Cu-MASN was dried overnight at 100 °C in a vacuum oven, then stirred in a 100 mM silver nitrate solution at room temperature for times varying from 10 min to 24 h. Solutions of were made by dissolving silver nitrate (target 9.5 wt% Ag, 1:1 mol Ag/mol Cu) in 50/50 vol/vol water/ethanol. After the exchange, the mixture was diluted to 50 mL with nanopure water and centrifuged, then decanted and washed with an additional 50 mL water. The precipitate was collected by final centrifugation and dried overnight at 100°C in a thoroughly purged vacuum oven.

4.2.6 Characterization

Powder X-ray diffraction (PXRD) was performed on a Rigaku SmartLab X-ray diffractometer with Cu-Kα (1.54 Å) radiation (40 kV, 44 mA). All samples were prepared fresh and handled with minimal exposure to atmosphere prior to scanning. All

samples were ground and evenly dispersed on an amorphous SiO_2 sample holder and scanned with a step size of 0.01° and scan rate of $1° \cdot min^{-1}$. High angle annular dark field scanning transmission electron microscopy (HAADF-STEM) imaging was performed on a FEI Titan TEM operated at 300 kV. The STEM probe had a convergence semiangle, α, of 10 mrad and a beam current of 25 pA (300 kV). HAADF-STEM images were acquired using a Fischione annular dark-field (ADF) detector with an inner semiangle, β, of 45 mrad. EDS data was simultaneously collected along with HAADF-STEM data on four silicon drift detectors with a solid angle of 0.7 steradians (SuperX) and analyzed using Bruker's Espirit software. HRTEM images were acquired using a FEI ThemIS microscope operated at 300kV with a FEI Ceta Camera. All electron microscopy and EDS data collection were carried out on fresh samples suspended by brief sonication in absolute ethanol and deposited on 400 mesh copper TEM grids with lacey carbon support. Inductively coupled plasma optical emission spectroscopy (ICP-OES) data were collected on a PerkinElmer Optima 7000 DV. Samples for ICP-OES were prepared by digestion in an aqueous solution comprised of 50_v% concentrated HNO_3 and 5_v% H_2O_2 (30% stock solution) at 85 °C, rapidly stirring in a sealed polypropylene container for 2 h prior to dilution with Milli-Q water.

4.3 Results and Discussion

4.3.1 Intra-Framework Metallization of MSN

Before examining intra-framework metallization of MSN, preliminary desulfurization experiments were conducted with sorbents prepared by the interior/exterior surface loading (wet impregnation) of various transition metal salts (18_w% M, M = Ag, Ce, Co, Cu, Ni, or Zn) onto MASN (Table 4.1). MASN was chosen

owing to its negative surface charge and the assumption that the metal cations in solution should better disperse and adhere to the MASN framework compared to MSN. Compared to Ag^{+}, which had the highest initial desulfurization capacity, Cu^{2+} and Ni^{2+} had next-best performance. The results of this preliminary study were then used to guide the investigation of both intra- and extra-framework metallization of MSN in the following work.

Table 4.1 Initial desulfurization capacity of several M^{n+}-MASN (18_{w}% M)

M	*mgS/g*
none	2.73
Ag^{+}	12.17
Cu^{2+}	5.35
Ni^{2+}	4.11
Zn^{2+}	3.48
Co^{2+}	3.01
Ce^{2+}	2.55

The initial work done in examining the incorporation of metals other than aluminum into the MSN framework of MCM-41 type nanoparticles followed a modified synthesis routine published by Derrien, et al.[4] Synthesis times were extended from 2 hr (standard for MSN or MASN) to 6 hours for mono- and 24 hours for bi-metallic intra-framework M-MSN. The reason for the prolonged time of synthesis was both empirical (pore quality materials, often resembling bulk material) and based on the understanding that while precipitation of silicate-template composites is relatively fast, the polymerization of the extended silica framework is slow, and the introduction of metallic species is expected to slow this process further.[20] The particle morphology and pore size

were confirmed by STEM and PXRD (Figure 4.1). STEM and EDS analysis of single metal substitution into the SiO_2 framework of MCM-41 type MSN (M-MSN, M = Cu, Co, Ce, Ni, or Nd) showed that substituting with nickel and copper had the most success (Figures 4.2 and 4.3, respectively), though the percent metal loading was not determined. STEM/EDS data for attempts with cobalt (Figure 4.4), cerium and neodymium (Figure 4.5), produced dual phase materials, wherein the MSN appeared mostly in tact morphologically (discrete nanoparticles) and in terms of phase (MCM-41), but a second metallic phase appeared to precipitate separately. PXRD analysis (Figure 4.6) of all metals attempted show that regardless of the likelihood of incorporation with the MSN framework, the mesoporous phase structure was largely intact, with the characteristic (100) peak in the nominal 2-theta range indicating a pore diameter of roughly 3 nm.

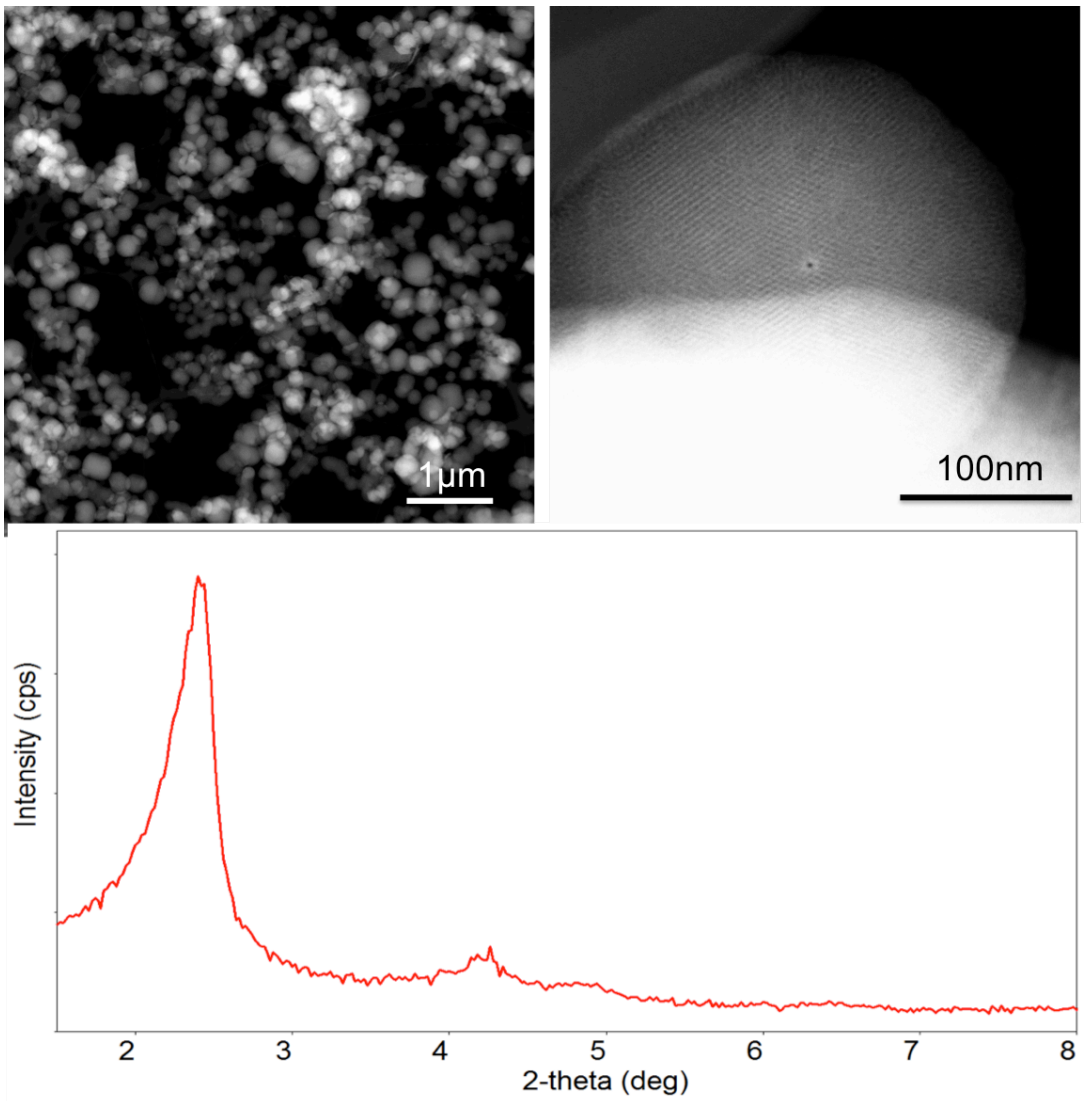

Figure 4.1 STEMs and PXRD of MSN synthesized by concentrated solution route.

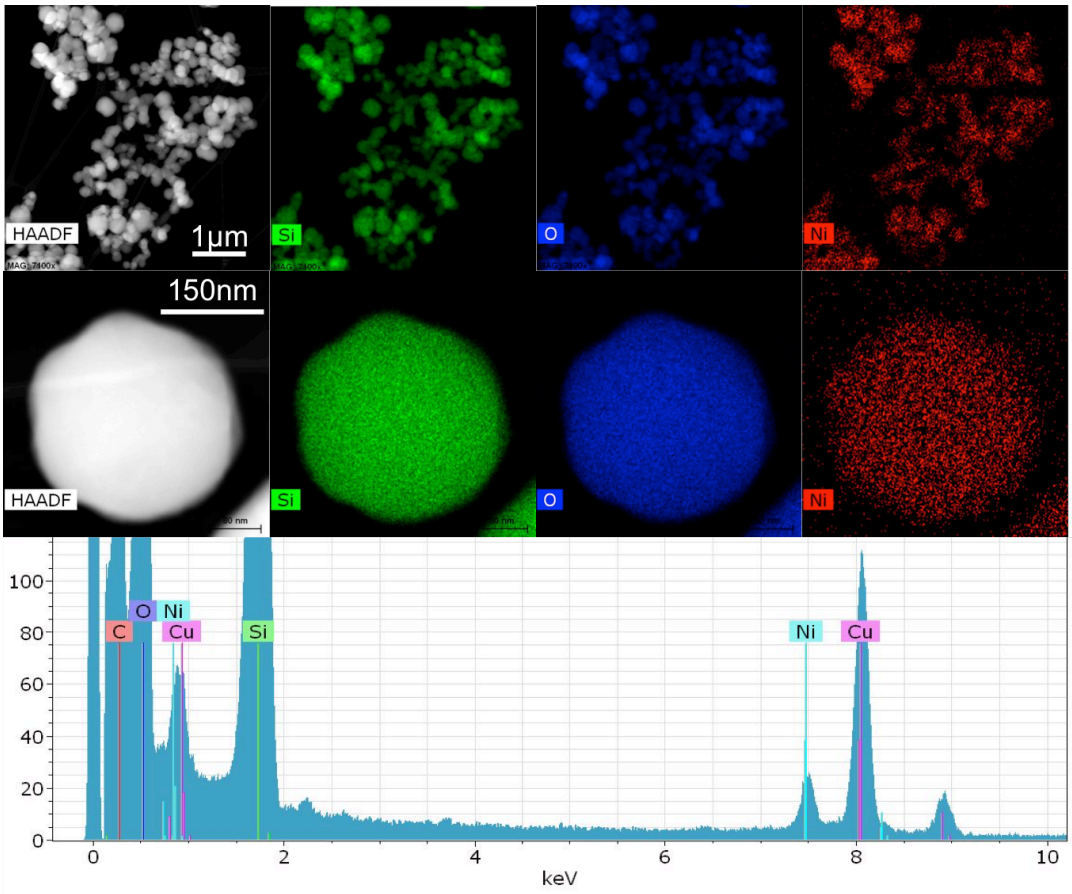

Figure 4.2 HAADF-STEM and EDS data for Ni-MSN.

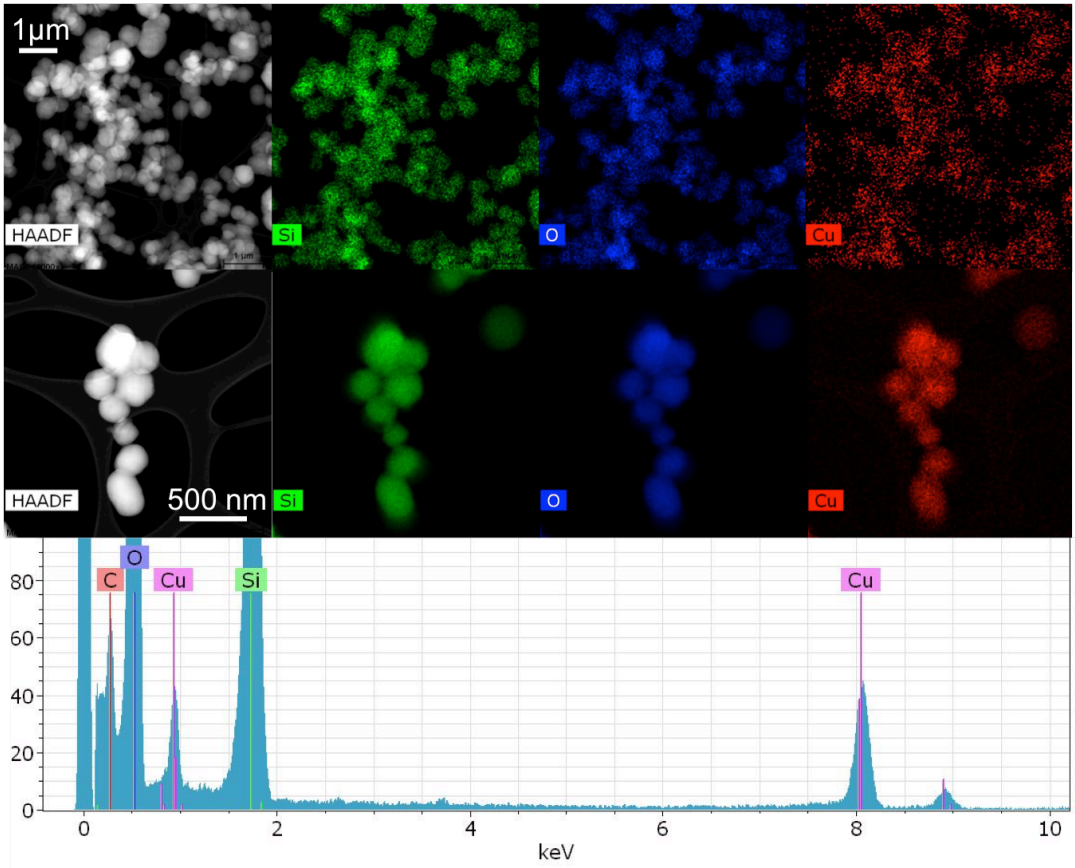

Figure 4.3 STEM and EDS data for Cu-MSN.

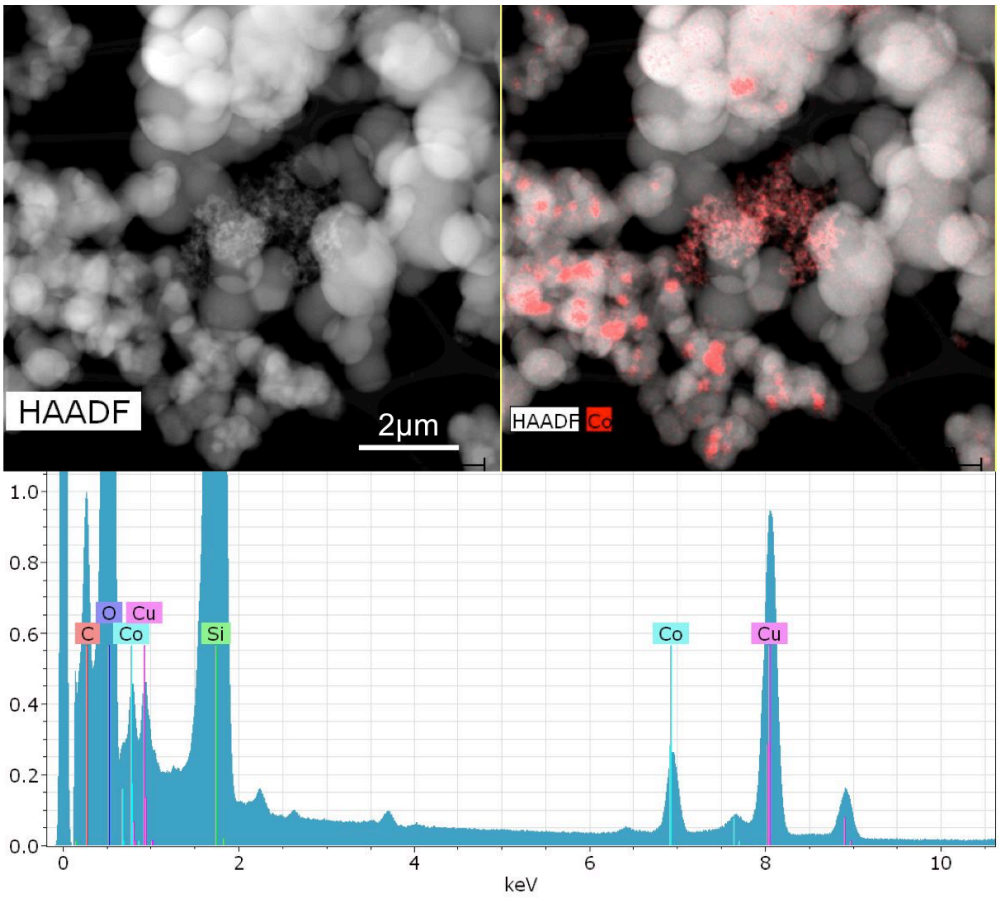

Figure 4.4 HAADF-STEM and EDS of Co-MSN, showing most Co has segregated as a separate phase from the MSN particles.

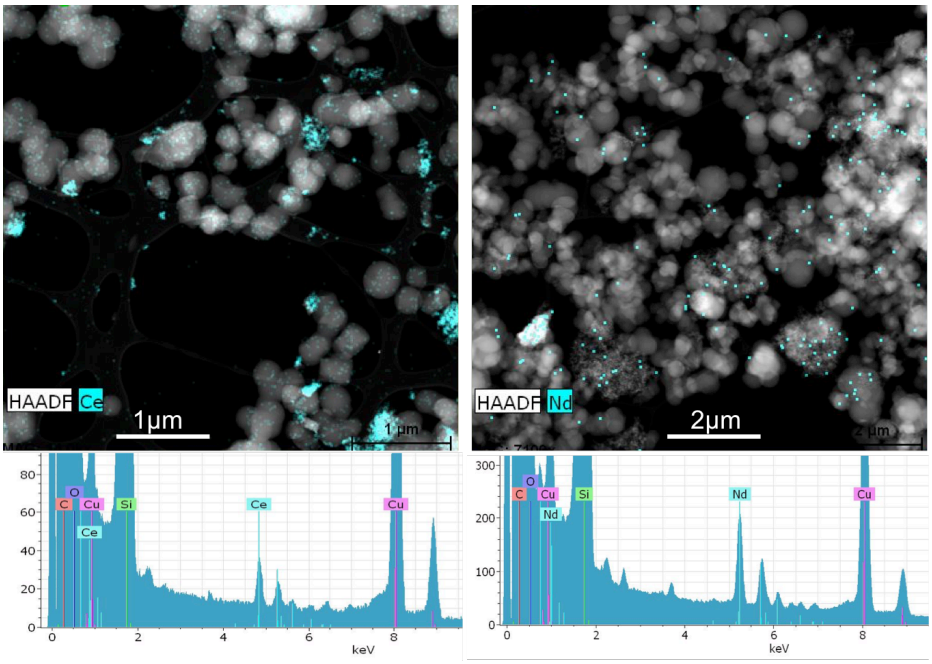

Figure 4.5. HAADF-STEM and EDS of (left) Ce-MSN and (right) Nd-MSN

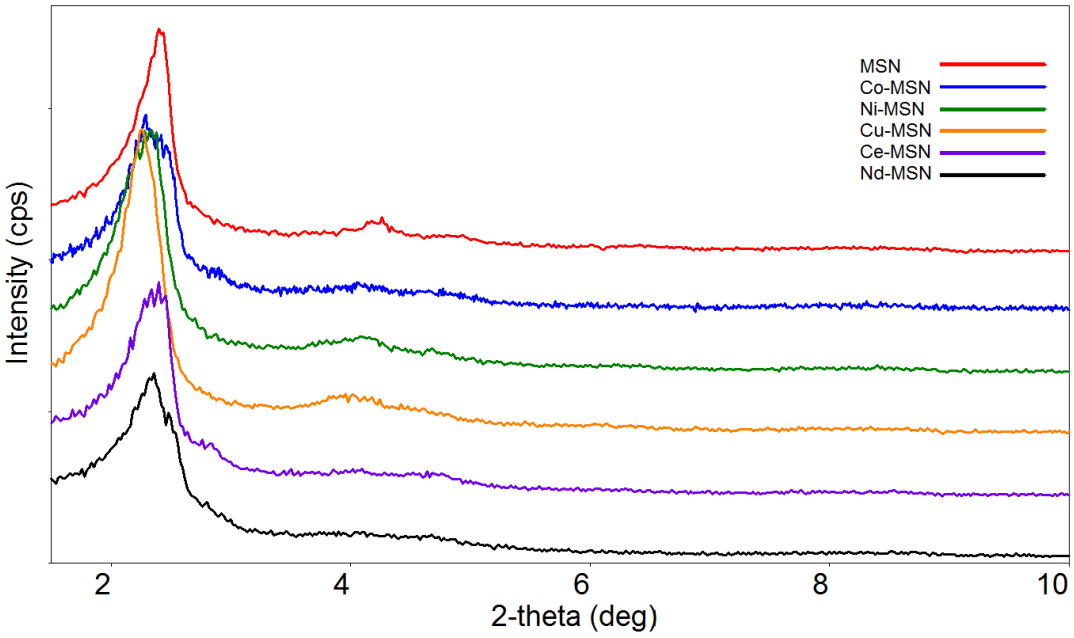

Figure 4.6 PXRD data comparing attempts at intra-framework incorporation of various transition metals into MSN (M-MSN).

Initial fuel tests with the two successful homogenous materials, Cu-MSN and Ni-MSN, revealed that Cu-MSN had higher initial desulfurization capacity for the removal of DBT from model fuel. In an attempt to improve the desulfurization capacity further, Cu-MSN was loaded with 10 $_w$% Ag by impregnation with $AgNO_3$ in an water/ethanol solution. The material turned gray immediately and eventually black in color. Figure 4.7 shows high-resolution detail of the Cu-MSN pore structure and Ag nanoparticle deposits both within the pores and possibly adhered to the exterior of the particles. It can be presumed that some of the Cu was in an oxidation state other than +2, and that this allowed from partial reduction of the silver ions upon impregnation. It was observed that some of the high contrast spots (shown by EDS in Figure 4.8 to be metallic Ag) were an artifact of interaction with the electron beam (formed in real time during scanning), but the majority were present immediately upon imaging. This artifact of imaging indicates that some silver was still present in ionic form, and/or the energy of the electron beam may have agglomerated tiny metallic silver nanoparticles. Interestingly, as can be seen in both Figures 4.7 and 4.8, the Ag nanoparticles tend to cluster toward the center of the Cu-MSN particles.

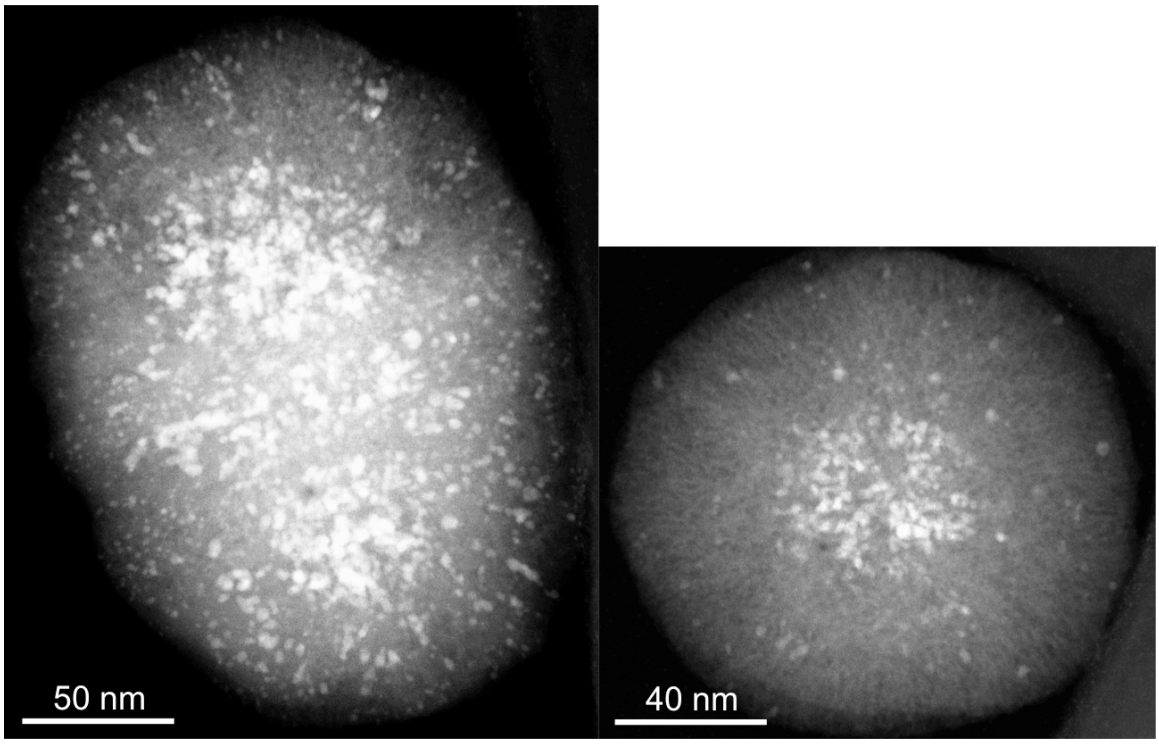

Figure 4.7 STEM of $AgNO_3$ impregnated Cu-MSN (Ag-Cu-MSN).

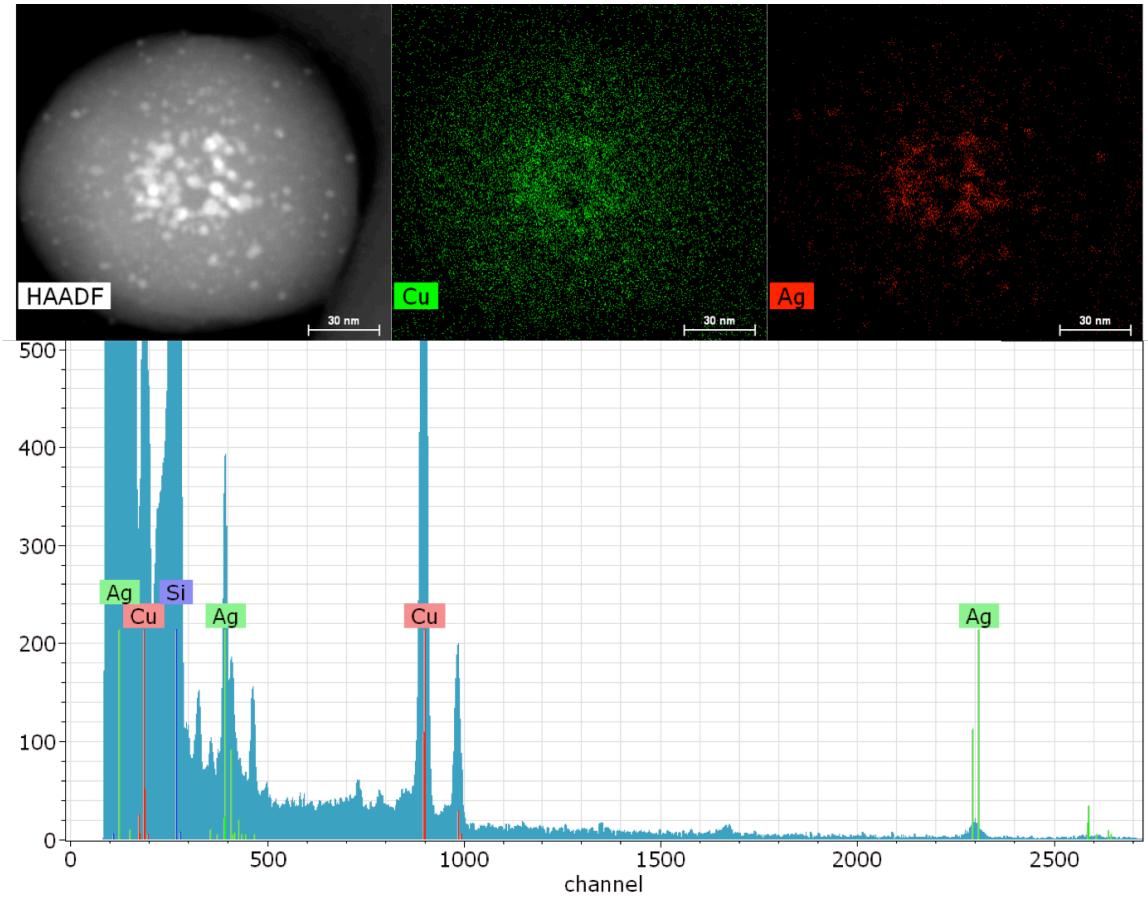

Figure 4.8 STEM and EDS of $AgNO_3$ impregnated Cu-MSN (Ag-Cu-MSN).

The further attempts to reduce the silver ions in the material yielded interesting results, which further indicate that not all of the silver ions converted to metallic form after initial impregnation. Figure 4.9 shows the results observed by STEM for the 90 minute plasma treatment of Ag-Cu-MSN in argon plasma. As can be seen, the composite particles look similar to the initially impregnated material, however many representative particles (such as the right-hand particle in Figure 4.9) have what appears to be a greater amount of reduced silver, and the observation of artifact Ag NPs forming under the electron beam was not observed. The dispersion of Ag NPs on/in the Cu-MSN

framework also appears to be finer and more even after plasma treatment, which may be the result of the etching effect of the plasma.

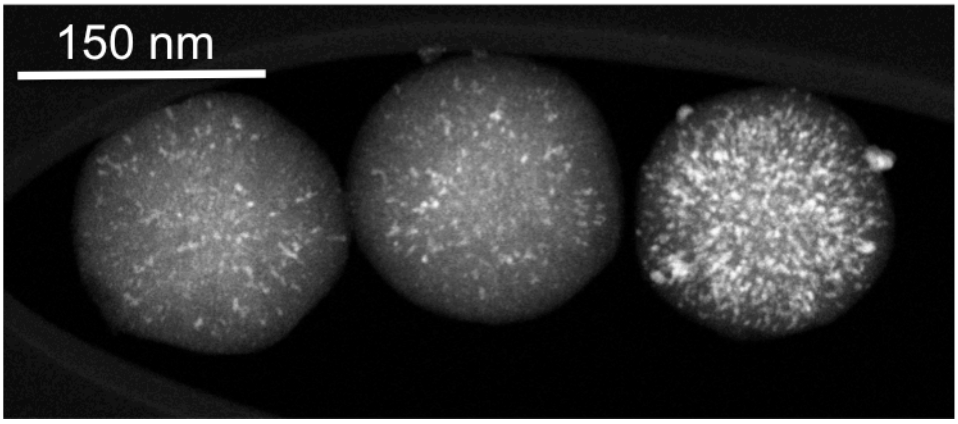

Figure 4.9 STEM of plasma treated Ag-Cu-MSN (PT-Ag-Cu-MSN)

Attempts to reduce the impregnated ionic silver using $NaBH_4$ yielded a material composite consisting of a large amount of metallic silver as a separate phase from Cu-MSN (Figure 4.10 and 4.11). This material was not considered further, owing to this phase separation.

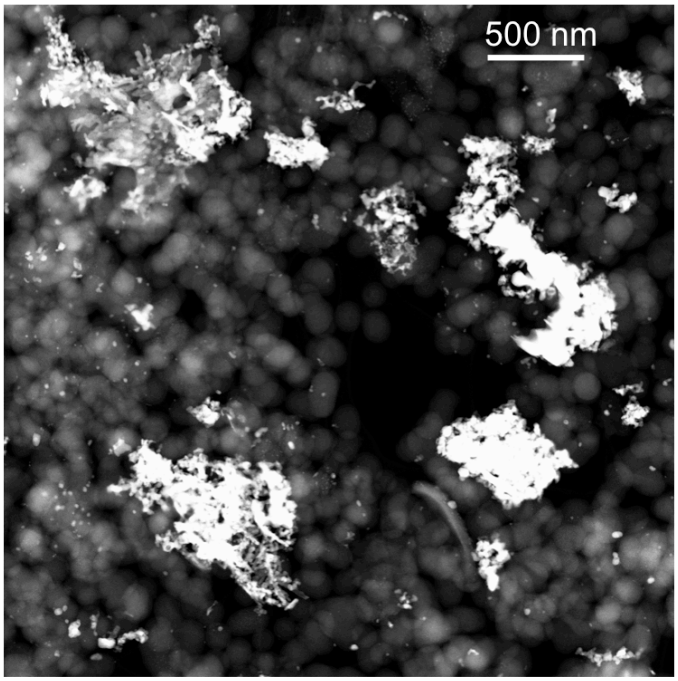

Figure 4.10 $NaBH_4$ treatment of Ag-Cu-MSN (BH_4-Ag-Cu-MSN) showing segregation of Ag and possibly Cu material outside of the Cu-MSN.

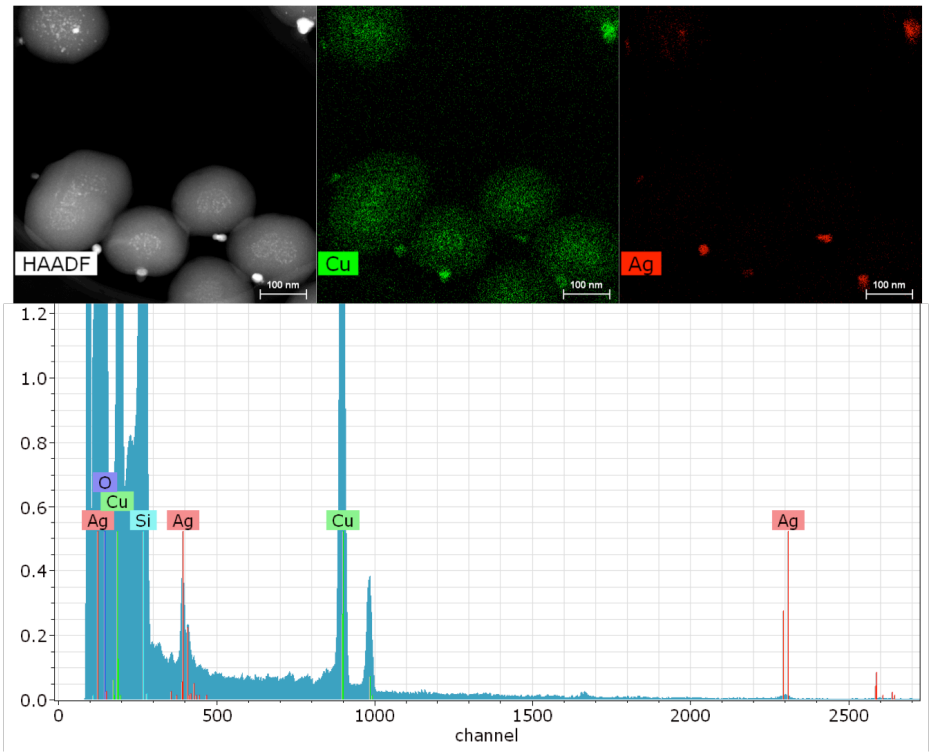

Figure 4.11 $NaBH_4$ treatment of Ag-Cu-MSN (BH_4-Ag-Cu-MSN), with EDS of extra-framework metal deposits.

Preliminary model fuel tests of M-MSN materials (Figure 4.12) were conducted on those materials judged successful on the basis of particle morphology and apparent homogenous metal species distribution. Cu-MSN initially outperformed Ni-MSN, and so further functionalization of the former with $AgNO_3$ (Ag-Cu-MSN) and subsequent plasma treatment (PT-Ag-Cu-MSN) were performed, and the resulting materials were tested for DBT adsorption from model fuel. Reduction of Ag-Cu-MSN using $NaBH_4$ produced material with large quantities of a bulk metallic (likely Ag) phase formed separate from the MSN particle phase, and so was not tested.

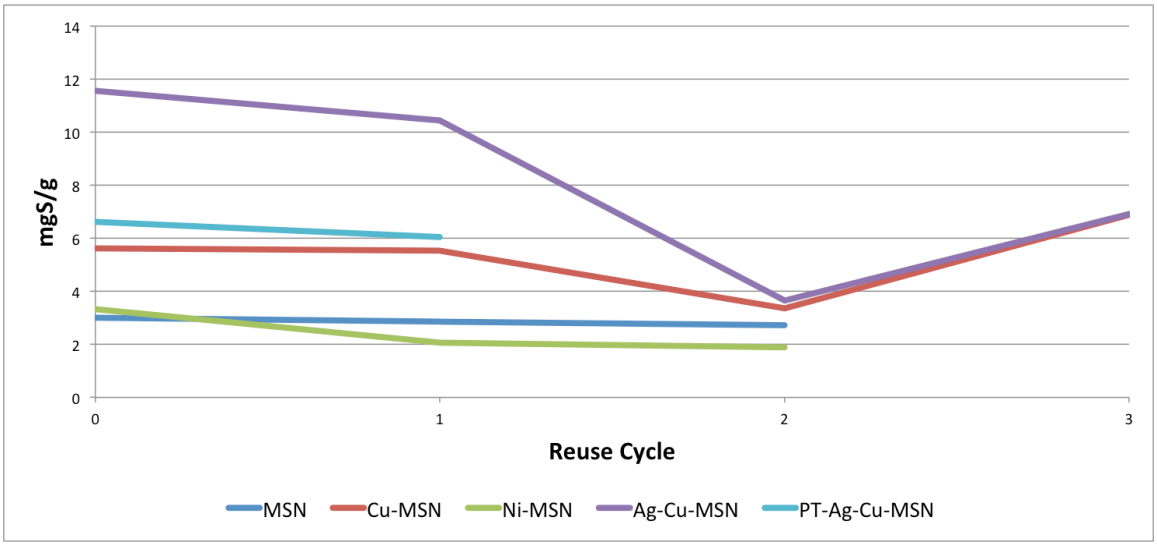

Figure 4.12 Model fuel tests comparing DBT adsorption of MSN, Cu-MSN, Ni-MSN, $AgNO_3$ impregnated Cu-MSN (Ag-Cu-MSN), and plasma treated Ag-Cu-MSN (PT- Ag-Cu-MSN).

4.3.2 Intra-framework bi-metallic Cu/Ni-MSN

Because Cu-MSN and Ni-MSN seemed to give the most homogenous material, suggesting potential intra-framework metal incorporation, or at least well-dispersed extra-framework metallization, the binary metallic material Cu/Ni-MSN was attempted next. However, the synthesis parameters used for the single metallization of M-MSN yielded particles that were highly fused, though appeared to retain good association of the metals with the MSN phase by STEM/EDS (Figure 4.13). Through trial and error, it was found that a traditional dilute solution synthesis of MSN yielded discrete particles of relatively monodisperse size (100 to 400 nm) of Cu/Ni-MSN (Figure 4.14). Both metals appear well associated with the framework as STEM/EDS data suggests (Figure 4.15). Figure 4.16 shows the fine structure of each particle, where the channel morphology can be just barely discerned, and a flaky surface morphology is seen. While it is difficult to tell from

this HAADF-STEM image, the channel morphology is very well defined, and its order confirmed by PXRD (see Figure 4.17 for comparison to the concentrated solution synthesized material).

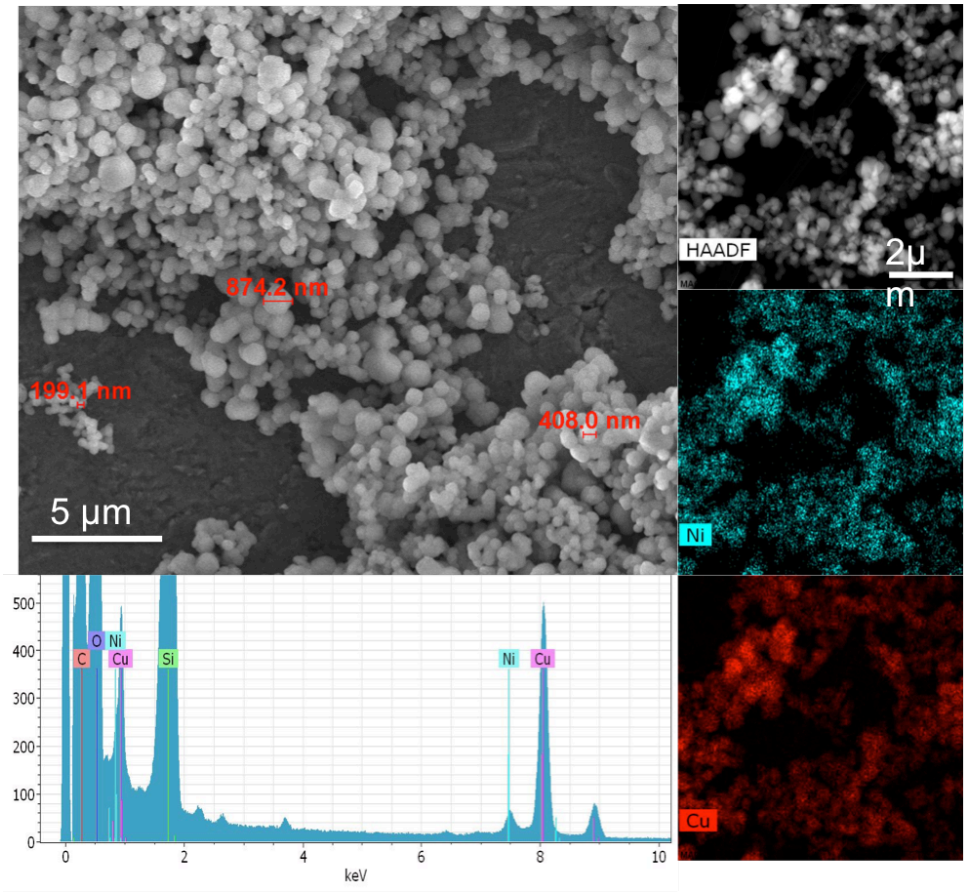

Figure 4.13 SEMs and EDS of Cu/Ni-MSN synthesis by concentrated solution route.

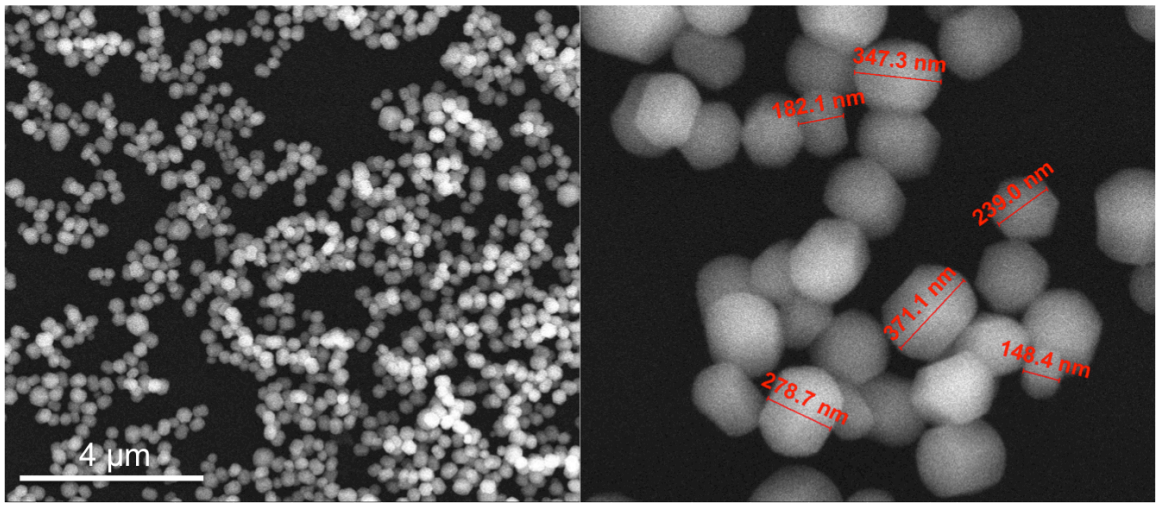

Figure 4.14 SEMs of Cu/Ni-MSN* (*synthesized with NH_4OH by dilute solution route).

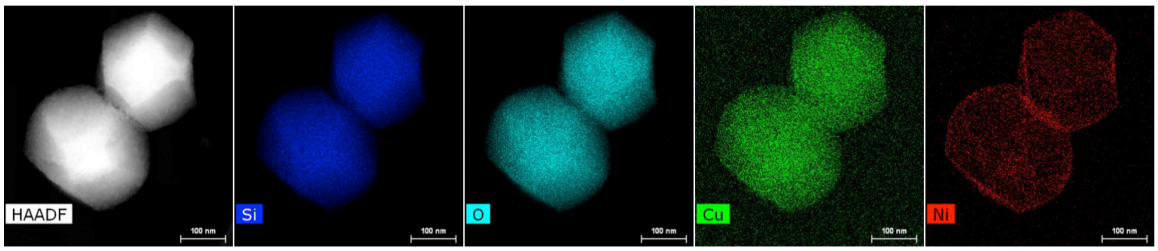

Figure 4.15 HAADF-STEM and EDS maps of Cu/Ni-MSN*.

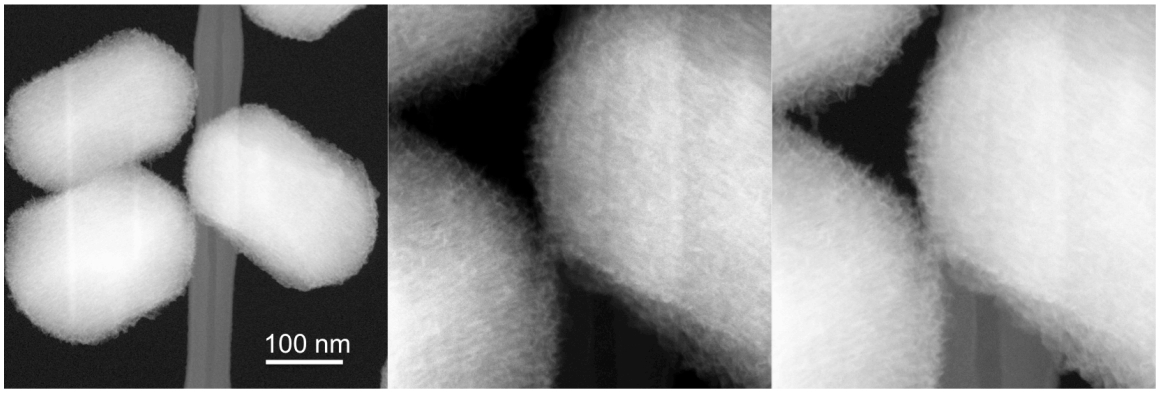

Figure 4.16 HAADF-STEM images of the fine structure of Cu/Ni-MSN*.

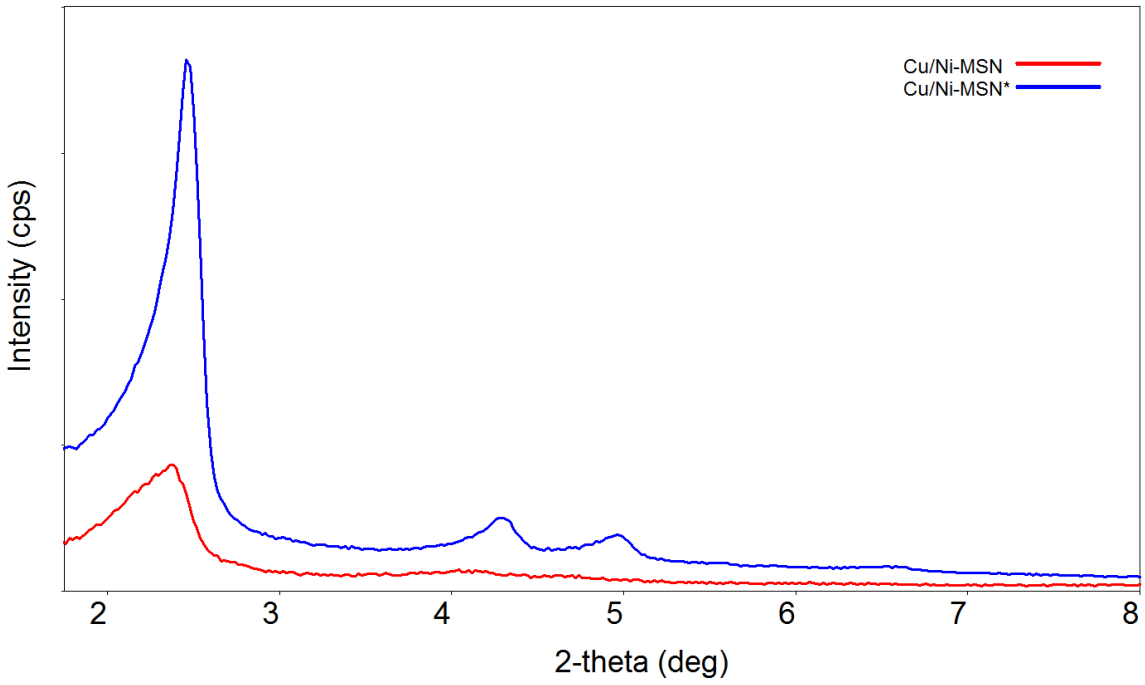

Figure 4.17 PXRD comparing Cu/Ni-MSN synthesized via concentrated synthesis solution route (as per M-MSN discussed above) vs Cu/Ni-MSN*.

Plasma treatment of as-synthesized Cu/Ni-MSN (PT-Cu/Ni-MSN) was carried out to attempt reduction of the incorporated Cu and Ni ions from the oxide lattice (whether that of the larger SiO_2 and/or metal oxide coating that may have formed alongside the silicate framework). The color change of the material after plasma treatment from light blue/green to brownish may have been an indication of partial reduction of Cu or Ni ionic or oxide species. This color change was not observed when plasma treating pure calcined MSN, so the explanation of the brown color as indicative of decomposition of residual CTAB can be ruled out. Addition of $AgNO_3$ to the plasma treated material caused it to turn gray in a matter of seconds, but then back to the original light blue/green after drying in a vacuum oven overnight. This color change may be the result of silver ion reduction to metallic Ag^0, implying an increased oxidation state of either Ni or Cu, followed by

oxidation of Ag^0 during the in vacuo drying step. It is difficult to determine any of this, based solely on the color change of the material, and no further characterization of the material at any of these steps was performed.

Attempts at reduction of the Cu and Ni species associated with MSN in Cu/Ni-MSN using $NaBH_4$ (BH_4-Cu/Ni-MSN) were inconclusive. STEM/EDS data (Figure 4.18) show that much of the Ni and Cu are still associated with the framework after $NaBH_4$ treatment, appearing homogenously incorporated or associate with the particles imaged. However, separate phase material was identifies which appears by EDS to be mostly composed of Cu in both the EDS map and spectrum. It may be that Cu is more easily removed from the framework (perhaps because it was only associated as in an extra-framework phase), or reacts with borohydride differently than Ni, and this is why the separate metallic phase is mostly composed of Cu. It may also simply be that this phase is a composite of Cu and Ni metal in the same ratio as these metals occur in association with the framework (vide infra).

The average atomic percentage of Cu and Ni in Cu/Ni-MSN was calculated by EDS to be 1.90% Cu and 0.60% Ni. No significant change in this composition was observed between fresh, PT-Cu/Ni-MSN, or BH_4-Cu/Ni-MSN, indicating that even though some material appears to form as a separate phase during the $NaBH_4$ treatment.

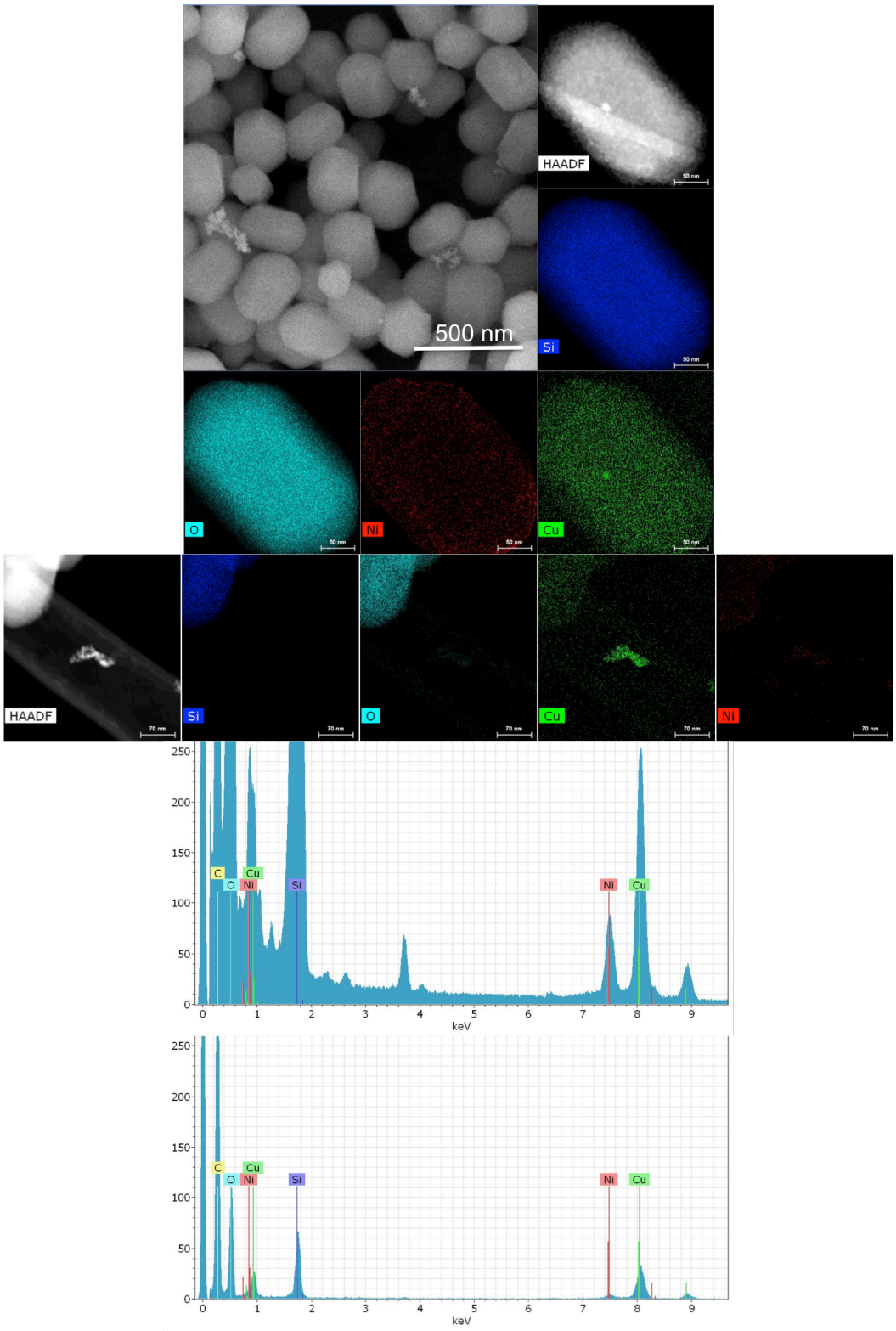

Figure 4.18 SEM and HAADF-STEM/EDS maps of BH_4-Cu/Ni-MSN (top image set and top spectrum) and associated phase (bottom image set and bottom spectrum).

Fuel testing of the of fresh Cu/Ni-MASN and silver nitrate impregnated Cu/Ni-MSN post plasma treatment (Ag-PT-Cu/Ni-MSN) were carried out (Figure 4.19), but the results were not remarkable compared with previous data for similarly impregnated (10_w% Ag) Ag-MSN. No testing of impregnated fresh material (Ag-Cu/Ni-MSN) was conducted, as reduction in oxidation state of the Cu and/or Ni species was considered necessary for meaningful interaction of the silver ions with the framework.

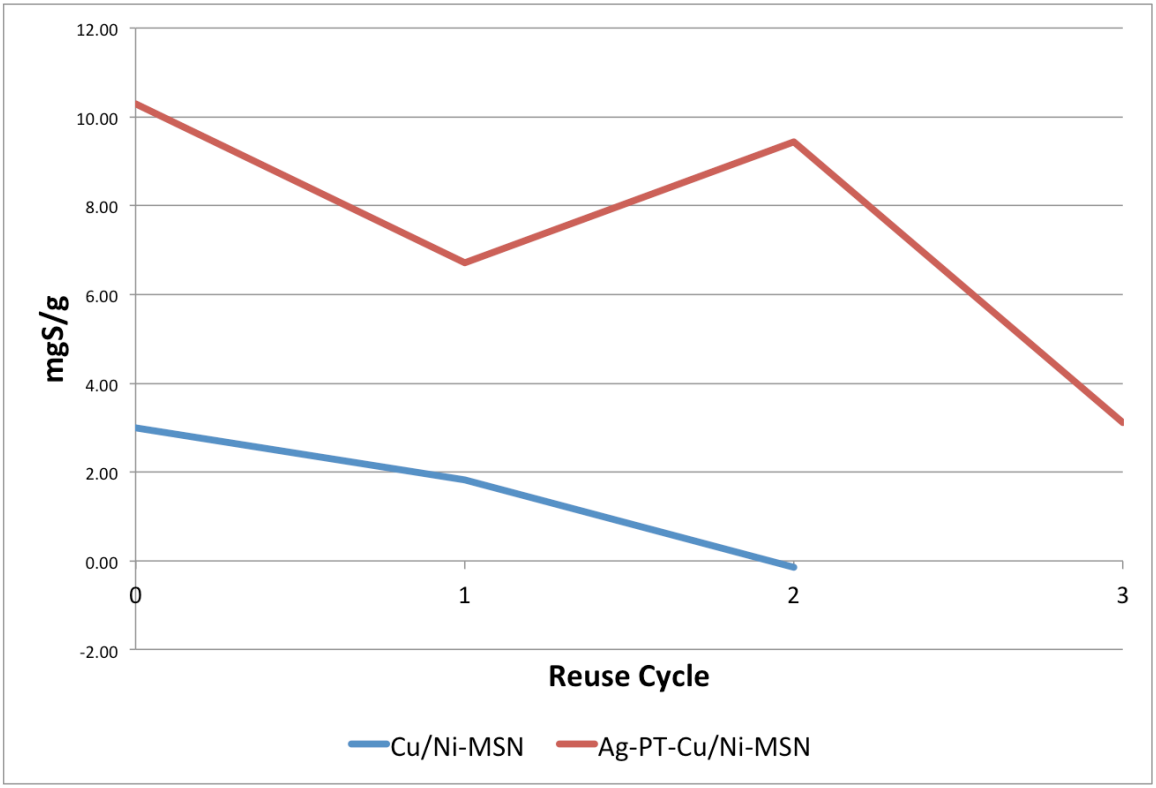

Figure 4.19 Fuel testing for fresh Cu/Ni-MSN* vs Ag-PT-Cu/Ni-MSN* with 10_w%Ag

4.3.3 Galvanic exchange of Ag^{+} for Cu^{0} in extra-framework Cu-MASN to form GE-Ag/Cu-MASN

The following work is for the attempted bi-metallic Ag/Cu metallization of mesoporous aluminosilicate nanoparticles (MASN). The synergistic effect between Ag and Cu has been shown to slow the oxidation rate of Cu in bi-metallic catalysis systems by electron transfer from Ag to Cu.[21] It was anticipated that an alloy or core-shell structure might form between the two metals during galvanic exchange. No conclusive evidence suggesting the presence of both metals in the composite is given here, and it remains to be tested whether the method of galvanic exchange is sufficient to create such particles. However, some interesting characterization of the attempted formation of this material follows.

The formation of extra-framework metallized Cu-MASN was achieved by $NaBH_4$ solution exposure of wet impregnated $Cu(NO_3)_2$-MASN to form Cu-MASN. This gave a mixed phase Cu and MASN material, where nanoparticles of Cu are observed by STEM/EDS (Figure 4.20). Interesting cage-like structures were seen by STEM to form on the outside of the MASN particles in extra-framework metalized Cu-MASN, in addition to tiny high contrast spots indicative of metallic phase material within the mesochannels of the support (Figure 4.21). EDS of an isolated group of these cages revealed their composition to consist of Cu and O. The oxidation of Cu may have occurred during handling. Powder XRD (Figure 4.22) confirmed that the crystallinity of these Cu particles were below the 5 nm crystalline domain size threshold necessary to give x-ray diffraction. The observed Cu NPs can therefore be assumed to be relatively amorphous.

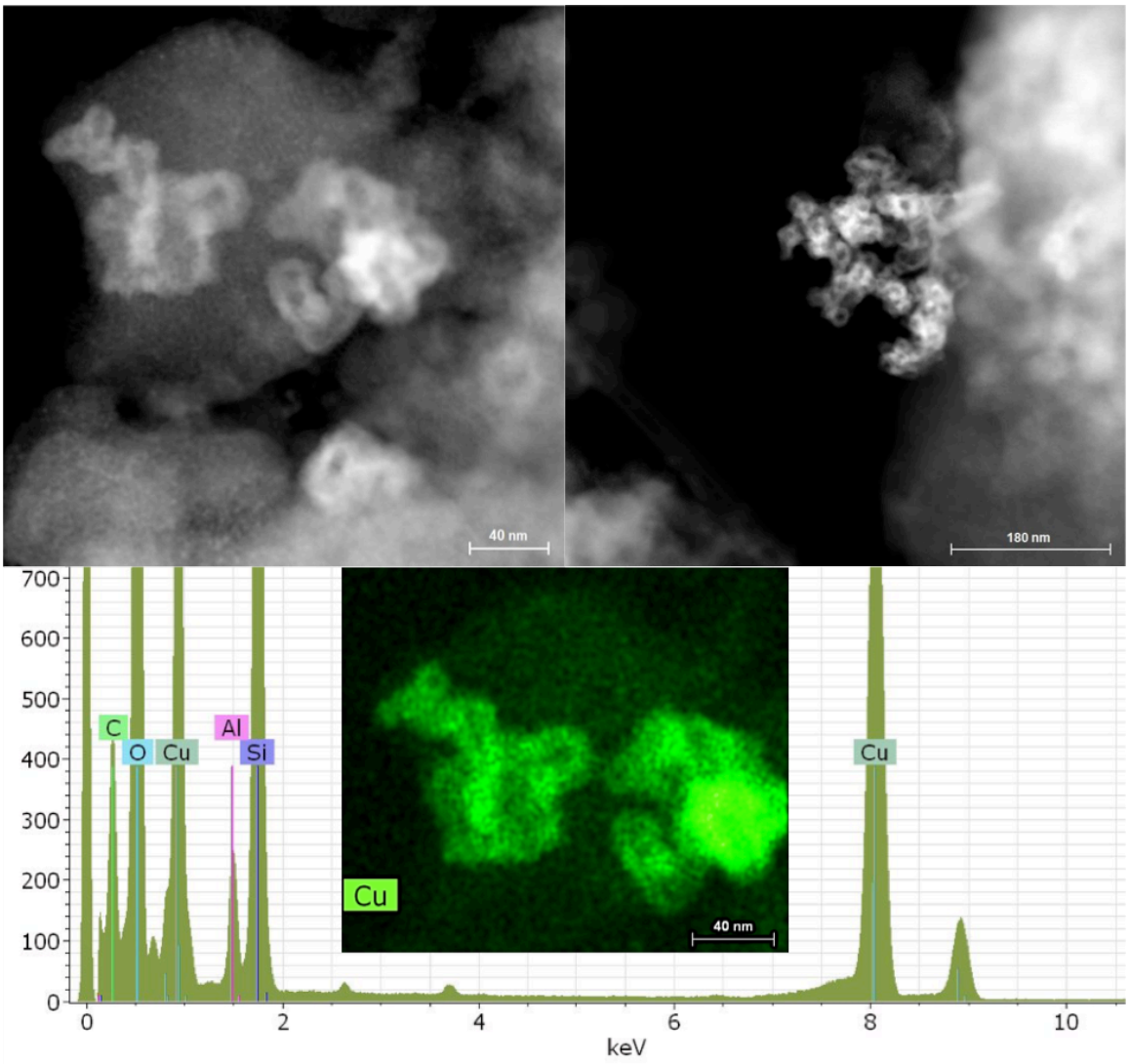

Figure 4.20 STEMs and EDS of Cu-MASN, showing strange cage-like structures attached to the surface of MASN.

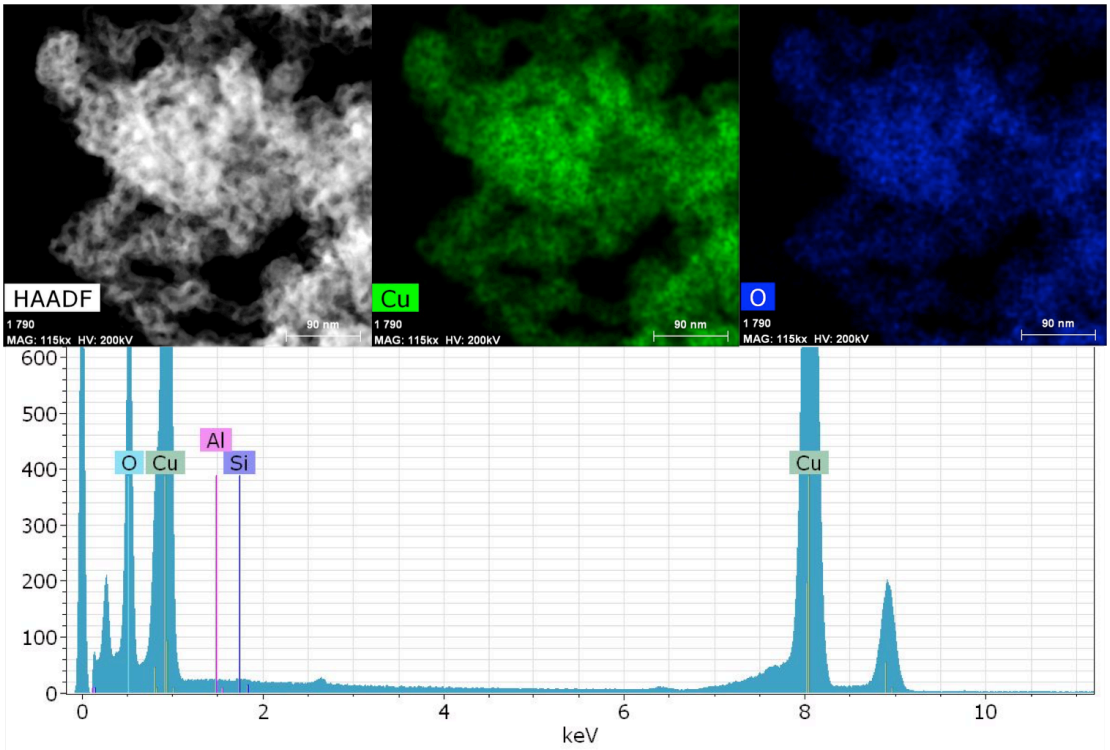

Figure 4.21 STEM and EDS of an isolated cluster of metallic particles typically adhered to MASN in Cu-MASN.

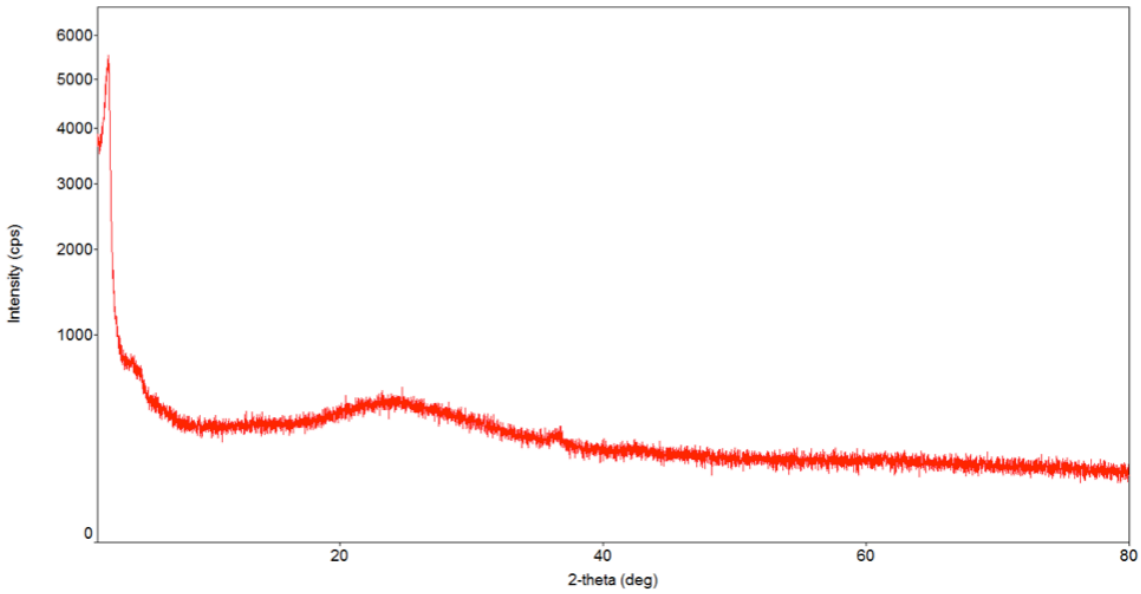

Figure 4.22 PXRD of Cu-MASN showing only the (100) peak for the MS phase, but no Cu or Cu_xO_y peaks.

Galvanic exchange reaction between ionic silver solution and Cu-MASN (Equation 1) was carried out (yielding GE-Ag/Cu-MASN) for various times to study the effect on desulfurization capacity. STEM/EDS examination of various GE times show that at 10 minutes, only Cu and Al are detected in the Cu-MASN material composite, though no Cu NPs are apparent on the exterior of the sample (Figure 4.23). Galvanic exchange for 90 minutes (Figure 4.24) gave a nice dispersion of Ag particles, which were large enough to produce x-ray diffraction (Figure 4.25). Continued exchange up to 24 hours gave a material with much larger Ag NPs (Figure 4.26).

$$Cu_{(s)} + 2Ag^{+}_{(aq)} \rightarrow Cu^{2+}_{(aq)} + 2Ag_{(s)} \quad (1)$$

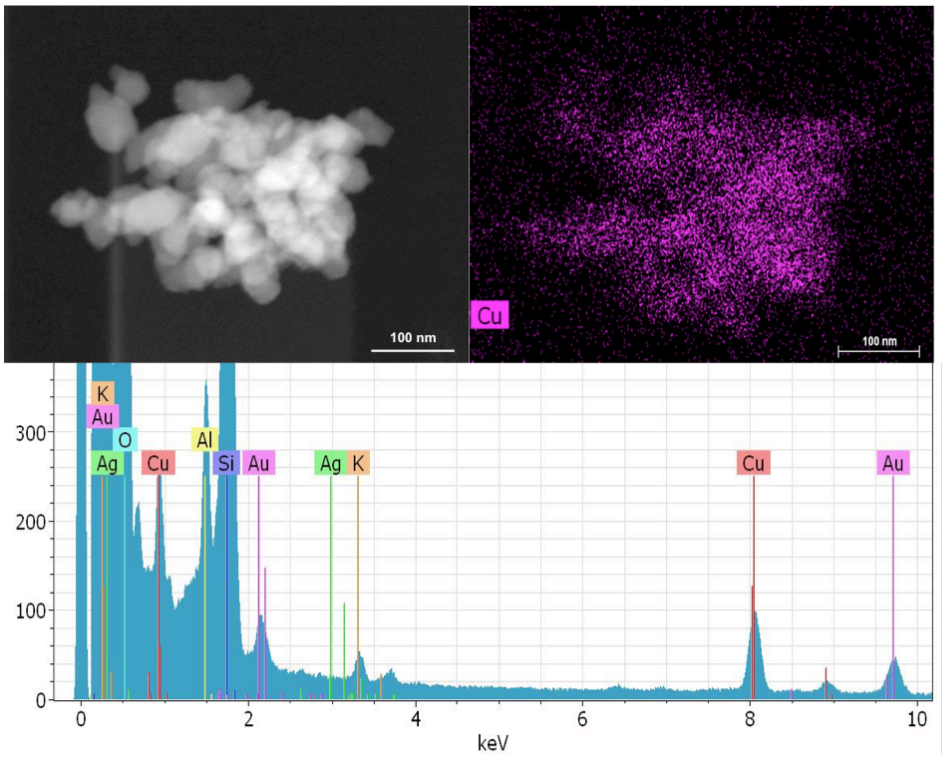

Figure 4.23 STEM/EDS of GE-Ag/Cu-MASN after 10 minutes of galvanic exchange reaction between Ag^{+} and Cu-MASN. The presence of Au in the spectrum is from the TEM grid used.

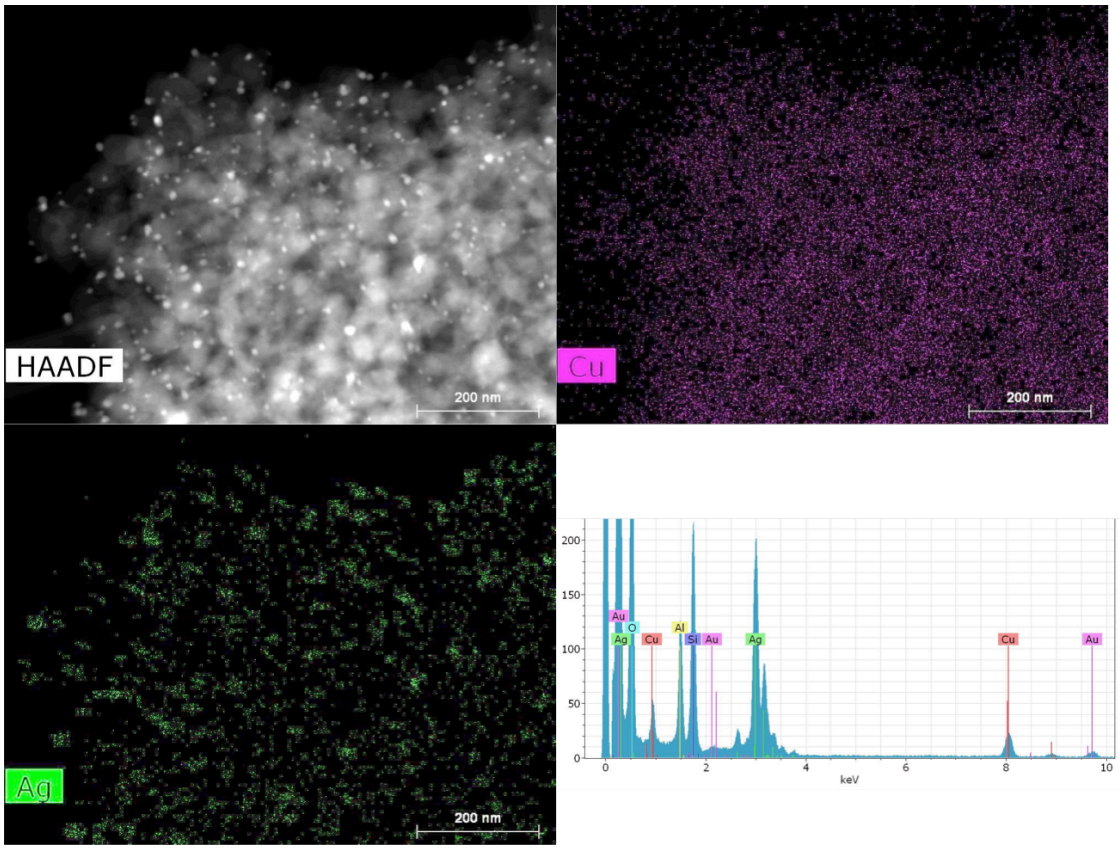

Figure 4.24 STEM/EDS of GE-Ag/Cu-MASN after 90 minutes of galvanic exchange reaction. The presence of Au in the spectrum is from the TEM grid used.

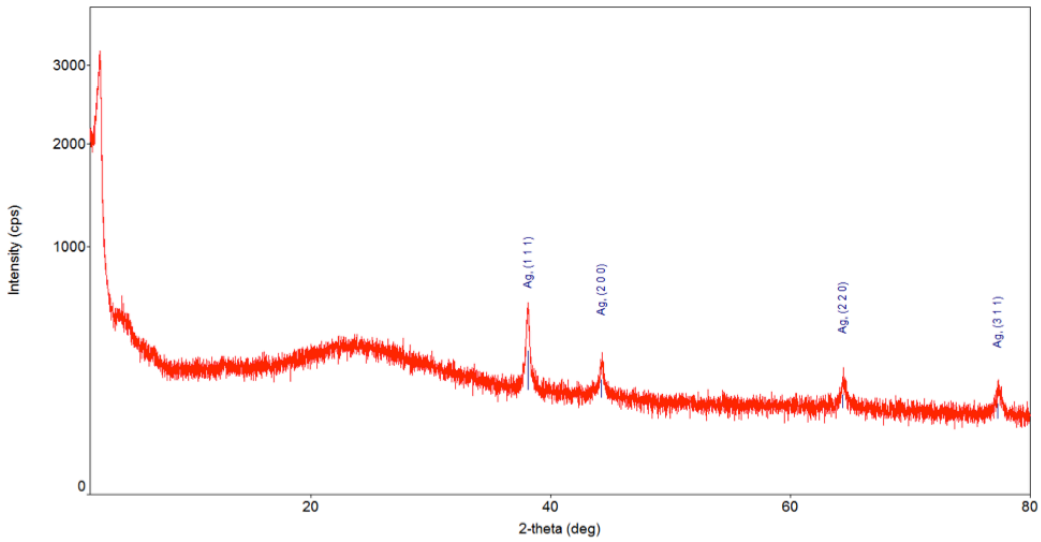

Figure 4.25 PXRD profile of GE-Ag/Cu-MASN after 90 minutes of galvanic exchange reaction.

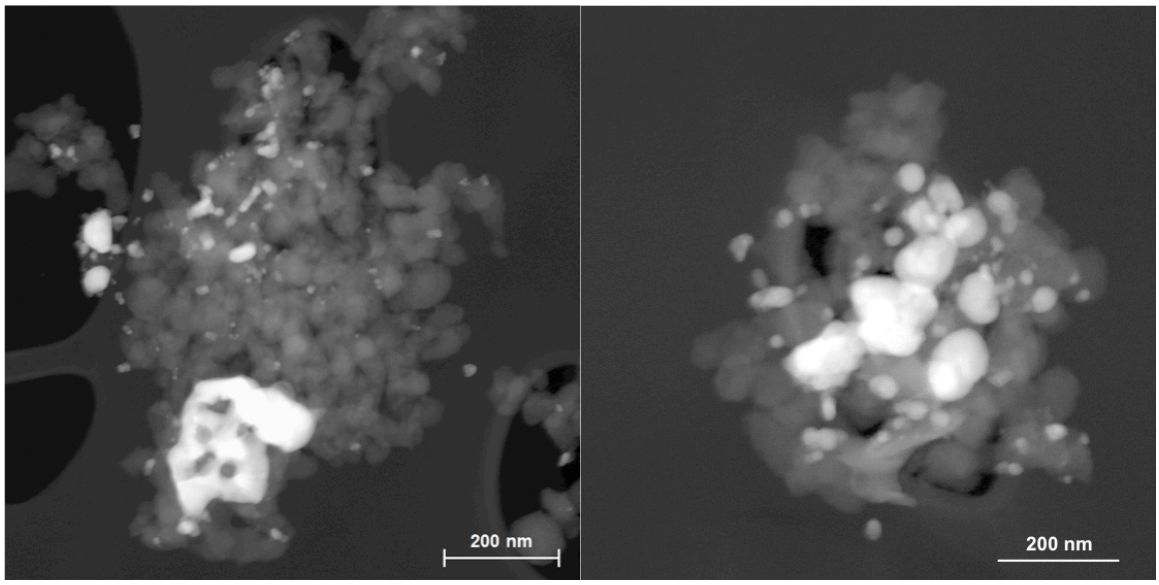

Figure 4.26 STEM of GE-Ag/Cu-MASN after 24 hr of galvanic exchange reaction.

Table 4.2 summarizes initial desulfurization capacities for the removal of DBT from model fuel, using GE-Ag/Cu-MASN adsorbent after 10 min, 30 min, 90 min, 3.5 hr and 24 hr of galvanic exchange reaction between Ag^{+} and Cu-MASN. Comparison materials, Cu-MASN and Ag-MASN, were both synthesized by impregation with the relevant metal salt (10_w%), followed by $NaBH_4$ reduction. The benefit of this GE method compared to simple reduction of impregnated silver ions (Ag-MASN) is not entirely clear when comparing the initial and reuse desulfurization capacities of the materials (Figure 4.27). The 90 minute GE material does seem to have the most consistent reuse desulfurization capacity for this single set of experimental data, but the batch testing method used to examine the removal of DBT from model fuel is known to give varying results upon replication. It seems clear from this preliminary data that the mono- and bi-metallic metalized MASN materials here perform similarly, within error of each other, as reusable desulfurization sorbents.

Table 4.2 Initial desulfurization capacities for GE-Ag/Cu-MASN synthesized with varying galvanic exchange times.

GE Reaction Time	*Initial mgS/g*
10 min	2.03
30 min	2.34
90 min	8.62
3.5 h	8.94
24 h	7.16

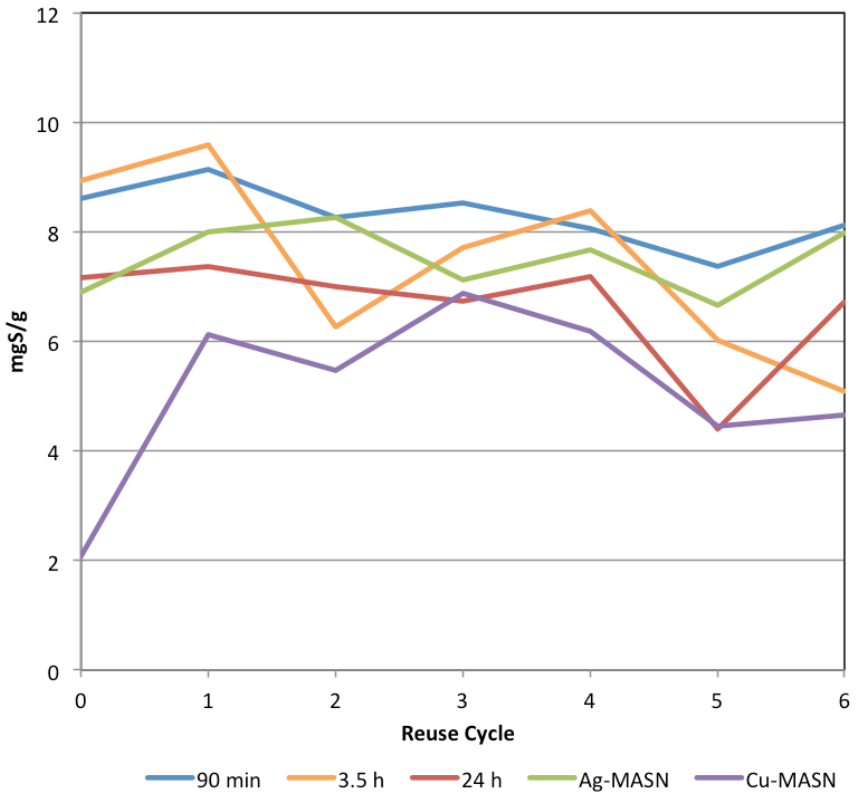

Figure 4.27 Comparison of desulfurization capacity of GE-Ag-Cu-MASN synthesized at various exchange times. Ag-MASN and Cu-MASN here refer to 10_w% metal loading followed by subsequent reduction with $NaBH_4$.

4.4 Conclusion and Future Work

Much work remains to be done to understand how to fabricate a successful metalized MSN adsorbent for removal of refractory organosulfur species from hydrocarbon fuels. From a material's standpoint, the thiophilic character of the target metal(s) species need to be well understood. For instance, should a metallic, ionic, or oxide version of a particular species or binary metal composite or alloy have the most suitable interaction with the organosulfur pollutants in question? This is a complicated question to address, since the affinity of the adsorption site should be carefully balanced so as to allow for successful adsorption as well as removal of organosulfurs without the need for aggressive cleaning procedures which will degrade the material (such as high temperatures or harsh chemical solvents). From an efficiency standpoint, the material must be reusable (preferably indefinitely), and display reasonably fast kinetics of adsorption and desorption upon cleaning. The price point of the materials is also a consideration, and has been the driving force in this work for examining non-noble metals (i.e Cu, Ni, and Ag in reduced quantities).

The work presented in this chapter represents many fits and starts, which were not fine-tuned with optimization of the material synthesis parameters, nor followed through with preliminary model fuel testing. For instance, the Ni-MSN materials were never functionalized with silver to determine if the potential for a synergistic effect between Ni and Ag might give rise to improved performance. Attempts to better characterize the intra- vs extra-framework incorporation of both Ni and Cu were begun on Cu/Ni-MSN* using EELS but have yet to realize any useful data on the location of the metallic species either within the SiO_2 framework or within separate oxide phases associated with the

MSN. Such characterization would be vital to correlating the adsorption performance of the material with the location and oxidation state of the metallic species.

The need for additional characterization of the materials discussed here include: Surface area and pore volume (BET/BJH); metal oxidation state and coordination environment (XPS and DRUV-Vis); and hydrothermal stability testing to determine if additional changes/degradation occur with use of the finished materials at high temperature aqueous systems. Spectroscopic analysis of metallic interactions with the silica or aluminosilicate support should also be conducted to determine if there is enhancement or detraction from metal performance in the given application.

4.5 References

(1) Qian, W.; Wang, H.; Chen, J.; Kong, Y. Spherical V-Fe-MCM-48: The Synthesis, Characterization and Hydrothermal Stability. *Materials* **2015**, *8* (4), 1752–1765. https://doi.org/10.3390/ma8041752.

(2) Li, W. B.; Zhuang, M.; Xiao, T. C.; Green, M. L. H. MCM-41 Supported Cu−Mn Catalysts for Catalytic Oxidation of Toluene at Low Temperatures. *J. Phys. Chem. B* **2006**, *110* (43), 21568–21571. https://doi.org/10.1021/jp063580g.

(3) Walcarius, A.; Etienne, M.; Lebeau, B. Rate of Access to the Binding Sites in Organically Modified Silicates. 2. Ordered Mesoporous Silicas Grafted with Amine or Thiol Groups. *Chem. Mater.* **2003**, *15* (11), 2161–2173. https://doi.org/10.1021/cm021310e.

(4) Derrien, G.; Charnay, C.; Zajac, J.; Jones, D. J.; Rozière, J. Copper-Containing Monodisperse Mesoporous Silica Nanospheres by a Smart One-Step Approach. *Chem. Commun.* **2008**, No. 27, 3118. https://doi.org/10.1039/b804593c.

(5) Patel, N.; Fernandes, R.; Edla, R.; Lihitkar, P. B.; Kothari, D. C.; Miotello, A. Superior Hydrogen Production Rate by Catalytic Hydrolysis of Ammonia Borane Using Co-B Nanoparticles Supported over Mesoporous Silica Particles. *Catal. Commun.* **2012**, *23*, 39–42. https://doi.org/10.1016/j.catcom.2012.02.030.

(6) Selvam, P.; Dapurkar, S. E. Catalytic Activity of Highly Ordered Mesoporous VMCM-48. *Appl. Catal. Gen.* **2004**, *276* (1–2), 257–265. https://doi.org/10.1016/j.apcata.2004.08.012.

(7) Betiha, M. A.; Hassan, H. M. A.; Al-Sabagh, A. M.; Khder, A. E. R. S.; Ahmed, E. A. Direct Synthesis and the Morphological Control of Highly Ordered Mesoporous AlSBA-15 Using Urea-Tetrachloroaluminate as a Novel Aluminum Source. *J. Mater. Chem.* **2012**, *22* (34), 17551. https://doi.org/10.1039/c2jm32941g.

(8) Piumetti, M.; Armandi, M.; Garrone, E.; Bonelli, B. An IR Spectroscopy Assessment of the Surface Acidity of Mesoporous VOx–SiO2 Catalysts. *Microporous Mesoporous Mater.* **2012**, *164*, 111–119. https://doi.org/10.1016/j.micromeso.2012.05.041.

(9) Gomez, S.; Garces, L.; Villegas, J.; Ghosh, R.; Giraldo, O.; Suib, S. Synthesis and Characterization of TM-MCM-48 (TM=Mn, V, Cr) and Their Catalytic Activity in the Oxidation of Styrene. *J. Catal.* **2005**, *233* (1), 60–67. https://doi.org/10.1016/j.jcat.2005.04.015.

(10) Samanta, S.; Das, S.; Samanta, P. K.; Dutta, S.; Biswas, P. A Mononuclear Copper(Ii) Complex Immobilized in Mesoporous Silica: An Efficient

Heterogeneous Catalyst for the Aerobic Oxidation of Benzylic Alcohols. *RSC Adv.* **2013**, *3* (42), 19455. https://doi.org/10.1039/c3ra41417e.

(11) Silvestre-Albero, J.; Sepúlveda-Escribano, A.; Reinoso, F. R. Preparation and Characterization of Zinc Containing MCM-41 Spheres. *Microporous Mesoporous Mater.* **2008**, *113* (1–3), 362–369. https://doi.org/10.1016/j.micromeso.2007.11.037.

(12) Kim, T.-W.; Chung, P.-W.; Lin, V. S.-Y. Facile Synthesis of Monodisperse Spherical MCM-48 Mesoporous Silica Nanoparticles with Controlled Particle Size. *Chem. Mater.* **2010**, *22* (17), 5093–5104. https://doi.org/10.1021/cm1017344.

(13) Levine, I. N. *Physical Chemistry*, 5th ed.; McGraw-Hill: Boston, 2002.
(14) Zelewsky, A. von. *Stereochemistry of Coordination Compounds*; Inorganic chemistry; Wiley: Chichester, England ; New York, 1996.

(15) Loh, A. S.; Davis, S. W.; Medlin, J. W. Adsorption and Reaction of 1-Epoxy-3-Butene on Pt(111): Implications for Heterogeneous Catalysis of Unsaturated Oxygenates. *J. Am. Chem. Soc.* **2008**, *130* (16), 5507–5514. https://doi.org/10.1021/ja711013n.

(16) Li, L.; Chen, M.; Huang, G.; Yang, N.; Zhang, L.; Wang, H.; Liu, Y.; Wang, W.; Gao, J. A Green Method to Prepare Pd–Ag Nanoparticles Supported on Reduced Graphene Oxide and Their Electrochemical Catalysis of Methanol and Ethanol Oxidation. *J. Power Sources* **2014**, *263*, 13–21. https://doi.org/10.1016/j.jpowsour.2014.04.021.

(17) Tabor, E.; Jíša, K.; Nováková, J.; Bastl, Z.; Vondrová, A.; Závěta, K.; Sobalík, Z. Role of Pt(0) in Bimetallic (Pt,Fe)-FER Catalysts in the N2O Decomposition. *Microporous Mesoporous Mater.* **2013**, *165*, 40–47. https://doi.org/10.1016/j.micromeso.2012.07.035.

(18) Park, K.-C.; Yim, D.-J.; Ihm, S.-K. Characteristics of Al-MCM-41 Supported Pt Catalysts: Effect of Al Distribution in Al-MCM-41 on Its Catalytic Activity in Naphthalene Hydrogenation. *Catal. Today* **2002**, *74* (3–4), 281–290. https://doi.org/10.1016/S0920-5861(02)00024-X.

(19) Ryoo, R.; Ko, C. H.; Kim, J. M.; Howe, R. Preparation of Nanosize Pt Clusters Using Ion Exchange of Pt(NH3) 4 2+ inside Mesoporous Channel of MCM-41. *Catal. Lett.* **1996**, *37* (1–2), 29–33. https://doi.org/10.1007/BF00813515.

(20) Monnier, A.; Schuth, F.; Huo, Q.; Kumar, D.; Margolese, D.; Maxwell, R. S.; Stucky, G. D.; Krishnamurty, M.; Petroff, P.; Firouzi, A.; et al. Cooperative Formation of Inorganic-Organic Interfaces in the Synthesis of Silicate Mesostructures. *Science* **1993**, *261* (5126), 1299–1303. https://doi.org/10.1126/science.261.5126.1299.

(21) Kim, N. R.; Shin, K.; Jung, I.; Shim, M.; Lee, H. M. Ag–Cu Bimetallic Nanoparticles with Enhanced Resistance to Oxidation: A Combined Experimental and Theoretical Study. *J. Phys. Chem. C* **2014**, *118* (45), 26324–26331. https://doi.org/10.1021/jp506069c.

Chapter 5

Conclusions and Future Work

5.1 Conclusions

The work presented here demonstrates the feasibility of using metal functionalized MSN for a variety of applications. The in-place plasma reduction of Ag^{+} to metallic Ag nanoparticles within the channels of MASN was successful in mitigating the loss of desulfurization capacity upon cycling. While the wet chemical reduction of Ni^{2+} using sodium borohydride, allowed for the partial leaching of the metal precursor and the subsequent coating of the MASN particle surface with a fine dispersion of NBC catalyst. In both cases the use of intra-framework aluminum was shown to complement and enhance the end material. Attempts to incorporate other metals (Cu and Ni) into the framework of MSN, was somewhat successful, though continued characterization is needed to determine whether these incorporations can be classified as intra- or extra-framework metallization. Finally, the binary Cu/Ag extra-framework metallization of MASN shows some promise to enhance the cyclability in adsorptive desulfurization. More characterization is necessary, here as well, to determine the bi-metallic character of the Ag/Cu system and its interaction, if any, with the MASN framework.

5.2 Future work

Continued effort to refine metalized MSN for adsorptive desulfurization should include column testing of actual JP-8, the intended target fuel. The components of JP-8 (which is only available via the department of defense) are many, including over a dozen different organosulfur pollutant species, and varying hydrocarbon species that may

compete for binding sites in a given sorbent. Preliminary cycling tests with PT-Ag-MASN for the desulfurization of JP-8 did not compare well with the model fuel testing to removed DBT from n-decane, where up to 6 cycles could be achieved without significant loss of capacity. This may be because the material is difficult to clean after use, or may have to do clumping or restricted binding site access when loaded in the adsorbent column. Successful function in a column is crucial for the commercial viability of such a sorbent.

Continued effort to determine the exact nature of the NBC coating in the NBC-MASN catalyst will help settle the debate about whether these compounds are nickel supported by borates or true nickel boride. The catalytic activity of the material may also be improved by using larger pore MS frameworks, such as SBA-15. Though such MS will have lower overall surface area, the potential for greater access within the mesochannels will increase the catalytic activity over that obtained using MCM-41 type nanoparticles.

For the mixed metal species work, XPS and EELS will be valuable in determining the oxidation state, and therefore possibly the location of the transition metal species within or on the MS framework. Metals substituted into the SiO_2 framework should have higher coordination than those at the surface, or present in surface metal oxide coating. Regardless of the placement of the metal species in Cu-, Ni- and Cu/Ni-MSN, the PXRD data indicate that the pore structure is intact and well ordered and the electron microscopy images do not reveal any significant defect in particle morphology. Based on these two observations, nitrogen isotherm data would be valuable, as it is likely that BET/BJH analysis will reveal that the surface area and pore volume are comparable to that of MCM-41.

Finally, the bimetallic GE-Ag-Cu-MASN system needs further investigation of the Ag-Cu particles, as well as investigation into their interaction with the MASN framework and optimization of adhesion. As the electron microscopy data show, the metallic particles appear to be mostly outside of the MASN, potentially detached overall, and the MASN acts more as a bulk excipient than a true scaffold. It is possible that there is not strong enough interaction between the MASN and Cu^{2+} to keep sufficient Cu close to the MASN particles after treatment with sodium borohydride, and then subsequent GE with $AgNO_3$. It may be more practical to use plasma treatment to reduce, or partially reduce Cu^{2+} in place within the mesochannels, as in PT-Ag-MASN.

SECTION TWO

Synthesis Routes Toward Metal Organic Framework Thin Films on Conductive Substrates

Abstract

Presented here are two facile methods for fabricating metal organic framework (MOF) thin films on the transparent conductive substrate indium tin oxide coated glass (ITO). The first method, presented in chapter 7, illustrates the successful electrochemical deposition of several MOFs on ITO which was previously deposited with metallic films composed of discrete or overlapping metallic nanostructures. The partial anodic degredation of these metal deposites served as the metal ion source for the growth of MOF films, with relatively low surface roughness and good lateral coverage. The second method, presented in chapter 8, details the successful hydrothermal growth of several isoreticular MOF (IRMOF) films grown on ITO previously hydrothermally deposited with oriented zinc oxide nanowire arrays. The ZnO nanowires serve as nucleation sites for the zinc based MOFs (IRMOF-1, -3, -8, and -9). Both the anodically electrodeposited MOF films and hydrothermally grown IRMOF films were characterized by grazing incidence X-ray diffraction (GIXRD) and electron microscopy. Additionally the electrodeposited films were characterized by in-situ elemental X-ray dispersive spectroscopy (EDS) to give some understanding of the state of the metal underlayer remaining after complete MOF film growth.

Chapter 6

Metal Organic Framework Thin Films

6.1 Introduction

Metal organic frameworks (MOFs) are an important class of highly porous, hybrid inorganic-organic crystalline coordination polymers. Research into the design and application MOFs builds upon that of porous inorganic materials such as zeolites, porous silicates, and aluminophosphates. The introduction of MOFs in the early 1990s by the works of Fujita and co-workers, [T001. 37] Kitagawa and co-workers, [T001.38] and Omar Yaghi and co-workers,[1] marked the beginning of a seemingly unending journey in the synthetic design of functionalized nanoporous solids. MOFs self-assemble from the combination of metal ions and organic ligand precursors, in organic solvents (e.g. DMF or ethanol) or water, typically over the course of hours or days. Synthesis conditions range from ambient temperature and pressure to autoclave synthesis at temperatures typically around 100 °C to 200 °C. Other (often faster) synthetic routes include sonochemical and mechanochemical (ball milling), microwave irradiation and electrochemical methods.[2]

Theoretically, innumerable combinations of metal nodes and organic linkers, corresponding to a vast array of surface chemistries and pore environments, have made the rational design of MOFs an exciting area of research for almost 30 years.[3] By careful consideration of the metal coordination environment, and organic linker geometry and functionality, MOFs can be tailored for specific applications. In Figure 6.1, the classic isoreticular series of IRMOF-1—16 illustrates how a single structural topology can be

retained, while the nanopore environment can be subtly altered with the substitution of different aromatic dicarboxylate ligands.[4]

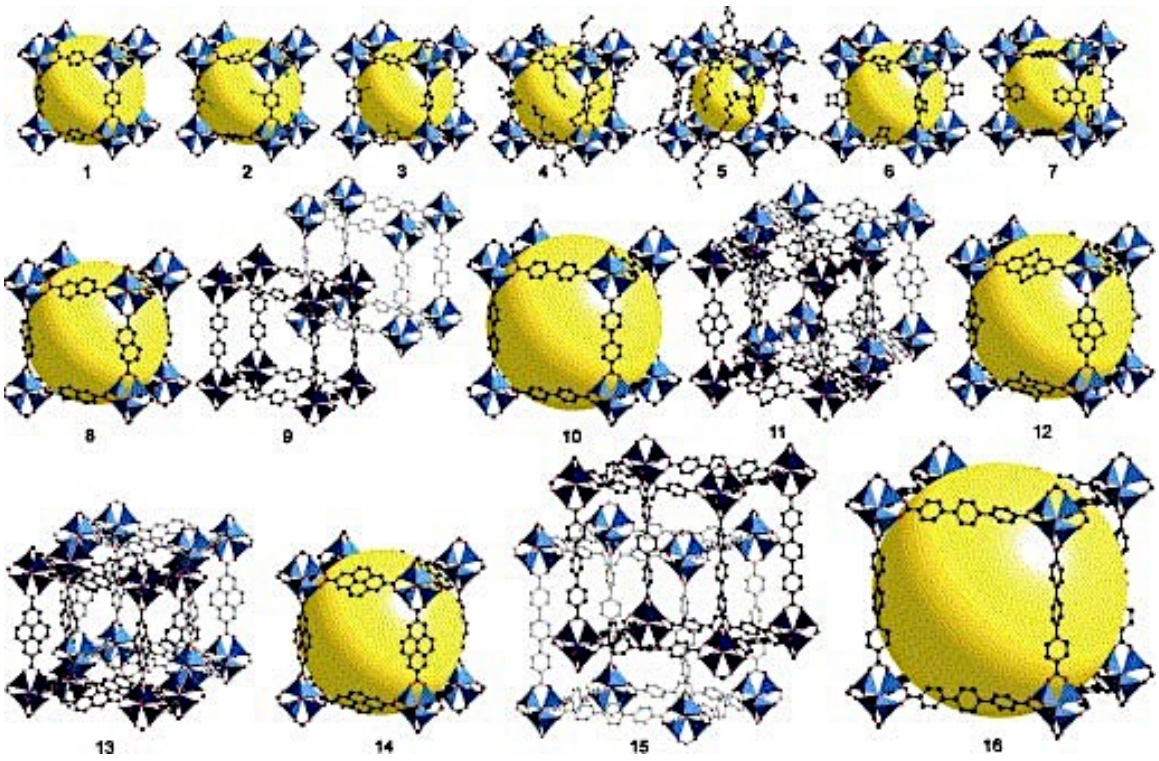

Figure 6.1 IRMOF-1-16. The series is based on the same zinc oxide (Zn_4O) node coordinated by different aromatic dicarboxylate ligands. The yellow spheres represent void space in the cubic topology. IRMOF-9, -11, -13, and -15 are the interpenetrated phases of IRMOF-10, -12, -14, and -16, respectively.

MOF synthesis techniques, to date, have largely centered around the bulk fabrication of microcrystalline powders. Early studies focused on the storage of gases such as carbon dioxide, methane, and hydrogen,[5] and drove the search for new topologies with ever increasing surface areas (some of the highest ever reported in porous solids). More recent applications of bulk MOF powders include gas adsorption and separation,[5,6] aqueous pollutant adsorption,[7] catalysis,[8] , chemical sensing,[2] optical coatings,[9] and drug

delivery,[10] to name a few. Additionally, a growing body of research aims to implement MOFs as integral features of solid-state microelectronics, in applications such as dielectric coatings,[11] chemical sensing,[12,13] and optoelectronics.[14,14,15] Synthetic methodologies for such device application will necessarily be different from those employed in bulk synthesis. Before considering circuit design or moving synthetic operations to the clean room, however, rudimentary fabrication techniques must be designed and refined.

6.2 MOF Thin Films

Bulk synthesis of most metal organic frameworks is somewhat straightforward, with experimentally determined mole ratios of metal and ligand precursors combined in the appropriate templating solvent; allowed to react at room temperature, or heated in an autoclave under autogenic pressure for several hours or days. However, many applications of MOFs may require more sophisticated synthesis considerations than those of bulk crystalline powders. The growth of MOFs as thin films on various substrates (gold, transition metals, alumina, silica, etc.) has important relevance to applications which involve the exploitation of electronic properties inherent in some MOFs, such as chemical sensing by electronic impedance, and photoharvesting applications. Considering these applications, the MOF should be anchored to a conductive substrate to allow for charge transfer.

Methods of thin layer MOF growth that have been reported to be successful include deposition from a colloidal solution of preformed crystallites, room temperature and solvothermal deposition from a mother solution, layer-by-layer (LbL) methods, deposition using a gel-layer approach, deposition on metal oxides, and electrochemical

deposition on conductive substrates. The layer-by-layer and gel-layer approaches have been reported to result in a highly oriented MOF film, known as a SURMOF (surface oriented MOF). The remaining approaches listed above tend to result in more randomly oriented polycrystalline films.[13,16–19]

Functionalization of the substrate is often required for MOF nucleation and thin film growth, and typically entails forming a self-assembled monolayer (SAM) of organic molecules, or a metal oxide layer to anchor the MOF to the substrate. SAM forming molecules are chosen based on the affinity for the substrate and the ability of their terminal functional moieties to mimic the coordination environment of the metal ions in the subsequent MOF film. Figure 6.2 illustrates this concept for a thiol terminated carboxylic acid SAM anchored to a gold substrate by its sulfur groups. The carboxylate groups are free to coordinate with the metal ions and initiate formation of the subsequent MOF film.

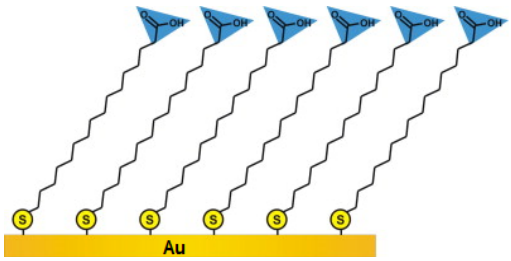

Figure 6.2 Sulfur-anchored alkylcarboxylic acid SAM on gold substrate.

Figures 6.3 and 6.4 illustrate the procedure involved in the layer-by-layer and gel-layer approaches, respectively. In both cases, a SAM is first formed and then the MOF is grown directly on the functionalized surface, either in sequence (layer-by-layer) or all at once (in the gel-layer method). The layer-by-layer approach entails sequential alternate exposures of the functionalized substrate to solutions of the metal or ligand precursors.

This can usually be carried out at room temperature and can be automated—which is fortunate considering that hundreds of repetitions of layering are often necessary to achieve an appreciable thickness.[19,20]

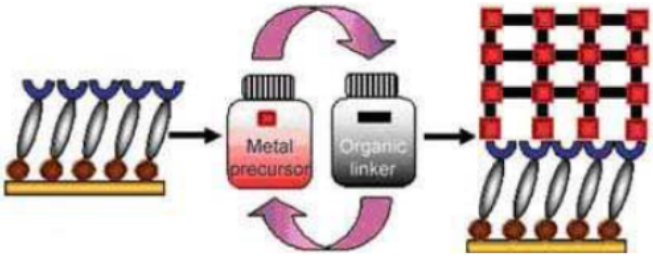

Figure 6.3 Layer-by-layer method of SURMOF growth on a SAM functionalized substrate.

The gel-layer approach entails holding the metal precursor suspended in a non-reactive viscous gel (such as high molecular weight polyethylene glycol), while a solution of the organic ligand is poured on top and allowed to percolate through the gel matrix. Formation of the MOF begins at the SAM surface with binding of the metal precursors in the gel, and proceeds evenly as the slow and steady supply of organic ligands move towards the growing MOF surface, coordinating with the suspended metal ions.[17]

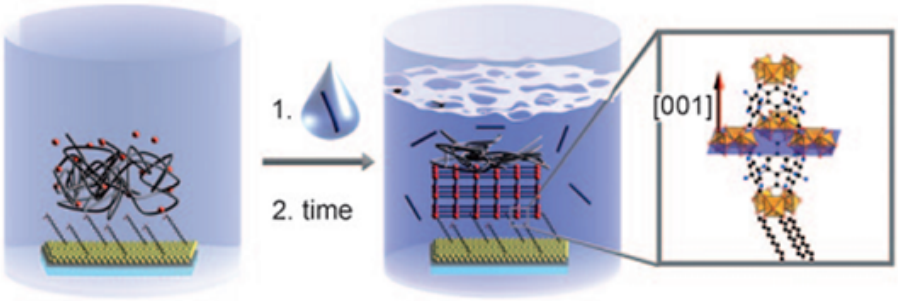

Figure 6.4 Gel-layer approach to SURMOF growth using a viscous gel matrix to suspend the metal precursor while the ligand is allowed to percolate down through the matrix to the growing MOF surface.

Alternative to the method of SAM functionalization, the substrate may be functionalized by providing a node analogue to chemically bond the growing MOF to the substrate. A metal substrate may have its surface oxidized, or a layer of metal oxide may be grown on a non-metallic substrate (such as silicon oxide glass), serving to mimic the nodal environment of the MOF.[21] Many metal oxides can be grown as nanoparticle thin films by a variety of techniques, resulting in different particle morphologies—spherical particles, tubes, plates, rods or wires. Metal oxides (such as ZnO) can provide a semiconducting conduit between the MOF and a conductive substrate, which may prove advantageous over the otherwise insulating nature of some (alkyl) SAMs.

Electrochemical deposition directly onto a metallic or other conductive substrate (glassy carbon, graphene, and indium or fluorine doped tin oxide coatings, to name a few) may have further advantages over both SAM and metal oxide substrate functionalization. Electrochemical MOF film deposition techniques typically rely on the anodic dissolution of a pure metallic substrate anode, or the pH induced deprotonation of carboxylic acid ligand groups at the cathode.[22] Although the resulting polycrystalline MOF orientation is usually completely random in electrochemical deposition, the intimate contact between MOF and substrate my be a valuable tradeoff over SURMOF growth on delicate, and often electronically insulating SAM functionalized substrates. The mechanical adherence of MOF films deposited electrochemically often appear as robust as those grown on native oxides, while offering the potential for direct MOF contact with a conductive substrate.[23]

6.3 References

(1) Li, H.; Eddaoudi, M.; O'Keeffe, M.; Yaghi, O. M. Design and Synthesis of an Exceptionally Stable and Highly Porous Metal-Organic Framework. *Nature* **1999**, *402* (6759), 276–279. https://doi.org/10.1038/46248.

(2) Meek, S. T.; Greathouse, J. A.; Allendorf, M. D. Metal-Organic Frameworks: A Rapidly Growing Class of Versatile Nanoporous Materials. *Adv. Mater.* **2011**, *23* (2), 249–267. https://doi.org/10.1002/adma.201002854.

(3) Yaghi, O. M.; O'Keeffe, M.; Ockwig, N. W.; Chae, H. K.; Eddaoudi, M.; Kim, J. Reticular Synthesis and the Design of New Materials. *Nature* **2003**, *423* (6941), 705–714. https://doi.org/10.1038/nature01650.

(4) Rowsell, J. L. C.; Yaghi, O. M. Metal–Organic Frameworks: A New Class of Porous Materials. *Microporous Mesoporous Mater.* **2004**, *73* (1–2), 3–14. https://doi.org/10.1016/j.micromeso.2004.03.034.

(5) Férey, G. Hybrid Porous Solids: Past, Present, Future. *Chem Soc Rev* **2008**, *37* (1), 191–214. https://doi.org/10.1039/B618320B.

(6) Kitagawa, S.; Kitaura, R.; Noro, S. Functional Porous Coordination Polymers. *Angew. Chem. Int. Ed.* **2004**, *43* (18), 2334–2375. https://doi.org/10.1002/anie.200300610.

(7) Colinas, I. R.; Silva, R. C.; Oliver, S. R. J. Reversible, Selective Trapping of Perchlorate from Water in Record Capacity by a Cationic Metal–Organic Framework. *Environ. Sci. Technol.* **2016**, *50* (4), 1949–1954. https://doi.org/10.1021/acs.est.5b03455.

(8) Lee, J.; Farha, O. K.; Roberts, J.; Scheidt, K. A.; Nguyen, S. T.; Hupp, J. T. Metal–Organic Framework Materials as Catalysts. *Chem. Soc. Rev.* **2009**, *38* (5), 1450. https://doi.org/10.1039/b807080f.

(9) Shekhah, O.; Liu, J.; Fischer, R. A.; Wöll, C. MOF Thin Films: Existing and Future Applications. *Chem. Soc. Rev.* **2011**, *40* (2), 1081. https://doi.org/10.1039/c0cs00147c.

(10) Sun, C.-Y.; Qin, C.; Wang, X.-L.; Su, Z.-M. Metal-Organic Frameworks as Potential Drug Delivery Systems. *Expert Opin. Drug Deliv.* **2013**, *10* (1), 89–101. https://doi.org/10.1517/17425247.2013.741583.

(11) Li, W.-J.; Liu, J.; Sun, Z.-H.; Liu, T.-F.; Lü, J.; Gao, S.-Y.; He, C.; Cao, R.; Luo, J.-H. Integration of Metal-Organic Frameworks into an Electrochemical Dielectric Thin Film for Electronic Applications. *Nat. Commun.* **2016**, *7* (1). https://doi.org/10.1038/ncomms11830.

(12) Shen, F.; Lu, P.; O'Shea, S. J.; Lee, K. H.; Ng, T. Y. Thermal Effects on Coated Resonant Microcantilevers. *Sens. Actuators Phys.* **2001**, *95* (1), 17–23. https://doi.org/10.1016/S0924-4247(01)00715-4.

(13) Zhang, X.; Wang, W.; Hu, Z.; Wang, G.; Uvdal, K. Coordination Polymers for Energy Transfer: Preparations, Properties, Sensing Applications, and Perspectives. *Coord. Chem. Rev.* **2015**, *284*, 206–235. https://doi.org/10.1016/j.ccr.2014.10.006.

(14) Maza, W. A.; Haring, A. J.; Ahrenholtz, S. R.; Epley, C. C.; Lin, S. Y.; Morris, A. J. Ruthenium(II)-Polypyridyl Zirconium(IV) Metal–Organic Frameworks as a New Class of Sensitized Solar Cells. *Chem. Sci.* **2016**, *7* (1), 719–727. https://doi.org/10.1039/C5SC01565K.

(15) Dogru, M.; Bein, T. On the Road towards Electroactive Covalent Organic Frameworks. *Chem Commun* **2014**, *50* (42), 5531–5546. https://doi.org/10.1039/C3CC46767H.

(16) Zacher, D.; Baunemann, A.; Hermes, S.; Fischer, R. A. Deposition of Microcrystalline [Cu3(Btc)2] and [Zn2(Bdc)2(Dabco)] at Alumina and Silica Surfaces Modified with Patterned Self Assembled Organic Monolayers: Evidence of Surface Selective and Oriented Growth. *J. Mater. Chem.* **2007**, *17* (27), 2785. https://doi.org/10.1039/b703098c.

(17) Shekhah, O.; Wang, H.; Paradinas, M.; Ocal, C.; Schüpbach, B.; Terfort, A.; Zacher, D.; Fischer, R. A.; Wöll, C. Controlling Interpenetration in Metal–Organic Frameworks by Liquid-Phase Epitaxy. *Nat. Mater.* **2009**, *8* (6), 481–484. https://doi.org/10.1038/nmat2445.

(18) Hermes, S.; Schröder, F.; Chelmowski, R.; Wöll, C.; Fischer, R. A. Selective Nucleation and Growth of Metal−Organic Open Framework Thin Films on Patterned COOH/CF_3 -Terminated Self-Assembled Monolayers on Au(111). *J. Am. Chem. Soc.* **2005**, *127* (40), 13744–13745. https://doi.org/10.1021/ja053523l.

(19) Fischer, R. A.; Wöll, C. Layer-by-Layer Liquid-Phase Epitaxy of Crystalline Coordination Polymers at Surfaces. *Angew. Chem. Int. Ed.* **2009**, *48* (34), 6205–6208. https://doi.org/10.1002/anie.200901090.

(20) Zacher, D.; Shekhah, O.; Wöll, C.; Fischer, R. A. Thin Films of Metal–Organic Frameworks. *Chem. Soc. Rev.* **2009**, *38* (5), 1418. https://doi.org/10.1039/b805038b.

(21) Zou, X.; Zhu, G.; Hewitt, I. J.; Sun, F.; Qiu, S. Synthesis of a Metal–Organic Framework Film by Direct Conversion Technique for VOCs Sensing. *Dalton Trans.* **2009**, No. 16, 3009. https://doi.org/10.1039/b822248g.

(22) Campagnol, N.; Van Assche, T. R. C.; Li, M.; Stappers, L.; Dincă, M.; Denayer, J. F. M.; Binnemans, K.; De Vos, D. E.; Fransaer, J. On the Electrochemical

Deposition of Metal–Organic Frameworks. *J. Mater. Chem. A* **2016**, *4* (10), 3914–3925. https://doi.org/10.1039/C5TA10782B.

(23) Van de Voorde, B.; Ameloot, R.; Stassen, I.; Everaert, M.; De Vos, D.; Tan, J.-C. Mechanical Properties of Electrochemically Synthesised Metal–Organic Framework Thin Films. *J. Mater. Chem. C* **2013**, *1* (46), 7716. https://doi.org/10.1039/c3tc31039f.

Chapter 7

Anodic electrodeposition of several metal organic framework thin films on indium tin oxide glass

Abstract

An electrochemical method for the rapid synthesis of a series of metal-organic framework (MOF) thin films on indium tin oxide (ITO) glass is presented here. ITO was first electrodeposited with either copper or zinc microcrystalline films (Cu-ITO and Zn-ITO, respectively) from simple aqueous/ethanol salt solutions. These metallic deposits served as the metal cation source during their partial anodic dissolution and the initial nucleation sites during electrochemical MOF (EMOF) film growth. Four different EMOF films were prepared by this method. HKUST-1 and the 2-D cationic framework $[Cu(C_{10}H_8N_2)^{2+}]Br_2$ (CBBr) were each grown on Cu-ITO. $Zn_6(OH)_3(BTC)_3(H_20)_3 \bullet 7H_2O$ (Zn-BTC, BTC = benzene tricarboxylate) and the 2-D framework $[Zn(BPDC)(H_2O)] \bullet H_2O$ (Zn-BPDC, BPDC = 2,2'-bipyridine-5,5'-dicarboxylate) were each grown on Zn-ITO. Physical characterization was carried out using grazing incidence X-ray diffraction (GIXRD), scanning electron microscopy (SEM) and energy-dispersive X-ray spectroscopy (EDS). Our results show these films were well adhered, homogenous, self-closing and of relatively low surface roughness in each case. The ability to vary the dimensionality, metal node, linker and charge of the EMOF on a conductive transparent substrate opens up a wide range of possible compositions, properties and applications.

7.1 Introduction

Metal organic frameworks (MOFs) are an important class of high surface area nanoporous crystalline materials, self-assembled into 1D, 2D, or 3D extended structures composed of metal-based nodes connected covalently by organic ligands.[1,2] Because the choice of metal and organic constituents allows for a high degree of tailoring of the MOF nano-environment, MOFs show potential for a wide variety of applications: gas storage and purification,[3] pollutant sequestration,[4] catalysis,[5] chemical sensing,[6] and integration into microelectronic devices,[7–9] to name a few. The vast majority of MOFs are essentially electrical insulators due to poor overlap between pi orbitals in the organic ligands and the d-orbitals of the metallic nodes. Only a handful of truly conductive MOFs have been reported,[10] though there are many reports of induced or tunable conductivity based on guest inclusion,[11] as well as the use of MOFs as dielectric coatings.[12,13] A recent review highlights the potential for integrating MOFs with solid-state electronics (LEDs, photovoltaics, ion-conductors, electrochemical sensors, etc.).[14] A major requirement for these device applications is intimate mechanical and electrical contact of the grown MOF films with their conductive substrates.[7,15] To date, there is a large and growing library of MOFs synthesized as microcrystalline powders, but few of these have been synthesized as thin films and even fewer have been grown on conductive or transparent conductive substrates.

Several MOF film synthesis techniques have been described in the literature, ranging from the adhesion of pre-formed MOF crystals onto a substrate by methods such as drop casting or spin coating, to direct growth on a substrate from the requisite metal salt and organic ligand precursors.[5] Most direct growth approaches offer better

mechanical contact between film and substrate than can be achieved by simple adhesion of pre-formed crystallites. Direct growth approaches typically require initial functionalization of the substrate surface with an organic self-assembled monolayer (SAM) to help nucleate the MOF film. One interesting approach is the layer-by-layer (LbL) method, which consists of repeated sequential exposure of the SAM-functionalized substrate to separate metal salt and organic ligand solutions.[16] While the LbL method benefits from precise control of film thickness, it can be quite time-consuming (several days) and labor intensive (hundreds of repetitions) to achieve appreciable film thickness, even given computer automation of the process.[17,18] Additionally, most of the SAMs used in LbL and other direct growth routes form an additional electrically insulating layer between the MOF and substrate.[7]

Electrochemical deposition is an emerging method of MOF thin film synthesis that shows promise for achieving both mechanical and electrical contact between MOF and substrate.[19] This method is rapid (minutes to hours) compared to LbL and no SAM functionalization is required for film nucleation. Electrochemical synthesis of MOFs was first implemented at BASF as a salt-free synthesis route for producing bulk MOF powders.[20] Researchers found that the dissolution of a metallic electrode at mild anodic potential, while immersed in an electrolyte containing the requisite organic ligand, resulted in a complete MOF film that remained tightly adhered to the anode.[21] Following this discovery, others have investigated the synthesis of several MOF films on various conductive substrates, grown under anodic and cathodic biases.[19,22–24] Electrochemically deposited MOF (EMOF) films can be synthesized under anodic or cathodic bias, at the respective electrodes. In anodic deposition, the MOF film self-assembles at the anode surface, where the local metal ion concentration is rapidly increased relative to the bulk

electrolyte solution which contains the organic linker. Cathodic deposition schemes require both metal salt and organic linker be present in solution. An increase in the local hydroxide concentration near the cathode surface, caused by the electrochemical reduction of oxoanions (e.g. NO_3^-) or a pro-base (e.g. Et_3NH^+/Et_3N), initiates MOF growth by deprotonation of (primarily) carboxylic acid ligands.[24–26]

It has been shown that manipulation of film characteristics (crystallite size and morphology, film thickness and homogeneity of coverage) can be more readily achieved in anodic deposition schemes by altering various synthesis parameters (voltage and current density, deposition time, solvent composition and temperature, and the concentrations of organic linker and conduction salt).[19,22] Control over these film characteristics appear more difficult for cathodic deposition due to the limited voltage window required to avoid the formation and co-deposition of oxides, hydroxides and reduced metallic species randomly dispersed within the MOF film. In cathodic deposition, there is also the extra requirement of an appropriate pro-base and buffer system to deter precipitation of the MOF in the bulk solution, while inducing the proper pH for ligand deprotonation at the cathode surface.[19] The narrow requirements and instability of cathodic deposition solutions, compared to the reusable anodic solutions, make the latter a more attractive scheme for industrial scale-up.

Anodically synthesized MOF films have recently been investigated for sensing of nitro compound explosives,[6] glucose[27] and humidity,[28] and for their mechanical properties and adherence to solid metallic substrates.[19,22,29] Electrochemical MOF deposition on other conductive substrates, including indium tin oxide (ITO), fluorine tin oxide (FTO) and glassy carbon, have only thus far been achieved cathodically.[19] To the best of our knowledge, the work by Jiang and coworkers is the first attempt to anodically

grow a MOF film on the transparent conductive substrate ITO.[30] These researchers showed that the well-studied copper based HKUST-1 can be anodically electrodeposited on ITO that was previously electrodeposited with copper (Cu-ITO). The high porosity (> 2000 $m^2 \cdot g^{-1}$),[31] good moisture and thermal stability,[32] and guest-mediated tunable conductivity[11] of HKUST-1 make its thin film fabrication relevant to electronic device applications.

Here, it was confirmed by a modified scheme that HKUST-1 can be grown as a well adhered and self-closing MOF film on Cu-ITO. Also synthesized by this method were a cationic copper 4,4'-bipyridine based MOF grown on Cu-ITO, as well as two zinc carboxylate based MOFs grown on zinc-deposited ITO (Zn-ITO). Characterization of these films revealed that MOF growth initiates on the surface of the metallic deposits. The resulting films appear self-sealing, relatively smooth and well adhered to ITO *via* the partially anodized metal deposits. Synthesis of MOF films on ITO by this method opens up new possibilities for the facile, inexpensive and potentially large-scale production of various MOF films on transparent conductive substrates. The metallic interface between MOF and substrate may also prove advantageous for electronics applications.

7.2 Experimental

Reagents: ITO coated glass (30-60 Ω/sq), zinc nitrate hexahydrate and copper (II) nitrate hemi(pentahydrate) were obtained from Sigma Aldrich. The 0.1 mm copper foil and 0.25 mm Zn foil were obtained from Alfa Aesar. Potassium bromide (KBr), benzene tricarboxylic acid (BTC), 4,4'-bipyridine, 2,2'-bipyridine-5,5'-dicarboxylic acid (BPDC) and tetrabutylammonium tetrafluoroborate ($TBABF_4$) were purchased from Spectrum

labs. Analytical grade dimethylformamide (DMF) and 200 proof ethanol were purchased from Acros Organics. Milli-Q water (18.2 Ω·cm) was used throughout all experiments.

Electrodeposition experiments were conducted on an in-house constructed two-electrode system, consisting of a polypropylene or quartz cuvette (1 cm × 1 cm × 4 cm height) and Keithley 6487 power source. Aqueous/ethanolic solutions were purged for 60 min in high-purity nitrogen, followed by 5 min in argon to remove oxygen prior to all synthesis steps. DMF was used as-received without drying or further purification. Copper and zinc metal foils were cleaned with acetone and then dipped briefly in 10v% nitric acid, followed by water rinse to remove native oxides. ITO chips (approximately 0.5 cm × 2.0 cm) were cleaned by sequential sonication in acetone, ethanol and finally water (15 min each). Both the metal depositing and MOF growth steps were carried out in approximately 2 mL of the respective solutions, with the working and counter electrodes held 1 cm apart. Both metal and subsequent MOF films grown on ITO were thoroughly rinsed in water and then ethanol to remove unreacted salts and organic ligands after deposition.

7.2.1 Synthesis of Cu-ITO

Cu-ITO electrodes were synthesized in a 3:1 v/v solution of ethanol and water containing 40 mM copper(II) nitrate hemi(pentahydrate). A pure copper foil counter electrode was used and the solution was heated to 55 ˚C prior to immersing the electrodes. A constant DC voltage of -1.0 V was applied for 90 sec to achieve a uniform single layer of evenly dispersed copper octahedra covering the ITO substrate.

7.2.2 Synthesis of Zn-ITO

Zn-ITO electrodes were synthesized in a 3:1 v/v solution of ethanol and water containing 10 mM zinc (II) nitrate hexahydrate. A pure zinc foil counter electrode was used and the solution was heated to 25 ˚C prior to immersing the electrodes. A constant DC voltage of -1.0 V was applied for 60 sec to achieve a dense and uniform layer of zinc plates covering the ITO substrate.

7.2.3 Synthesis of HKUST-1 on Cu-ITO

HKUST-1 film grown on Cu-ITO was synthesized in a 3:1 v/v solution of ethanol and water consisting of 40 mM BTC and 25 mM $TBABF_4$. A pure copper foil counter electrode was used and the solution was heated to 55 ˚C prior to immersing the electrodes. A constant DC voltage of 0.75 V was applied for 2 to 50 min, depending on the desired MOF coverage.

7.2.4 Synthesis of CBBr Cu-ITO

CBBr film grown on Cu-ITO was synthesized in a 3:1 v/v solution of ethanol and water consisting of 40 mM bipy, 50 mM $TBABF_4$ and 5 mM of KBr. In each synthesis, a pure copper foil counter electrode was used. The solution was heated to 45 ˚C prior to immersing the electrodes. A constant DC voltage of 2.25 V was applied for 5 to 50 min, depending on the desired MOF coverage.

7.2.5 Synthesis of Zn-BPDC on Zn-ITO

Zn-BPDC film grown on Zn-ITO was synthesized in a 5:1 v/v solution of DMF and water consisting of 4 mM BPDC and 2.5 mM $TBABF_4$. A pure zinc foil counter

electrode was used. The solution was heated to 80 ˚C prior to immersing the electrodes. A constant DC voltage of 0.75 V was applied for 10 to 30 min, depending on the desired MOF coverage.

7.2.6 Synthesis of Zn-BTC on Zn-ITO

Zn-BTC, or $Zn_6(OH)_3(BTC)_3(H_20)_3 \bullet 7H_2O$, film was grown on Zn-ITO in a 3:1 v/v solution of ethanol and water consisting of 40 mM BTC and 25 mM $TBABF_4$. A pure zinc foil counter electrode was used. The solution was heated to 55 ˚C prior to immersing the electrodes. A constant DC voltage of 0.75 V was applied for 5 to 30 min, depending on the desired MOF coverage.

7.2.7 Characterization

Grazing incident angle X-ray diffraction (GIXRD) measurements were performed on a Rigaku SmartLab diffractometer with Cu-Kα (1.54056 Å) radiation operated at 44 mA and 40 kV. Samples were analyzed using parallel beam optics with the incident angle held at 0.6° or 0.8° omega, at a scan rate of 0.5°/min (step size of 0.01°). Scanning electron microscopy (SEM) images were taken on a FEI Quanta 3D dual beam microscope operated at 5.00 kV and 6.66 pA. All films were imaged without Au coating or additional preparation. Integrated image scans were used when charging of the MOF layer was apparent. High angle annular dark field scanning transmission electron microscopy (HAADF-STEM) imaging was performed on an FEI Titan TEM operated at 300 kV. The STEM probe had a convergence semiangle, α, of 10 mrad and a beam current of 35 pA (300 kV). HAADF-STEM images were acquired using a Fischione annular dark-field (ADF) detector with an inner semiangle, β, of 45 mrad. EDS data was

simultaneously collected along with HAADF-STEM data on four silicon drift detectors with a solid angle of 0.7 steradians (SuperX) and analyzed using Bruker's Espirit software. Samples were prepared by mechanically removing the MOF film from its ITO substrate with a razor blade and then briefly sonicated in ethanol before drop casting on a lacey carbon coated copper TEM grid.

7.3 Results and Discussion

Four EMOF films grown on either Cu-ITO or Zn-ITO are discussed below. Grazing incidence X-ray diffraction was used to phase identify each film by comparison to previously published powder diffraction profiles, or those calculated from single crystal data. The progress and characteristics of film growth were monitored using scanning electron microscopy (SEM). In each case, the synthesis parameters (voltage and duration of bias, solution temperature and the linker and conduction salt concentrations) were carefully optimized to produce MOF films with uniform coverage and the lowest possible surface roughness.

Figure 7.1 illustrates the general EMOF synthesis process, specifically for HKUST-1 on Cu-ITO. First, copper was electroplated onto clean ITO from a simple copper nitrate solution (3:1, ethanol:water) to give a moderately dense single layer of monodisperse copper octahedra. The size and coverage density of deposited Cu microcrystals could be tuned by changing the voltage, time of applied bias and/or concentration of copper nitrate. It was found, however, that 90 sec of applied cathodic bias (-1.0 V) in a 40 mM Cu^{2+} solution was optimal to avoid vertical stacking of Cu microcrystals. These conditions gave a uniform surface dispersion of roughly 2 micron

sized copper octahedra separated by periodic gaps of a few microns (Figure 7.1a). The Cu-ITO was then cleaned and placed in a 55 ˚C solution (3:1, ethanol:water) containing benzene tricarboxylic acid (BTC) linker and tetrabutylammonium tetrafluoroborate ($TBABF_4$) as a conduction salt. SEM imaging of HKUST-1 growth after 2 min at 0.75 V revealed the seeding of MOF crystals on the facets of copper octahedra (Figure 7.1b,c). After 50 min, isolated copper octahedra were completely covered in HKUST-1 microcrystals (Figure 7.1d). SEM imaging of HKUST-1 growth after 50 min indicates a continuous layer of HKUST-1 on Cu-ITO (Figure 7.1e,f) where Cu had been deposited under optimal conditions.

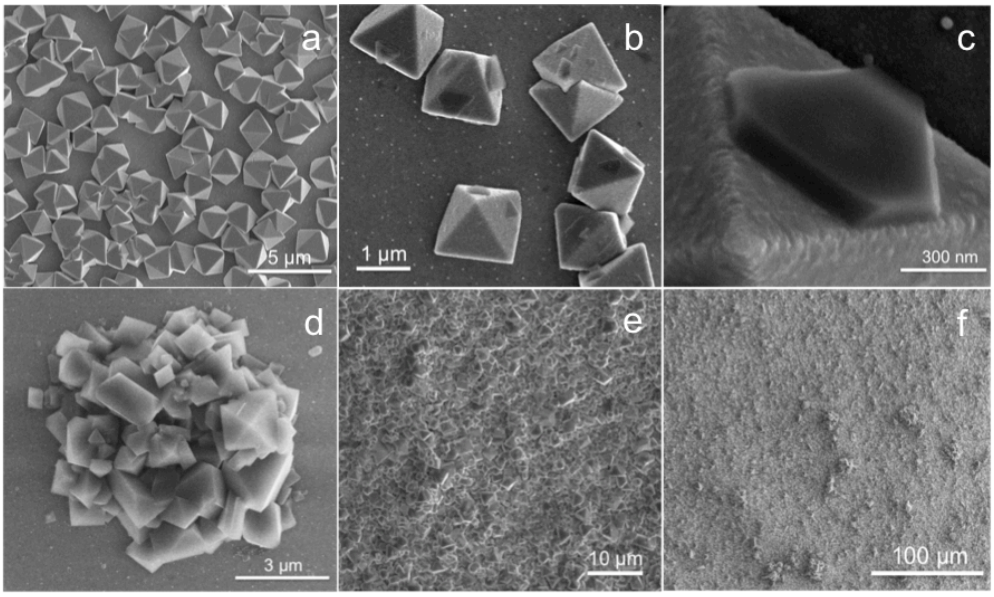

Figure 7.1 SEMs of HKUST-1 grown on Cu-ITO at 0.75 V: a) Copper octahedra grown by electrodeposition on ITO (-1.0 V for 90 sec); b-c) The beginning of HKUST-1 growth on Cu octahedra after 2 min; d) An isolated copper octahedron covered by MOF crystals after 50 min of growth; e) Typical film coverage after 50 min of growth; f) A 0.1 mm^2 section of film illustrating the relative smoothness and continuity of the HKUST-1 film after 50 min of growth.

The phase purity of HKUST-1 grown on Cu-ITO was confirmed by GIXRD (Figure 7.2) High angle annular dark field scanning transmission electron microscopy (HAADF-STEM) and elemental dispersive X-ray spectroscopy (EDS), performed on films mechanically dislodged from ITO, revealed that the copper octahedra do not completely dissolve by the time a continuous HKUST-1 film has grown. Figure 7.3 gives the imaging and spectroscopy data for material removed from the 50 min film synthesis of HKUST-1 on Cu-ITO, showing a partially eroded copper microcrystal imbedded in an enveloping HKUST-1 crystal. In considering potential electronic applications, the remaining copper may be advantageous as a metallic conduit between the MOF and ITO in the absence of direct MOF-ITO contact. Additionally, the periodic gaps between copper deposits for Cu-ITO grown in this manner may be advantageous in applications where photo-stimulation of the anode film is desired.

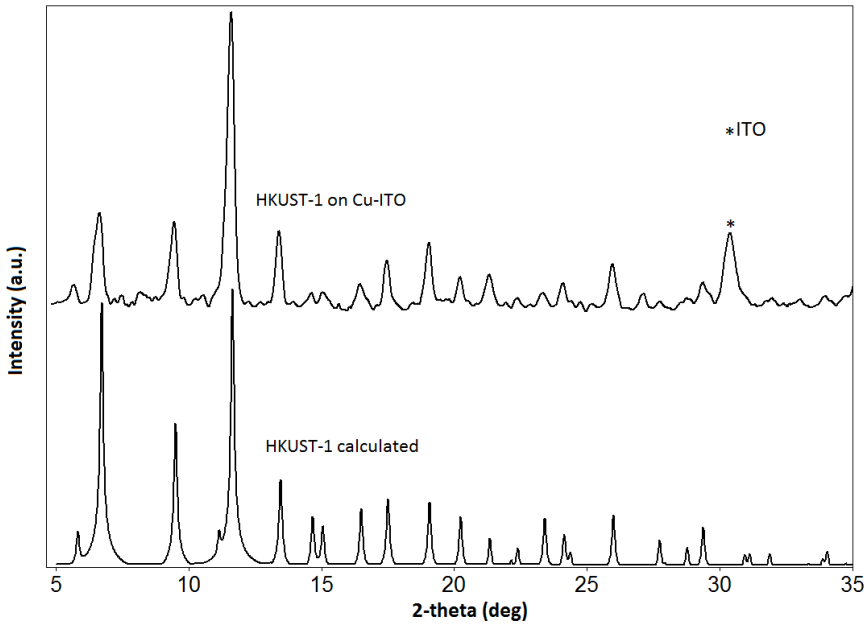

Figure 7.2 GIXRD of HKUST-1 electrochemically deposited on Cu-ITO for 50 min at 0.75 V (top profile), compared with the calculated powder pattern for HKUST-1 (bottom profile).

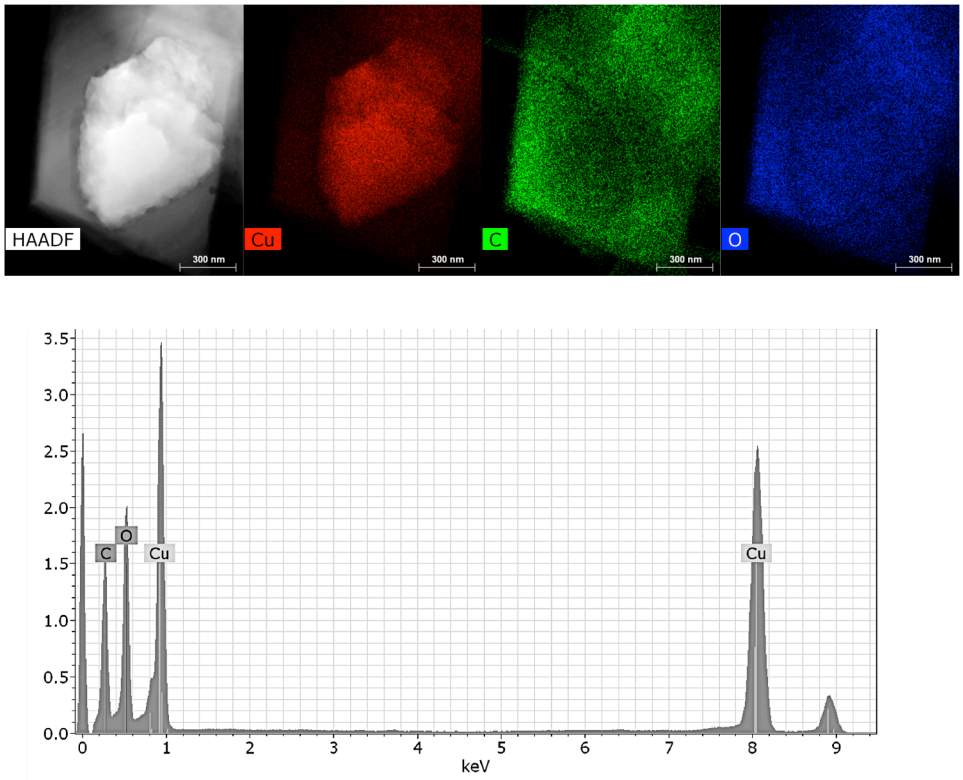

Figure 7.3 Top: High angle annular dark field image and respective elemental maps for Cu, C and O of a partially decomposed copper octahedron (bright contrast in HAADF image) embedded a single crystal of HKUST-1; Bottom: EDS spectrum of the above sample. The presence of copper in the spectrum is due to copper in both the sample and from the TEM grid.

A complete mechanistic study of the growth of HKUST-1 on Cu-ITO is beyond the scope of this multiple film study. Fransaer *et al*., however, have made a reasonable attempt to explain the mechanism of HKUST-1 growth and adhesion on solid copper substrates grown by anodic deposition.[19] The authors categorized the MOF growth in four stages: (1) initial nucleation at the anode surface; (2) growth of MOF islands; (3) intergrowth of these islands and progressive nucleation to create a continuous coverage of the substrate; (4) film exfoliation after prolonged dissolution of the underlying metal substrate. They found that MOF growth proceeds laterally to fill the void spaces between

MOF islands before a secondary MOF layer begins to stack upon the first. It was found that similar film growth characteristics for HKUST-1 grown on Cu-ITO, even though the pre-deposited copper on ITO does not form a continuous layer. Rather, the copper film consists of single or clustered octahedra with periodic gaps of up to several microns (Figure 7.1a). In the case of solid copper substrates, this self-closing growth can be explained by the higher resistivity of the MOF film in the electric field: the MOF film likely inhibits the rate of dissolution of the copper substrate beneath it compared to areas of bare copper. Given our results, it may be speculated that the copper ions also continue to percolate out from between individual MOF crystals, or through the MOF nano-channels [channel size for HKUST-1 is known to be 0.9 × 0.9 nm[33] and the diameter of the copper (II) ion is 0.456 nm[34]].

In addition to HKUST-1 on Cu-ITO, the growth of $[Cu(C_{10}H_8N_2)^{2+}]Br_2$, a 2-D cationic layered MOF composed of copper 4,4'-bipyridine polymers charge-balanced by bromide, referred to here as CBBr, was also investigated. GIXRD confirmed the phase identity of this MOF (Figure 7.4). CBBr on Cu-ITO had similar growth characteristics to those observed for HKUST-1, with small MOF seed crystals nucleating on and then filling in the gaps between copper octahedra. A higher voltage and longer time of applied anodic bias were needed, however, to observe CBBr formation on copper octahedra. Figure 7.5 shows CBBr grown on Cu-ITO for applied bias times between 20 and 50 min at 2.25 V. The higher voltage necessary to induce growth of CBBr compared to HKUST-1 is likely due to the neutral charge of the 4,4'-bipyridine ligand and possibly the need for higher copper ion concentration to initiate MOF nucleation at the anode. At anodic potential lower than 2.25 V, growth was relatively sparse even after 50 min and CBBr formed instead in the bulk solution. At 0.75 V, the Cu octahedra eventually eroded off

the ITO before any MOF deposits formed, indicating that the critical concentration of Cu^{2+} ions necessary to initiate MOF nucleation was not achieved at the anode surface. At potentials higher than 2.25 V, film growth was faster but as in the low voltage scenario, a significant amount of CBBr also formed in the bulk solution. Additionally, increasing the concentration of bromide ion from 5 to 15 mM dramatically hastens the growth time of a self-closing CBBr film from 50 min to 10 min at 2.25 V. Increasing the concentration of the counter ion in this way, however, also led to a rougher topology, with increased appearance of vertical stacks of MOF as well as larger MOF crystals and less degradation of the Cu octahedra (Figure 7.6). This result indicates that the counter ion concentration plays a critical role in the nucleation and growth processes of this particular cationic framework.

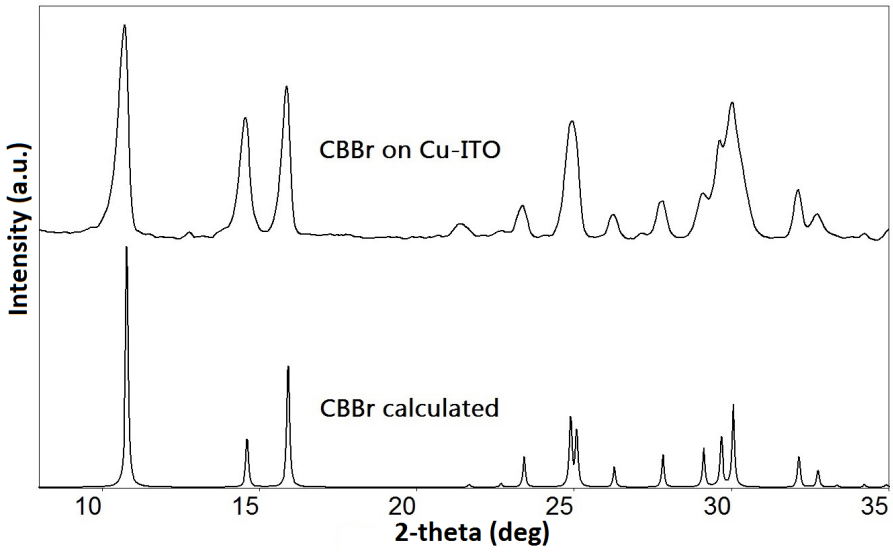

Figure 7.4 GIXRD of copper bipyridine bromide (CBBr) electrochemically deposited on Cu-ITO for 50 min at 2.25 V (top profile), compared to the calculated powder pattern from single crystal data (bottom profile).

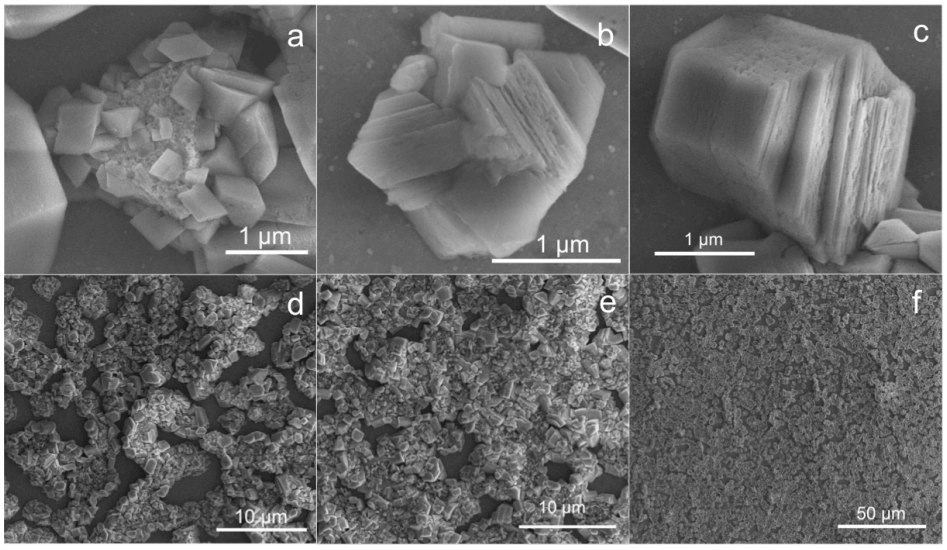

Figure 7.5 SEMs of CBBr grown on Cu-ITO at 2.25 V: a) MOF crystals growing on a partially anodized Cu octahedron after 5 min; b) Complete MOF coverage of an isolated Cu octahedron after 20 min; c) A single crystal of CBBr grown adjacent to a MOF-covered isolated copper octahedron; d) MOF film coverage at 20 min; e-f) MOF film coverage at 50 min.

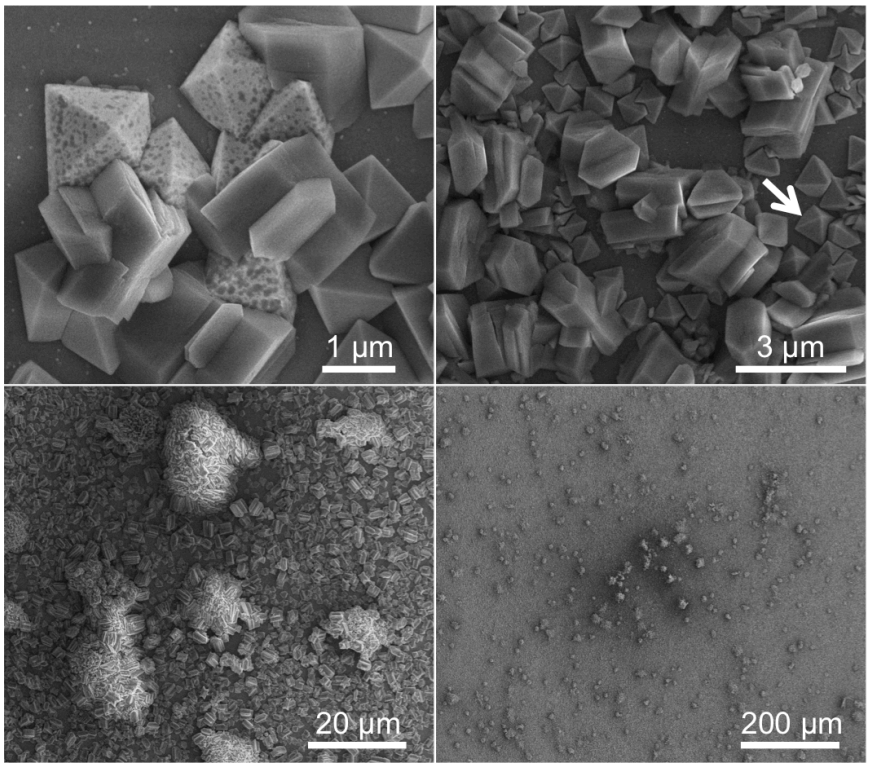

Figure 7.6. CBBr grown on Cu-ITO after 10 min with 15 mM Br^- counter ion present in solution. White arrow indicates one example of a Cu octahedron.

The HAADF-STEM and EDS (Figure 7.7) show the same structural character of remaining Cu crystals embedded in surrounding CBBr MOF, as occurred with HKUST-1 grown on Cu-ITO. Interestingly, the EDS spectrum shows that no fluorine is present in the structure, even though tetrafluoroborate was present in far greater concentration than bromide during synthesis. Copper bipyridine tetrafluoroborate is a known structure[35,36] and PXRD peaks indicative of this phase were not present. A small amount of chlorine was also observed by EDS, likely a contaminant present during synthesis. Chlorine can be substituted for bromine to give a homologous structure.[37]

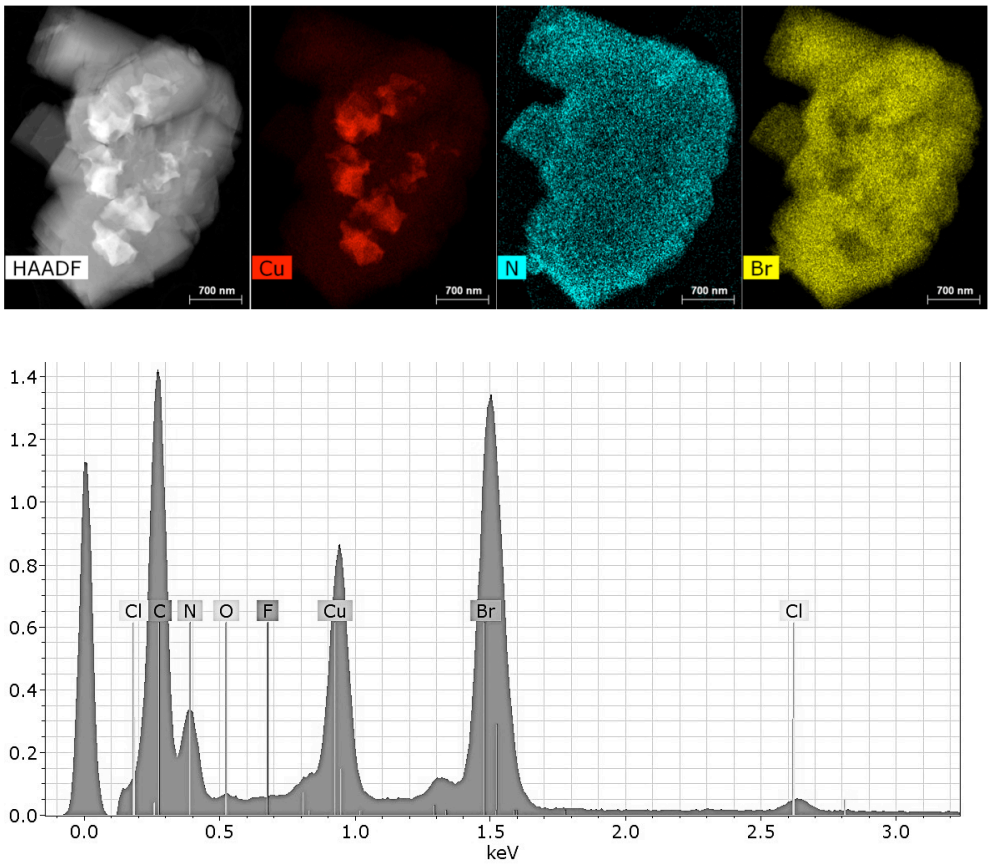

Figure 7.7 Top: HAADF-STEM and corresponding elemental maps for Cu, N and Br of a partially decomposed copper octahedron embedded a cluster of CBBr crystals; Bottom: EDS spectrum of the above sample.

Two initial examples of Zn-based EMOF films were also grown on Zn-ITO. The electrodeposition of zinc on ITO resulted in a denser layer of metal deposits than for Cu-ITO under optimal conditions. 60 sec at a cathodic bias of 1.0 V in a room temperature solution (3:1, ethanol:water) containing 10 mM Zn^{2+} gave a uniform layer of tightly packed zinc plates (Figure 7.8a). Zn-ITO was introduced into a solution containing 2,2'-bipyridine-5,5'-dicarboxylic acid (BPDC) to form a thin film of the 2-D MOF $[Zn(BPDC)(H_2O)]\bullet H_2O$ (denoted as Zn-BPDC), which was identified by GIXRD (Figure 7.9). This MOF was grown in a solution of DMF and water (5:1), as the linker is

sparingly soluble in both ethanol and water. Additional water, however, was necessary for MOF growth since it's part of the MOF structure and likely because DMF is not an adequate ion conductor. A temperature of 80 ˚C was also necessary to fully dissolve BPDC in this solution. SEM imaging (Figure 7.8b-d) shows the plate-like morphology of Zn-BPDC covering the zinc plates after 10 and 30 min of growth. HAADF-STEM and EDS mapping of this film revealed similar growth characteristics as those seen for HKUST-1 and CBBr grown on Cu-ITO, with remaining Zn metal embedded within the MOF (Figure 7.10).

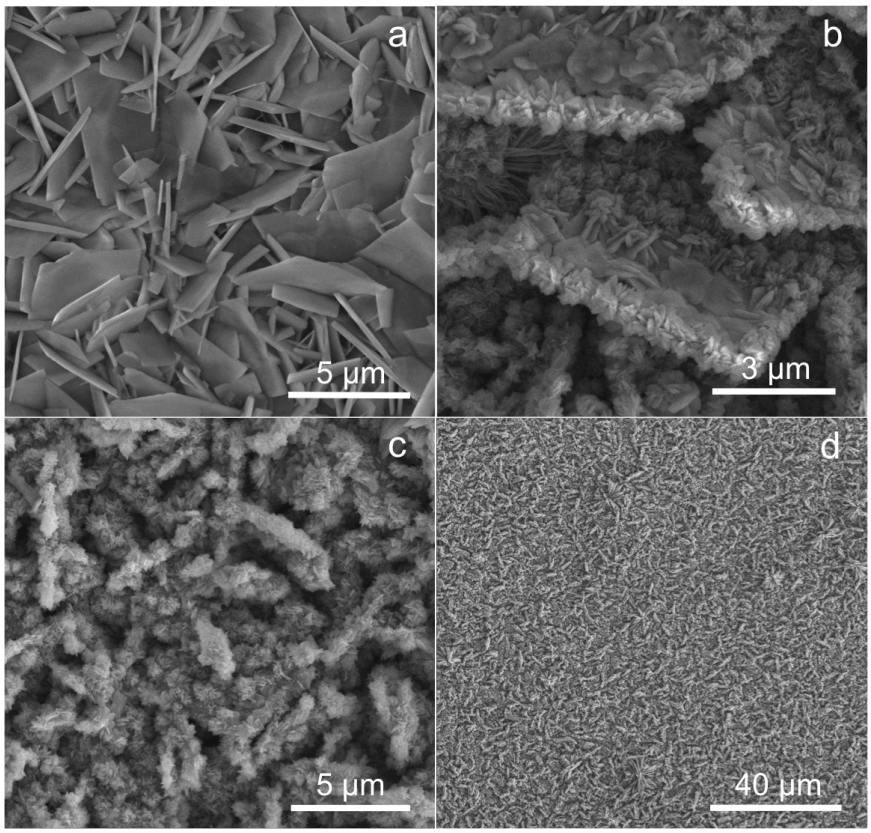

Figure 7.8 SEMs of Zn-BPDC grown on Zn-ITO at 0.75 V: a) Zn plates deposited on ITO (-1.0 V for 60 sec); b) MOF growth after 10 min; c-d) MOF growth after 30 min.

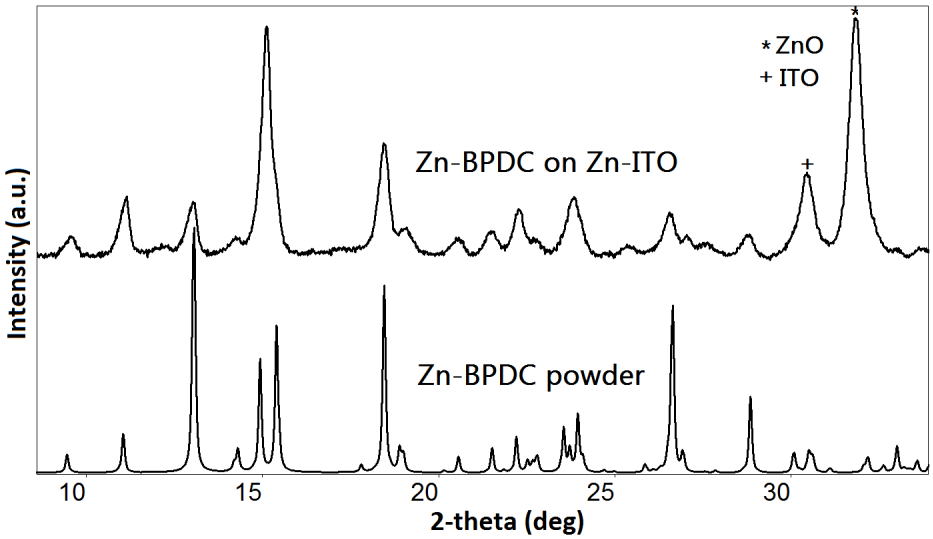

Figure 7.9 GIXRD of Zn-BPDC electrochemically deposited on Zn-ITO for 30 min at 0.75 V (top profile), compared to the experimental powder profile (bottom).

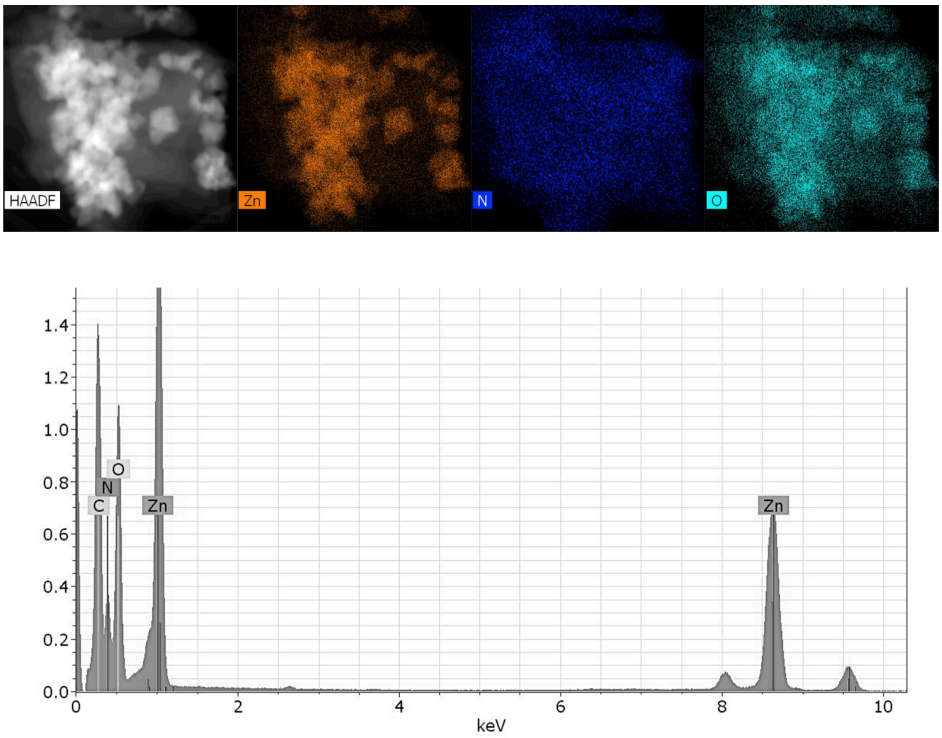

Figure 7.10 Top: HAADF-STEM and corresponding elemental maps for Zn, N and O of partially decomposed zinc plates embedded in a cluster of Zn-BPDC crystals; Bottom: EDS spectrum for Zn-BPDC grown on Zn-ITO.

A second Zn-based EMOF film comprised of $Zn_6(OH)_3(BTC)_3(H_20)_3 \bullet 7H_2O$ was also anodically grown on Zn-ITO and identified by GIXRD (Figure 7.11).[38] This MOF, referred to here as Zn-BTC, grew well under the same synthesis conditions used for HKUST-1 on Cu-ITO. Figure 7.12 shows the needle morphology of the MOF film, which grew rapidly and completely covered the zinc plates of Zn-ITO within 30 min. Interestingly, Zn-BTC grew in regions of bare ITO, several millimeters away from any previously deposited zinc (Figure 7.12d), a phenomena not observed with the other EMOFs discussed above. This observation may be due to the lower zinc ion concentration necessary to initiate the MOF growth.

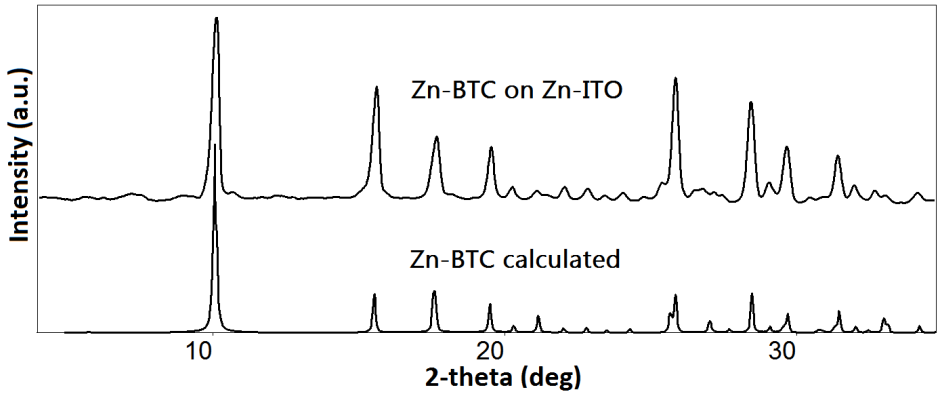

Figure 7.11 GIXRD of Zn-BTC electrochemically deposited on Zn-ITO for 30 min at 0.75 V (top profile), compared to the calculated profile from single crystal data (bottom).

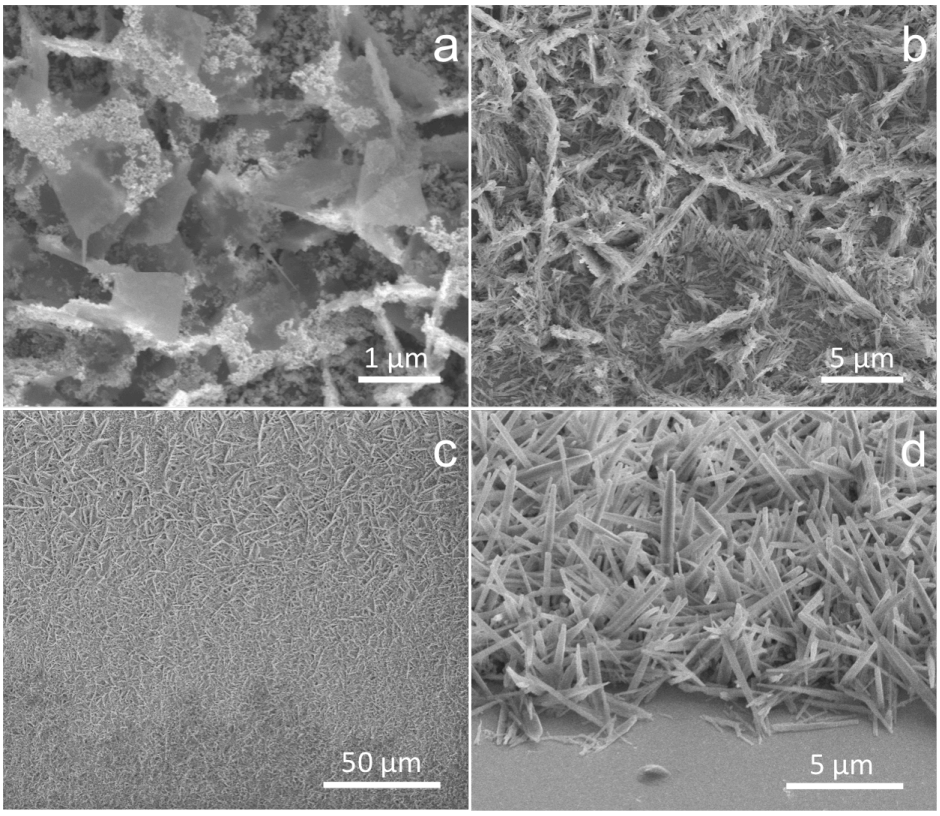

Figure 7.12 SEMs of Zn-BTC grown on Zn-ITO at 0.75 V: a) Zn-BTC grown on Zn-ITO after 5 min; b-c) Growth of Zn-BTC on Zn-ITO after 30 min; d) Growth ofZn-BTC on a region of bare ITO.

All four of the MOF films studied here exhibit hole-closing growth before the metal previously deposited on ITO is entirely consumed. It may be advantageous to have some metal remaining as a mechanical and electrical interface between the MOF layer and ITO. Because the growing MOF crystals surround the dissolving metal nanocrystals, the amount of underlying metal present in the final MOF-M-ITO (M = Cu or Zn) should be controllable both by the initial amount of metal deposited and the extent of consumption of these deposits during MOF growth.

7.4 Conclusions

Several examples of MOF film growth by anodic electrodeposition on the transparent conductive substrate ITO, previously deposited with metallic microcrystalline films, were successful. It may be anticipated that this synthetic approach be of broader interest toward the integration of MOFs into electronic devices. The simplicity of the chemistry involved in anodic (compared to cathodic) EMOF film growth schemes, as well as the homogeneity and self-sealing nature of these films, and residual metal-ITO-MOF interface remaining after film growth, are attributes well suited for electronics applications where transparent conductive substrates such as ITO are required or advantageous. Several factors could be part of a follow-up study, including the possible existence and degree of oxide interface between the MOF, metal deposits and ITO after film growth. Efforts are currently underway to determine the degree of electrical contact between MOF and ITO, as mediated through the residual metallic deposits after MOF film growth. These characterization experiments have thus far proven to be extremely challenging when working with MOFs that are inherently insulating. The growth of more conductive EMOF films, or intercalation of guest species which might increase electronic conductivity, are possible approaches to consider when attempting to perform characterization of electrical contact between the MOF and substrate.

7.5 References

(1) Chui, S. S. A Chemically Functionalizable Nanoporous Material [Cu3(TMA)2(H2O)3]N. *Science* 1999, *283* (5405), 1148–1150. https://doi.org/10.1126/science.283.5405.1148.

(2) Stock, N.; Biswas, S. Synthesis of Metal-Organic Frameworks (MOFs): Routes to Various MOF Topologies, Morphologies, and Composites. *Chem. Rev.* 2012, *112* (2), 933–969. https://doi.org/10.1021/cr200304e.

(3) Li, J.-R.; Sculley, J.; Zhou, H.-C. Metal–Organic Frameworks for Separations. *Chem. Rev.* 2012, *112* (2), 869–932. https://doi.org/10.1021/cr200190s.

(4) Colinas, I. R.; Silva, R. C.; Oliver, S. R. J. Reversible, Selective Trapping of Perchlorate from Water in Record Capacity by a Cationic Metal–Organic Framework. *Environ. Sci. Technol.* 2016, *50* (4), 1949–1954. https://doi.org/10.1021/acs.est.5b03455.

(5) Bétard, A.; Fischer, R. A. Metal–Organic Framework Thin Films: From Fundamentals to Applications. *Chem. Rev.* 2012, *112* (2), 1055–1083. https://doi.org/10.1021/cr200167v.

(6) Campagnol, N.; Souza, E. R.; De Vos, D. E.; Binnemans, K.; Fransaer, J. Luminescent Terbium-Containing Metal–Organic Framework Films: New Approaches for the Electrochemical Synthesis and Application as Detectors for Explosives. *Chem Commun* 2014, *50* (83), 12545–12547. https://doi.org/10.1039/C4CC05742B.

(7) Stavila, V.; Talin, A. A.; Allendorf, M. D. MOF-Based Electronic and Opto-Electronic Devices. *Chem Soc Rev* 2014, *43* (16), 5994–6010. https://doi.org/10.1039/C4CS00096J.

(8) Martinez Joaristi, A.; Juan-Alcañiz, J.; Serra-Crespo, P.; Kapteijn, F.; Gascon, J. Electrochemical Synthesis of Some Archetypical Zn 2+ , Cu 2+ , and Al 3+ Metal Organic Frameworks. *Cryst. Growth Des.* 2012, *12* (7), 3489–3498. https://doi.org/10.1021/cg300552w.

(9) Buchan, I.; Ryder, M. R.; Tan, J.-C. Micromechanical Behavior of Polycrystalline Metal–Organic Framework Thin Films Synthesized by Electrochemical Reaction. *Cryst. Growth Des.* 2015, *15* (4), 1991–1999. https://doi.org/10.1021/acs.cgd.5b00140.

(10) Sheberla, D.; Sun, L.; Blood-Forsythe, M. A.; Er, S.; Wade, C. R.; Brozek, C. K.; Aspuru-Guzik, A.; Dincă, M. High Electrical Conductivity in Ni_3 (2,3,6,7,10,11-Hexaiminotriphenylene) $_2$, a Semiconducting Metal–Organic Graphene

Analogue. *J. Am. Chem. Soc.* 2014, *136* (25), 8859–8862. https://doi.org/10.1021/ja502765n.

(11) Talin, A. A.; Centrone, A.; Ford, A. C.; Foster, M. E.; Stavila, V.; Haney, P.; Kinney, R. A.; Szalai, V.; El Gabaly, F.; Yoon, H. P.; et al. Tunable Electrical Conductivity in Metal-Organic Framework Thin-Film Devices. *Science* 2014, *343* (6166), 66–69. https://doi.org/10.1126/science.1246738.

(12) Usman, M.; Mendiratta, S.; Lu, K.-L. Metal-Organic Frameworks: New Interlayer Dielectric Materials. *ChemElectroChem* 2015, *2* (6), 786–788. https://doi.org/10.1002/celc.201402456.

(13) Li, W.-J.; Liu, J.; Sun, Z.-H.; Liu, T.-F.; Lü, J.; Gao, S.-Y.; He, C.; Cao, R.; Luo, J.-H. Integration of Metal-Organic Frameworks into an Electrochemical Dielectric Thin Film for Electronic Applications. *Nat. Commun.* 2016, *7* (1). https://doi.org/10.1038/ncomms11830.

(14) Stassen, I.; Burtch, N.; Talin, A.; Falcaro, P.; Allendorf, M.; Ameloot, R. An Updated Roadmap for the Integration of Metal–Organic Frameworks with Electronic Devices and Chemical Sensors. *Chem. Soc. Rev.* 2017, *46* (11), 3185–3241. https://doi.org/10.1039/C7CS00122C.

(15) Kreno, L. E.; Leong, K.; Farha, O. K.; Allendorf, M.; Van Duyne, R. P.; Hupp, J. T. Metal–Organic Framework Materials as Chemical Sensors. *Chem. Rev.* 2012, *112* (2), 1105–1125. https://doi.org/10.1021/cr200324t.

(16) Zhuang, J.-L.; Terfort, A.; Wöll, C. Formation of Oriented and Patterned Films of Metal–Organic Frameworks by Liquid Phase Epitaxy: A Review. *Coord. Chem. Rev.* 2016, *307*, 391–424. https://doi.org/10.1016/j.ccr.2015.09.013.

(17) Gu, Z.-G.; Pfriem, A.; Hamsch, S.; Breitwieser, H.; Wohlgemuth, J.; Heinke, L.; Gliemann, H.; Wöll, C. Transparent Films of Metal-Organic Frameworks for Optical Applications. *Microporous Mesoporous Mater.* 2015, *211*, 82–87. https://doi.org/10.1016/j.micromeso.2015.02.048.

(18) Arslan, H. K.; Shekhah, O.; Wohlgemuth, J.; Franzreb, M.; Fischer, R. A.; Wöll, C. High-Throughput Fabrication of Uniform and Homogenous MOF Coatings. *Adv. Funct. Mater.* 2011, *21* (22), 4228–4231. https://doi.org/10.1002/adfm.201101592.

(19) Campagnol, N.; Van Assche, T. R. C.; Li, M.; Stappers, L.; Dincă, M.; Denayer, J. F. M.; Binnemans, K.; De Vos, D. E.; Fransaer, J. On the Electrochemical Deposition of Metal–Organic Frameworks. *J Mater Chem A* 2016, *4* (10), 3914–3925. https://doi.org/10.1039/C5TA10782B.

(20) MÜLLER, U. (BASF AG). A METHOD FOR ELECTROCHEMICAL PRODUCTION OF A CRYSTALLINE POROUS METAL ORGANIC SKELETON MATERIAL. WO/2005/049892, February 6, 2005.

(21) Mueller, U.; Schubert, M.; Teich, F.; Puetter, H.; Schierle-Arndt, K.; Pastré, J. Metal–Organic Frameworks—Prospective Industrial Applications. *J Mater Chem* 2006, *16* (7), 626–636. https://doi.org/10.1039/B511962F.

(22) Li, W.-J.; Tu, M.; Cao, R.; Fischer, R. A. Metal–Organic Framework Thin Films: Electrochemical Fabrication Techniques and Corresponding Applications & Perspectives. *J Mater Chem A* 2016, *4* (32), 12356–12369. https://doi.org/10.1039/C6TA02118B.

(23) Ameloot, R.; Stappers, L.; Fransaer, J.; Alaerts, L.; Sels, B. F.; De Vos, D. E. Patterned Growth of Metal-Organic Framework Coatings by Electrochemical Synthesis. *Chem. Mater.* 2009, *21* (13), 2580–2582. https://doi.org/10.1021/cm900069f.

(24) Li, M.; Dincă, M. Reductive Electrosynthesis of Crystalline Metal–Organic Frameworks. *J. Am. Chem. Soc.* 2011, *133* (33), 12926–12929. https://doi.org/10.1021/ja2041546.

(25) Liu, H.; Wang, H.; Chu, T.; Yu, M.; Yang, Y. An Electrodeposited Lanthanide MOF Thin Film as a Luminescent Sensor for Carbonate Detection in Aqueous Solution. *J Mater Chem C* 2014, *2* (41), 8683–8690. https://doi.org/10.1039/C4TC01551G.

(26) Li, M.; Dincă, M. On the Mechanism of MOF-5 Formation under Cathodic Bias. *Chem. Mater.* 2015, *27* (9), 3203–3206. https://doi.org/10.1021/acs.chemmater.5b00899.

(27) Cheng, K.-Y.; Wang, J.-C.; Lin, C.-Y.; Lin, W.-R.; Chen, Y.-A.; Tsai, F.-J.; Chuang, Y.-C.; Lin, G.-Y.; Ni, C.-W.; Zeng, Y.-T.; et al. Electrochemical Synthesis, Characterization of Ir–Zn Containing Coordination Polymer, and Application in Oxygen and Glucose Sensing. *Dalton Trans.* 2014, *43* (17), 6536. https://doi.org/10.1039/c3dt53504e.

(28) Bradshaw, D.; Garai, A.; Huo, J. Metal–Organic Framework Growth at Functional Interfaces: Thin Films and Composites for Diverse Applications. *Chem Soc Rev* 2012, *41* (6), 2344–2381. https://doi.org/10.1039/C1CS15276A.

(29) Van de Voorde, B.; Ameloot, R.; Stassen, I.; Everaert, M.; De Vos, D.; Tan, J.-C. Mechanical Properties of Electrochemically Synthesised Metal–Organic Framework Thin Films. *J. Mater. Chem. C* 2013, *1* (46), 7716. https://doi.org/10.1039/c3tc31039f.

(30) Jiang, L.-L.; Zeng, X.; Li, M.; Wang, M.-Q.; Su, T.-Y.; Tian, X.-C.; Tang, J. Rapid Electrochemical Synthesis of HKUST-1 on Indium Tin Oxide. *RSC Adv* 2017, *7* (15), 9316–9320. https://doi.org/10.1039/C6RA26646K.

(31) Wong-Foy, A. G.; Matzger, A. J.; Yaghi, O. M. Exceptional H $_2$ Saturation Uptake in Microporous Metal–Organic Frameworks. *J. Am. Chem. Soc.* 2006, *128* (11), 3494–3495. https://doi.org/10.1021/ja058213h.

(32) Lee, Y.-R.; Kim, J.; Ahn, W.-S. Synthesis of Metal-Organic Frameworks: A Mini Review. *Korean J. Chem. Eng.* 2013, *30* (9), 1667–1680. https://doi.org/10.1007/s11814-013-0140-6.

(33) Prestipino, C.; Regli, L.; Vitillo, J. G.; Bonino, F.; Damin, A.; Lamberti, C.; Zecchina, A.; Solari, P. L.; Kongshaug, K. O.; Bordiga, S. Local Structure of Framework Cu(II) in HKUST-1 Metallorganic Framework: Spectroscopic Characterization upon Activation and Interaction with Adsorbates. *Chem. Mater.* 2006, *18* (5), 1337–1346. https://doi.org/10.1021/cm052191g.

(34) Persson, I. Hydrated Metal Ions in Aqueous Solution: How Regular Are Their Structures? *Pure Appl. Chem.* 2010, *82* (10). https://doi.org/10.1351/PAC-CON-09-10-22.

(35) Jiang, D.; Mallat, T.; Meier, D. M.; Urakawa, A.; Baiker, A. Copper Metal–Organic Framework: Structure and Activity in the Allylic Oxidation of Cyclohexene with Molecular Oxygen. *J. Catal.* 2010, *270* (1), 26–33. https://doi.org/10.1016/j.jcat.2009.12.002.

(36) Onishi, S.; Ohmori, T.; Ohkubo, T.; Noguchi, H.; Di, L.; Hanzawa, Y.; Kanoh, H.; Kaneko, K. Hydrogen-Bond Change-Associated Gas Adsorption in Inorganic–Organic Hybrid Microporous Crystals. *Appl. Surf. Sci.* 2002, *196* (1–4), 81–88. https://doi.org/10.1016/S0169-4332(02)00048-X.

(37) Masciocchi, N.; Cairati, P.; Carlucci, L.; Mezza, G.; Ciani, G.; Sironi, A. Ab-Initio X-Ray Powder Diffraction Structural Characterization of Co-Ordination Compounds: Polymeric [{MX $_2$ (Bipy)} $_n$] Complexes (M = Ni or Cu; X = Cl or Br; Bipy = 4,4′-Bipyridyl). *J Chem Soc Dalton Trans* 1996, No. 13, 2739–2746. https://doi.org/10.1039/DT9960002739.

(38) Li, W.-J.; Lü, J.; Gao, S.-Y.; Li, Q.-H.; Cao, R. Electrochemical Preparation of Metal–Organic Framework Films for Fast Detection of Nitro Explosives. *J Mater Chem A* 2014, *2* (45), 19473–19478. https://doi.org/10.1039/C4TA04203D.

Chapter 8

IRMOF Thin Films Templated on Oriented Zinc Oxide Nanowires

Abstract

Presented here is a new method for the synthesis of metal organic framework (MOF) thin films templated on vertically oriented zinc oxide (ZnO) nanowire arrays. The ZnO templates were first grown on indium tin oxide (ITO), by a simple hydrothermal method, followed by hydrothermal growth (in conventional or microwave oven) of several iso-reticular MOFs (IRMOFs). The method is facile and results in pin-hole free polycrystalline films, approximately 25 microns thick. Grazing incidence X-ray diffraction (GIXRD) and scanning electron microscopy (SEM) were used to confirm MOF phase purity and morphology, respectively. with potential applications in sensing, membranes, catalysis, and photoharvesting.

8.1 Introduction

Metal organic frameworks (MOFs) consist of multivalent metal ion or metal oxide nodes connected by multidentate organic linkers to form highly porous crystalline coordination polymers. MOFs have been a research focus for several decades now, due to the seemingly unlimited potential for tailoring of their pore size and surface chemistry. Originally of practical interest for their potential applications in gas absorption and storage, MOFs have subsequently shown promise in heterogeneous catalysis, ion exchange, pollutant trapping, and as molecular sieves.[1–4]

Several research groups have recently shown evidence that some MOFs exhibit semiconducting properties, and may be utilized in photovoltaics, photocatalysis and

resistance-based chemical sensing.[5–11] One of the oldest and most studied cases is that of IRMOF-1, which consists of zinc oxide nodes (Zn_4O_{13}) connected by terephthalic acid linkers. Photluminescence studies of IRMOF-1 have indicated that ligand to metal charge transfer (LMCT) occurs upon photoexcitation of electrons in the benzene ring of the terephthalic acid ligand. Zinc oxide is known to be semiconducting, and IRMOF-1 has been described as a three-dimensional lattice of zinc oxide quantum dot's sensitized by its aromatic ligands acting as photoantennae.[9] Figure 8.1 illustrates the results of work conducted by Bordiga and coworkers on the photoluminescence of IRMOF-1 as compared to that of zinc oxide nanoparticles and terephthalate disodium salt. They found that while the absorption maxima of both IRMOF-1 and the terepthalate salt occur in the same region, the emission spectra are quite divergent, with that of IRMOF-1 being only slightly blue-shifted with respect to bulk ZnO. This indicates ligand to metal charge transfer, with electron-hole recombination and photoemission occurring at the Zn_4O_{13} nodes.[6]

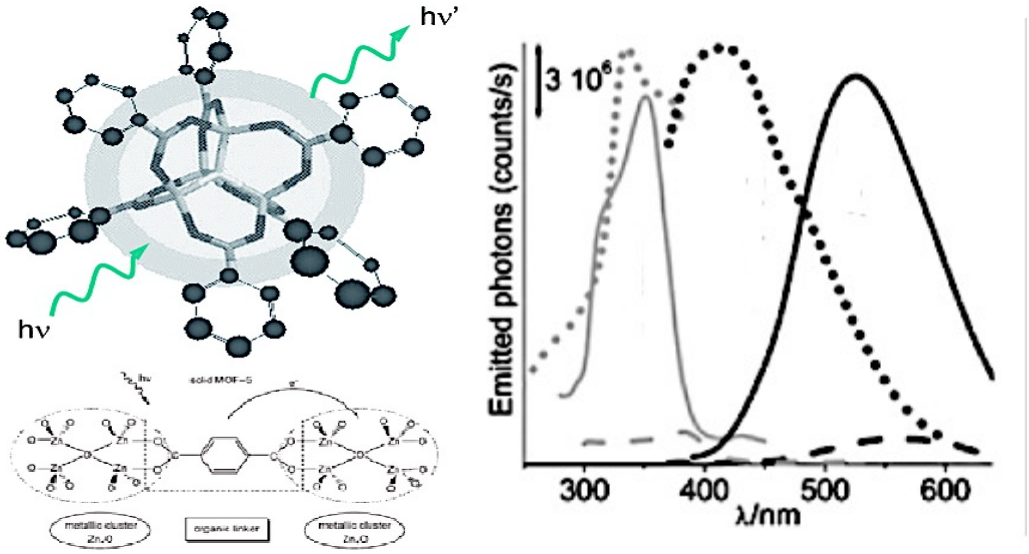

Figure 8.1. Left: Illustration of sensitized Zn_4O_{13} quantum dot and LMCT. Right: Photoluminescence spectra of IRMOF-1 compared to its ligand and node constituents. Grey curves (excitation scans), black curves (emission scans). IRMOF-1 (solid line, λ_{em} ~ 538 nm and λ_{ex} ~ 350 nm); terephthalate disodium salt (dotted line, λ_{em} ~418 nm and λ_{ex} ~ 335 nm); ZnO nanoparticles (dashed line, λ_{em} ~560 nm and λ_{ex} ~380 nm).

The work of Gascon and coworkers indicates that the band gap of IRMOF-1 analogs (structures retaining the Zn_4O_{13} node, aromatic dicarboxylate ligand, and 3-D topology) can be tuned using various ligands bearing different aromatic systems. Figures 8.2 and 8.3 illustrate the band gap energies and similar topologies of IRMOF-1 and several of its analogs. The absorption maximum of IRMOF-1 is 350 nm, tailing off into the visible spectrum at 500 nm. Lowering the band gap energy should shift this maximum into the visible spectrum, a desirable quality for photoharvesting applications.[7]

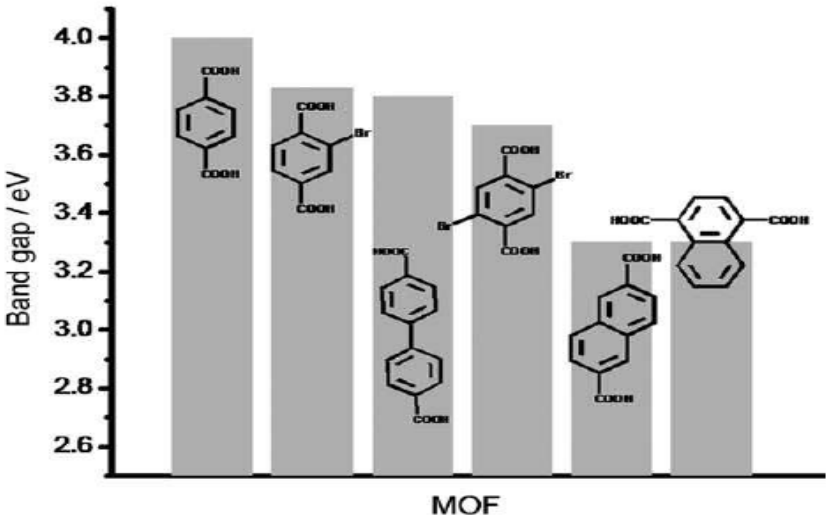

Figure 8.2. Band gaps for several IRMOF-1 analogs sporting different aromatic ligands.

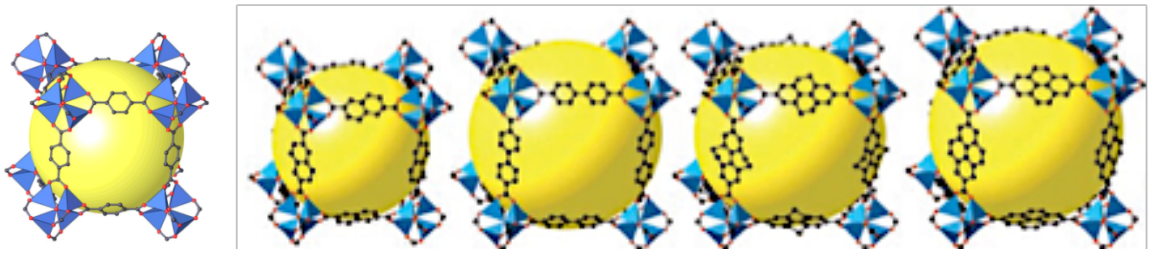

Figure 8.3. Topologies for IRMOF-1 (far left) and several of its analogs.

Zinc oxide is a wide band gap semiconductor (3.3 eV) of which thin films have been extensively explored and utilized in applications such as optical coatings, corrosion protection and semiconductor thin film devices.[12] One-dimensional ZnO nanowires have been shown to function as electrical conduits between light harvesting molecules and a conductive substrate in a photoelctrochemical cell.[13] Figure 8.4 illustrates why an array of vertically oriented nanowires, as compared to spherical particle films, greatly increases the efficiency of electron transfer to the conductive substrate. In an array, electrons are confined to each 1-D semiconductor wire, whereas in particle films electrons move

through a multitude of grain boundaries as they hop from particle to particle. This hopping greatly increases the likelihood of electron-hole recombination.[12]

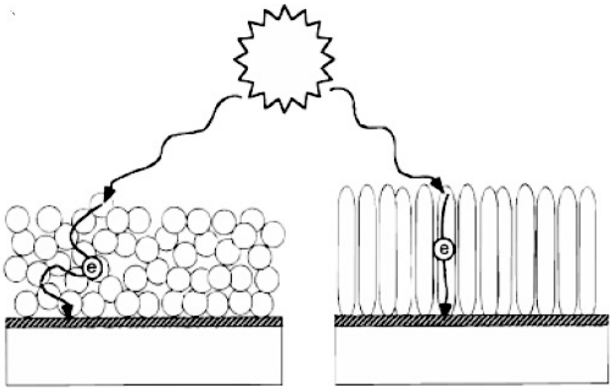

Figure 8.4. Electron transport through ZnO particle film (left) and through a vertically oriented ZnO nanowire array (right).

Li and coworkers demonstrated that vertically oriented arrays of zinc oxide nanowires grown on ITO can be used as photoanodes in water splitting (Figure 8.5).[13] Furthermore, their group demonstrated that doping of these nanowires with quantum dots of CdS or CdSe greatly increased their light absorption capabilities. Sensitizers, such as CdS and CdSe, which have smaller band gaps than ZnO act as light harvesters and inject electrons into the ZnO nanowires. In the water splitting scenario, hydrolysis itself drives electron-hole recombination. Using a suitable electrolyte and counter electrode, Law and coworkers have demonstrated a viable photoharvesting cell using similar sensitized ZnO based photoanodes.[14]

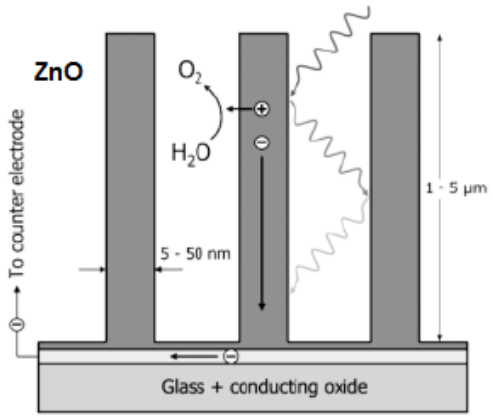

Figure 8.5 Water splitting using photoanode of ZnO nanowires.

Because of the semiconducting properties of some MOFs, described above, it may be advantageous to grow them on semiconducting1 ZnO. Zhan et. al. have shown that ZnO nanowires can serve as sacrificial templates in the growth of a zinc and imidazole based MOF, which grows as a kind of shell around the disintegrating ZnO crystals vertically grown on ITO (Figure 8.6). The nanowires were reported to decrease in diameter, providing Zn^{2+} to the growing MOF, proportional to the increase in thickness of the MOF shell.[15] This ore-shell approach, where the MOF film is only a few layers thick and potentially envelopes the entire nanowire, may prove more successful in photovoltaics applications than the polycrystalline film approach, or even the SURMOF approach. The core-shell approach would provide a semiconducting nanowire with a photosensitizing MOF shell, and could be an improvement to DSSC approaches where molecular dyes or quantum dots are adhered randomly throughout the array.

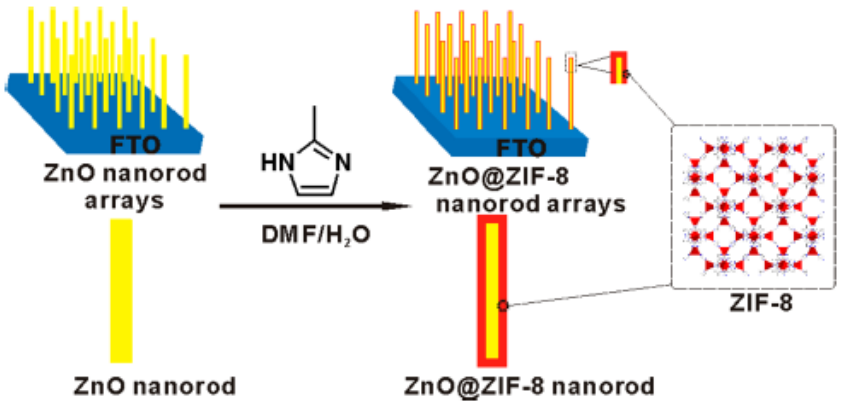

Figure 8.6 ZIF-8 MOF shell coating ZnO nanowires.

Oriented zinc oxide nanowires can be grown from high temperature (400^0C) vapor phase methods or from solution based synthesis at comparably lower temperatures ($25\text{-}200^0$C). Vapor phase methods result in highly oriented and tightly packed arrays of nanowires, but are energy intensive and require specialized equipment. Low temperature solution based methods are simple, inexpensive and allow synthesis on a larger variety of substrates than vapor deposition, but require special considerations to achieve oriented growth.[12]

Obtaining solution based oriented growth of ZnO nanowires requires the use of a growth directing agent such as hexamethylenetetramine (HMTA), which acts simultaneously as a pH-buffer and growth templating agent. Nanowires (long, thin hexagonal needles) and nanobelts (broad, flat hexagonal plates) are two typical ZnO single crystal formations. In order to sustain the growth of ZnO single crystals in an ordered fashion two factors have been shown to be important: the concentration of zinc hydroxide complexes ($Zn(OH)_2$, $[Zn(OH)_3]^{1-}$ and $[Zn(OH)_4]^{2-}$) in solution must remain low, and growth must proceed from a single crystal plane. If the concentration of zinc hydroxide is too high, 0-D nanoparticles precipitate from the solution and no crystal

growth is observed.[16,17] Many salts of Zn^{2+} (nitrate, acetate, formats, perchlorate, and chlorides) will form zinc hydroxide complexes in solution and quickly lower the pH. HMTA acts as a pH buffer because it dissociates slowly in solution (below 100^0C) to form formaldehyde and ammonia, and in the process generates hydroxide ions at a steady rate.[16] Although HMTA is a poor ligand of Zn^{2+} and does not form stable complexes with the ion, its weak association with Zn^{2+} has been suggested to play a part in the mediation of zinc hydroxide formation. HMTA has also been suggested to direct ZnO nanowire growth by preferentially adsorbing onto the polar facet (0001) of the growing nanocrystal, thereby directing growth in the direction of the unhindered non-polar plane (0010). Absorption onto the non-polar face would result in nanobelts, which are observed when sulfate is present in solution.[16]

Herein, it will be shown that vertically oriented zinc oxide nanowires (bearing the same Zn_4O structure as that of the Zn_4O_{13} clusters in IRMOF-1[11]) grown on ITO can serve as a functional platform upon which to grow zinc oxide based IRMOFs.

8.2 Experimental

8.2.1 Zinc oxide nanowire synthesis

Indium tin oxide (ITO) slides (2 cm x 1 cm, Sigma-Aldrich) were first seeded with zinc oxide, using a 5 mM ethanolic solution of zinc acetate dihydrate [Zn(CH3CO2)2•2H2O, 98%, Mallinckrodt Chemicals], drop cast on the conductive surface, then gently rinsed with pure ethanol and allowed to dry under a gentle stream of atmosphere. This process of soaking, rinsing and drying was repeated five times. The zinc acetate seeded slides were then placed on a hotplate (seeded side up) and heated to 350 ^{0}C for 20 minutes in atmosphere to form a zinc oxide seed layer.

ZnO seeded ITO slides were placed (ZnO side down) at a 45 degree angle in a 20 mL glass scintillation vial, and fully submerged in 20mL of an aqueous solution of 25 mM zinc nitrate hexahydrate ($Zn(NO_3)_2 \bullet 6H_2O$, 99.5%, Fisher Scientific) and 25 mM hexamethylenetetramine (HMTA, $C_6H_{12}N_4$, 99.1 %, Fisher Scientific). The synthesis vials were sealed with Teflon lined caps and placed in a static oven at 90 ^{0}C for four hours. The vials were then removed from the oven and allowed to cool to ambient temperature before being opened. The slides were removed and rinsed with dionized water and allowed to dry either at room. ZnO nanowire synthesis times were varied from one hour up to twelve hours in an attempt to determine the effect of nanowire length and density on subsequent MOF growth. The zinc oxide nanowire arrays were examined using both x-ray diffraction and scanning electron microscopy to determine their phase and orientation.

8.2.2 IRMOF thin film synthesis on ZnO nanowire arrays

The ZnO nanowire arrays were dried overnight, then immersed (ZnO side down) in 20 mL glass scintillation vials filled with a dimethylformamide (DMF, C3H7NO, 99.8 %, Macron) based IRMOF precursor solution, and heated in a static oven at 90 ^{0}C. The precursor solution and synthesis time were varied according to the particular IRMOF desired. In general zinc nitrate hexahydrate and one drop of hydrogen peroxide (30 %, Fischer Chemicals) were first added to half fill the 20 mL scintillation vial containing the ZnO nanowire array, then the appropriate organic ligand and HMTA solution (made separately in DMF) was added to fill the scintillation vial—this was done to minimize precipitation of MOF in the bulk solution. At the end of synthesis, the vials were allowed to cool to ambient temperature, and all IRMOF coated slides were rinsed with pure DMF

to remove non-adhered precipitate and any unreacted precurors. IRMOF-1 was grown for 20 hours, in a solution containing 9 mM terephthalic acid ($C_8H_6O_4$, 98+ %, Alfa Aesar), 12.5 mM zinc nitrate hexahydrate, and 5 mM HMTA. IRMOF-3 was grown for 24 hours, in a solution containing 13 mM zinc nitrate hexhydrate, 19 mM 2-aminoterepthalic acid ($C_8H_7NO_4$, 99 %, Sigma-Aldrich), and 13 mM of HMTA. IRMOF-8 was grown for 20 hours, in a solution containing 20 mM zinc nitrate hexahydrate, 20 mM 2,6-naphthalenedicarboxylic acid (C12H8O4, 98 %, TCI), and15 mM HMTA. IRMOF-9 was grown for 20 hours, in a solution containing 20 mM zinc nitrate hexahydrate, 20 mM 4,4'- biphenyldicarboxylic acid (C14H10O4, 98 %, Acros Organics), and 10 mM HMTA.

Microwave synthesis of IRMOF-1 was carried out in a DMF solution containing 1.56 mM zinc nitrate hexahydrate and 1.13 mM therphthalic acid, heated to of 90 ^{0}C (using 150 W irradiation, monitored by an infrared probe) for 10 minutes, in an Anton Paar Multiwave 3000 rotary microwave.

8.2.3 Characterization of ZnO nanowire arrays and IRMOF films

Zinc oxide nanowire arrays and IRMOF films were characterized by grazing incidence X-ray diffraction (GIXRD) using a Rigaku SmartLab diffractometer (Cu Kα radiation, λ = 1.54056 Å, operated at 44 mA and 40 kV). Parallel beam optics were employed, with a grazing incidence angle of 0.3^0, scan speed of 1.0 ^{0}/min, and step size of 0.01^0. Scanning electron microscopy (SEM) data was collected using a Carl Zeis Ultra 55 Field Emission Scanning Electron Microscope, operated at 5 kV and approximately 5 pA. Samples were first sputter coated with a 10nm layer of platinum to disperse surface charge evenly.

8.3. Results and Discussion

Figure 8.7 illustrates the growth process and morphology of the vertically orientated arrays of zinc oxide nanowires grown on ITO, and subsequent growth of IRMOF films. Figure 8.8 shows SEM cross-sectional views of the nanowire array with a seed layer of solid zinc oxide (highlighted by horizontal cursor lines), and after subsequent growth of IRMOF-1. Figure 8.9 shows a top-down view of the nanowire array. Longer nanowire growth times did not produce any noticeable effect on nanowire formation. Attempts to grow ZnO nanowires on clean glass substrate (microscope slides) tended to form uneven, patchy film, with large zones lacking coverage, that were easily removed by mechanical force or sonication, compared to those grown on ITO. MOF growth on these ZnO coated glass slides were also uneven and weakly bonded to the substrate as compared to syntheses using ITO. It can therefore be reasoned that the ITO acts as a strong binding intermediate between the silicon oxide surface and the zinc oxide seed layer.

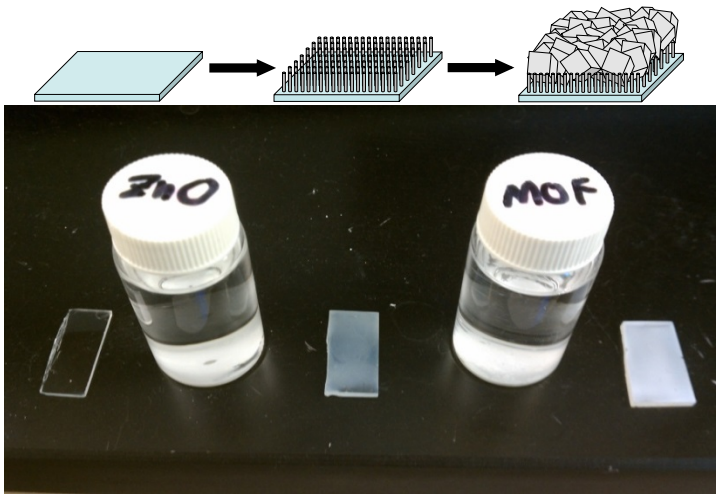

Figure 8.7 A graphic illustration (top) and photograph (bottom) of a polycrystalline IRMOF film (right) grown on zinc oxide nanowire array (middle), previously grown on an ITO slide (left).

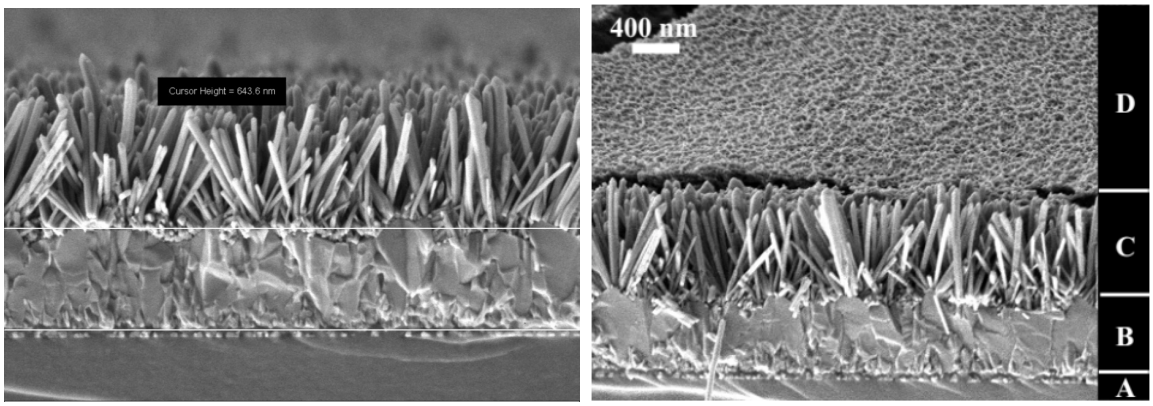

Figure 8.8 SEM cross-section images of (left) ZnO nanowire array (with ZnO seed layer shown between horizontal lines, 643.6 nm thick) on ITO substrate, and (right) IRMOF-1 grown on ZnO nanowire array (layers A: ITO; B: ZnO seed layer; C: ZnO nanowires, and D: IRMOF-1).

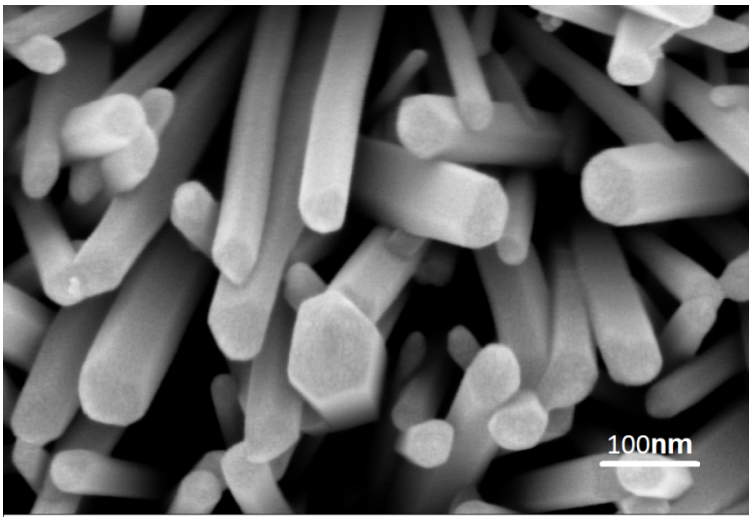

Figure 8.9 Top down view of ZnO nanowire array

The zinc oxide nanowire arrays serve as a nucleation layer upon which the MOF microcrystals grow, and attempts to grow IRMOFs on either bare ITO or ZnO seeded ITO were not successful. Likewise, no MOF crystallites adhered to the backside of the ITO slides (bare glass). Since the nanowires grown here are not tightly packed or perfectly vertically oriented, but rather grow in an array of semi-acicular clusters, it is understandable that a randomly oriented polycrystalline MOF film will result.

IRMOF film growth was monitored by Scanning electron microscopy (SEM) to determine the necessary growth time to achieve maximal film coverage. Figure 8.10 shows the coverage of IRMOF-1 at 5 hours, versus 20 hours, of growth. SEM and grazing incidence X-ray diffraction (GIXRD) were used to further characterize the four IRMOFs synthesized in this work. Figure 8.11 shows SEM images for the four IRMOF films, and figure 8.12 gives their respective GIXRD data.

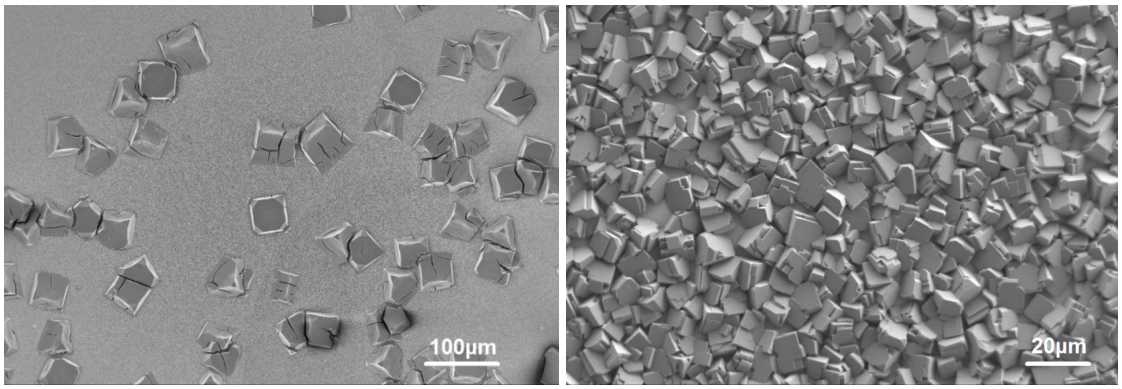

Figure 8.10 SEM of film coverage of IRMOF-1 after 5 hours (left) and after 20 hours (right) of growth.

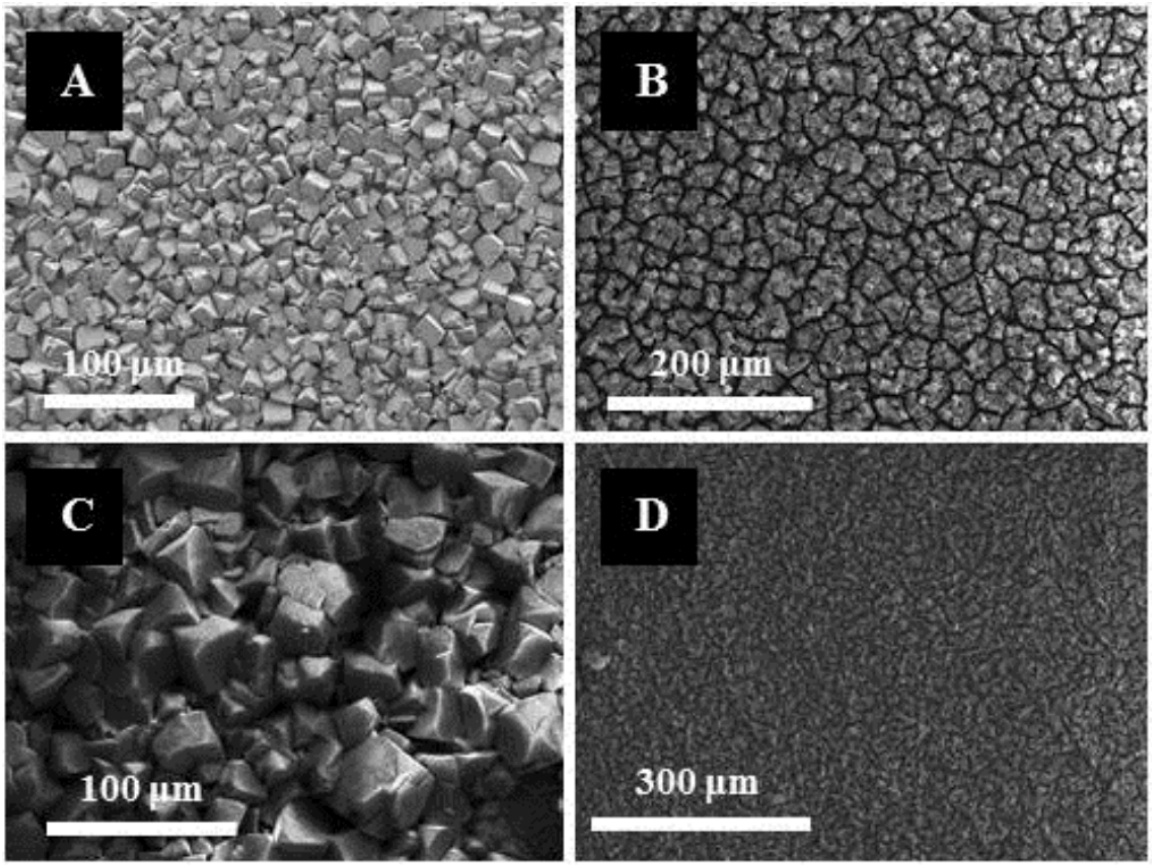

Figure 8.11 SEM images of (A) IRMOF1, (B) IRMOF-3, (C) IRMOF-8, and (D) IRMOF-9 films grown on ZnO nanowire arrays.

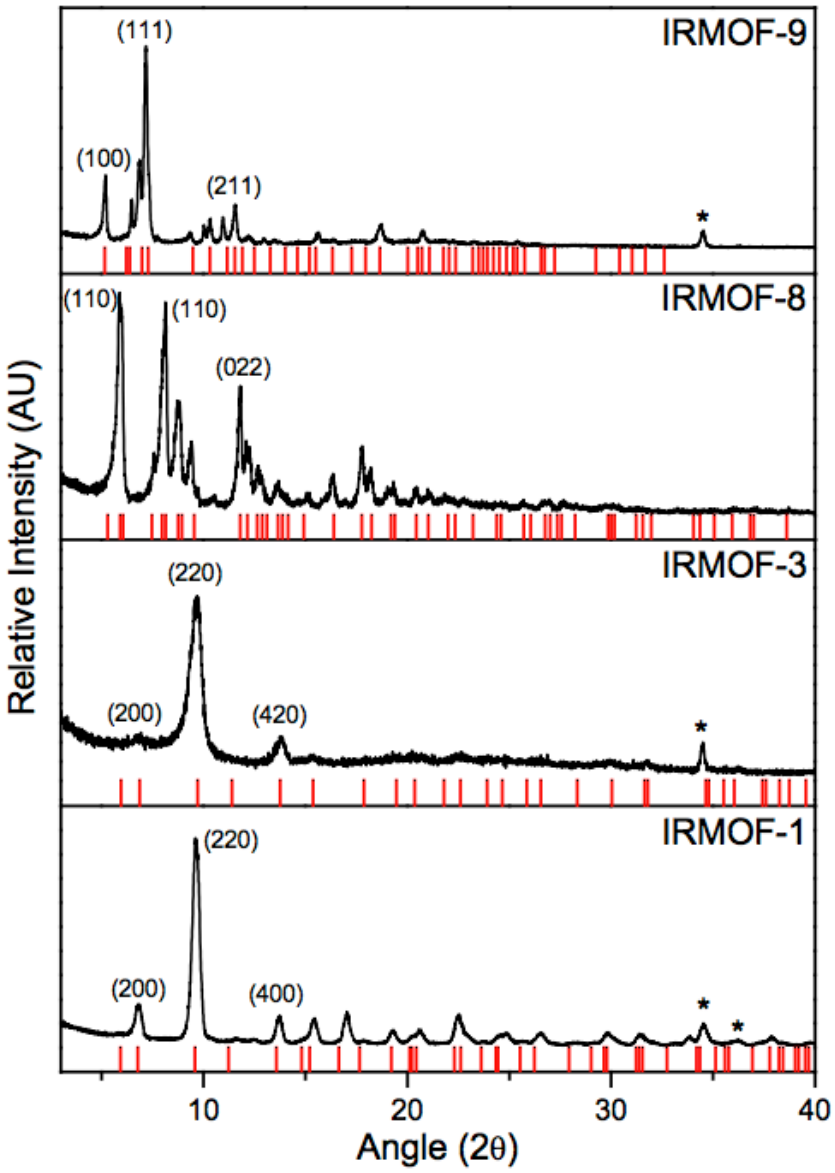

Figure 8.12 GIXRD data for IRMOF films compared to their calculated powder patterns (red bars). Asterisks indicate peaks indexed to zinc oxide.

Of the four IRMOF films, IRMOF-3 shows the lowest crystallinity. As a result, the crystallographic preferred orientation (CPO) indexing method[18] was used to quantify the degree of orientation for each film, except IRMOF-3. Figure 8.13 shows the GIXRD pattern for each IRMOF compared to its corresponding powder pattern. The *hkl* indicies labled in the powder patterns denote the peaks used to perform the CPO index

calculation. IRMOF-1 displayed (220) out-of-plane orientation ($CPO_{220/200}$ = 26), IRMOF-8 displayed no preferred orientation ($CPO_{110/110}$ = 1.6), and IRMOF-9 displayed only minor prfered orientation with respect to the (111) plane ($CPO_{111/110}$ = 15). Given the likelihood of MOF nucleation at random along the ZnO nanowires, it is not expected that these values should hold constant between different syntheses of the same IRMOF, however. To that effect, these films should likely be considered randomly oriented on average.

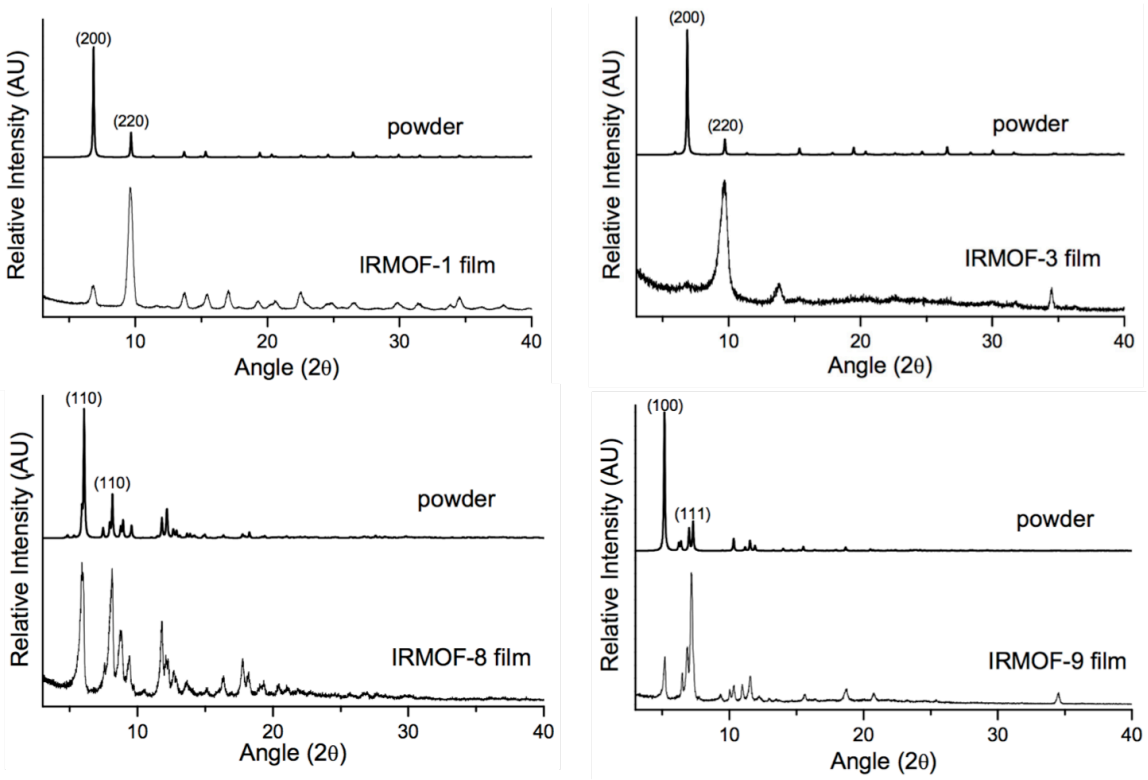

Figure 8.13 GIXRD patterns of IRMOF films compared to their respective powder patterns. *hkl*-indicies in powder pattern indicate peaks used to calculate CPO index.

Microwave synthesis was explored as a faster synthesis option, but the film coverage results were generally poorer. Figure 8.14 illustrates the growth of IRMOF-1 after 10 minutes at 90 ^{0}C. It is interesting to note the ZnO nanowires protruding through

the thin IRMOF film, indicating nucleation occurs along the sides of the nanowires. Clear evidence of an initial IRMOF layer and a subsequent secondary growth layer is indicated by the larger crystallites which appear to grow on top of the initial layer. Figure 8.15 shows the GIXRD pattern which confirms the phase purity of the MOF. The low peak intensity, compared to the conventional oven synthesis, may be explained by the thinner film growth in the case of microwave synthesis.

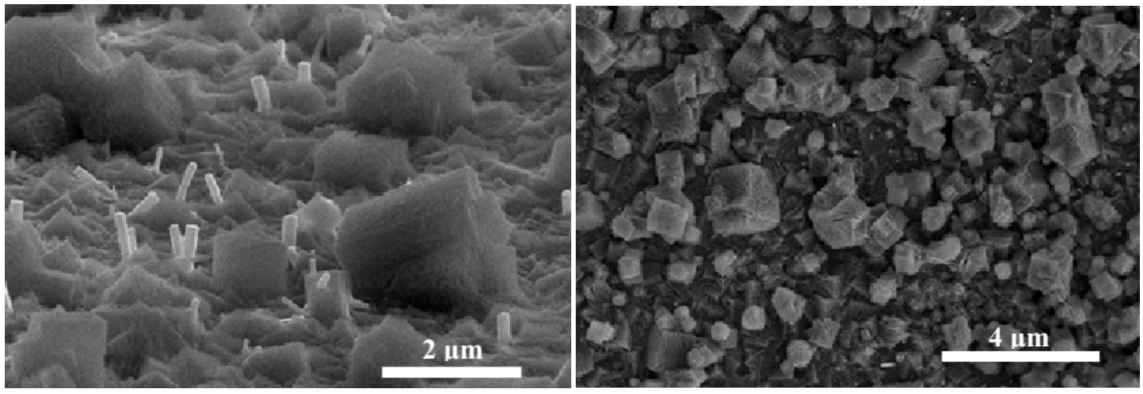

Figure 8.14 SEM images of microwave synthesized IRMOF-1 from the side view (left) and top down (right).

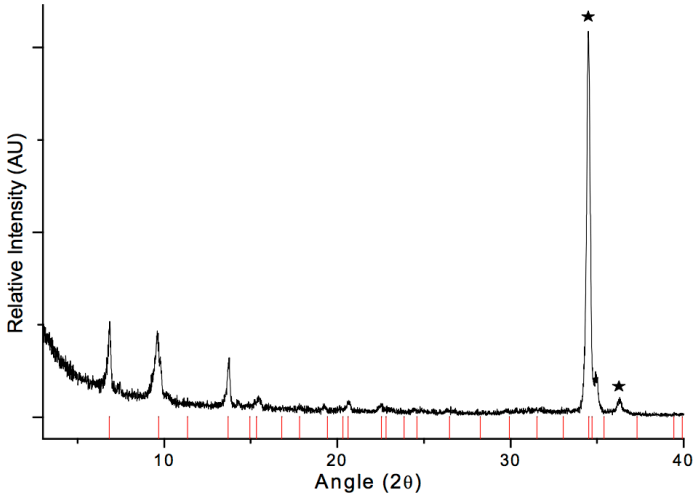

Figure 8.15 GIXRD pattern for microwave synthesized IRMOF-1. The asterisks labeled peaks were indexed to ZnO.

8.4 Conclusion

A new approach to MOF thin film formation on vertically oriented zinc oxide nanowire arrays grown on ITO has been developed. Scanning electron microscopy, as well X-ray diffraction, was used to verify the presence of the ZnO nanowires and four distinct IRMOF films. Both the ZnO nanowire arrays and IRMOF films were well adheared, and the IRMOF films were relatively phase pure and pin-hole free in each case. IRMOFs did not grow on bare glass, ITO or ZnO seeded ITO, indicating the necessity of the oriented nanowires, with their high surface area, for IRMOF nucleation. The recent work demonsterating the potential semiconducting properties of IRMOF-1 should make this synthesis method relevant to photoharvesting applications, where MOFs may be advantageous due to their high surface area and customizable surface chemistry.

8.5 References

(1) Serre, C.; Millange, F.; Surblé, S.; Férey, G. A Route to the Synthesis of Trivalent Transition-Metal Porous Carboxylates with Trimeric Secondary Building Units. *Angew. Chem. Int. Ed.* **2004**, *43* (46), 6285–6289. https://doi.org/10.1002/anie.200454250.

(2) Férey, G. Hybrid Porous Solids: Past, Present, Future. *Chem Soc Rev* **2008**, *37* (1), 191–214. https://doi.org/10.1039/B618320B.

(3) Park, Y. K.; Choi, S. B.; Kim, H.; Kim, K.; Won, B.-H.; Choi, K.; Choi, J.-S.; Ahn, W.-S.; Won, N.; Kim, S.; et al. Crystal Structure and Guest Uptake of a Mesoporous Metal–Organic Framework Containing Cages of 3.9 and 4.7 Nm in Diameter. *Angew. Chem. Int. Ed.* **2007**, *46* (43), 8230–8233. https://doi.org/10.1002/anie.200702324.

(4) Horcajada, P.; Serre, C.; Maurin, G.; Ramsahye, N. A.; Balas, F.; Vallet-Regí, M.; Sebban, M.; Taulelle, F.; Férey, G. Flexible Porous Metal-Organic Frameworks for a Controlled Drug Delivery. *J. Am. Chem. Soc.* **2008**, *130* (21), 6774–6780. https://doi.org/10.1021/ja710973k.

(5) Alvaro, M.; Carbonell, E.; Ferrer, B.; Llabrés i Xamena, F. X.; Garcia, H. Semiconductor Behavior of a Metal-Organic Framework (MOF). *Chem. - Eur. J.* **2007**, *13* (18), 5106–5112. https://doi.org/10.1002/chem.200601003.

(6) Bordiga, S.; Lamberti, C.; Ricchiardi, G.; Regli, L.; Bonino, F.; Damin, A.; Lillerud, K.-P.; Bjorgen, M.; Zecchina, A. Electronic and Vibrational Properties of a MOF-5 Metal–Organic Framework: ZnO Quantum Dot Behaviour. *Chem Commun* **2004**, No. 20, 2300–2301. https://doi.org/10.1039/B407246D.

(7) Gascon, J.; Hernández-Alonso, M. D.; Almeida, A. R.; van Klink, G. P. M.; Kapteijn, F.; Mul, G. Isoreticular MOFs as Efficient Photocatalysts with Tunable Band Gap: An Operando FTIR Study of the Photoinduced Oxidation of Propylene. *ChemSusChem* **2008**, *1* (12), 981–983. https://doi.org/10.1002/cssc.200800203.

(8) Llabrés i Xamena, F. X.; Corma, A.; Garcia, H. Applications for Metal−Organic Frameworks (MOFs) as Quantum Dot Semiconductors. *J. Phys. Chem. C* **2007**, *111* (1), 80–85. https://doi.org/10.1021/jp063600e.

(9) Silva, C. G.; Corma, A.; García, H. Metal–Organic Frameworks as Semiconductors. *J. Mater. Chem.* **2010**, *20* (16), 3141. https://doi.org/10.1039/b924937k.

(10) Tachikawa, T.; Choi, J. R.; Fujitsuka, M.; Majima, T. Photoinduced Charge-Transfer Processes on MOF-5 Nanoparticles: Elucidating Differences between Metal-Organic Frameworks and Semiconductor Metal Oxides. *J. Phys. Chem. C* **2008**, *112* (36), 14090–14101. https://doi.org/10.1021/jp803620v.

(11) Civalleri, B.; Napoli, F.; Noël, Y.; Roetti, C.; Dovesi, R. Ab-Initio Prediction of Materials Properties with CRYSTAL: MOF-5 as a Case Study. *CrystEngComm* **2006**, *8* (5), 364–371. https://doi.org/10.1039/B603150C.

(12) Weintraub, B.; Zhou, Z.; Li, Y.; Deng, Y. Solution Synthesis of One-Dimensional ZnO Nanomaterials and Their Applications. *Nanoscale* **2010**, *2* (9), 1573. https://doi.org/10.1039/c0nr00047g.

(13) Li, Y.; Zhang, J. Z. Hydrogen Generation from Photoelectrochemical Water Splitting Based on Nanomaterials. *Laser Photonics Rev.* **2009**, *4* (4), 517–528. https://doi.org/10.1002/lpor.200910025.

(14) Law, M.; Greene, L. E.; Johnson, J. C.; Saykally, R.; Yang, P. Nanowire Dye-Sensitized Solar Cells. *Nat. Mater.* **2005**, *4* (6), 455–459. https://doi.org/10.1038/nmat1387.

(15) Zhan, W.; Kuang, Q.; Zhou, J.; Kong, X.; Xie, Z.; Zheng, L. Semiconductor@Metal–Organic Framework Core–Shell Heterostructures: A Case of ZnO@ZIF-8 Nanorods with Selective Photoelectrochemical Response. *J. Am. Chem. Soc.* **2013**, *135* (5), 1926–1933. https://doi.org/10.1021/ja311085e.

(16) Govender, K.; Boyle, D. S.; Kenway, P. B.; O'Brien, P. Understanding the Factors That Govern the Deposition and Morphology of Thin Films of ZnO from Aqueous Solution. *J Mater Chem* **2004**, *14* (16), 2575–2591. https://doi.org/10.1039/B404784B.

(17) Abd El Aal, E. E. Effect of Cl− Anions on Zinc Passivity in Borate Solution. *Corros. Sci.* **2000**, *42* (1), 1–16. https://doi.org/10.1016/S0010-938X(99)00052-9.

(18) Bux, H.; Feldhoff, A.; Cravillon, J.; Wiebcke, M.; Li, Y.-S.; Caro, J. Oriented Zeolitic Imidazolate Framework-8 Membrane with Sharp H_2/C_3H_8 Molecular Sieve Separation. *Chem. Mater.* **2011**, *23* (8), 2262–2269. https://doi.org/10.1021/cm200555s.

Chapter 9

Conclusions and Future Work

9.1 Conclusions

The work presented in chapters 7 and 8 demonstrates two new approaches to MOF film synthesis on the conductive transparent substrate ITO. The synthesis of MOF films on conductive and transparent substrates, such as ITO, presents the opportunity to take advantage of the unique properties of MOFs that can participate in photo-stimulation, ligand to metal charge transfer, and/or guest-mediated conductivity. The simplicity of the chemistry involved in both the anodic electrodeposition of MOF films on metal deposited ITO, and the hydrothermal deposition of MOF films on ZnO nanowire arrays grown on ITO, should indicate the relative ease of scalable production. Additionally, the microwave synthesis of MOF films grown on ZnO nanowire arrays, and the electrochemical deposition method should be of particular interest for scale up production, as the synthesis time is dramatically shortened compared to conventional hydrothermal methods or LbL methods of growing MOF films on SAM functionalized supstrates.

9.2 Future Work

Applications in chemical sensing, modifiable dielectric coatings, and optioelectronics come to mind when considering the uses for MOF films grown on ITO. Future work with both anodic electrodeposition and hydrothermal growth on ZnO-ITO should be driven with specific applications in mind, rather than pure proof of concept that

such structures can be formed on ITO substrate. In particular, the synthesis of truly conductive MOF films on ITO would prove interesting for photovoltaics applications.

Particular limitations exist with the use of IRMOFs as they tend to be inherently unstable outside of the DMF templating solvent. Additionally the use of different metal oxides and different oxide layer morphologies (shorter nanowires or nanoseeds) should be explored to enhance potential application of MOF films deposited on semiconductor metal oxide coated ITO. Simple photovoltaic cell experiments, using MOF-MO-ITO, may be designed using $I_3/3I^-$ electrolyte and a platinum sputtered counter electrode. Preliminary work in this vein could help determine not only which MOFs will be suitable and stable over time, but also how different metal oxides, and the morphology of the MO layer, affect the light harvesting and electron shuttling properties of the MOF-MO-ITO.

Utilizing the film synthesis techniques described in chapters 7 and 8 to integrate MOFs into electronic devices will require a great deal of refinement. For instance, the randomly oriented polycrystalline, and often multi-layered, morphology of these films present immediate challenges to the characterization of electronic conductivity, as well as many envisioned electronic applications—where thin, single layer, preferably oriented (to take advantage of anisotropic effects) MOF films are desired. Ideally, an imaging technique such as conductive AFM (CAFM) that can simultaneously probe electronic conductivity of the pure MOF film, or after intercalation of some conductivity altering guest species (like in the case of TCNQ@HKUST-1),[1] would give valuable insight into the applicable limits of MOF film thickness and orientation on a conductive substrate. The small, thin crystals of HKUST-1 or CBBr, grown on Cu octahedra deposits in Cu-ITO within the first few minutes of applied bias, are ideal candidates for CAFM characterization. These

characterization experiments were in fact attempted for HKUST-1 grown on Cu-ITO—though the results were inconclusive. Attempting such experiments with the fully grown EMOF films would be presumably less successful, just as conductivity experiments using two-point probe measurements on compressed MOF pellets show remarkably lower conductivity than experiments carried out on single MOF microcrystals.[2,3] In both cases, characterization of single crystal layers are necessary to differentiate between intrinsic and defect mediated conductivity—the later arising primarily from grain boundary effects, inherent in multilayer polycrystalline films. Additional characterization methods will be needed in order to probe other potentially exploitable MOF film properties, particularly as applicable to chemical sensing, such as resistance switching,[4] guest-tunable spin crossover,[5] and reversible ferromagnetic-antiferromagnetic behaviors.[6]

None of the MOFs presented in chapter 7 are known to be intrinsically conductive. Those built using carboxylate ligands have been theoretically and experimentally determined to be insulators,[1,7] while no conductivity research could be found on CBBr. The intrinsic and induced conductivity of HKUST-1 has been extensively studied,[1,7–10] and its successful growth by anodic deposition on ITO may present value to the research community. The other three EMOF films are more or less illustrative of the wider applicability of this method, using different metal and ligand combinations via the same electrochemical processes. This versatility is desirable, since there is growing evidence that the conductivity of the MOF can be intrinsically tuned by appropriate choice of metal, linker, and linker modification.

The IRMOF films grown on ZnO nanowire arrays in chapter 7 may be of value to research focusing on light harvesting applications of MOFs. Aromatic ligands used

to design MOFs can act as photoantennae, participating in ligand-to-metal charge transfer. In this sense, the organic ligands of MOFs act as the dye in a dye sensitized solar cell (DSSC). For such applications, closed shell zinc(II) cations in the MOF framework may be preferable, as they limit the opportunity for electron-hole recombination, making IRMOF's of relevant interest.[11] The porosity of the MOF can serve to hold electrolyte in such applications as well.

Energy harvesting applications, such as photovoltaics, will require determining the appropriate MOF based on band gap, proper alignment of MOF LUMO and HOMO levels with the conduction band of the semiconductor upon which they are grown (TiO_2, ZnO, etc), as well as with the valance band of the electrolyte used in the photovoltaic cell. To date, few band gap studies have been conducted to determine values for the large library of candidate MOFs.[11]

Considering MOF thin film materials integrated into modern electronics will require even more refinement of both deposition methods. Whether a MOF layer is to be integrated into a multi-layer chip, during conventional microfabrication, (e.g. as an embed dielectric layer) or as an outer layer coating (e.g. chemical sensing) will greatly impact the manner in which the MOF (and subsequent material layers) is deposited (and protected, if need be, during subsequent material layer depositions).

As stated in the *Handbook of thin film deposition: techniques, processes, and technologies* (3rd edition), the first steps toward the integration of MOFs in microelectronics will be mastering deposition with precise control over film composition homogeneity, thickness, roughness, and crystallographic orientation (depending on application).[12] The work present here covers a least a few of these considerations (depositions by EMOF procedure were of homogenous films with

controllable thickness and roughness). But, over all, these techniques require more finesse to achieve single layer films, with appropriate characterization of the MOF-substrate (metal or oxide) contact.

9.3 References

(1) Talin, A. A.; Centrone, A.; Ford, A. C.; Foster, M. E.; Stavila, V.; Haney, P.; Kinney, R. A.; Szalai, V.; El Gabaly, F.; Yoon, H. P.; et al. Tunable Electrical Conductivity in Metal-Organic Framework Thin-Film Devices. *Science* **2014**, *343* (6166), 66–69. https://doi.org/10.1126/science.1246738.

(2) Chen, D.; Xing, H.; Su, Z.; Wang, C. Electrical Conductivity and Electroluminescence of a New Anthracene-Based Metal–Organic Framework with π-Conjugated Zigzag Chains. *Chem. Commun.* **2016**, *52* (10), 2019–2022. https://doi.org/10.1039/C5CC09065B.

(3) Sun, L.; Campbell, M. G.; Dincă, M. Electrically Conductive Porous Metal-Organic Frameworks. *Angew. Chem. Int. Ed.* **2016**, *55* (11), 3566–3579. https://doi.org/10.1002/anie.201506219.

(4) Pan, L.; Liu, G.; Li, H.; Meng, S.; Han, L.; Shang, J.; Chen, B.; Platero-Prats, A. E.; Lu, W.; Zou, X.; et al. A Resistance-Switchable and Ferroelectric Metal–Organic Framework. *J. Am. Chem. Soc.* **2014**, *136* (50), 17477–17483. https://doi.org/10.1021/ja508592f.

(5) Amoore, J. J. M.; Neville, S. M.; Moubaraki, B.; Iremonger, S. S.; Murray, K. S.; Létard, J.-F.; Kepert, C. J. Thermal- and Light-Induced Spin Crossover in a Guest-Dependent Dinuclear Iron(II) System. *Chem. - Eur. J.* **2010**, *16* (6), 1973–1982. https://doi.org/10.1002/chem.200901809.

(6) Kurmoo, M.; Kumagai, H.; Chapman, K. W.; Kepert, C. J. Reversible Ferromagnetic–Antiferromagnetic Transformation upon Dehydration–Hydration of the Nanoporous Coordination Framework, [Co3(OH)2(C4O4)2]·3H2O. *Chem. Commun.* **2005**, No. 24, 3012. https://doi.org/10.1039/b500614g.

(7) Erickson, K. J.; Léonard, F.; Stavila, V.; Foster, M. E.; Spataru, C. D.; Jones, R. E.; Foley, B. M.; Hopkins, P. E.; Allendorf, M. D.; Talin, A. A. Thin Film Thermoelectric Metal-Organic Framework with High Seebeck Coefficient and Low Thermal Conductivity. *Adv. Mater.* **2015**, *27* (22), 3453–3459. https://doi.org/10.1002/adma.201501078.

(8) Neumann, T.; Liu, J.; Wächter, T.; Friederich, P.; Symalla, F.; Welle, A.; Mugnaini, V.; Meded, V.; Zharnikov, M.; Wöll, C.; et al. Superexchange Charge Transport in Loaded Metal Organic Frameworks. *ACS Nano* **2016**, *10* (7), 7085–7093. https://doi.org/10.1021/acsnano.6b03226.

(9) Liu, J.; Wächter, T.; Irmler, A.; Weidler, P. G.; Gliemann, H.; Pauly, F.; Mugnaini, V.; Zharnikov, M.; Wöll, C. Electric Transport Properties of Surface-Anchored Metal–Organic Frameworks and the Effect of Ferrocene Loading. *ACS Appl.*

Mater. Interfaces **2015**, *7* (18), 9824–9830. https://doi.org/10.1021/acsami.5b01792.

(10) Hendon, C. H.; Walsh, A. Chemical Principles Underpinning the Performance of the Metal–Organic Framework HKUST-1. *Chem. Sci.* **2015**, *6* (7), 3674–3683. https://doi.org/10.1039/C5SC01489A.

(11) Stassen, I.; Burtch, N.; Talin, A.; Falcaro, P.; Allendorf, M.; Ameloot, R. An Updated Roadmap for the Integration of Metal–Organic Frameworks with Electronic Devices and Chemical Sensors. *Chem. Soc. Rev.* **2017**, *46* (11), 3185–3241. https://doi.org/10.1039/C7CS00122C.

(12) *Handbook of Thin Film Deposition: Techniques, Processes, and Technologies*, 3rd ed.; Seshan, K., Ed.; Elsevier ; William Andrew: Amsterdam ; Boston : Waltham, 2012.

Appendix

A.1 Supplemental Information (Chapter 3)

Table S3.1 Catalyst screening results[a]

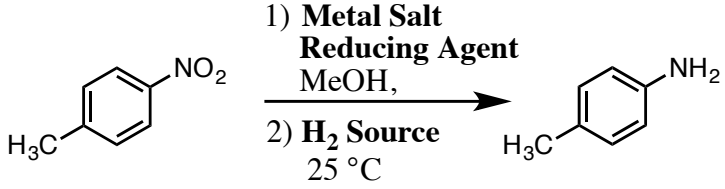

Entry	Metal Salt	Reducing Agent	Support	H_2 Source	Yield (%)[b]
1	$ZnBr_2$	$NaBH_4$	--	$N_2H_4 \bullet H_2O$	0%
2	$InCl_3$	$NaBH_4$	--	$N_2H_4 \bullet H_2O$	0%
3	$CuCl_2$	$NaBH_4$	--	$N_2H_4 \bullet H_2O$	0%
4	$InBr_3$	$NaBH_4$	--	$N_2H_4 \bullet H_2O$	0%
5	$NiCl_2 \bullet 6H_2O$	$NaBH_4$	--	$N_2H_4 \bullet H_2O$	85%
8	$NiCl_2 \bullet 6H_2O$	--	--	$N_2H_4 \bullet H_2O$	0%
9	--	$NaBH_4$	--	$N_2H_4 \bullet H_2O$	0%
10	--	$NaBH_4$	MASN	$N_2H_4 \bullet H_2O$	0%
11	$NiCl_2 \bullet 6H_2O$	$NaBH_4$	MASN	$N_2H_4 \bullet H_2O$	94%
12	$NiCl_2 \bullet 6H_2O$	$NaBH_4$	--	$N_2H_4 \bullet$Acetate	0%
13	$NiCl_2 \bullet 6H_2O$	$NaBH_4$	MASN	$N_2H_4 \bullet$Acetate	15%[c]

[a] Reaction conditions: nitroarene (2 mmol), metal salt (10 mol%), reducing agent (20 mol%), hydrazine hydrate (10 mmol), MeOH (8 mL), 25 °C, 24 h, under argon atmosphere.

[b] Isolated yield.

[c] Ratio based on NMR.

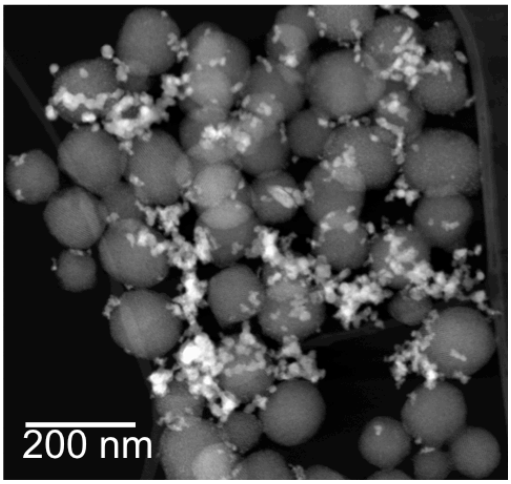

Figure S3.1 NBC supported on mesoporous silicate nanoparticles (NBC-MSN), showing large particles of NBC not bound to MSN.

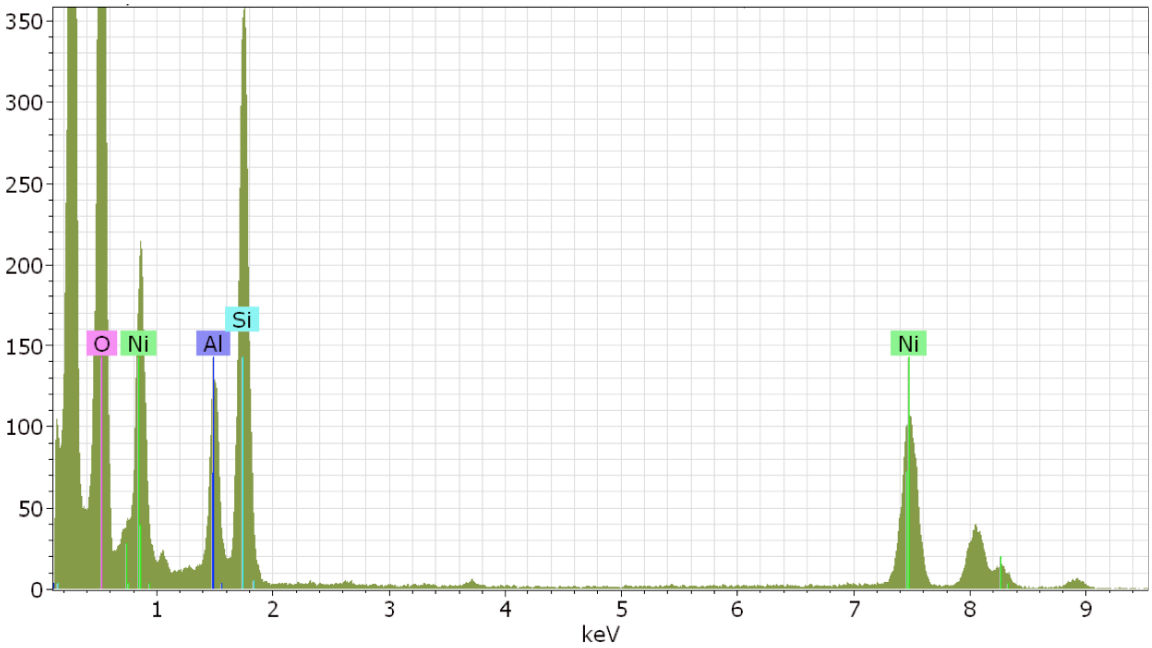

Figure S3.2 EDS spectrum for NBC-MASN.

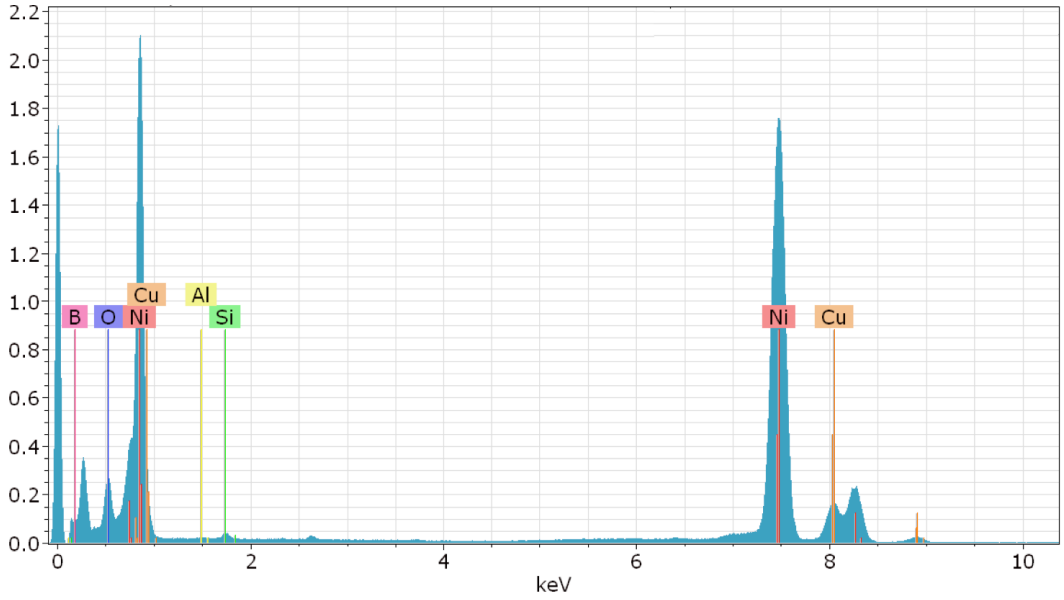

Figure S3.3 EDS spectrum for NBC.

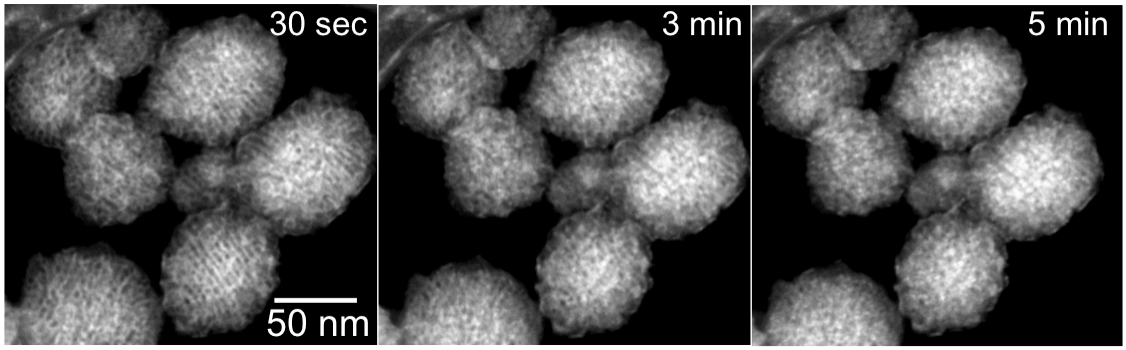

Figure S3.4 Segregation/crystallization of Ni in NBC-MASN after electron beam exposure for 5 min.

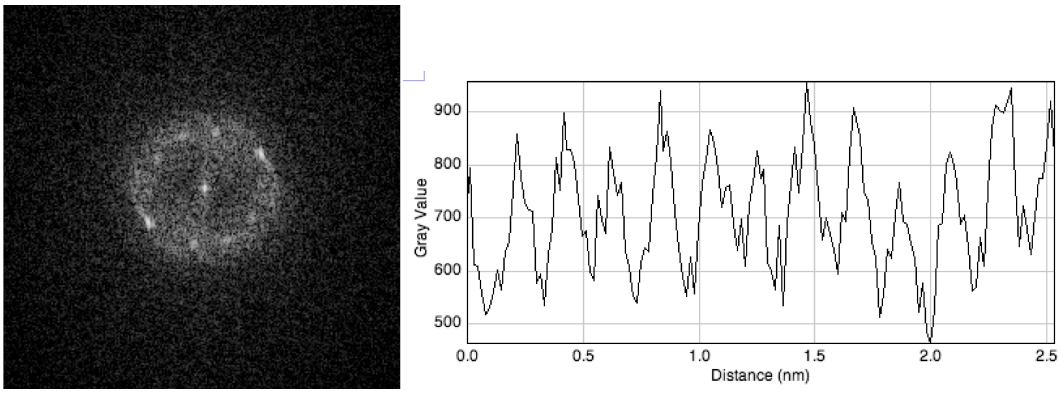

Figure S3.5 The electron diffraction pattern from Ni in the unsupported NBC material (left) and the lattice spacing plot from the corresponding HRTEM (right).

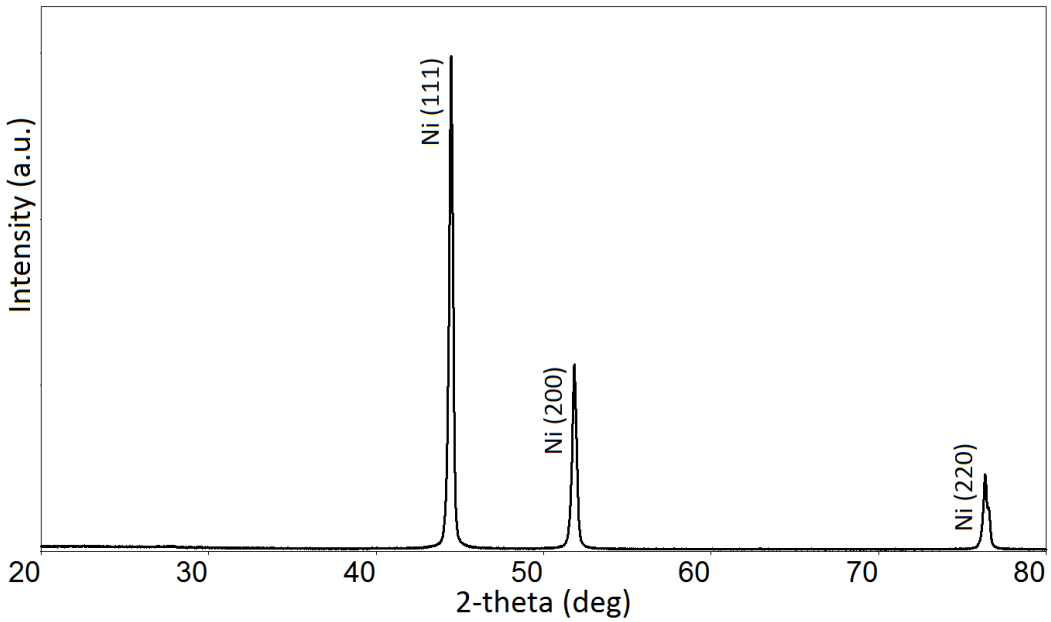

Figure S3.6 PXRD of NBC-MASN after MeOH reflux followed by $N_{2(g)}$-calcination.

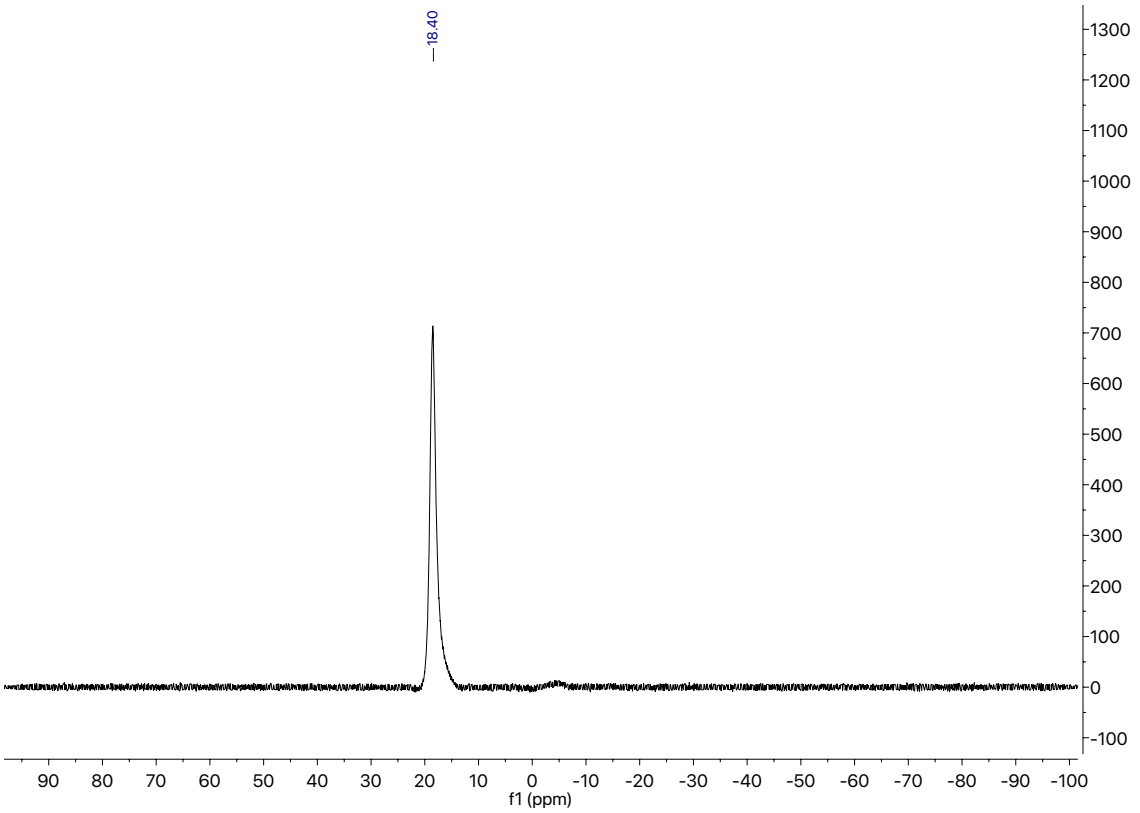

Figure S3.7 ^{11}B NMR of NBC refluxed in methanol for 3 h.

Table S3.2 Gas evolution analysis of NBC for differing ratios of Ni:BH_4 and NBC-MASN

$NiCl_2$:$NaBH_4$	$NiCl_2$	$NaBH_4$	H_2 Evolved	Theoretical Amount of H_2	Percentage of H_2 Evolved
1:2	0.5 mmol	1 mmol	2.05 mmol	4 mmol	51%
1:1	0.5 mmol	0.5 mmol	0.85 mmol	2 mmol	43%
1:0.5	0.5 mmol	0.25 mmol	0.54 mmol	1 mmol	54%

Ni:$NaBH_4$	Ni-MASN	$NaBH_4$	H_2 Evolved	Theoretical Amount of H_2	Percentage of H_2 Evolved
1:2	0.15 mmol	0.3 mmol	0.71 mmol	1.256 mmol	56%

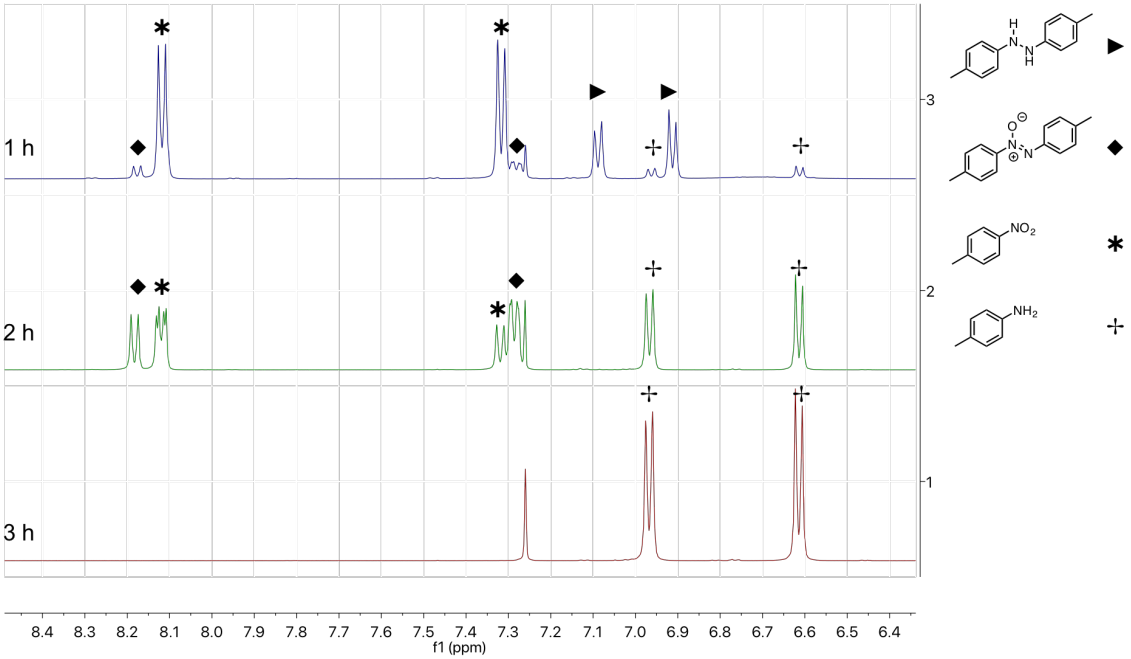

Figure S3.8 Intermediates formed during the catalysis after 1 h, 2 h, and 3 h.

NMR Data

Chemical shifts in ppm are referenced to the signal of the solvent ($CDCl_3$, δ_H = 7.26). Coupling constants *J* are given in Hz and signal multiplicities are abbreviated as s (singlet), d (doublet), t (triplet), m (multiplet), and br (broad). The proton and carbon spectra follow the list of chemical shifts in the same order.

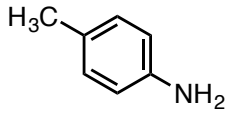

4-Toluidine[1]
^{1}H NMR (500 MHz, Chloroform-*d*): δ 7.00 (d, *J* = 7.5 Hz, 2H), 6.63 (d, *J* = 8.2 Hz, 2H), 3.46 (s, 2H), 2.27 (s, 3H). ^{13}C NMR ($CDCl_3$, 500 MHz): δ 143.8, 129.8, 127.8, 115.3, 20.5

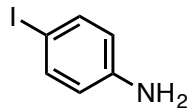

4-Iodo-aniline[2]
^{1}H NMR (500 MHz, Chloroform-*d*): δ 7.41 (d, *J* = 8.6 Hz, 2H), 6.47 (d, *J* = 8.7 Hz, 2H), 3.49 (s, 2H). ^{13}C NMR ($CDCl_3$, 500 MHz): δ 137.9, 117.3

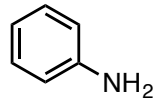

Aniline[1,2]
^{1}H NMR (500 MHz, Chloroform-*d*): δ 7.19 (t, 2H), 6.77 (t, *J* = 7.4 Hz, 1H), 6.69 (d, *J* = 7.5 Hz, 2H), 3.66 (s, 2H). ^{13}C NMR ($CDCl_3$, 500 MHz): δ 143.4, 129.3, 118.6, 115.2

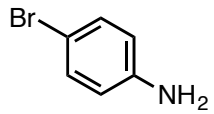

4-Bromo-aniline[1-3]
^{1}H NMR (500 MHz, Chloroform-*d*): δ 7.24 (d, *J* = 8.5 Hz, 2H), 6.57 (d, *J* = 8.6 Hz, 2H), 3.65 (s, 2H). ^{13}C NMR ($CDCl_3$, 500 MHz): δ 145.4, 132.0, 116.7, 110.2

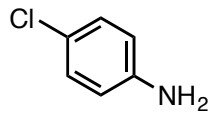

4-Chloro-aniline[1,2,4]
^{1}H NMR (500 MHz, Chloroform-*d*): δ 7.10 (d, *J* = 8.7Hz, 2H), 6.60 (d, *J* = 8.7 Hz, 2H), 3.60 (s, 2H). ^{13}C NMR ($CDCl_3$, 500 MHz): δ 144.9, 129.1, 123.1, 116.3

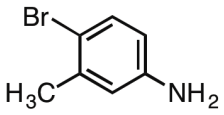

4-Bromo-3-methylaniline[5,6]

^{1}H NMR (500 MHz, Chloroform-*d*): δ 7.25 (d, *J* = 8.0 Hz, 1H), 6.57 (s, 1H), 6.39 (d, *J* = 8.1 Hz, 1H), 3.59 (bs, 2H), 2.30 (s, 3H). ^{13}C NMR ($CDCl_3$, 500 MHz): δ 145.7, 138.4, 132.7, 117.5, 114.3, 112.9, 22.9

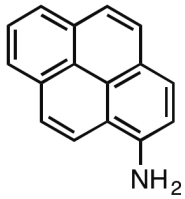

1-Aminopyrene[7]

^{1}H NMR (500 MHz, Chloroform-*d*): δ 8.05 (d, *J* = 6.2 Hz, 2H), 7.98 (s, 3H), 7.91 (d, *J* = 8.5 Hz, 2H), 7.82 (s, 1H), 7.39 (s, 1H), 4.52 (bs, 2H). ^{13}C NMR ($CDCl_3$, 500 MHz): δ 140.9, 132.2, 131.6, 127.6, 126.1, 125.5, 124.3, 124.1, 123.8, 123.6, 120.2, 116.9, 113.9

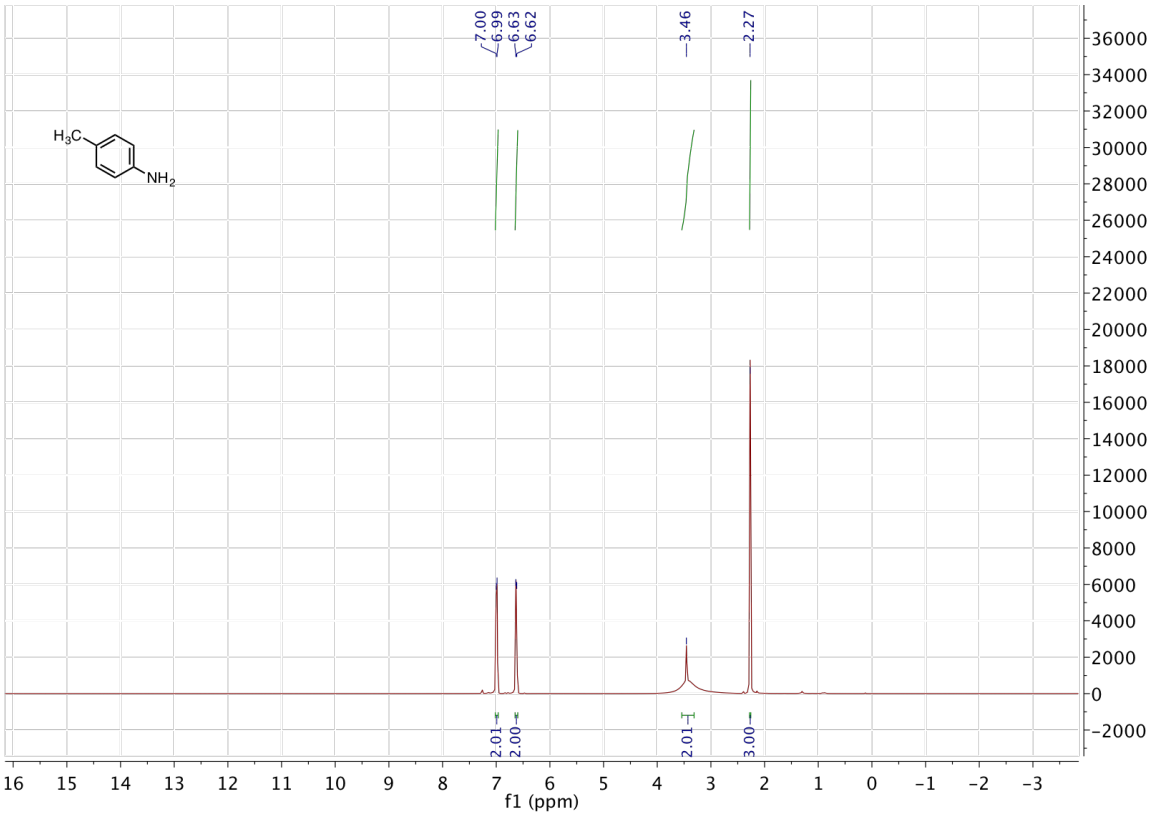

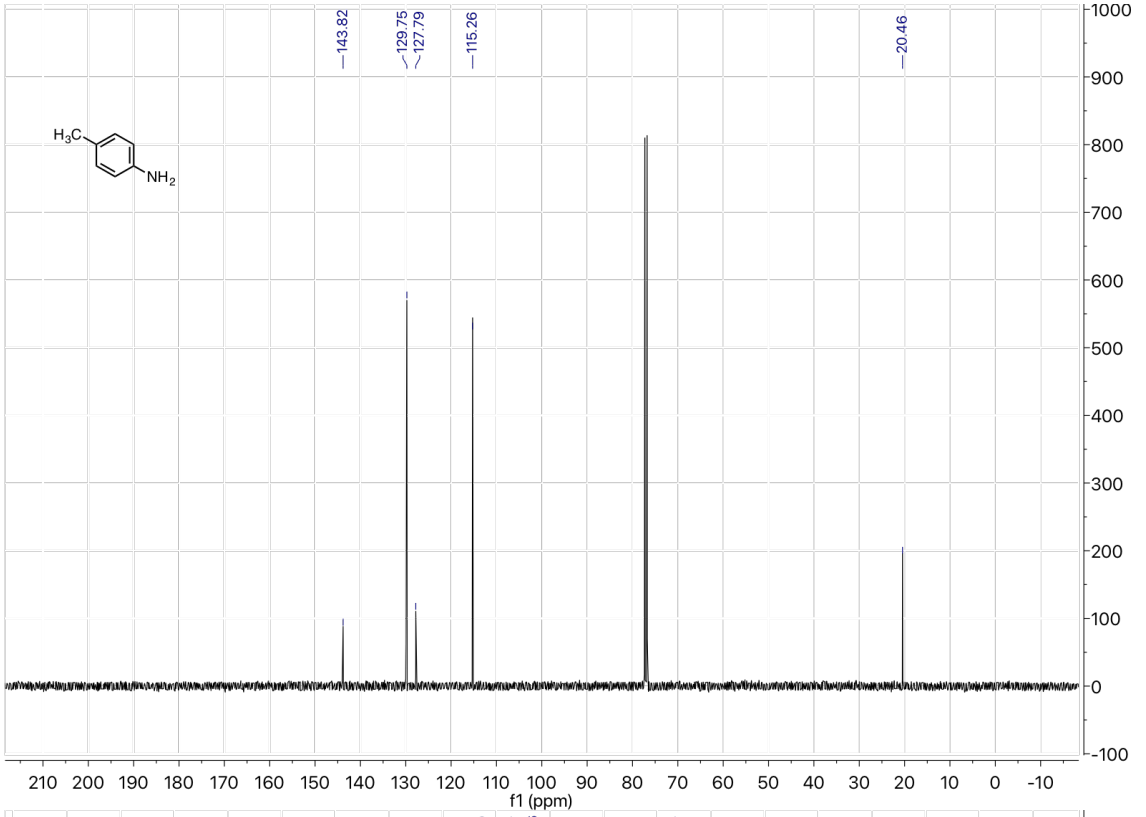
143.82
129.75
127.79
115.26
20.46
H3C
NH2
f1 (ppm)

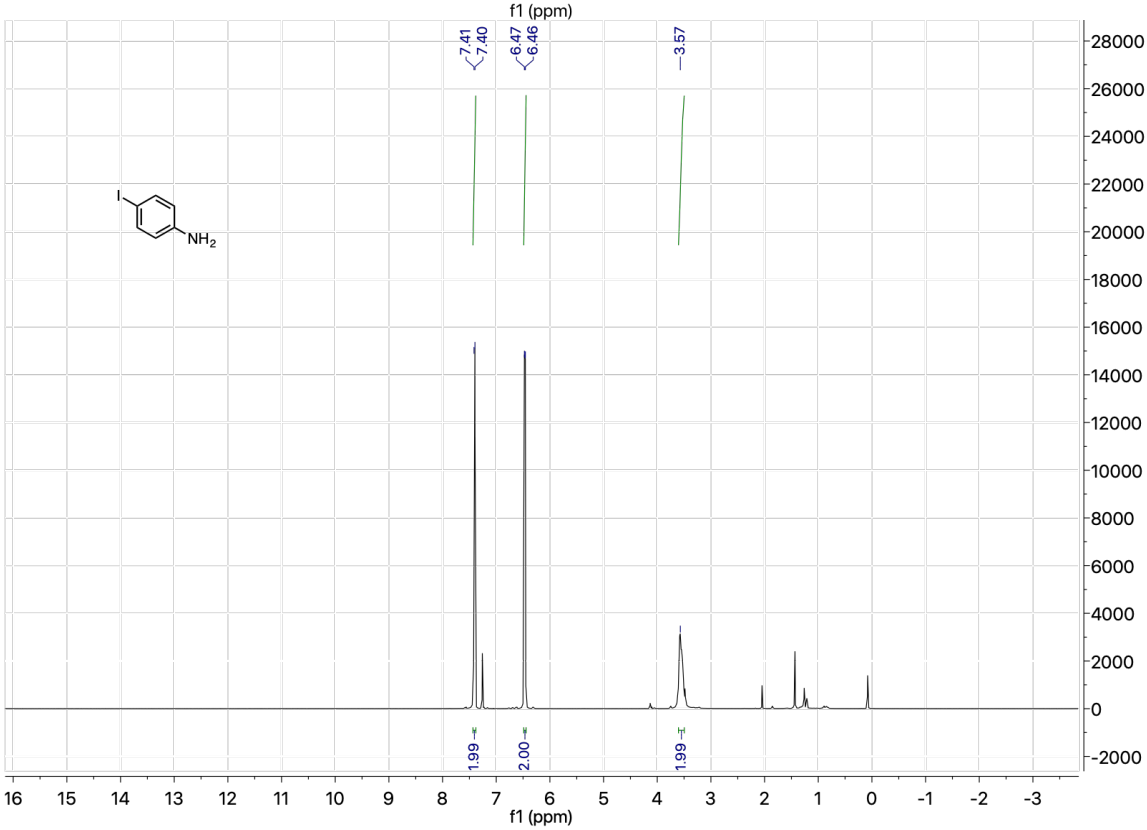
7.41
7.40
6.47
6.46
3.57
I
NH2
1.99
2.00
1.99
f1 (ppm)

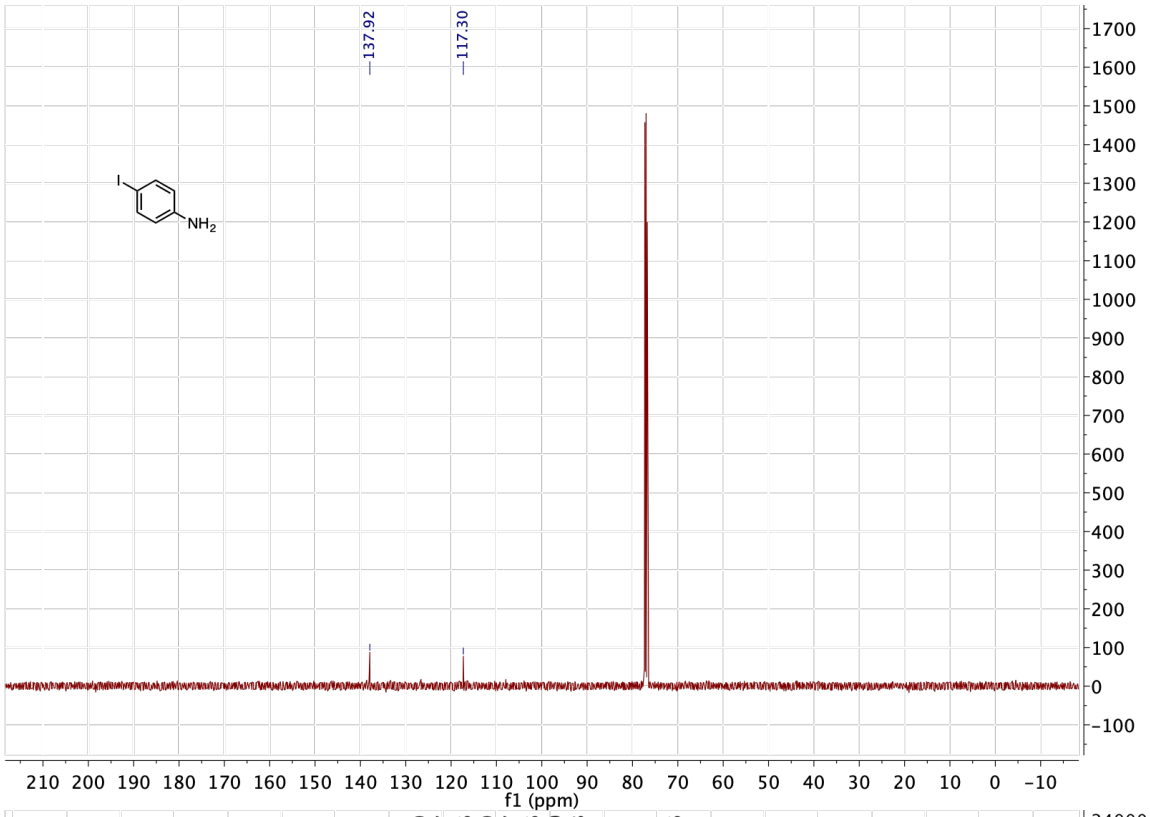
137.92
117.30
I
NH2
f1 (ppm)

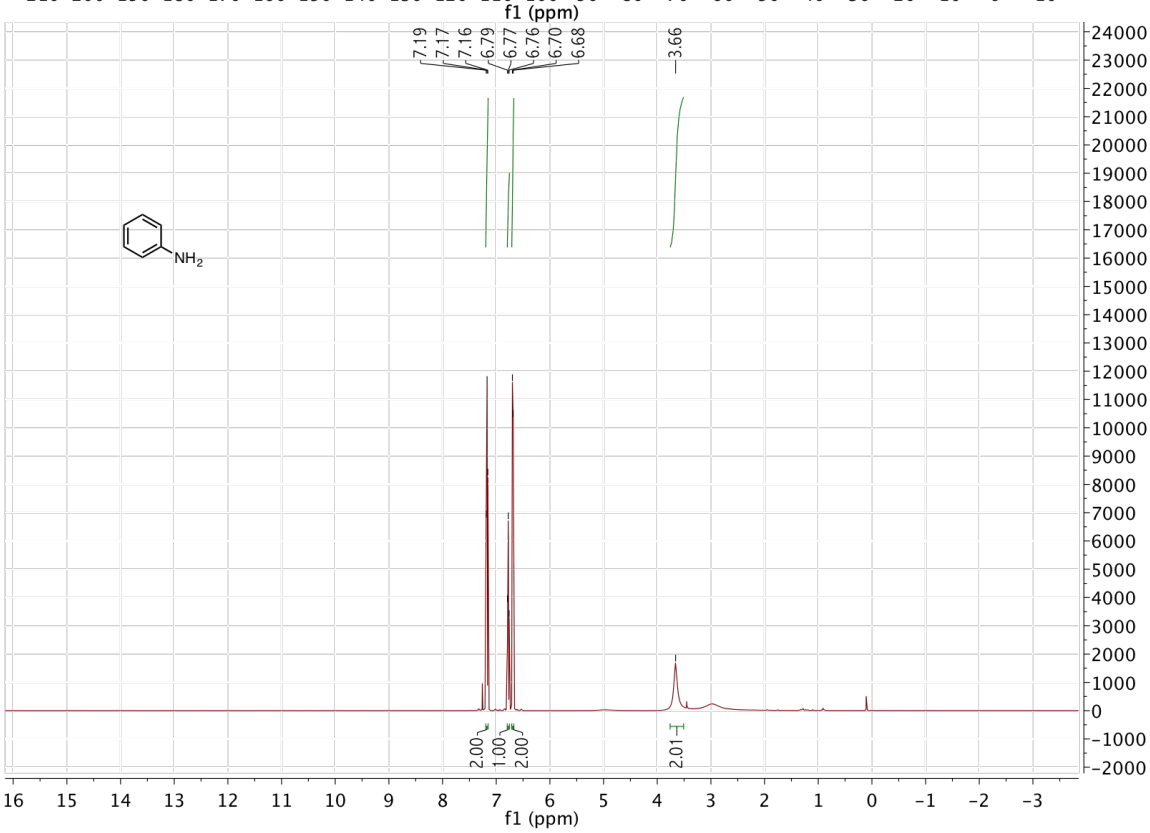
7.19
7.17
7.16
6.79
6.77
6.76
6.70
6.68
3.66
NH2
2.00
1.00
2.00
2.01
f1 (ppm)

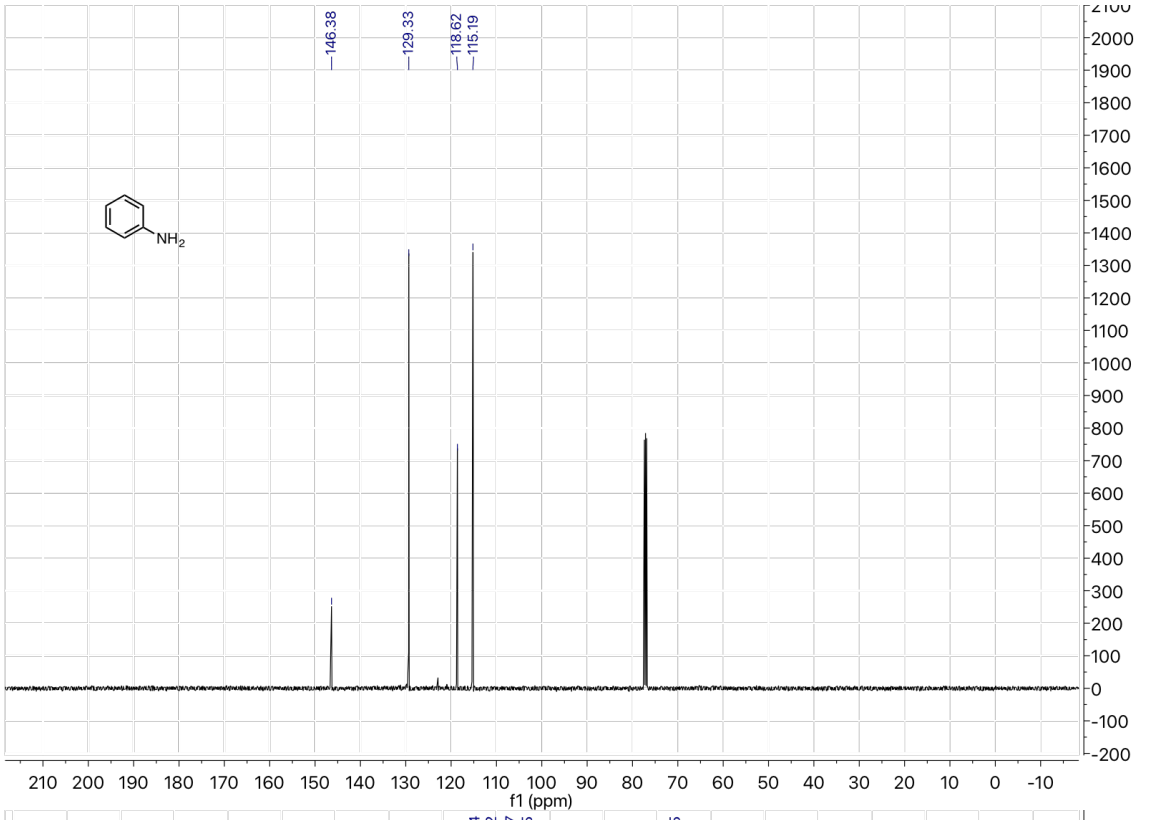
146.38
129.33
118.62
115.19
NH2
f1 (ppm)

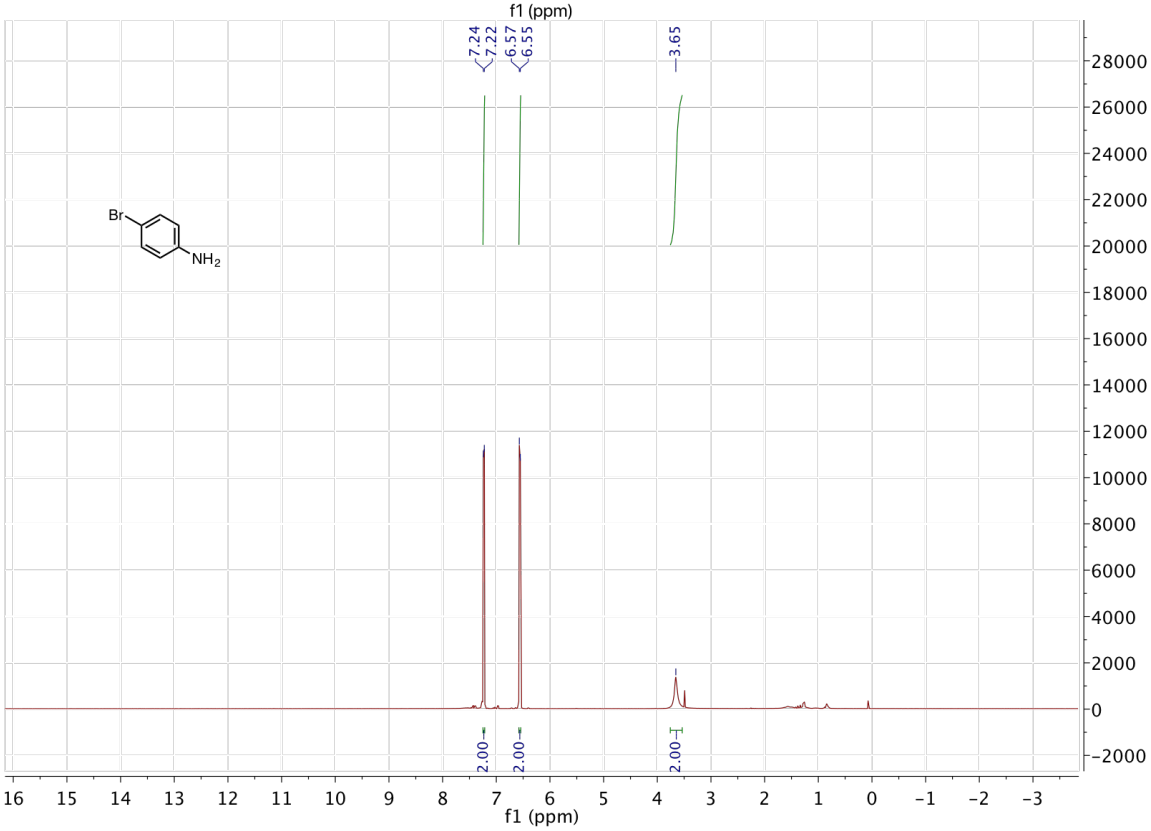
7.24
7.22
6.57
6.55
3.65
Br
NH2
2.00
2.00
2.00
f1 (ppm)

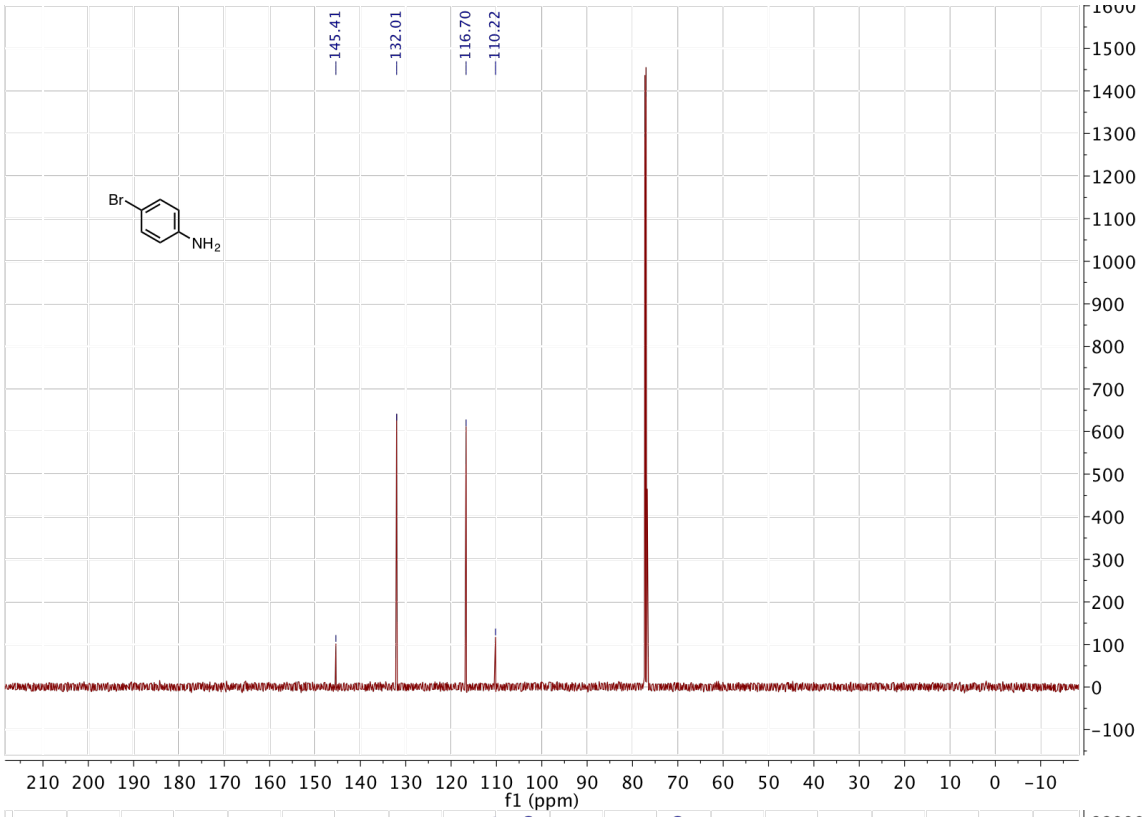
145.41
132.01
116.70
110.22
Br
NH2
f1 (ppm)

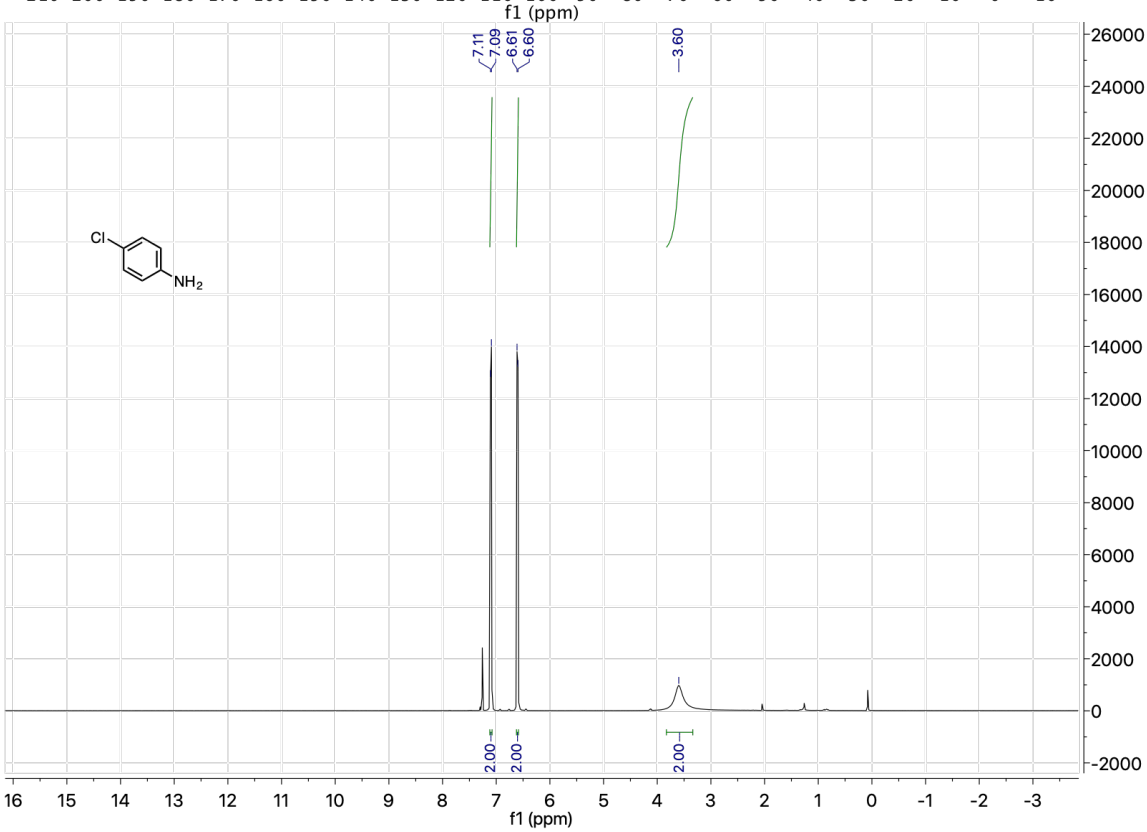
7.11
7.09
6.61
6.60
3.60
Cl
NH2
2.00
2.00
2.00
f1 (ppm)

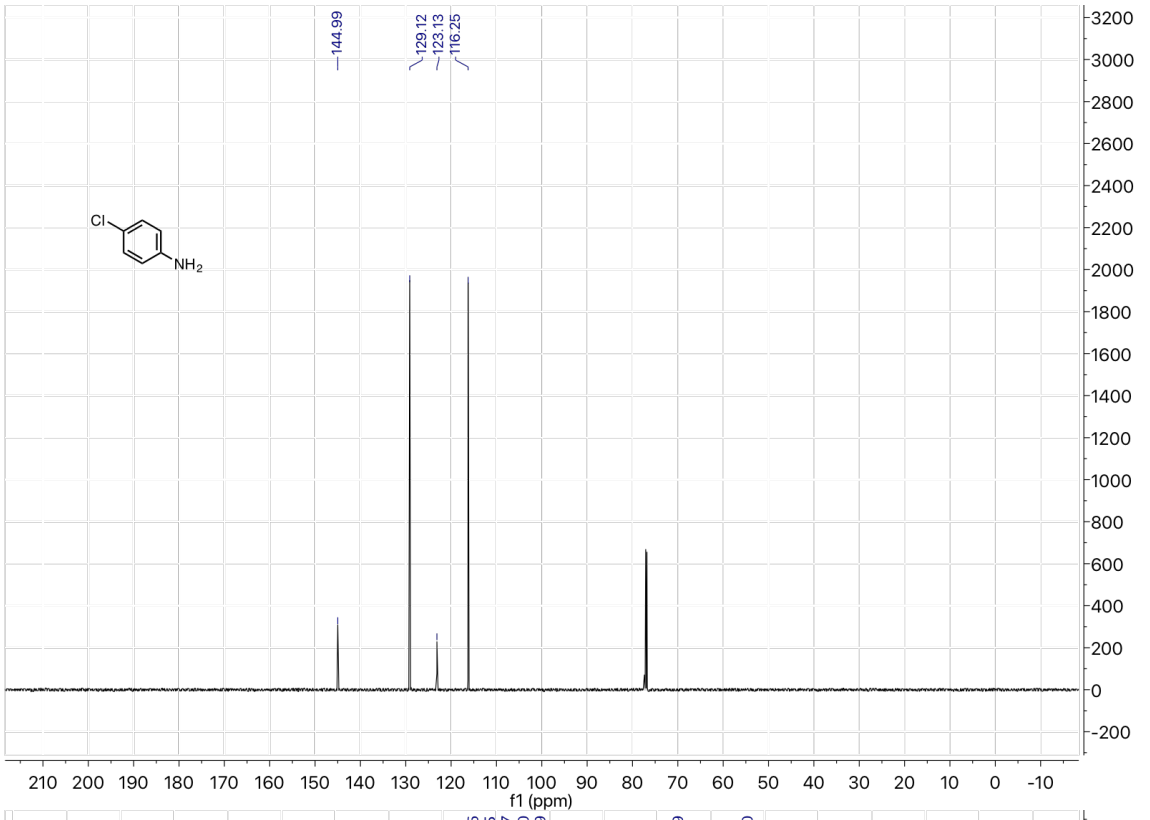
144.99
129.12
123.13
116.25
Cl
NH2
f1 (ppm)

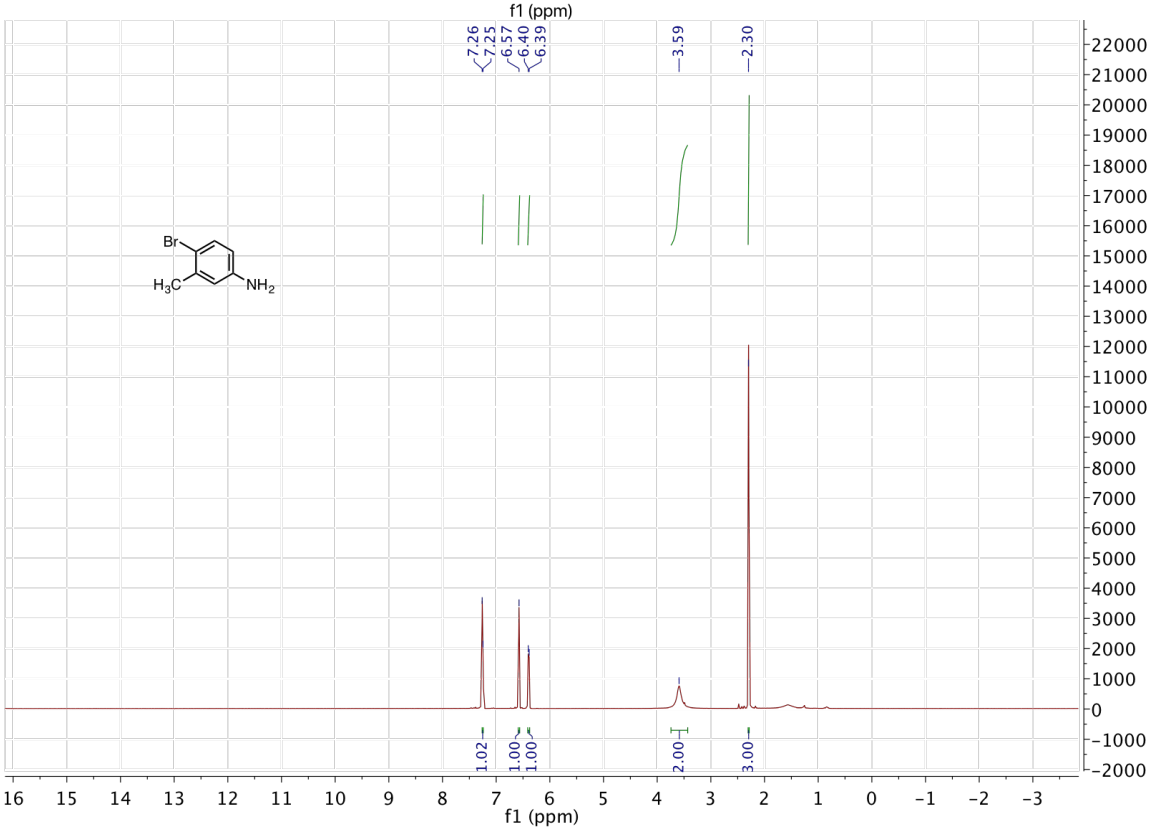
7.26
7.25
6.57
6.40
6.39
3.59
2.30
Br
H3C
NH2
1.02
1.00
1.00
2.00
3.00
f1 (ppm)

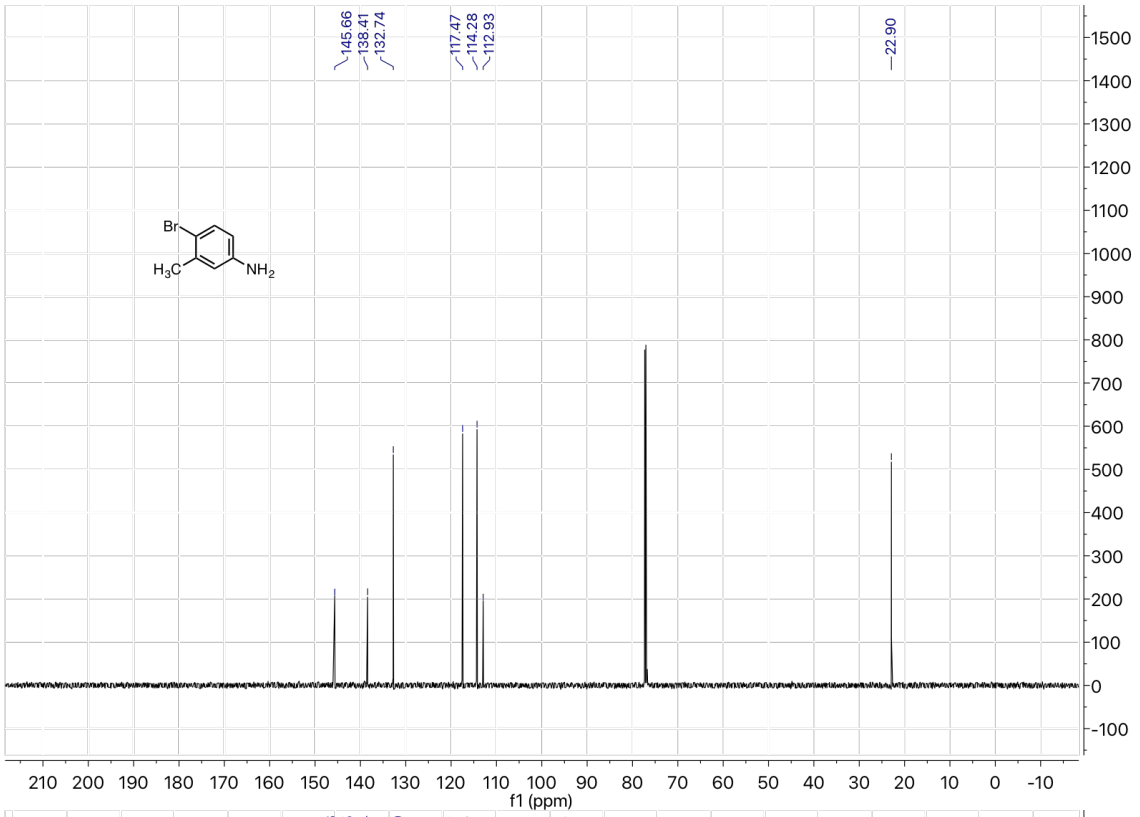
145.66
138.41
132.74
117.47
114.28
112.93
22.90
Br
H3C
NH2
f1 (ppm)

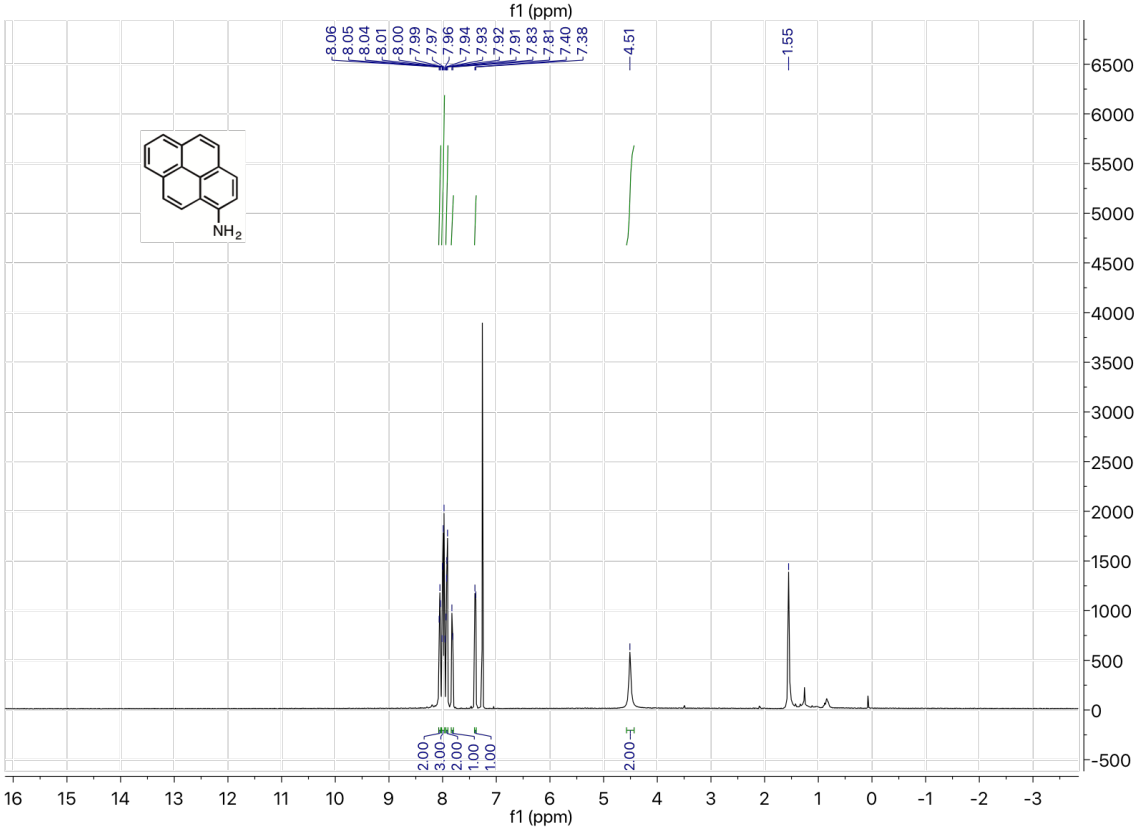
8.06
8.05
8.04
8.01
8.00
7.99
7.97
7.96
7.94
7.93
7.92
7.91
7.83
7.81
7.40
7.38
4.51
1.55
NH2
2.00
3.00
2.00
1.00
1.00
2.00
f1 (ppm)

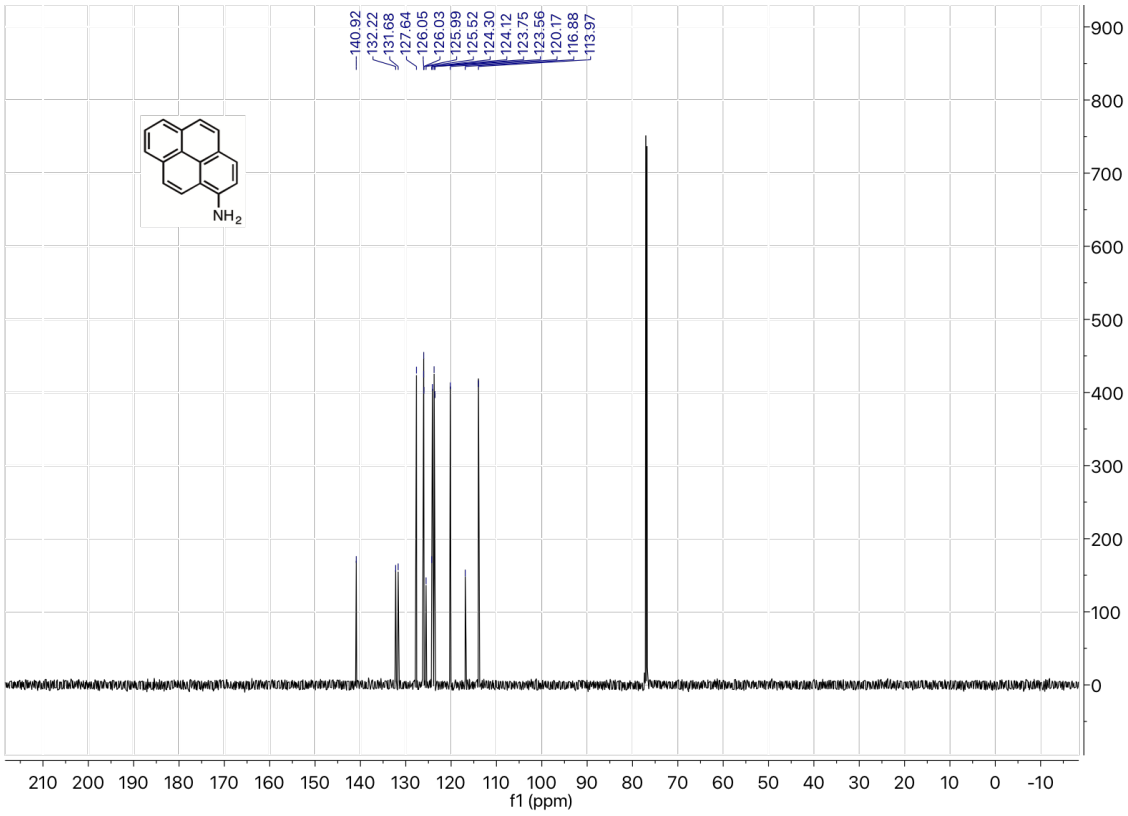
140.92
132.22
131.68
127.64
126.05
126.03
125.99
125.52
124.30
124.12
123.75
123.56
120.17
116.88
113.97
NH2
900
800
700
600
500
400
300
200
100
0
210 200 190 180 170 160 150 140 130 120 110 100 90 80 70 60 50 40 30 20 10 0 -10
f1 (ppm)

A.2 References

(1) Zhang, J.-W., Lu, G.-P.; Cai, C. Chemoselective Transfer Hydrogenation of Nitroarenes by Highly Dispersed NI-Co BMNPs. *Catal Commun*. **2016**, *84*, 25-29.

(2) Cantillo, D.; Moghaddam, M.M.; Kappe, C. O. C. O. Hydrazine-Mediated Reduction of Nitro and Azide Functionalities Catalyzed by Highly Active and Reusable Magnetic Iron Oxide Nanocrystals. *J. Org. Chem*. **2013**, *78*, 4530-4542.

(3) Kavala, V.; Naik, S.; Patel, B.K. A New Recyclable Ditribromide Reagent for Efficient Bromination under Solvent Free Condition. *J. Org. Chem*. **2005**, *70*, 4267-4271.

(4) Shen, Q.; Hartwig, J.F. Palladium-Catalyzed Coupling of Ammonia and Lithium Amide with Aryl Halides. *J. Am. Chem. Soc*. **2006**, *128*, 10028-10029.

(5) Jiang, L.; Lu, X.; Zhang, H.; Jiang, Y.; Ma, D. CuI/4-Hydro-L-proline as a More Effective Catalytic System for Coupling of Aryl Bromides with *N*-Boc Hydrazine and Aqueous Ammonia. *J. Org. Chem*. **2009**, *74*, 4542-4546.

(6) Trunz, B.B.; Jędrysiak, R.; Tweats, D.; Brun, R.; Kaiser, M.; Suwiński, J.; Torreele, E. 1-Aryl-4-nitro-1*H*-imidazoles, a new promising series for the treatment of human African trypanosomiasis. *Eur. J. Med. Chem*. **2011**, *46*, 1524-1535.

(7) Wang, C.-Y.; Fu, C.-F.; Liu, Y.-H.; Peng, S.-M.; Liu, S.-T. Synthesis of Iridium Pyridinyl N-Heterocyclic Carbene Complexes and Their Catalytic Activities on Reduction of Nitroarenes. *Inorg. Chem*. **2007**, *46*, 5779-5786.